New Thermodynamic Equilibrium and Computational Fluid Dynamics Approaches for Modelling Biomass Gasifiers

IBRAHIM, AHMAD

New Thermodynamic Equilibrium and Computational Fluid Dynamics Approaches for Modelling Biomass Gasifiers.

Ahmad Ibrahim

A Thesis presented for the degree of
Doctor of Philosophy

Department of Engineering
Durham University
United Kingdom
July 2025

Abstract

Two different routes can be taken to produce valuable energy from biomass: thermochemical and biochemical conversion routes. The focus of this thesis is the subject of the former, namely biomass gasification by addressing the challenges that come with the optimisation and operation of an efficient biomass gasifier using detailed equilibrium and computational fluid dynamics models.

An advanced and comprehensive thermochemical equilibrium model for a downdraft biomass gasifier has been developed to enhance the understanding of gasifier behaviour near equilibrium conditions via prediction of the syngas yield from the reduction zone. The model incorporates the thermodynamic equilibrium of the overall gasification reaction through a stoichiometric approach and includes the prediction of minor gasification byproducts, specifically hydrogen sulphide and ammonia, as sulphur- and nitrogen-based contaminants, respectively. A key feature of the model is the incorporation of a new empirical correlation, derived from relevant existing experimental data, to account for tar mass yield in generic downdraft biomass gasifiers. Additionally, the governing model equations are solved in a fully coupled manner, with the Boudouard reaction applied to predict char yield and the ammonia synthesis reaction used to estimate ammonia production. Notably, the model operates without correction factors and effectively predicts methane concentration, addressing a limitation commonly observed in existing equilibrium models. The outputs of the model include syngas composition, tar and char yields, gasification temperature, cold gas efficiency, and lower heating value for various biomass feedstocks with specified ultimate analyses, across a range of equivalence ratios and moisture contents. Where available, model predictions are compared to corresponding experimental data and demonstrate strong agreement.

Next, computational fluid dynamics is utilised to model a downdraft biomass gasifier through an established solver incorporating the porous media assumption. A detailed and comprehensive chemical reaction scheme is constructed, portraying the chemical reactions occurring in a real unit, efficiently identifying the appropriate range of operating conditions by which the system yields optimum products

by tuning the working parameters accordingly to satisfy the production of species from the chemical reactions. The solver, originally designed for modelling biomass gasification in fixed-bed applications, is adapted to include a moving porous bed. Another novel feature of the model is its automatic replenishment functionality, which allows the biomass feedstock to be continually supplied from the top while generating desirable output products at the bottom. The porous bed includes a self-propagating front which facilitates chemical reactions. Transport equations are formulated inside the porous media by applying the spatial averaging methodology and responsible for predicting solid and gas temperature profiles, product gas composition, flow velocity, porosity distribution, and more. The resulting predictions are compared against existing experimental results and those from different CFD approaches for downdraft gasifiers, highlighting the applicability of the solver in addressing fixed-bed biomass gasification challenges.

Declaration

The work in this thesis is based on research carried out at the Department of Engineering, Durham University, United Kingdom. No part of this thesis has been submitted elsewhere for any other degree or qualification and it is all my own work unless referenced to the contrary in the text.

Acknowledgements

All praises and thanks to God for giving me the strength, health, and patience to complete this body of work. My journey through the academic and research process has been filled with challenges and moments of inspiration, and I believe that God's guidance and grace have played an integral role in this endeavour. I would like to express my deepest gratitude to the following individuals and institutions who have played an indispensable role in the completion of this thesis:

My Family

I am extremely grateful to my family for their unflagging encouragement, love, and understanding during the highs and lows of my doctorate journey. Their unwavering belief in me has been a constant source of motivation.

My Supervisors - Dr Sergii Veremieiev and Professor Philip H Gaskell

I am proudly thankful to both my supervisors, Dr Sergii Veremieiev and Professor Philip H Gaskell, for their unwavering support, guidance, and invaluable insights throughout my time as a research student at Durham University. Their dedication to fostering my academic growth and their patience in reviewing and refining this thesis have been instrumental in shaping the final outcome of the body of work.

My Review Team - Professor Grant Ingram and Dr Lian Gan

I extend my sincere appreciation to the members of my Review Team, Professor Grant Ingram and Dr Lian Gan, for their constructive feedback, thoughtful suggestions, and expertise in their respective fields. Their input has enriched the quality and depth of this thesis.

Dr Pawel Zuk

I would like to acknowledge and thank Dr Pawel Zuk for his patience, support, and guidance in offering mentorship and inspiration, playing a pivotal role in shaping my research interests. Dr Zuk has contributed to manipulating an existing code to suit a porous bed motion and a replenishment feature, and focused time and effort in my understanding of the model assumption.

Dr Ahmed Salem

I would like to also extend my gratitude and thanks to Dr Ahmed Salem for their continuous support in offering invaluable theoretical insights related to my work.

I would like to acknowledge the indispensable resources and facilities offered by Durham University, including all the academic, IT, technical, and administrative staff members of the University, specifically the Engineering Department for their continuous support and help in my research journey.

Thank you to all those mentioned above and countless others who have contributed, directly or indirectly, to the completion of this thesis. Your support and encouragement have been instrumental in this research project.

Contents

List of Figures

List of Tables

List of Symbols

A	Pre-exponential factor (s^{-1})
A_s	Cross-sectional area (m^2)
a	Absorption coefficient (m^{-1})
C_{conv}	Convective heat transfer coefficient
C_{mass}	Mass transfer coefficient
C_p	Specific heat capacity (J/kg K)
Da_i	Damkohler number (W/m^2)
D_c	Darcean resistance (m^{-2})
D_{eff}	Fluid diffusion coefficient
E_s	Equivalent emission of solid
G	Incident radiation (W/m^2)
h	Enthalpy (J/mol)
s	Entropy (J/mol K)
h_{vap}	Enthalpy of vaporisation of water at standard temperature
M	Molar mass of chemical species (kg/mol)
m	Mass (kg)
m_{gas}	Number of moles of gasifier input air per one mole of biomass

m_{comb} Number of moles of combustion input air per one mole of biomass

N_{gas} Number of moles of dry producer gas

R Universal gas constant (J/mol K)

y_i Weight percentages of chemical species (%)

t Time (s)

k_{eff} Thermal conductivity (W/m K)

g Gibbs free energy (J/mol)

x_i Number of moles of gaseous species in the gasification reaction

z_i Number of moles of gaseous species in the combustion reaction

n_i Number of moles of gaseous species in the pyrolysis reaction

$\dot{m}$ Mass flowrate (kg/s)

T Temperature (K)

p Pressure (Pa)

u Velocity (m/s)

Y Mass fraction

X Mole fraction

V Volume (m^3)

$\mathbf{g}$ acceleration due to gravity (m/s^2)

K Anisotropy tensor of solid matrix

N Total number of time steps

Greek Symbols

α Number of atoms of hydrogen in the biomass feedstock

β Number of atoms of oxygen in the biomass feedstock

λ Number of atoms of nitrogen in the biomass feedstock

δ Number of atoms of sulphur in the biomass feedstock

ϵ Porosity

ρ Density (kg/m^3)

ν Stoichiometric coefficients

γ	Lagrange multiplier
μ	Dynamic viscosity
Ω_r	Rate of reaction
$\dot{\omega}$	Volumetric mass change
$\sigma_{scatter}$	Scattering coefficient

Abbreviations

CFD	Computational Fluid Dynamics
CGE	Cold gas efficiency (%)
DBG	Downdraft Biomass Gasifier
ER	Equivalence ratio
FC	Fixed carbon in the fuel (%)
HGE	Hot gas efficiency (%)
HHV	Higher heating value (J/kg)
HTAG	High Temperature Agent Gasification
LHV	Lower heating value (J/kg)
MC	Moisture content in the fuel (%)
RMSD	Root-mean-square deviation
SV	Superficial velocity (m/s)
SA	Surface area to volume ratio
2D	Two-dimensional
1D	Three-dimensional
VM	Volatile matter in the fuel (%)

Dedication

To my family,

For the unwavering support, endless encouragement, and boundless love that have been the pillars of my journey. Your belief in me has been my greatest inspiration.

CHAPTER 1

Introduction

1.1 Biomass as a renewable energy source

Fossil fuels such as coal, oil, and gas are a convenient source of energy production having, for many decades, effectively met the energy demands of the global economy. They currently supply around 80% of the global energy requirement [1]. However, a major and increasingly urgent problem associated with this is that when fossil fuels burn they release an abundant amount of carbon dioxide (CO_2), a greenhouse gas, into the air, trapping heat in the atmosphere and consequently contributing to the current global warming crisis. Furthermore, they contain impurities that can generate pollutants such as sulphur dioxide (SO_2), nitrogen oxides (NO_x), and particulate matter during gasification. With growing evidence of the climate change effects of global warming, environmental awareness has increased causing a global energy shift toward the use of dependable, affordable and cleaner alternatives [2]. Biomass has become one such promising avenue, as its modern application is considered a very optimistic clean-energy alternative. Although biomass production is invariably accompanied by the release of CO_2, it is still widely viewed and referred to as a renewable energy source. Arguably, at present it is the only renewable that

can directly replace fossil fuels due to its abundant availability, simple storage and transportation requirements, and its synthesis of different fuels and chemicals [2].

Useful gaseous and liquid end products can be obtained from biomass through two major conversion pathways: thermochemical and biochemical processes. The thermochemical conversion route umbrella consists of four processes:

1. Combustion
2. Gasification
3. Pyrolysis
4. Liquefaction

Combustion involves high temperature conversion of biomass into CO_2 and steam in the presence of excess air. Gasification, on the other hand, involves a chemical reaction in an oxygen-deficient environment whereby the biomass is mainly converted into carbon monoxide (CO) and hydrogen (H_2). Pyrolysis occurs at relatively low temperatures (400-800 °C) in the total absence of oxygen. Finally, liquefaction involves the decomposition of large feedstock molecules into smaller molecule liquids at relatively low temperatures and in the presence of a catalyst. From the above conversion technologies gasification, specifically biomass gasification, comes with renewability, environmental and socio-political benefits [2].

- Renewability: Biomass is renewable as it is unlikely to be depleted with consumption due to its CO_2 cycling feature mentioned above.
- Environmental: The gasification of a biomass fuel emits less CO_2 from its combustion on a unit heat release basis. Furthermore, it is easier to extract sulphur from gasification than combustion. For example, the sulphur in combustion appears in the form of sulphur dioxide, which is relatively difficult to remove from the flue gas. However, in gasification the sulphur appears mostly in the form of hydrogen sulphide, resulting in an easier extraction of the sulphur by absorption.

- Socio-political: Biomass is a locally sourced resource, and for a biomass-based power plant to achieve economic viability, its feedstock must ideally be sourced within a limited radius. This localised sourcing requirement supports the growth of industries related to biomass cultivation, collection, and transportation in the surrounding area. Furthermore, fluctuations in the global political landscape have shown that supply chains and feedstock prices can be highly volatile, leading to sudden increases in costs. In contrast, locally produced biomass offers a more stable supply, less susceptible to such uncertainties.

Biomass gasification converts carbonaceous materials into a biofuel made up of syngas, a mixture of H_2 and CO in a high temperature environment, usually between 800-1100°C [3], using air, steam or oxygen as a gasification agent. The end product is also termed producer gas as it consists of various other species such as methane (CH_4), CO_2 and water vapour (H_2O). Gasification is more efficient than direct combustion as it provides increased conversion rates and a higher quality syngas, containing a higher energy content. The produced syngas can be further treated downstream for use in gas engines, to produce methanol and ammonia, or converted to synthetic fuel via the Fischer-Tropsch process [2].

At present the gasification of fossil fuels, such as coal and natural gas, occurs more frequently than of biomass as it is more convenient in today's energy industry than its renewable counterpart for a number of reasons. Firstly, fossil fuels are often more readily available and less expensive than biomass feedstocks. Secondly, the gasification of fossil fuels has been more extensively researched, developed, and commercialised compared to biomass gasification, presenting a more mature infrastructure and an established supply chain for fossil fuel gasification [2, 4]. Fossil fuel and biomass gasification both produce syngas, however the difference in their contributions to greenhouse gas emissions lies primarily in the carbon cycle and the source of carbon (C) involved. When fossil fuels are gasified, the C within them is released back into the atmosphere as CO_2, adding it to the atmospheric carbon pool, and increasing the concentration of greenhouse gases. On the other hand, when biomass is gasified, the CO_2 released is roughly equal to the amount that was absorbed by the biomass material during its formation/growth. As a result, there is no addition of

CO_2 to the atmosphere [5]. Consequently, biomass gasification is becoming increasingly prominent due to its sustainability and renewability characteristics. Gasifiers come in different types, each with their own design specifications and performances depending on biomass type, its moisture content (MC), the gasification agent used and the power required to generate output. Furthermore, a typical gasifier is split into distinct zones, each playing an important role in producing desired outputs.

The refinement of a particular gasification process, either by performing experimental investigations or through the use of mathematical models, requires extensive knowledge of the underlying behaviour which encompasses complex chemical and physical interactions between multi-phases. This thesis addresses issues in relation to the development of different biomass gasification mathematical models, their solution and ability to predict a required end-product, leading to an effective research advancement in the field.

1.2 Research Challenges and Opportunities

The intricate physical and chemical processes occurring within a biomass gasifier pose significant modelling challenges in determining the optimal operating conditions. Different predictive modelling approaches require a well-matched homogeneous and heterogeneous chemical reaction scheme, tuned to the appropriate operating parameters, to ensure a stable conversion of biomass feedstock into the desired syngas output. The relative proportions of H_2 and CO in syngas is an important consideration; even so, due to the highly heterogeneous nature of biomass feedstock, accurately predicting the syngas ratios based solely on physical and chemical properties has proved a formidable task. Consequently, precise specification of the operating conditions becomes essential to achieve the desired syngas composition effectively.

Furthermore, the generation of tars as an undesirable by-product of biomass gasification poses a significant challenge and has become a subject of extensive investigation [2]. Tars are unwanted because of their tendency to cause condensation, leading to blockages in downstream equipment and other operational issues.

Additionally, their dynamic behaviour makes modelling them complex. Therefore, a primary focus of the current study has been the effective determination of the boundaries of tar formation within biomass gasifiers, with the goal of minimising their production whenever feasible.

Lastly, the development of a Computational Fluid Dynamics (CFD) model using the open-source software OpenFOAM adds a unique aspect to this study. OpenFOAM-based CFD models for biomass gasification are scarce in the literature, with most previous such models having relied on the use of Ansys Fluent [6] and other CFD software due to the perceived simplicity in studying and analysing gasifier behaviour. This is primarily attributed to the lack of a built-in solver in OpenFOAM's database for effectively simulating fixed bed configurations with heterogeneous reactions associated with downdraft gasifiers. Consequently, a pre-established solver with functionalities closely aligned to the desired objectives is utilised, leading to the additional challenges highlighted below.

The first of these is the need to become familiar with OpenFOAM's chemical solver, a tool that has never been employed previously in the analysis of the chemical and physical interactions within biomass gasification. The second key challenge lies in handling of the intricate gasification chemical reaction scheme, as the recently developed solver [7] has not undergone extensive analysis under such complex conditions. This requires determining whether the chemical reactions are sufficiently exothermic to sustain a propagating front or if they will extinguish via a thorough examination of the kinetic parameters of the reaction scheme.

Next, dealing with the multiphase nature of a biomass gasifier introduces complexities related to mass and heat transfer within both the gas and solid phases. The implementation of the reaction scheme further complicates the identification of specific reactions occurring in different parts of the gasifier, especially when distinguishing the various reacting zones in a downdraft gasification unit. The CFD model proposed here relies on the porous media assumption, which adds another layer of complexity in determining the equivalence ratio (ER) and initial conditions of the system. The ER is a critical operating parameter in air gasification, significantly influencing gas quality and gasification temperature. To precisely identify

the ER, a meticulous and systematic procedure had to be established, taking into consideration the amount of consumed air within the system.

1.3 Novelty and Key Findings

To address the issues outlined above, the overall aim of the thesis is to develop two comprehensive predictive mathematical models in order to tackle the research gaps. The models are compared with both corresponding experimental data and the theoretical work of others, where such comparisons are possible.

The first is a thermochemical equilibrium model, which utilises the stoichiometric global gasification reaction. It incorporates a new empirical correlation, derived from relevant experimental data, to more accurately predict the mass tar yield. Additionally, it calculates the gasification temperature through an energy balance using a coupled system of equations, resulting in improved convergence properties. The model also includes the boudouard reaction to predict char formation and considers the production of minor contaminating species, investigating their influence under varying operating conditions. Furthermore, the syngas composition predicted by the model is validated against experimental data obtained from various state-of-the-art downdraft biomass gasifiers (DBGs).

The principal outcomes of the constructed equilibrium model encompassed verified syngas composition, gasification temperature, tar and char yields, and the levels of sulphur-based and nitrogen-based contaminant gases. These findings were explored for different operating conditions, particularly varying ER and MC. Moreover, an analysis of the syngas energy content was conducted under varying operational parameters. Conclusions are drawn: regarding the reliability of the tar empirical correlation; involving a detailed parametric study of the predictions obtained; concerning affirmation that the model offers reliable estimations across a broad spectrum of outcomes without the need for corrective adjustments.

Subsequently, a CFD model is presented and solved within the open-source software OpenFOAM environment. It employs a recently-compiled solver called **porousGasificationFoam** [7], specifically designed for thermal and chemical con-

version in a stationary porous media. This choice was motivated by the absence of a built-in solver in OpenFOAM's database that can handle coupled homogeneous and heterogeneous reactions, which are typical in fixed bed gasification systems. The CFD model incorporates a comprehensive chemical reaction scheme that mirrors a real DBG. It distinguishes between distinct zones participating in the gasification process at the initial and transient conditions, namely the drying, pyrolysis, oxidation, and reduction zones, offering insights regarding the regions in which endothermic and exothermic chemical reactions are taking place.

The solver is adapted to account for a moving porous media bed, where the biomass feedstock is replenished from the top and undergoes a series of physical and chemical processes, generates the desired outputs and allows for the simultaneous occurrence of homogeneous and heterogeneous chemical reactions. Unlike previous CFD models in which chemical reactions are restricted in gasifier zones, the proposed CFD model utilises a chemical reaction scheme which occurs simultaneously, instead of a sequential output-input relationship.

The findings from using the CFD model included a validated syngas composition, gas and solid phase temperature profiles, tar and char yields, velocity profiles, and porous media distribution encompassing the biomass and humidity consumption. The predictions were explored for different operating conditions, particularly varying the air velocity and the inlet air temperature. The varying of operating parameters in the model lead to the enhancement of the gasification process to yield a better quality syngas composition. Conclusions are drawn: regarding the effect of certain operating conditions on the conversion efficiency of the gasifier and the effective use of the porous media assumption in tackling fixed bed gasification applications.

1.4 Thesis structure

The thesis is structured as follows:

Chapter 1 motivates biomass as a renewable energy source, addressing the necessity for cleaner energy production methods and highlighting the inadequacies of current outdated techniques. Various thermochemical conversion methods are

discussed, with particular emphasis on the advantages of gasification over other approaches. The research challenges in the field of biomass gasification modelling are mentioned, emphasising the opportunities available to tackle them in the present study. Finally the novelty and key findings from the developed models are briefly discussed, underscoring the contributions made within the field of biomass gasification modelling.

Chapter 2 includes an appraisal of the past modelling work and experimental investigations carried out for DBGs. A thorough analysis of prior work is provided, evaluating the significance and contributions of each study to the field of biomass gasification.

Chapter 3 provides a comprehensive overview of the biomass gasification process. It introduces the fundamental concept of biomass, focusing on its properties and composition. A detailed examination of the gasification process follows, including an analysis of its stages, types of gasifiers, and the chemical reactions intrinsic to the process. The discussion extends to the influence of diverse operating conditions on gasifier performance and subsequently offers insights and detailed analyses of the different modelling approaches one can implement to design a gasification model.

Chapter 4 introduces the formulations implementation and method of solution of the new thermodynamic equilibrium model. The results of which are discussed and comparisons made with complementary experimental data and existing theoretical results. In particular, the effects of varying operating parameters are explored.

Chapter 5 introduces the methodology and solution techniques utilised to construct a comprehensive and predictive CFD model of a downdraft gasifier. The results obtained are compared against relevant experimental and modelling outputs. The chapter also highlights distinctive outcomes and novel insights generated by the model.

Chapter 6 summarises the research findings. Recommendations for future research are provided, emphasising areas that require further exploration and development.

1.5 Summary

This chapter offers a clear motivation for the research undertaken, providing definitions for the subject matter and demonstrating its benefits. The research challenges are subsequently elaborated, pinpointing gaps in the existing literature and outlining how this thesis aims to address them. Additionally, it emphasises the uniqueness of the study, highlighting its key discoveries. Lastly, the chapter outlines the structure of the thesis, providing insight into its progression. This positions the outlined work to undergo a thorough literature review, which will be presented in the following chapter.

CHAPTER 2

Literature Review

A thorough and detailed appraisal is provided below of the relevant experimental and theoretical modelling work conducted to-date on DBGs. These include those which have been used for the purposes of supporting the results of the modelling work reported here, and validation of the same. Since modelling is the primary focus of the thesis, the review provided delves into the core discoveries of each approach, tracing their development from simplified models to recent advancements within the specific field. Additionally, it explores their limitations and identifies areas where further enhancements are needed by addressing the key knowledge gaps in the existing literature. A similar examination is undertaken in relation to related experimental investigations, highlighting the contributions made to the advancement of this field. Such investigations have played a pivotal role in progressing fundamental knowledge and insights, which, in turn, can be harnessed for the validation of mathematical models, as is the case in Chapter 4 in particular.

2.1 Thermodynamic Equilibrium Models

Thermodynamic equilibrium models play a crucial role in elucidating the complex chemical processes in DBGs by predicting the equilibrium composition of gasification products. The models are used to estimate major gas species, such as CO, CO_2, and N_2, though they tend to overestimate H_2 and underestimate CH_4. Their predictions provide valuable insights into energy content and gas utilisation, aiding in process optimisation.

Researchers have extensively examined the influence of operating parameters (e.g., temperature, pressure, ER) and feedstock characteristics (e.g., MC, ash content) on gas composition and heating value. Equilibrium models also help identify conditions that promote undesirable tar formation, guiding strategies for its minimisation. However, due to their assumption of chemical equilibrium, they struggle to accurately predict tar content and capture the full complexity of gasification kinetics.

Despite their adaptability to various biomass feedstocks, equilibrium models often omit minor contaminating species (e.g., H_2S, NH_3), which arise from certain biomass compositions. Sensitivity analyses and optimisation efforts, including empirical corrections, enhance model alignment with experimental data but compromise reliability. To address these limitations, equilibrium models are increasingly integrated with kinetic models and detailed chemical mechanisms, offering a more comprehensive representation of the gasification process.

2.1.1 Detailed appraisal of contributions to the field

Zainal et al. [8] developed a stoichiometric equilibrium model and applied to various feedstock to determine the composition of the resulting syngas and the oxygen content in a DBG by utilising a simplified iteration of (R17) - see section 3.4.1.1 in Chapter 3. They investigated the effects of the initial MC and the temperature in the gasification zone on the calorific value and the produced syngas. They concluded how different components constituting the producer gas is influenced with increasing MC. At the time of its development, the model was a first-of-its-kind, but

failed to show how predictions compare with pertinent experimental data or provide any validation of the results.

Mountouris et al. [9] also developed an analogous model, which focused on the thermodynamic assessment of plasma gasification. Their study involved estimating the resultant gas composition, conducting energy and exergy analyses. Interestingly, their model employed the same simplified version of (R17), albeit with the inclusion of C as an additional by-product. Notably, their model illustrates the variability of predictions in response to changes in MC and temperature. This serves to offer a comprehensive parametric analysis of biomass gasification. It also surpasses the model introduced by Zainal et al. [8] by its capability to predict soot formation. However, it is important to note that like the former model, this one also lacks validation against experimental results.

Following this, Melgar et al. [10] proceeded to construct a stoichiometric equilibrium model that expanded its scope to encompass additional constituents of the overall gasification reaction, including O_2 and SO_2. To achieve chemical equilibrium within the system, they incorporated reactions (R11) and (R5) of section 3.3.3 in Chapter 3. Through their predictions, the model effectively computes the calorific values of the resulting syngas and the Cold Gas Efficiency (CGE). This effort provides not only a means of validating the model but also facilitates a parametric analysis of the projected outcomes.

A streamlined thermodynamic equilibrium model, specifically tailored to municipal solid waste as the biomass feedstock was devised by Jarungthammachote et al. [11] . This model hinged on the utilisation of thermodynamic equilibrium constants governing gasification reactions. To ascertain gasification temperature, they harnessed the Newton-Raphson method. Additionally, the model incorporates correction factors to fine-tune the equilibrium constants of the chemical reactions, aiming for improved alignment with experimental data. Regrettably, this model, akin to previous ones, fell short in substantiating its predictions through relevant experimental validation.

Sharma [12] later formulated a thermodynamic equilibrium model designed to prognosticate syngas composition and reaction temperature. The latter was initially

estimated and subsequently refined through an iterative process. While this model relies on a simplified rendition of the overarching gasification reaction, it also introduces a kinetic counterpart in tandem with the equilibrium model. This kinetic model was constructed based on reaction rates associated with char reduction zone reactions. This dual approach facilitated a robust comparison between equilibrium and kinetic models, allowing for their predictions to be benchmarked against experimental data. Impressively, both modelling methodologies demonstrate commendable agreement with the experimental results. Furthermore, the work incorporated a parametric study to illustrate the impact of temperature on syngas composition.

An equilibrium model grounded in the overarching gasification reaction, augmented by the incorporation of H_2S as a by-product was developed by Huang et al. [13] . This model meticulously considered elemental balances of the involved species and the associated chemical reactions to compute equilibrium constants. Notably, the model encompassed a diverse array of biomass feedstocks, thereby offering insights into the divergent predictions stemming from distinct biomass sources. While the model demonstrated adeptness in aligning syngas composition with experimental data, its performance dwindled when incorporating char into the model. Consequently, the researchers employed correction factors to rectify the model's composition, encompassing char as a gasification by-product.

Karamarkovic and Karamarkovic. [14] developed a thermochemical equilibrium model that deals with investigating the efficiency and potential improvements of the gasification process, highlighting the significance of temperature in influencing energy and exergy losses. They employed mass balances of gas species as well as achieving chemical equilibrium from chemical reactions. The key findings of the study highlight the temperature-dependent trends in energy and exergy efficiencies. The analysis reveals the temperature range within which the gasification process achieves optimal efficiency in terms of energy and exergy utilisation. Additionally, the study aids in uncovering the mechanisms driving energy and exergy losses at different temperatures, shedding light on potential areas for improvement.

Abuadala et al. [15] conducted a comprehensive parametric study on H_2 production through steam gasification. In their investigation, they assumed that 5% of the

biomass C content remains unreacted as char, and tar was modelled as benzene, employing the empirical correlation proposed by Corella et al [16]. The simulation of steam gasification involved varying the biomass quantity while keeping the steam and gasifier temperature constant, followed by changing the operating temperature while maintaining a constant amount of steam and biomass. The model is able to identify biomass quantity and temperature influences on the predicted syngas composition. The work concludes that higher steam-biomass ratios lead to a weak enhanced H_2 production, particularly in bench-scale units.

Vaezi et al. [17] devised a stoichiometric equilibrium framework to investigate the gasification process of heavy fuel oils. The predicted syngas composition was achieved from material balances and equilibrium constants of the global gasification reaction, and demonstrates how the predictions are influenced by operating conditions such as temperature, pressure and ER. A key finding of the model provides valuable insights into the feasibility and behaviour of gasifying heavy fuel oils. The research reveals the potential composition of syngas and highlight the challenges associated with the gasification of such complex feedstocks. The study concludes that the gasification of heavy fuel oils at an ER of 0.32, yields a considerable calorific value of the syngas. However, the model does not take into account the production of some important and unwanted by-products of gasification.

A stoichiometric equilibrium model specifically for predicting the composition and heating value of producer gas obtained from a commercial small-scale DBG was developed by Roesch et al. [18], considering eight different biomasses. The model was used to compute gas composition across a range of temperatures within the reaction zone, disregarding unwanted by-products of gasification and going for a more simplified approach. The model accounts for different correlations which adjust and modify the predictions obtained. The key findings of the study provide insights into the factors influencing the composition of producer gas in small-scale DBGs. By developing a predictive model, this research contributes to enhancing the understanding of the gasification process and its outcomes, which is crucial for optimising gasifier performance and assessing its applicability for various applications.

Azzone et al. [19] provide a thermodynamic equilibrium model of a DBG moti-

vated by the use of agricultural residues as a feedstock. A simplified version of the global gasification reaction was employed, not taking into account tars. The chars in the model were investigated through the use of an empirical correlation to describe C fraction representing the amount of char participating in equilibrium reactions. A parametric study was carried out to observe the influence of MC, pressure and ER on the syngas composition and the heating value of the producer gas.

Barman et al. [20] subsequently developed a realistic equilibrium model of a DBG, incorporating tar as a by-product of gasification. The model is based on the global gasification reaction with an additional tar component to account for tar formation. The model employed for different biomass feedstock and a parametric study of the predictions was performed for validation purposes, highlighting good agreement with experimental data. However, it was observed, during their analyses, that some gaseous components like CH_4 deviated from chemical equilibrium, prompting modification of the model through the use of correction factors which stabilised the producer gas composition against experimental data.

A stoichiometric equilibrium model for a DBG, aimed at shedding light on the interplay of specific parameters impacting the gasification process, particularly concerning distinct feedstocks was formulated by Mendiburu et al. [21]. The study encompassed the evaluation of four different models, each geared towards determining syngas composition. One of these models was grounded in theoretical equilibrium constants, which were subsequently refined by means of two correction factors akin to previous methodologies. One particular model emerged as notably precise and adaptable, surpassing the efficacy of some previously established models. The variation of ER and MC was systematically explored, delving into the consequential effects on gaseous components.

A robust stoichiometric thermodynamic equilibrium model aimed at determining the syngas composition within a DBG is provided by Gagliano et al. [22]. This model is uniquely inclusive of tar and char components, with fixed proportions set at 4.5% and 10.5%, respectively, based on previous investigations [23, 24]. A rigorous validation process is executed to assess the model's predictions, which exhibited satisfactory agreement after incorporating correction factors to fine-tune equilib-

rium constants. The study also elucidated the impact of MC on temperature and Lower Heating Value (LHV) of the produced gas. Notably, the authors propose a correlation linking MC with ER, unveiling a proportional relationship between the two variables. Consequently, they affirmed the model's credibility in predicting syngas trends, heating values, and equilibrium temperature, albeit contingent upon the incorporation of specific convenient correction factors.

Rupesh et al. [25] devised a thermodynamic equilibrium model tailored to air-steam gasification. The model factors in char conversion and tar formation by incorporating empirical correlations. Much like the approach in [19], they employed a C conversion factor. This factor, determined by ER and temperature, governs the quantity of char within the system. The study also employed an empirical correlation from [16] to ascertain tar formation. A comprehensive parametric study was executed to assess the impacts of variables such as ER, steam-to-biomass ratio, and gasification temperature on syngas composition. The study's pivotal outcomes indicated that, at a temperature of 1000 K, a steam-to-biomass ratio of 1, and an ER of 0.25, the maximum mole fraction of H_2 reached 14.89%. The model effectively illuminated the influence of operational parameters on predictions and enabled the examination of multiple gasification agents for forecasting syngas composition. It also facilitated a comparison between the outcomes produced by these agents. However, a noteworthy limitation of the model arises from its description of char formation, which is achieved via the incorporation of an empirical correlation representing C participation in chemical reactions.

Aydin et al. [26] constructed a semi-empirical equilibrium model tailored for a DBG, with the principal objective of determining syngas composition and quantifying tar and char yields across an extensive array of feedstocks. Their approach encompassed the establishment of an empirical correlation contingent upon the ER, centering on the C fraction actively involved in chemical reactions. They validated the syngas composition against experimental data. Furthermore, they introduced corrective adjustments to equilibrium constants, refining the composition predictions. A noteworthy advantage of their model lies in its capacity to illustrate the interplay between ER and tar yield variation, thus offering valuable insights into the

influence of ER on pivotal gasification byproducts.

2.2 Kinetic models

Kinetic models are essential for understanding the intricate chemical reactions in downdraft biomass gasification, providing insights into reaction rates, mechanisms, and time-dependent behaviour. They elucidate key processes, including drying, pyrolysis, combustion, and gasification, offering a detailed view of biomass conversion. While the general gasification process is well understood, further research is needed on high-temperature reaction kinetics and the influence of heterogeneous catalysts, particularly in pyrolysis, oxidation, and gasification reactions.

These models quantify reaction rates, determining the conversion of biomass into syngas, tar, and char under varying conditions such as temperature, pressure, and residence time. Their adaptability to diverse biomass feedstocks, incorporating proximate and ultimate analyses, broadens their applicability. Kinetic models also play a crucial role in optimising operating conditions and predicting tar formation, aiding in the development of strategies for its minimisation.

Like equilibrium models, they require validation against experimental data to ensure accuracy. Though informative on reactor hydrodynamics, gasification kinetics, and syngas composition, these models do not capture the spatial distribution of temperature, species concentration, and flow dynamics within a gasifier. Most kinetic models lack the ability to fully simulate variations in particle size, and fail to provide and understanding of gas-solid interactions within the unit, which is a key aspect of the gasification process.

2.2.1 Detailed appraisal of contributions to the field

Wang and Kinoshita [27] were among the pioneers to establish a prominent biomass gasification kinetic model, primarily founded upon surface reaction mechanisms. This model entails the derivation of rate constants, achieved by minimizing deviations between experimental data and theoretical outcomes across varied residence times and temperatures. The model underwent validation against a broad spectrum

of ER values, attesting to its robustness.

In a subsequent endeavour, Giltrap et al. [28] embarked on constructing a steady-state model encapsulating gas-char reactions within a DBG. This undertaking was rooted in the reaction pathways introduced by [27]. Distinguished by an innovative twist, they amplified the reaction rates through a "Char Reactivity Factor," effectively denoting the relative reactivity of diverse char species. The model exhibited prowess in forecasting gas composition, though it exhibited a tendency to overestimate CH_4 concentration. Noteworthy room for improvement proposed by the author lay in the incorporation of additional data concerning initial gas concentration at the uppermost point of the reduction zone. Furthermore, they suggested a refinement of the model's representation of the correlation between pyrolysis product volume and temperature, which held the potential to bolster its predictive precision.

Di Blasi [29] delves into the transient dynamics of gasification processes, particularly in the context of downdraft gasifiers characterised by distinct zones of reactions. The primary focus of the study is to comprehend and characterise the dynamic behaviour of stratified downdraft gasifiers, which exhibit varying temperature and composition profiles within different sections of the gasifier. Generally, this dynamic behaviour is influenced by factors such as feedstock properties, gasification rate, and operational conditions. The key findings of the study are anticipated to provide valuable insights into the time-dependent behaviour of stratified downdraft gasifiers. The research uncovers the dynamic response of different gasification zones to changes in feedstock, operating conditions, and load variations. Additionally, the study offers insights into the stability and controllability of these gasifiers under various transient scenarios. Overall, the research undertaken contributes to the understanding of the transient behaviour of stratified downdraft gasifiers, shedding light on the challenges and opportunities associated with their dynamic operation.

A kinetic model of a solar DBG utilising high C content feedstock with steam was developed by Gordillo et al. [30]. The goal was to calculate the dynamic and steady state profiles of gas and solid phases based on mass and heat balances, indicating favourable reviews of the DBG. The char reactivity factor (CRF) is taken into account with an exponential variation, and results compared with experimental data

from a solar packed bed gasifier. The study concludes that taking into account the temperature gradient theory when designing the gasifier significantly improves the gasifiers performance.

Inayat et al. [31] modelled H_2 enriched gas production via steam gasification in the presence of CaO, incorporating mass and heat balances and reaction kinetics calculations. The research centres around the optimisation and understanding of H_2 production through the gasification of biomass feedstock. The key findings of the study provide valuable insights into the optimal operating conditions for H_2 production from oil palm empty fruit bunches using steam gasification. By systematically conducting a parametric study, the research reveals the interplay between variables and their impacts on H_2 yield and gas composition.

Babu and Sheth [32] developed a kinetic model for the reduction zone of a DBG to study the effect of the CRF. The model utilises reaction rates of the main reactions as well as molar and energy balances. The findings of the study report that increasing the CRF exponentially along the reduction bed length, yielded better predictions of the temperature and composition profiles when compared with corresponding experimental data. The research contributed to advancing the understanding of specific gasification zones within downdraft gasification, while also offering insights into optimising the syngas composition through the utilisation of reactions rates.

A kinetic model for a fixed bed gasifier based on the conservation of mass and energy in a simplified one-dimensional flow, chemical equilibrium in the gas phase, and a Langmuir-Hinshelwood correlation describing the reaction kinetics in the char was formulated by Gobel et al. [33]. The model was used to undertake a parametric study for different predictions for a range of operating conditions, and identified a new control strategy aimed at maintaining a constant bed height by simultaneously changing the rate of addition of air and biomass. This resulted in a stationary char bed, even after drastic changes in operating conditions. The model results were compared with measurements obtained from a 100 kW two-stage gasification demonstration plant.

One of the most notable kinetic models is that proposed by Paul and Salem [34] to predict the optimum working conditions of a DBG, in which a set of kinetics

and principle equations at each zone of the gasifier were described. The model deals with a wide range of feedstock and is capable of estimating gas composition, tar content, temperature and the height of each zone including temperature of the gasifier, velocity and pressure distribution at the reduction zone. The model takes into consideration the different reacting zones of the biomass gasifier and the results obtained conclude that biomass with less than 10% MC and an ER range between 0.3-0.35 leads to generation of a higher syngas yield with a low tar content.

2.3 CFD models

CFD models play a crucial role in analysing fluid flow, heat transfer, and chemical reactions within DBGs, offering a comprehensive understanding of complex in-gasifier processes. These models simulate gas, biomass particles, and volatile flow, providing detailed visualisations of flow regime, mixing, and temperature distributions across gasification zones such as drying, pyrolysis, combustion, and reduction. They also predict species transport, including gas components, tar, and volatiles, aiding in gas composition analysis and tar formation prediction. Incorporating reaction kinetics, CFD models identify reaction zones, quantify rates, and track gas-solid interactions, crucial for understanding char and ash behaviour. Optimised against various operating conditions, they assist engineers in reactor design, process optimisation, and scaling from laboratory to industrial levels. Future advancements aim to integrate more sophisticated chemical kinetics, transient behaviour, and enhanced particle dynamics for improved real-world applicability.

However, developing sophisticated CFD models requires a deep understanding of the gasifier's geometry, including the shape and dimensions of the reactor, as well as a detailed knowledge of the initial and boundary conditions such as inlet velocities, biomass feeding rates, and initial temperatures. This is still a subject of current research which is needed to improve the characterisation and representation of these parameters in CFD simulations. Also, challenges remain in accurately modelling tar due to intricate chemical reactions associated with its formation, including polymerisation, cracking, and condensation of volatile organic compounds released from

biomass pyrolysis.

2.3.1 Detailed appraisal of contributions to the field

Rogel and Aguillon [35] developed a CFD model for a stratified DBG formulated as a hybrid one-dimensional and two-dimensional (1D+2D) model, taking into consideration pine wood pellets as a biomass feedstock. The model incorporates reactions for drying, primary pyrolysis, secondary tar cracking, combustion, gasification and particle shrinkage. The model is utilised to predicted temperature profiles, gas composition, producer gas LHV and C conversion efficiency, and to produce temperature and gas composition contours for specific initial conditions. It provides adequate reproduction of the dynamic behaviour and the steady state configuration depending on the air/biomass feed rate of the downdraft wood gasifier. Within the model, there are inherent limitations and uncertainties associated with the complex process of gasification/combustion, but results in predictions agreeing satisfactorily with experimental data.

Wu et al. [36] engineered a 2D CFD model aimed at comprehending the behaviour of a DBG. The model was constructed using the Euler-Euler multiphase approach, successfully encapsulating multiple critical phases of the gasification process including drying, pyrolysis, combustion, and gasification. To depict the gas phase, the standard k-ϵ turbulence model was adopted, and the model's outcomes were meticulously matched against empirical data. The comparison yielded a notable level of concurrence, underlining the model's reliability in approximating real-world scenarios. The study also ventured into parameter analyses, which revealed intriguing findings. In particular, the research delved into High Temperature Agent Gasification (HTAG) technology, where external super-heated air and steam act as heat sources. The investigations unveiled that this approach significantly curtailed the necessity for combustion within the gasifier. This innovative technique demonstrated its efficacy by generating syngas characterised by elevated H_2 composition and concurrently minimising tar content, thereby corroborating the viability of the HTAG strategy.

The development of a numerical model coupled with experimental investigations

within a DBG was undertaken by Janajreh and Shrah [37]. In their endeavour, woodchips served as the selected feedstock, and the Lagrangian particle approach was adopted [38]. The numerical simulation was executed using a meticulously constructed high-resolution mesh that accounted for both solid and gaseous phases, and incorporating he k-ϵ turbulence model. The computation encompassed temperature distribution and species evolution, with subsequent comparison against empirical data. To gauge the model's effectiveness, the study involved assessing its CGE, which is the ratio between energy of generated syngas to the energy of the biomass fed to the gasification system. The findings convey that equilibrium modelling is insufficient to encapsulate the intricate physics and chemistry manifesting within the downdraft configuration. This shortcoming was attributed to the complex flows inherent in such systems, distinguishing them from alternative configurations, such as entrained flow gasifiers, characterised by elevated temperature distributions.

Ephraim et al. [39] simulated biomass char gasification in a downdraft reactor to achieve syngas production. The simulation was carried out using OpenFOAM and was a 1D steady state model accounting for reaction kinetics and fluid flow in a porous char bed. A sensitivity analysis was performed with the aim of investigating the influence of the bed inlet temperature on the syngas composition and char conversion. The model is also capable of calculating the different reaction rates of the various chemical reactions employed in the system as a function of gasifier height. The model showcased its capability of predicting important gasification outcomes with varying parametric inputs for the purposes of optimising the design and operation of downdraft gasifiers.

A 2D CFD model dedicated to the biomass gasification of rice husk, encompassing all integral zones of the gasifier was developed by Murugan et al. [40]. The model was developed within DesignModeler of the Ansys Fluent framework, and the ensuing analysis was conducted employing Ansys Fluent. Notably, a species-transport model was employed to effectively simulate chemical reactions and ascertain the compositions of distinct gaseous species. An essential facet of this research involved the execution of a comprehensive parametric analysis, scrutinising the influence of various factors, including ER, on the composition of producer gas, higher heating

value (HHV), and the internal temperature distribution within the gasifier. Subsequent to meticulous investigation, the study derived that the HHV of the producer gas registers at 5.19 MJ/Nm^3, while prognostications indicated that maximum zone temperatures were attained at an ER of 0.30.

A 2D CFD model of a 20kW DBG, utilising a comprehensive volatile break-up approach was successfully developed by Kumar and Paul [41]. The model takes into account all four zones of the gasifier and is evaluated using an output-input relationship between respective reacting zones, while the solid phase is modelled via the Lagrangian approach namely the discrete phase model (DPM) [42]. This approach considers the trajectory of a particle through the continuous phase of fluid. They have also constructed a revised chemical reaction scheme, including reactions participating in their respective zones. The study analysed how the syngas composition varied with the ER, offering valuable insights into the gasifier's performance. The devised methodology was based on a sequential output-input relationship, taking into consideration specific chemical reactions occurring in restricted zones. The work concluded by establishing the implemented CFD modelling approach to be a promising way to simulate biomass gasification processes in downdraft configurations.

Ngamsidhiphongsa et al. [43] formulated a 2D species-transport CFD model, targeting an Imbert DBG. The aim was to scrutinise the intricacies of tar cracking reactions and assess the impact of gasifier design parameters, such as throat diameter and height of the air nozzle, on overall gasifier performance. The focal point of their analysis was centered on tar concentration, particularly how it varied with the manipulation of the throat diameter. Notably, the research unveiled a noteworthy trend: diminishing the throat diameter corresponded with a reduction in tar content to an impressively low value of 0.005 g/Nm^{-3}. Furthermore, the study delved into the influence of nozzle-to-throat lengths, revealing that their reduction led to decreases in both tar and H_2 compositions. However, the findings also indicated that the CGE exhibited fluctuations under these parameter alterations. Consequently, the research underscored the necessity for a balanced approach when optimising the design of an Imbert downdraft gasifier. It emphasised the need to strike a harmo-

nious compromise between minimising tar content and preserving CGE to enhance the overall gasifier design.

A 2D axisymmetric CFD model tailored for a DBG was devised by Pandey et al. [44]. Utilising the Ansys Fluent software, this model demonstrated the capability to ascertain the syngas composition and gasification temperature across multiple ER values. The findings of the study unveil a distinct pattern: an augmentation in ER led to a reduction in the concentrations of CO, H_2, and CH_4, while concomitantly witnessing a notable upsurge in CO_2 and N_2 levels. By delineating gaseous composition contours under specific operational scenarios, the study vividly illustrated the interplay of these constituents. Moreover, the research encompassed an insightful parametric exploration of gasification temperature under varying conditions. The CFD model delivered an enhanced comprehension of the dynamic interrelations governing the syngas composition and gasification temperature in the context of downdraft biomass gasification.

Salem and Paul [45] extended their prior work [41], focusing on unraveling the spatiotemporal progression of intricate tar species within a DBG. The model framework remained congruent with their earlier study [41], with the notable addition of an extensive array of tar species reactions. This augmented model offered an intricate exploration of the interplay between these tar species and the variable operational conditions, thereby offering insight on their pronounced impact.

Yan et al. [46] developed a 3D CFD multiphase flow model, together with a thermal-equilibrium model to study the operation of a downdraft biomass gasifier. The effect of reduction bell dimension and operating conditions on temperature distribution and syngas production were investigated, which sheds light on the improvement of the design and operation of the reactor. It was found that the syngas production could be improved by varying the size of the reduction bell.

2.4 ANN models

Though the primary focus of this thesis does not centre on Artificial Neural Network (ANN) models, a discussion of them has been included due to their inte-

gration within the broader spectrum of modelling approaches relevant to biomass gasification. While the specifics of their model formulation and implementation are not addressed, their significant impact on the advancement of biomass gasification research warrants acknowledgment. ANN models have significantly advanced gasification modelling by predicting syngas composition, tar content, and process by-products, aiding in optimisation and efficiency improvements. They facilitate the refinement of operational parameters, enhance energy yields, and enable adaptive control systems that dynamically adjust gasification conditions in real time. Additionally, ANN models contribute to understanding feedstock variability, conducting sensitivity analyses, and improving model reliability. Their integration with kinetic and CFD models has led to hybrid approaches that enhance predictive accuracy and process control, making them a valuable tool in biomass gasification research.

2.4.1 Appraisal of contributions to the field

Arnavat et al. [47] designed and established two ANN models: one for a circulating fluidised bed gasifier and another for a bubbling bed gasifier. These models effectively determined the composition and yield of the producer gas. The impact of ash, MC, C, O_2, and H_2 in dry biomass, as well as ER and T, were analysed for both gasifier types. The study demonstrated the potential of the models to contribute significantly to research in biomass gasification modelling. The results obtained indicated a strong agreement with previously published experimental data, revealing a low root-mean-square deviation (RMSD). Notably, the biomass composition influenced the producer gas composition by 31.7% to 54.1% in the case of the circulating bed gasifier, and 28.9% to 52.3% for the bubbling bed gasifiers.

Sreejith et al. [48] developed a feed-forward ANN model to predict gasification temperature and producer gas composition, taking into account the presence of tar. The accuracy of the ANN prediction closely matched the experimental findings, as evidenced by statistical parameters including the coefficient of correlation, RMSD, average percentage error, and covariance. Experimental results indicated that the maximum H_2 concentration achieved was 29.2%, while the ANN model achieved 28.2% at an ER of 0.277. The corrected equilibrium model, validated with sig-

nificant air-steam gasification experimental data, exhibited an average accuracy of 95.1%. The study highlighted that the ANN model (RMSD = 2.64) outperformed the corrected equilibrium model (RMSD = 5.96) in predicting product gas composition. Additionally, the study proposed a comprehensive ANN model capable of simulating various process conditions in fluidised bed gasification, adaptable to a range of biomass feedstocks.

Baruah et al. [49] developed an ANN model for a DBG. This model was effectively employed to anticipate the gas composition of the four primary gases: CH_4, CO, CO_2, and H_2. The model's input parameters encompassed the chemical composition of biomass, ash content, MC, and the temperature within the reduction zone. Structurally, the model comprised an input layer, a hidden layer, and an output layer. Training of the network was executed employing reported experimental data. The outputs generated by the ANN models were found to align well with experimental data, with an absolute fraction of variance exceeding 0.99 for CH_4 and CO, and surpassing 0.98 for CO_2 and H_2. These findings underscore the potential applicability of the model in predicting the percentage composition of the four major gaseous species.

Ascher et al. [50] formulated an extensive ANN model for the gasification process, compiling 10 crucial metrics to evaluate the performance of gasification technology. This model represents a pioneering approach that can be applied to various feedstock types, gasifying agents, and reactor alternatives. It demonstrated a robust predictive capability, as evidenced by a high coefficient of determination of 0.9310. The model focuses on the efficacy of neural network training and evaluates the anticipated producer gas composition, char and tar yields, as well as the syngas LHV. The study concludes that the model exhibits remarkable precision in predicting outcomes, with an RMSD of 0.1307. Moreover, it has the potential to facilitate the development of integrated gasification designs by integrating these models with life cycle assessments, cost-benefit analyses, and multi-objective optimisation.

2.5 Experimental Work

Although the principle focus of this thesis is the modelling of a DBG, it is important to review the associated and complementary experimental investigations that produce a means of informing the modelling process and determining their efficiency.

2.5.1 Detailed appraisal of contributions to the field

Barrio et al. [51] conducted an empirical study involving a laboratory-scale stratified downdraft gasifier situated at the Norwegian University of Science and Technology (NTNU). This investigation encompassed the gasification of wood pellets and yielded an approximate producer gas output of 12.5 Nm^3/hr, corresponding to a feed rate of 5 kg/hr. A comprehensive scrutiny of the 30 kW gasifier is presented, supplemented by an intricate account of the measurement apparatus utilised. The outcomes of this study encompass the composition of the producer gas and the temperature distribution throughout the height of the gasifier.

The performance of a DBG using furniture wood and wood chips was investigated by Zainal et al. [52]. The experiment performed consisted of a blow-type downdraft gasifier with a cone structure, feeding system, start-up system and air supply system. A parametric study was carried out to analyse the effects of ER on the gas composition and the calorific value of the producer gas. The key finding is that the calorific value increase with ER initially, attains a peak then decreases as ER continues to increase. It was also observed that complete conversion of biomass did not take place even with optimal ER.

Dogru et al. [53, 54] investigated the production potential of hazelnut shells and sewage sludge in a DBG with varying feeding rate, to observe its influence on the syngas composition and the zone temperatures. A by-product analysis was carried out to study the effects of the feeding rate on the gasification by-products including tars, ash and remaining chars.

Jayah et al. [55] conducted an experimental investigation on the gasification of rubberwood used for tea drying. The work carried out was a part of a larger evaluation of a NERD (National Engineering Research and Development) centre downdraft

wood gasifier for tea manufacturing in Sri Lanka [56]. The findings of this experimental investigation has become a leading reference and benchmark for a variety of researchers conducting modelling work on downdraft gasifiers, as it provides a thorough analysis of the gasification product compositions achieved, including the influence of the operating parameters, most notably the ER, on various outputs.

An investigation of biomass conversion via oxygen/steam gasification within a downdraft gasifier was embarked up on by Lv et al. [57]. Through air gasification, they attained a maximum H_2 yield of 45.16 g H_2 / kg biomass. Various operating conditions, including feeding rate, steam rate, ER, and throat temperature, influenced gas yield, composition, tar yield, and LHV.

Avdhesh Sharma [58] documented the outcomes of a study involving a 75 kW experimental DBG, encompassing temperature profiles, gas composition, calorific value, and pressure drop trends across the porous gasifier bed. They also addressed issues related to leakage and re-fabrication techniques, highlighting that higher bed temperatures during firing mode enhanced the conversion of non-combustible components.

An extensive experimental investigation on an Imbert DBG across a wide range of operational conditions was undertaken by Sheth and Babu [59]. Employing a gas chromatograph with a thermal conductivity detector, they analysed the generated producer gas composition, relating it to varying parameters such as air flow rate, initial MC, ER, and biomass consumption rate. Their study revealed a continuous increase in producer gas production with higher ER values. The optimal ER within their experimental setup was approximately 0.205, yielding maximum syngas concentration.

Both experimental and theoretical investigations into heat and mass transfer during wood pyrolysis were conducted by Park et al. [60]. Employing wood spheres within a vertical tube furnace, they identified sequential endothermic and exothermic reactions through temperature measurements. A numerical study utilising various pyrolysis kinetics led to a proposed pyrolysis model consisting of three parallel endothermic reactions producing tar, gas, and intermediate solid.

Martinez et al. [61] explored wood gasification within a moving bed downdraft

reactor employing a two-stage air supply. This configuration aimed to enhance producer gas quality, particularly reducing tar concentration. Their investigation encompassed gas composition measurements at different ER values, revealing useful gas power and cold gas efficiency of around 40 kW and 68%, respectively, for an ER of 0.40. They observed that biomass devolatilization in the pyrolysis zone yielded lighter compounds, which underwent easier cracking upon traversing the combustion zone.

Erlich and Fransson [62] undertook experiments to explore the repercussions of char bed characteristics, notably porosity and pressure drop, on gasification performance. This research utilised pellet-type feedstocks composed of wood and palm oil residues. Their findings showcased that wood gasification displayed increased producer gas richness through adjustments in air-fuel ratios.

The gasification of woody biomass using a bench-scale packed-bed reactor was investigated by Ueki et al. [63]. Their experiment involved the gasification of black pine pellets with air as the gasification agent, employing both downdraft and updraft configurations. To assess the tar content, samples of the syngas were collected at the gasifier's exit. The syngas produced under updraft and downdraft conditions had an LHV of 4.8 MJ/Nm^3 and 3.8 MJ/Nm^3, respectively. Interestingly, the study discovered that maintaining control over the packed-bed's height was more manageable in the downdraft configuration, and it also resulted in a lower tar content. This phenomenon could be attributed to the fact that in the downdraft setup, tar has to pass through a partial combustion or higher-temperature zone, which contributed to its reduced presence in the syngas.

An experimental study on a bench-scale DBG was performed by Yoon et al. [64] using rice husk and rice husk pellets as feedstocks inputted at around 40-60 kg/hr against an air supply of around 50-75 Nm^3/hr. The results of this study demonstrated the better conversion properties of rice husk pellets due to a higher synthetic gas composition and a cold gas efficiency.

A DBG unit was constructed by Guangul et al. [65, 66] with a novel height adjustment mechanism for changing the position of gasifying air and steam inlet. Through their experiments on oil palm fronds, they observed enhanced proportions

of H_2, CO, and CH_4 in the gas composition when they preheated the gasifying air. Furthermore, this preheating method resulted in an improved syngas HHV, which increased from 4.66 to 5.31 MJ/Nm^3. In summary, the findings from these two studies highlight the feasibility of using oil palm fronds as an alternative energy source through gasification and underscore the benefits of preheating the gasifying air in enhancing syngas quality.

Gai and Dong [67] pursued a study on the viability of converting non-woody biomass, specifically corn straw, through downdraft biomass gasification utilising air as the gasification agent. Their conclusions underscored the substantial influence of operational parameters on both gasifier temperature profiles and the composition distribution of the product gas. Notably, they discerned that suboptimal ERs, both higher and lower, led to compromised producer gas quality. An ER range of 0.28 to 0.32 was identified as optimal. Varying operating conditions yielded distinct results in terms of LHV, gas yield, gasification efficiency, and tar concentration.

Dutta et al. [68] carried out an experimental study of the downdraft gasification of five locally available feedstocks, namely Bamboo, Gulmahor, Neem, Dimaru and Shisham, using a 10 kW_{th} gasifier. A thermodynamic model was then developed using appropriate assumptions for comparisons with the experimental work. The gas composition of the products were studies against a range of MC's, concluding the gasification of Bamboo to be of the highest quality amongst the remaining biomasses.

A feasibility study of Jatropha shell gasification for captive power generation in a downdraft gasifier was investigated by Maiti et al. [69]. Upon gasification, the calorific value of the producer gas was evaluated to be around 5.2 MJ/Nm^3, with an efficiency of 64.8% over an 8 hr continuous operation. The gasifier was interfaced to a 100% producer gas engine, and continuous power generation was demonstrated with overall efficiency of 24.5%. Results concluded that captive power obtained in this manner would obviate the need for external sources of power for the operations of deshelling, screw pressing, oil refining, glycerol purification, and soap making in the integrated biodiesel production process.

The work of Striugas et al. [70] is well-known for showcasing and evaluating the performance of automatically operated multi-fuel downdraft gasifier for energy

production, in particular, the influence of operating conditions such as the ER on the tar and char yields of downdraft gasifiers.

Guo et al. [71] also studied the effects of design and operating parameters on the gasification process of corn stalk in a downdraft gasifier. Feeding rate and air flow rates were varied at different experimental runs in order to examine their influence on the gasification performance. While this was conducted, tar sampling was initiated using separation techniques and weighted to study ER influence on the tar yield.

Biomass gasification in a downdraft gasifier with a two-stage air supply was investigated by Galindo et al. [72]. In their work, a deep analysis of the effects of operating conditions on gas quality was performed as the air flow was varied between 18 Nm^3/hr and 22 Nm^3/h while examining the quality of the syngas over these parameters. Results obtained demonstrated a fuel gas with tar and particulate matter of 54.25 $\pm$ 0.66 mg/Nm^3 and 102.4 $\pm$ 1.09 mg/Nm^3, respectively, for a total air flow rate equal to 20 $\pm$ 0.45 Nm^3/hr. Notably, the use of a two-stage air supply in the gasification process led to a significant reduction in the tar content within the producer gas, achieving a remarkable 87% decrease, all while experiencing only a slight increase in gasification efficiency.

Kirsanovs et al. [73] undertook an experimental investigation of a downdraft gasifier using wood chips as fuel, offering an examination of the effects of MC on the syngas production and gasification temperature. The gasifier was operated at different thermal capacity thresholds to study the fuel supply influence and the gasification process performance.

The performance of a 10 kW DBG using lignite and sawdust briquettes (70:30, %wt.) as feedstock, while operating the unit at seven different ER's was experimentally investigated by Upadhyay et al. [74]. An analysis of the fuel and air consumption rates was carried out and the effects of ER on the syngas composition and gasification temperature demonstrated.

Patuzzi et al. [75] carried out an extensive and unique monitoring review survey of the production plants housing state-of-the-art small scale DBGs in the south Tyrolean region of Italy. A detailed mapping of the existing plants in the region was undertaken, followed by an assessment of the biomass and char flows in the

region and finally an on-site plant monitoring survey in order to evaluate gasifier performances, including syngas composition, LHV of the syngas and a thorough analysis on the gasification char contents.

Finally, Awais et al. [76] conducted an investigation into the gasification process of sugarcane bagasse and coconut shells within a DBG. They introduced variations in the feeding rate, ranging between 30 to 40 kg/hr. The study delved into the influence of ER on several gasification parameters, including syngas composition, heating value, syngas yield, gasification efficiency, and tar content. For tar collection, a copper condenser was employed, utilising this method to regulate the system's temperature. The impact of the gasification agent on gas composition and the reactor's zone temperature was also subject to analysis.

2.6 Summary

To summarise, past thermodynamic equilibrium models have greatly enhanced the understanding of downdraft biomass gasification, providing predictions for gas composition, operational parameters, and tar reduction strategies. Despite their limitations, hybrid models are being developed to better capture gasification complexities. While some historic models pioneered new avenues, others merely reiterated existing concepts, and the practical applicability of numerous emerging models is limited.

Kinetic models have elucidated reaction mechanisms, quantified rates, and informed operational parameters, aiding the scale-up of industrial gasifiers and improving reactor behaviour understanding. These models guide the design of larger gasifiers and are being refined to include secondary reactions, catalytic effects, and particle-gas interactions.

CFD models have advanced knowledge of flow dynamics, temperature dispersion, and reaction kinetics, enhancing gasification system development. Although challenges remain in multiphase flow and turbulence modelling, ongoing improvements aim to increase the precision of these models. The scarcity of OpenFOAM-based CFD models highlights the need for a suitable solver for thermal and chemical conversion in fixed bed applications.

Experimental studies on DBGs have provided valuable insights into feedstock behaviour, operating conditions, gas composition, and performance optimisation, laying the foundation for designing efficient and sustainable gasification systems and validating theoretical models.

This Chapter establishes a robust foundational basis by exploring the specificities of prior research in the field of biomass gasification, encompassing both theoretical and practical works. Through a detailed literature review, a comprehensive understanding of the fundamental principles underlying the gasification process is established. With this solid grounding, a grasping of the complexities involved in gasification is established, which is crucial for developing a systematic methodological framework that will serve as the procedural guide for the subsequent modelling efforts.

CHAPTER 3

Biomass Gasification and Modelling Fundamentals

3.1 Introduction to Biomass

In brief, biomass refers to organic materials that come from living organisms, primarily plants and microorganisms, and can be used as a source of renewable energy [77]. Common sources of biomass are agricultural, forest, municipal, energy, and biological. Although it is accompanied by the release of CO_2 emissions, it is widely considered to be a potential source of renewable energy due to the cycling of CO_2 emission, enabling a net zero carbon footprint [2]. Biomass contains a large array of complex organic compounds, moisture, and a minority amount of inorganic impurities known as ash. The organic compounds comprise four principle elements; C, H_2, O_2, and N_2. Depending on the type of biomass feedstock, it may also contain small amounts of S and chlorine (Cl), but these species are rarely present. The composition of biomass is typically categorised into several key components, making up the organic matter found in biomass and can very depending on its type, its source, and its intended use. The main constituents of biomass, as shown in Fig 3.1, include [2]:

- Cellulose; which is a complex carbohydrate, forming the structural component

of plant cell walls and provides strength to plant tissues.

- Hemicellulose; which is another carbohydrate found in plant cell walls, less rigid than cellulose and consists of various sugars.
- Lignin; which is a complex, non-carbohydrate polymer that provides support to plan cell walls.

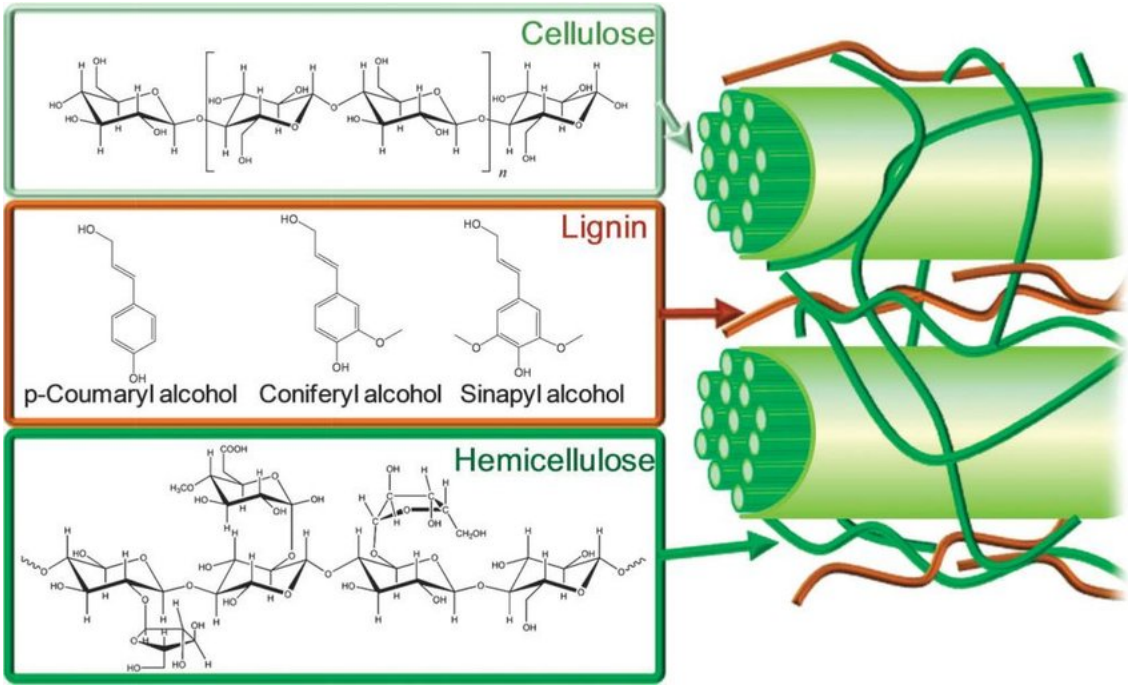

Figure 3.1: The structure of lignocellulosic biomass with cellulose, hemicellulose, and lignin as main constituents [78].

3.1.1 Ultimate Analysis

The ultimate analysis of a biomass feedstock describes the composition of the hydrocarbon fuel in terms of its basic elements, except for its moisture and inorganic constituents. A typical ultimate analysis is defined as:

$$y_C + y_H + y_O + y_N + y_S + y_{ASH} + \text{MC} = 100\% \ , \tag{3.1}$$

where, y_C, y_H, y_O, y_N, y_S, and y_{ASH} are the weight percentages of C, H_2, O, N_2, S, and ash respectively. The MC represents the moisture content in the fuel. Not all

feedstock contain all of these elements and in fact the majority of fuels do not contain S. It is important to note that H_2 or O_2 in the ultimate analysis does not include the H_2 and O_2 in the moisture, but only that present in the organic components of the feedstock. Feedstocks with a low sulphur content, particularly ligno-cellulosic biomass, maintain a major advantage in their utilisation in energy conversion when SO_2 emission is taken into consideration [2].

From the ultimate analysis of the biomass feedstock, on a dry basis its chemical composition $CH_\alpha O_\beta N_\lambda S_\delta$ is determined via the following expressions:

$$\alpha = \frac{y_H \times M_C}{y_C \times M_H} \ , \ \beta = \frac{y_O \times M_C}{y_C \times M_O} \ , \ \lambda = \frac{y_N \times M_C}{y_C \times M_N} \ , \ \delta = \frac{y_S \times M_C}{y_C \times M_S} \ , \tag{3.2}$$

where α, β, λ and δ are the number of atoms of the respective chemical species per one atom of carbon in the biomass (standard definition), while M_C, M_H, M_O, M_N and M_S are their molar masses in kg/mol. The molar mass of biomass on a dry-basis is expressed as:

$$M_{bm} = \frac{M_C}{y_C} \times 100\% \ , \tag{3.3}$$

where subscript bm denotes a quantity of biomass.

3.1.2 Proximate Analysis

A proximate analysis establishes the composition of the biomass based on gross components such as MC, volatile matter (VM), ash, and fixed carbon (FC). It is a relatively simple and inexpensive process, and utilises different standard techniques to determine the individual components of the biomass. The VM of the fuel is the condensable and non-condensable vapour released when the fuel is heated, its amount depending on the rate of heating and its temperature. To account for the amount of VM, the fuel is heated to a standard temperature and at a standard rate in a controlled environment.

Table 3.1: The ultimate and proximate analysis of different biomass feedstocks

Biomass Feedstock	Ultimate Analysis					Proximate Analysis			
	$y_C(wt.\%d.b.)$	$y_H(wt.\%d.b.)$	$y_O(wt.\%d.b.)$	$y_N(wt.\%d.b.)$	$y_S(wt.\%d.b.)$	$y_{FC}(wt.\%d.b.)$	$y_{VM}(wt.\%d.b.)$	$y_{ASH}(wt.\%d.b.)$	HHV(MJ/kg)
Rubberwood [55]	50.6	6.5	42	0.2	-	19.2	80.1	0.7	20.98
Wood pellets [51]	50.67	6.18	40.97	2	0.18	-	-	1	20.7
Rice husk [64]	33.14	5.14	37.20	0.55	0.1	20.1	60	23.85	15.81
Bamboo [68]	48.39	5.86	39.21	2.04	-	15.2	80.3	4.5	19.62
Neem [68]	45.1	6	41.5	1.7	-	12.65	81.75	5.6	18.38
Pellets [75]	46.97	5.82	39.52	0.06	0.31	-	-	0.85	19.18
Wood chips 1 [75]	49.99	5.24	41.07	0.17	0.67	-	-	0.06	19.36
Wood chips 2 [75]	48.51	5.51	36.86	0.10	0.43	-	-	0.89	19.64
Wood chips 3 [75]	46.83	5.92	39.84	0.06	0.33	-	-	0.41	19.23
Wood chips 4 [73]	49.44	6.06	43.51	-	-	-	-	1	19.87
Lignite [74]	37.80	4.93	40.394	1.625	0.141	31.03	42.07	15.11	16.37
Mixed wood chips [70]	48.77	5.85	44.52	0.05	0.01	12.8	75.8	0.8	17.3
Softwood pellets [70]	49.20	6.20	44.06	0.08	0.06	15.2	79.2	0.4	19
Rape straw pellets [70]	39.60	5.60	48.54	0.78	0.08	17.2	62.5	5.4	16.2
Poultry litter pellets [70]	43.98	5.16	31.98	4.63	0.75	15.3	63.6	13.5	16.8
Sewage sludge - sawdust pellets [70]	41.08	5.51	26.90	3.77	0.94	14.3	59.5	21.8	17.8
Forest waste [79]	53.1	6.2	36.62	1.11	0.07	-	-	2.9	19.2

Ash is the inorganic solid residue after the fuel is completely burnt. Its primary ingredients are silica, aluminium, iron, and calcium, with traces of magnesium, titanium, sodium, and potassium. The ash obtained from biomass conversion does not necessarily come entirely from the biomass itself, but could be from subsequent handling during which it can pick up a considerable amount of impurities. The ash content in biomass feedstocks is usually minor, but may play a role in biomass utilisation especially if it contains alkali metals such as potassium. These metals can lead to agglomeration, fouling, and corrosion in boilers and gasifiers [2]. A study conducted by [80] showed that reactivity in gasification systems was influenced by the presence of ash-forming elements, not only at the active char sites, but also through prohibition of contact between char and gasification agent by ash layer formation with properties highly depending on ash composition. High ash concentrations can form a barrier on the char surface during gasification, impeding the access of the gasification agent, thus reducing gasification rates.

On the other hand, new studies such as that presented by [81], proposed an innovative strategy that reutilises ash into gasification process based on its potential catalysis to improve gas products. Their study demonstrated the feasibility of this approach, as the results revealed that loading ash exhibited catalytic activity that promoted CO formation, which correlated with the metal active sites provided by the ash and led to an improvement in dry and/or steam reforming, thus improving H_2 production. The reutilisation of ash proved that it is able to achieve a dual objective of improving gas product quality and reducing SO_2 emissions.

Due to its inherently low amount in the biomass and inactivity in gasification reactions, it is considered to be inert in biomass gasification models as its impact on the final gas composition is negligible.

High MC is a major characteristic of biomass and it can be as high as 90%. The MC drains much of the deliverable energy from a gasification plant, as the energy utilised in evaporation is unrecoverable. It as an essential input design parameter which must be accounted for in the assessment of the energy penalty or the cost of drying biomass. Biomass moisture is often expressed on a dry basis. For example, if $m_{bm,wet}$ kg mass of wet biomass becomes $m_{bm,dry}$ kg mass after drying, then its dry

basis moisture content, MC_{dry}, is expressed as:

$$\mathrm{MC}_{dry} = \frac{\mathrm{m}_{bm,wet} - \mathrm{m}_{bm,dry}}{\mathrm{m}_{bm,dry}} \ . \tag{3.4}$$

This can give a moisture percentage greater than 100% for very wet biomass, thus the basis of moisture should be specified. The wet-basis moisture (MC_{wet}) is given by the following:

$$\mathrm{MC}_{wet} = \frac{\mathrm{m}_{bm,wet} - \mathrm{m}_{bm,dry}}{\mathrm{m}_{bm,wet}} \ , \tag{3.5}$$

giving a relationship between $\mathrm{MC}_{\mathrm{wet}}$ and $\mathrm{MC}_{\mathrm{dry}}$ as such:

$$\mathrm{MC}_{dry} = \frac{\mathrm{MC}_{wet}}{1 - \mathrm{MC}_{wet}} \tag{3.6}$$

Finally, the FC in a fuel is determined using the following relationship:

$$\mathrm{FC} = 1 - \mathrm{MC} - \mathrm{VM} - \mathrm{ASH} \ , \tag{3.7}$$

which represents the solid carbon in the biomass, remaining in the char after pyrolysis. Biomass carbon is obtained from photosynthetic fixation of CO_2, thus all of it is organic. The value of varying FC, measured under standard conditions, gives a useful evaluation parameter of the fuel. For gasification analysis, FC is an essential parameter since the conversion of fixed carbon into gases determines the rate of gasification and its yield [2]. Table 3.1 provides the ultimate and proximate analysis for a range of biomass feedstocks used in the present work.

3.1.3 Properties of biomass

This section provides a thorough analysis on the thermophysical properties of biomass of direct relevance to gasification.

3.1.3.1 Physical properties

The physical properties of biomass influence its pyrolysis and gasification behaviour. For example, permeability is a significant factor in pyrolysis, whereby high perme-

ability enables pyrolysis gases to be trapped in the pores, increasing the residence time in the reaction zone. They are also associated with the material's density. Three characteristic densities are defined for a granular biomass: true, apparent, and bulk.

The true density is the mass per unit volume occupied by the solid constituent of biomass. The true density, ρ_{true}, is defined as follows:

$$\rho_{true} = \frac{\mathrm{m}_{bm,total}}{V_{solid}} \ , \tag{3.8}$$

where $\mathrm{m}_{bm,total}$ is the total mass of the biomass and V_{solid} is the solid volume in the biomass. The cell walls contain the major solid content of a biomass. For a common wood, the true density of the cell wall is typically 1530 kg/m^3 and is constant for most wood cells [82]. The true density of the biomass can be measured with a pycnometer, or estimated using the ultimate analysis and the true density of its constituent elements [2].

The apparent density, $\rho_{apparent}$, is based on the apparent or external volume of the biomass, including its pore volume. The apparent density considers the internal pores of a biomass particle and is defined as:

$$\rho_{apparent} = \frac{\mathrm{m}_{bm,total}}{V_{apparent}} \ , \tag{3.9}$$

where $V_{apparent}$ is the apparent volume of the biomass including solids and internal pores. The pore volume of the biomass expressed as a fraction of its total volume is known as its porosity, ϵ, an important property of the biomass. Apparent density is most commonly used for design calculations as it is the easiest to measure and gives the actual volume occupied by a particle in a system [2].

The bulk density, ρ_{bulk}, is defined as follows:

$$\rho_{bulk} = \frac{\mathrm{m}_{bm,total}}{V_{bulk}} \ , \tag{3.10}$$

where V_{bulk} is the bulk volume occupied by the biomass particles. The bulk volume includes the interstitial volume between the particles, depending on how the biomass

is packed. The interstitial volume expressed as a function of the total packed volume is known as the bulk porosity, ϵ_b. The above three biomass densities are related as follows [2]:

$$\rho_{apparent} = \rho_{true}(1 - \epsilon) \ , \tag{3.11}$$

$$\rho_{bulk} = \rho_{apparent}(1 - \epsilon_b) \ . \tag{3.12}$$

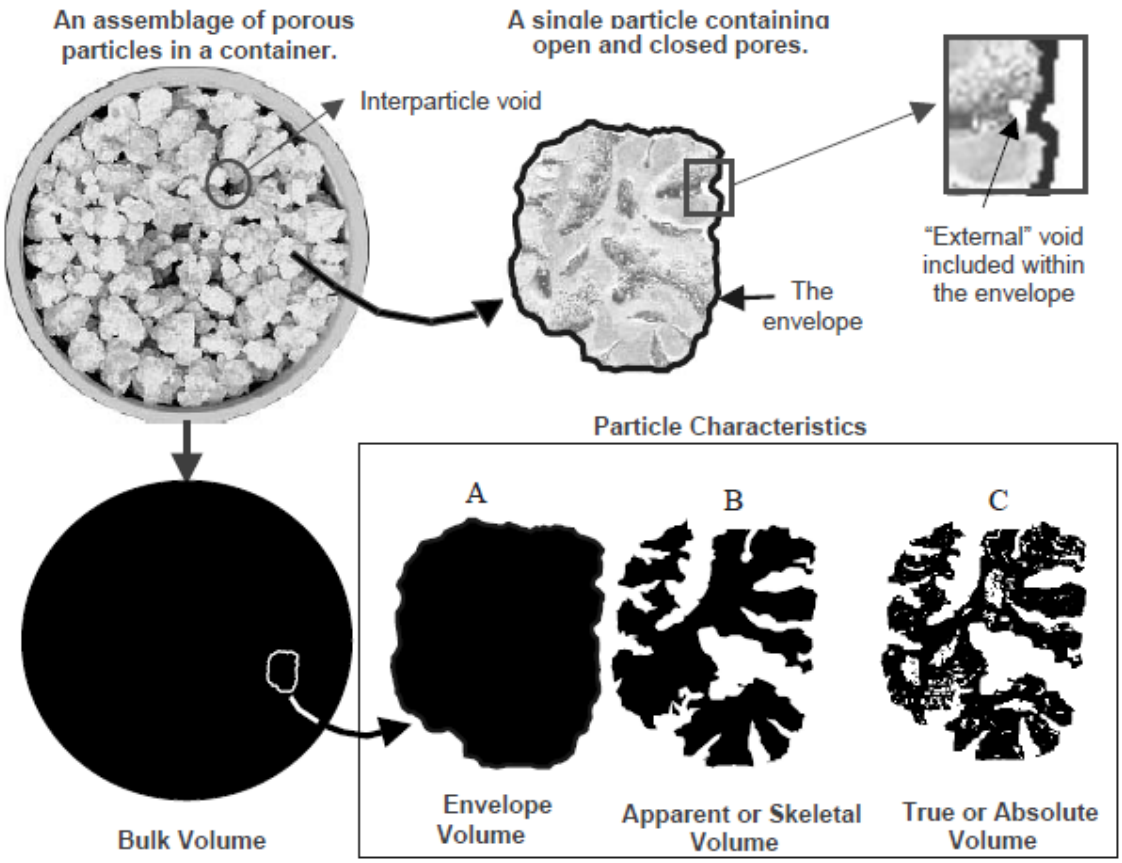

Figure 3.2: Illustration showing the difference between the types of densities [83].

ϵ can be defined either on a dry basis, ϵ_{dry} (i.e. when the biomass is completely dry), and on a wet basis, ϵ_{wet} (i.e. when MC > 0):

$$\epsilon_{dry} = \frac{V_{total} - V_{bm}}{V_{total}} \ , \tag{3.13}$$

$$\epsilon_{wet} = \frac{V_{total} - V_{bm} - V_{water}}{V_{total}} \ . \tag{3.14}$$

In the above, V_{total} is the total volume, V_{bm} is the volume of the biomass material,

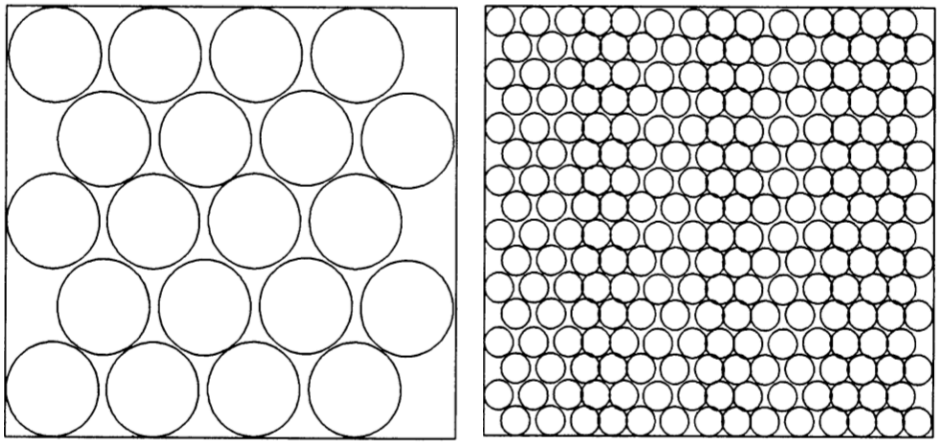

(a) Coarse particles porous media (b) Fine particles porous media

Figure 3.3: Monodispersions of coarse and fine particles, containing identical ϵ, but different pore size distributions [84].

and V_{water} is the volume of the water occupying the pores. As such, we can arrive at a relationship between ϵ_{dry} and ϵ_{wet}:

$$\epsilon_{wet} = \epsilon_{dry} - \frac{\text{MC} \times \rho_{true} \times (1 - \epsilon_{dry})}{\rho_{water}(1 - \text{MC})} \ . \tag{3.15}$$

As the MC inherent in the biomass increases, ϵ_{wet} will decrease and become smaller as it accounts the presence of moisture within the pores.

Besides ϵ, the pore size distribution also plays a major role on the flow dynamics of a biomass material. The pore size distribution describes the distribution of pores that make up the overall ϵ. Consider the two porous media regimes in Fig. 3.3, where Fig. 3.3(a) illustrates a coarse particle regime while Fig. 3.3(b) shows a fine particle regime. Both regimes contain spheres in the same packing arrangement, described as hexagonal close packing and have the same ϵ. However, it is important to distinguish the pore size distribution between the two regimes. Water could easily flow through the pore system in Fig. 3.3(a), but with much more difficulty in Fig. 3.3(b). This highlights the interconnectedness between ϵ and pore size distribution as two regimes with the same ϵ can have extremely different pore size distribution.

3.1.3.2 Heating value

The heating value of biomass, also referred to as the calorific or energy value, refers to the amount of energy that can potentially be released when a given quantity of biomass is burned or converted into heat through combustion or other thermal processes. This value is typically expressed in units of J/kg and is an important factor when considering the energy potential of biomass for various applications. The heating value associated with each type of biomass may vary depending on several factors including the initial MC of the biomass, the type of biomass, ρ_{true}, and the chemical composition. A typical biomass feedstock, as well as the syngas, is associated with two types of heating value: HHV and LHV [2]

The HHV is defined as the amount of heat energy released by the unit mass or volume of fuel (initially at 25 °C) once it is combusted and the products have returned to the initial temperature. The HHV takes into account not only the energy released from the combustion of the carbon and hydrogen in the biomass but also the energy released when the water vapour produced during combustion condenses back into liquid water. This is why it is sometimes referred to as the gross calorific value or gross heating value [2].

Alternatively, the LHV of biomass, also known as the net calorific value (NCV), is defined as the amount of heat released by fully combusting a given quantity of biomass, but it does not take into account the heat released when the water vapour in the combustion products remains in a gaseous state (i.e., it does not consider the heat of vaporisation). In other words, it represents the heat energy that can be practically extracted from the combustion of biomass under typical operating conditions where the water vapour is not condensed [2]. The molar LHV can be calculated from the specific HHV (J/kg) of the biomass, HHV_{bmspec}, on a dry basis [85–87] as:

$$\mathrm{LHV}_{bm} = \mathrm{HHV}_{bmspec} \times M_{bm} - h_{vap}\left(\frac{\alpha}{2}\right) \ , \tag{3.16}$$

where h_{vap}=44,000 J/mol is the enthalpy of vaporisation of water at standard temperature. The specific HHV_{bmspec} (MJ/kg) is calculated via an empirical correlation

proposed by Channiwala and Parikh [88], namely:

$$\mathrm{HHV}_{bmspec} = 0.3491y_C + 1.1783y_H + 0.1005y_S - 0.1034y_O - 0.0151y_N - 0.0211y_{ASH} \ . \tag{3.17}$$

y_C, y_H, y_O, y_N, y_S and y_{ASH} can be obtained from the ultimate analysis of the biomass feedstock. Eq. 3.17 is derived experimentally using 225 data points and validated for an additional 50 data points. The validity of the correlation has been established for fuels having a wide range of elemental composition, and offers an average absolute error of 1.45% and bias error of 0.00%, thereby cementing its versatility.

3.1.3.3 Thermodynamic properties

As gasification is a thermochemical conversion process, the thermodynamic properties of a biomass strongly influence its gasification. Three important thermodynamic properties are discussed in this section which are thermal conductivity (k_{eff}), specific heat (C_p), and heat of formation of biomass ($h^{\circ}_{f,bm}$).

Biomass particles, however small they may be, are subject to heat conduction along and across their fibre, influencing their pyrolysis behaviour. Thermal conductivity of biomass changes with ρ and MC. Various correlations have been developed for the calculation of the k_{eff}, one of which was developed by MacLean [89]:

$$k_{eff} = sg(0.2 + 0.004 \times \mathrm{MC}) + 0.0238 \ , \text{for MC} > 40\% \ , \tag{3.18}$$

$$= sg(0.2 + 0.0055 \times \mathrm{MC}) + 0.0238 \ , \text{for MC} < 40\% \ , \tag{3.19}$$

where sg is the specific gravity of the fuel. Due to the microscopic structure of biomass, its k_{eff} along its fibres is different from that across them. k_{eff} also is reliant on the biomass MC, ϵ, and temperature T. Other correlations for the calculation of the k_{eff} of biomass also exist. In the developed CFD model, the k_{eff} of the biomass is obtained directly from literature and no correlation used to estimate it.

C_p is an influential thermodynamic property of biomass, often required for thermodynamic calculations. It is a property which is found to depend on temperature

and MC, estimated through several correlations. Most notably, the experimentally derived correlation of Thunman et al [90] are used extensively (kJ/kg.K):

$$C_{p,dry} = 2.45T + 531.2 \ , \tag{3.20}$$

$$C_{p,wet} = \left(\frac{C_{p,dry} + 4190 \frac{\mathrm{MC}}{1-\mathrm{MC}}}{1 + \frac{\mathrm{MC}}{1-\mathrm{MC}}} \right) + \left(23.55T - 1320 \frac{\mathrm{MC}}{1-\mathrm{MC}} - 6191 \right) \frac{\mathrm{MC}}{1-\mathrm{MC}} \ . \tag{3.21}$$

Several others exist such as the experimentally derived correlations of Jenkins [91]:

$$C_{p,dry} = 0.266 + 0.00116T \ , \tag{3.22}$$

$$C_{p,wet} = \mathrm{MC} \times C_{p,H_2O} + (1 - \mathrm{MC}) C_{p,dry} \ , \tag{3.23}$$

and the experimentally derived correlations of TenWolde et al [92]:

$$C_{p,dry} = 0.1031 + 0.003867T \ , \tag{3.24}$$

$$C_{p,wet} = \frac{C_{p,dry} + 4.19\mathrm{MC}}{(1 + \mathrm{MC})} + (0.02355T - 1.32\mathrm{MC} - 6.191) \times \mathrm{MC} \ , \tag{3.25}$$

which were established via regression analyses of available data from the literature. According to Table 3.2, the correlation suggested by [90] and [92] exhibits good alignment with the estimated C_p, whereas the prediction by [91] deviates. Hence, the correlation by [90] is selected.

Table 3.2: C_p of wood predicted via the above correlations at $T = 298.15$ K.

C_p (kJ/kg K)	Thunman et al. [90]	TenWolde et al. [92]	Jenkins et al. [91]
$C_{p,dry}$	1.26	1.26	0.29
$C_{p,wet}$	1.63	1.59	0.68

Finally, $h^{\circ}_{f,bm}$ is the enthalpy change when 1 mole of compound is formed at standard state (25 °C, 1 atm) from its constituent elements in their standard state. For example, hydrogen and oxygen are stable in their elemental form and as such their enthalpy of formation is zero. However, when they combine to form a compound such as steam, an amount of energy equivalent to 241.8 kJ is released, making the

heat of formation of steam equal to -241.8 kJ/mol. This energy amount is taken out of the system and is given a negative sign to indicate an exothermic reaction [2]. The biomass formation enthalpy is computed as a function of the molar LHV (J/mol) of the biomass [85–87], according to:

$$h^{\circ}_{f,bm} = \mathrm{LHV}_{bm} + \sum_{i=1}^{4} \nu_i h^{\circ}_{f,i} \ , \tag{3.26}$$

where ν_i are the stoichiometric coefficients of the products under complete combustion, $h^{\circ}_{f,i}$ is the heat of formation of species i, and $\sum_{i=1}^{4}$ is repeated over all products of (R18) - see section 3.3.4.2.

3.2 Brief Historical Background

Gasification, as an industrial process, has a rich history dating back to the early 19$^{\text{th}}$ century. Its roots can be traced to the production of town gas for lighting, heating, and cooking in the 19$^{\text{th}}$ and early 20$^{\text{th}}$ centuries. One of the earliest instances of gasification was the gasification of coal to produce town gas, which was used for various domestic and industrial applications.

The technology gained further attraction during World War II, as gasifiers were implemented to produce synthetic fuels and chemicals due to scarcity of petroleum-based fuels. These gasifiers played a crucial role in ensuring fuel availability during the war.

In the mid-20$^{\text{th}}$ century, gasification technology expanded to include the conversion of various feedstocks such as biomass, municipal solid waste, and even organic residues from industrial processes. This diversification was driven by the need for cleaner and more sustainable energy solutions.

In recent decades, with growing emphasis on renewable energy and environmental sustainability, gasification has gained renewed interest. Its potential to produce syngas, which can be used for the production of electricity, chemicals, and transportation fuels, has positioned gasification as a promising technology for achieving energy security and reducing greenhouse gas emissions.

Today, gasification is a key process in the production of syngas and has found applications in various industries, including power generation, chemicals, and fuel production. Ongoing research and development efforts continue to improve the efficiency, cost-effectiveness, and environmental sustainability of gasification technologies, positioning it as a crucial component of the future energy landscape [2].

Another prominent thermochemical conversion process is combustion, which involves a chemical reaction between a fuel and an oxidant, typically oxygen, resulting in the release of heat and the generation of various products. It is a well established process used for heat generation and power production in various industries, including electricity generation, heating, and transportation.

Table 3.3: Advantages and disadvantages associated with both gasification and combustion.

Technology	Advantages	Disadvantages
Gasification	Higher efficiency Feedstock Versatility Syngas production Reduced emissions Waste reduction	Complexity Higher initial investment Feedstock quality
Combustion	Simplicity Familiarity Lower Initial investment Direct heat production	Lower efficiency Emission issues Limited feedstock flexibility

Both gasification and combustion involve the transformation of organic materials, such as coal, biomass, or waste into useful forms of energy. While they share some similarities, each process is associated with its own set of advantages and disadvantages. Table 3.3 provides the pros and cons associated with each type of technology.

3.3 Overview of the Gasification Process

Given the definition of biomass gasification, the process of gasification is complicated due to the complexity of the heterogeneous and homogeneous chemical reactions involved. There are different stages in a biomass gasifier which the feedstock passes

through, enabling different species distributions. Also, there are different types of biomass gasifiers, each of which enable a different producer gas composition and operate at different thermal efficiencies, resulting in varied gasifier performances. The operating conditions of a generic biomass gasifier also strongly influences its performance, thus establishing the quality and type of end-product. In this section, a detailed analysis of the gasification process is presented along with a thorough investigation of the ideal operating conditions which yield a high quality producer gas.

3.3.1 Stages of gasification

A typical biomass gasifier is characterised by four different stages in the reactor in which the biomass feedstock and its decompositional species have to pass through to achieve the desired end-product. Practically, there is no well-defined boundary between the different stages, and they usually occur interchangeably, but for modelling purposes, they are treated one following the other. The different zones listed in sequential order are:

1. Drying zone; whereby the abundant amount of MC accompanying different biomass feedstocks is dried at around 100 - 200°C reducing energy losses and increases the quality of the end product. Depending on the type of feedstock, the MC of the material usually ranges between 5% - 35%. Research and experimental work has established that every kilogram of moisture in biomass takes away a minimum of 2260 kJ of non-recoverable extra energy from the gasifier to vaporise water. While it is futile to remove the moisture inherently residing within biomass cell structures, efforts can be made to extract surface moisture, making the drying zone essential for the gasification process [2, 93]. The process of drying can be described by the following mass balance:

$$\mathrm{m}_{\mathrm{H_2O}(l)} \rightarrow \mathrm{m}_{\mathrm{H_2O}(g)} \ , \tag{R1}$$

   where subscripts (l) and (g) signify liquid and gas phases respectively.

2. Pyrolysis zone; whereby the dry biomass feedstock is thermally decomposed

in the absence of air and in the presence of high temperatures (150-700°C), releasing volatiles components and a residue containing char and ash. The volatiles produced are a mixture of light hydrocarbons, CO, H_2, CO_2, H_2O, and tars. The decomposition occurs homogeneously and heterogeneously in which the process can be described by the following:

$$\text{biomass} \rightarrow \text{char} + \text{volatiles} + \text{tar} + \text{ash} \; . \tag{R2}$$

3. Oxidation zone; whereby the volatile material of the biomass gets oxidised under exothermic reactions at high temperatures, releasing the heat needed for endothermic reactions. The oxidation temperature is about 800 - 1400 °C, in which both partial and complete oxidation reactions take place for char and other gaseous components which were produced from the pyrolysis zone [93].

4. Reduction zone; whereby various chemical reactions, mainly endothermic, occur in the absence of oxygen to produce syngas. The main reactions taking place in this zone are the boudouard, water-gas, water-gas shift and methanation reactions, along with others which are detailed and discussed in section 3.3.3.

All the stages in downdraft biomass gasification are equally important as all four of them have different objectives in achieving a high quality syngas product.

3.3.2 Types of gasifiers

Gasifier design is one of the major influences of product output, especially with respect to the amount of tars generated. The type of gasifier implemented depends on different variables and characteristics including fuel availability, MC, shape and size and end user applications. They vary depending on the requirements of the feedstock and requirements of the end products. They can be classified and differentiated mainly on the basis of their gas - solid contacting mode and the use of the gasification agent and the temperature range in which the gasifier is operating. Gasifiers are broadly divided into three principle types: fixed or moving bed,

fluidised bed, and entrained flow. Each is further subdivided into specific types as discussed [2].

Table 3.4: Advantages and disadvantages of different gasifier types [94].

Gasifier Type	Advantages	Disadvantages
Updraft	· Simple design and low-cost process · Suitable for small-scale applications · Suitable for high MC	· High tar content · Require intensive cleaning
Downdraft	· Simple design and low cost · Low tar content · High energy efficiency	· Suitable for low MC · Requires cooling of syngas
Cross-flow	· Ease of operation · Simple gas cleaning	· High tar content · Low overall energy efficiency
Circulating bed	· Good mixing and heat transfer · Efficient conversion · Feedstock flexibility · Operates at high temperatures	· Complex design and operation · High initial capital cost · Requires sophisticated gas cleaning
Bubbling bed	· Suitable for fast reactions · Good mixing and heat transfer · High conversion rates	· Bed agglomeration · Complex design and operation · High initial capital cost · Particle attrition
Entrained Flow	· High conversion efficiency · Suitable for large scale applications · Feedstock flexibility	· High operating temperature and pressure, requiring more durable materials · High tar content · High capital and maintenance costs

3.3.2.1 Fixed-bed gasifiers

In fixed-bed gasifiers, the fuel moves down the unit as a plug, contacting the gasification agent in the upward or downward direction, depending on the specific gasifier type. They are traditionally inexpensive to build and come in small sizes, which is one of their major attractions. Both mixing and heat transfer in fixed-bed gasifiers are rather poor, making it difficult to achieve a uniform distribution of fuel, temperature and gas composition through the cross-section of the gasifier. In one of the oldest and simplest designs, the gasification agent in an updraft gasifier, such as the one portrayed in Fig. 3.4, travels upwards while the bed of fuel moves downward, resulting in counter-current interaction between the feedstock and the medium.

The product gas leaves from the top of the gasifier and the gasification agent enters the bed through a grate or distributor found typically at the lower end of the unit. These types of gasifiers are suitable for high-ash (up to 25%) and high MC (up to 60%), low volatile biomass fuels. Tar formation is very high in these units, potentially exceeding 150 g/Nm^3. Otherwise, they utilise combustion heat

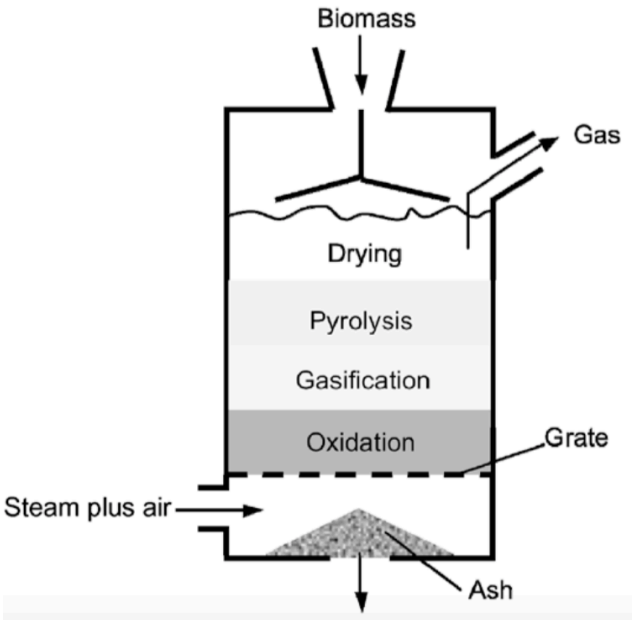

Figure 3.4: Schematic of a fixed-bed updraft gasifier [2].

very effectively, achieving high cold-gas efficiencies and increasing their suitability for direct firing, where the gas produced is burnt in a furnace or boiler with no cleaning or cooling required. Downdraft gasifiers, illustrated in Fig.3.5, are co-current reactors where the gasification agent enters the unit at a certain height below the the pyrolysis zone. The biomass fuel and the gasification agent interact in a co-current manner, resulting in the product gas leaving from the bottom through a bed of hot ash.

Since it passes through the high-temperature zone of hot ash, the tar in the product gas finds favourable conditions for cracking, resulting in significantly low tar production rates as 99% of it is burnt in the combustion zone. This type of gasifier is simple, maintains a low cost and the produced syngas can be used in further gas turbines and internal combustion engines.

In a cross-flow gasifier, the biomass, fed at the top of the unit, moves downward while the air enters from the side, resulting in the product gas leaving from the upper side at about the same level of the biomass feed. This type of configuration is mainly used for the gasification of charcoal with low ash contents. Unlike downdraft and updraft configurations, this type of gasifier releases the product from the side walls opposite to the entry point as indicated in Fig. 3.6. Excess O_2 in front of

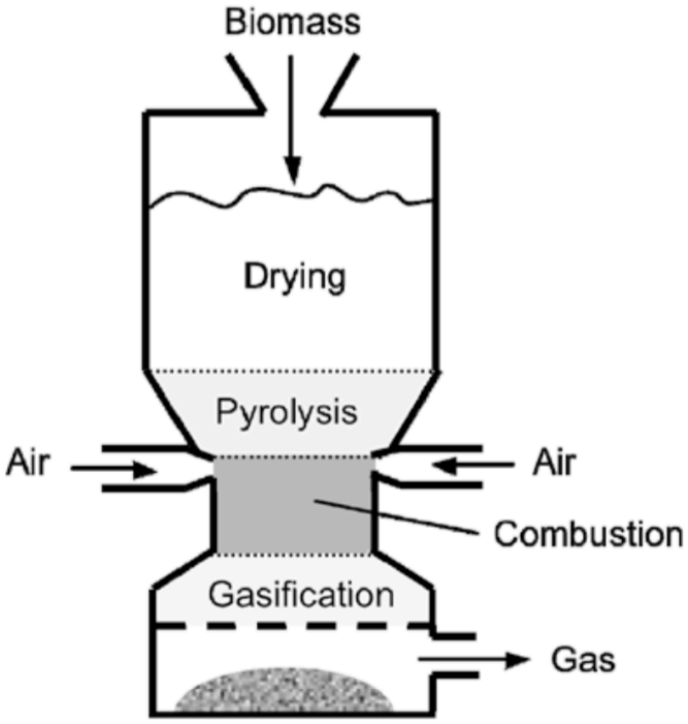

Figure 3.5: Schematic of a fixed-bed downdraft gasifier [2].

the nozzles facilitates combustion of the char, creating a high temperature zone (¿ 1500 °C). The remaining char is then gasified to CO downstream in the subsequent zone. The combustion and gasification zones are formed around the air entrance, resulting in ash being removed from the bottom. This unit is characterised by low overall energy efficiencies with a gas having a high tar content [2, 85].

3.3.2.2 Fluidised-bed gasifiers

Fluidised bed gasifiers are emerging as a convenient technology due to their fuel type flexibility, boasting an advantage over fixed bed gasifiers because of their uniform temperature distribution in the reduction zone. This is accomplished by using a bed of fine granular material (e.g. sand). into which air is circulated, fluidising the bed. One major problem in fluidised bed gasifiers is bed agglomeration causing loss of adequate fluidisation. These gasifiers are appropriate for stationary processes, usually suitable for medium to large scale installations. The gas temperature at the outlet is relatively high (800-900 °C), containing alkaline vapours. This is due to thorough mixing within these types of configurations, sustaining a constant temperature in

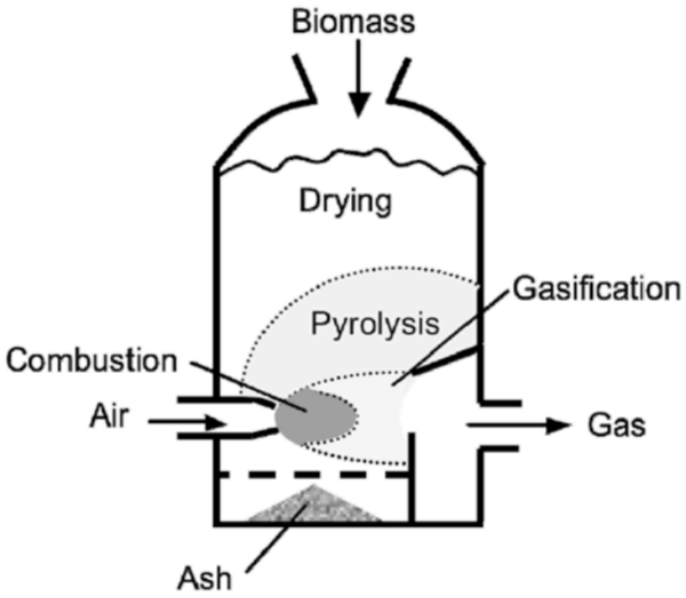

Figure 3.6: Schematic of a fixed-bed cross-flow gasifier [2].

the reactor bed, allowing the gasifier to operate at high enough temperatures to achieve an acceptable C conversion rate.

Two main types of fluidised bed gasifiers are in current use: circulating bed and bubbling bed gasifiers. Fig.3.7 shows a circulating bed gasifier, which is based on a mechanism of continuous circulation of the bed material between the reaction vessel and a cyclone separator, where the ash is separated and the bed material and char return to the reaction vessel. Capable of coping with high capacity biomass throughputs, they can be operated at high pressures and deliver output gases without requiring further compression. On the other hand, bubbling bed gasifiers, such as the one in Fig.3.8 pyrolyse the biomass, forming char, gaseous components and tar in a fine bed material placed above a grate through which air is fed. High molecular weight tar reacts with the hot bed material, delivering a product gas with a lower tar content [85].

3.3.2.3 Entrained-flow gasifiers

Fig. 3.9 illustrates an entrained flow gasifier, in which fine particles and the gasification agent are fed co-currently, resulting in the oxidant or steam surrounding or entraining the solid particles as they flow through the gasifier in a dense cloud. They operate at high temperature and pressure, characterised by a significant turbulent

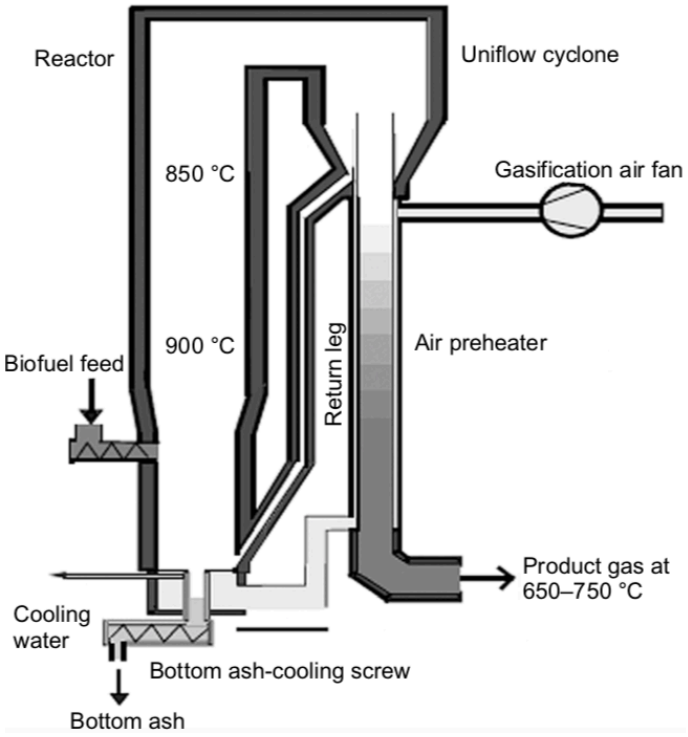

Figure 3.7: Schematic of a circulating fluidised-bed gasifier [2].

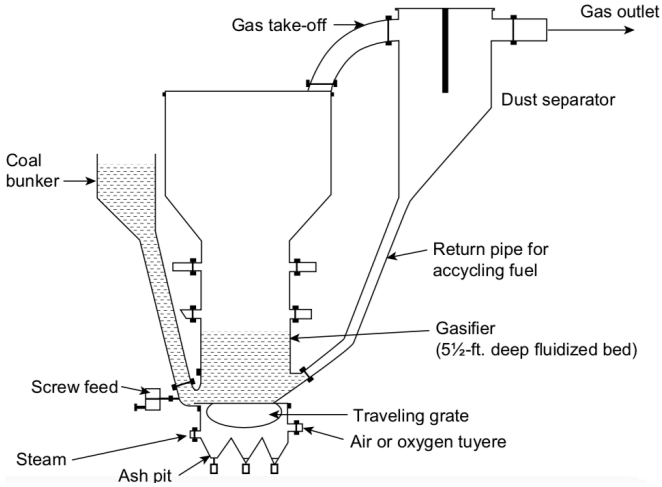

Figure 3.8: Schematic of a bubbling fluidised-bed gasifier [2].

flow, causing rapid feedstock conversion, allowing high throughput. Gasification reactions occur at an extremely high rate, with high carbon conversion efficiencies (98 - 99.5%). Because of the high operating temperatures, entrained-flow gasifiers melt ash into vitreous inert slag. This type of gasifier introduces additional water through the use of slurry pumps, resulting in an increased H_2 - CO ratio, but with lower gasifier thermal efficiency [85].

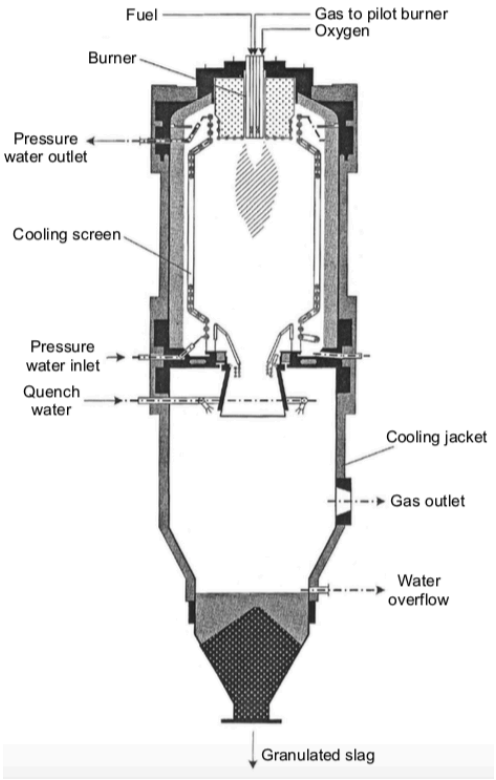

Figure 3.9: Schematic of an entrained-flow gasifier [2].

3.3.3 Typical chemical reactions

During biomass gasification, the biomass primarily undergoes drying after which the feedstock experiences thermal degradation in the pyrolysis zone. The pyrolysis products react with themselves and with the gasification agent to form ultimate gasification products. The char produced is a product containing unconverted carbon, some hydrocarbons and ash. While the quantity of char is largely dependent on the reactor and operational conditions, the amount of ash depends on the type

of feedstock used. The following is a list of the most relevant chemical reactions occurring in a gasification process [2]:

- Carbon Reactions

  1. Boudouard

$$C + CO_2 \rightarrow 2CO \ , \tag{R3}$$

  2. Water-gas or steam

$$C + H_2O \rightarrow CO + H_2 \ , \tag{R4}$$

  3. Hydrogasification

$$C + 2H_2 \rightarrow CH_4 \ , \tag{R5}$$
$$C + 0.5O_2 \rightarrow CO \ , \tag{R6}$$

- Oxidation Reactions

$$C + O_2 \rightarrow CO_2 \ , \tag{R7}$$
$$CO + 0.5O_2 \rightarrow CO_2 \ , \tag{R8}$$
$$CH_4 + 1.5O_2 \rightarrow CO + 2H_2O \ , \tag{R9}$$
$$H_2 + 0.5O_2 \rightarrow H_2O \ , \tag{R10}$$

- Shift Reaction

$$CO + H_2O \rightarrow CO_2 + H_2 \ , \tag{R11}$$

- Methanation Reactions

$$2CO + 2H_2 \rightarrow CH_4 + CO_2 \ , \tag{R12}$$

$$CO + 3H_2 \rightarrow CH_4 + H_2O \ , \tag{R13}$$

$$CO_2 + 4H_2 \rightarrow CH_4 + 2H_2O \ , \tag{R14}$$

- Steam Reforming Reactions

$$CH_4 + 0.5O_2 \rightarrow CO + 2H_2 \ , \tag{R15}$$

$$CH_4 + H_2O \rightarrow CO + 3H_2 \ . \tag{R16}$$

Depending on the modelling approach, all or some of the above chemical reactions might be implemented. As will be seen subsequently, thermodynamic equilibrium models only utilise independent chemical reactions, avoiding the computation of repeated information. In a CFD model, most of the above chemical reactions will be implemented alongside additional reactions describing the drying and pyrolysis zones, further adding to the complexity of the model. Biomass char is typically more porous and reactive than coke, maintaining a ϵ ranging from 40-50%, while that of coal char is between 2-18%.

The process of pyrolysis and char reactions are typically heterogeneous chemical reactions, whereby the reactants are in two or more phases. Pyrolysis involves the breaking down of the feedstock into the different pyrolytic products making up the biomass and unreacted char reacts with the different pyrolytic products. Simultaneously, chemical reactions amongst the evolved gases also take place which are called homogeneous chemical reactions.

The key difference between heterogeneous and homogeneous reactions lies in the phase of the reactants. Examples of heterogeneous reactions include (R3) and (R4), whereas homogeneous chemical reactions include (R11) and (R8). (R3) to (R7) depict how the char reacts with different gasification agents, such as O_2, CO_2, and H_2O, to produce lower-molecular-weight gases like CO and H_2. The rate of (R6) is the fastest of (R3), (R4), (R5) and (R6), rapidly consuming the O_2, leaving little

amounts for other reactions. The rate of (R4) is 3 to 5 orders of magnitude slower than that of (R6), (R3) is 6 to 7 orders of magnitude slower and (R5) is the slowest among the four [95].

The rates of the chemical reactions are an essential tool in the analysis of the different pathways that the reactions can take. As will be seen when developing a CFD model in Chapter 5, how fast and slow the reactions are and how well they compete with each other effectively determine the syngas composition.

3.3.4 Operating conditions

The composition and quality of the producer gas leaving a gasifier are highly influenced by its operating parameters. One of the major challenges in biomass gasifier design is to determine the appropriate range of operating conditions that will yield the desired end-product. Moreover, with the involvement of a complex chemical reaction scheme encompassing both homogeneous and heterogeneous reactions, identifying suitable operating conditions becomes even more challenging.

To address this issue, researchers have extensively studied gasification models and conducted numerous experimental investigations on state-of-the-art biomass gasifiers. As a result, a range of operating conditions that are considered suitable has been identified. This section delves into and discusses these operating conditions and their significance in achieving desired gasification outcomes.

3.3.4.1 Gasifying agent

The choice of gasifying agent significantly impacts the composition and heating value of the producer gas. Three commonly used agents are air, steam, and O_2, each offering distinct characteristics and applications.

Air gasification is both straightforward and cost-effective, making it suitable for small-scale applications. However, it results in a syngas with a relatively low LHV - see section 3.1.3.3 - due to the increased N_2 content from the air.

On the other hand, O_2 gasification enhances the LHV by removing N_2, making it an attractive option for generating syngas with high C sequestration and storage capabilities. Nonetheless, it is important to note that utilising oxygen gasification

comes with increased plant operating costs, as it necessitates the implementation of an air separation unit and additional storage and distribution systems.

Lastly, steam gasification produces a high-quality syngas with elevated H_2 content and a high LHV, and is often performed with steam/O_2 mixtures to optimise its efficiency [85]. The addition of O_2 with steam can accelerate the gasification reactions, facilitating the partial oxidation of the feedstock and leading to a faster conversion of the hydrocarbons into syngas. By controlling the ratio of O_2 and steam, it is possible to manipulate the reaction pathways and the composition of the syngas produced. For example, introducing steam into the gasification process promotes steam reforming reactions, increasing the H_2 concentration in the syngas. Furthermore, adding O_2 can help in partial oxidation reactions, which can crack larger hydrocarbon molecules (i.e. tars) into smaller, more useful gaseous components, reducing tar formation and improving the quality of the syngas. Each gasifying agent presents its own set of advantages and limitations, and selection of the most suitable one depends on the specific requirements and objectives of the gasification process.

3.3.4.2 Equivalence ratio

The ER is arguably the most critical operating condition affecting biomass gasification. This parameter represents the ratio, in the case of air gasification, between the masses/moles of air and biomass on a dry and ash-free basis under actual operating conditions, which are the conditions supplied to undergo the process, compared to the same ratio under stoichiometric conditions, which is the ideal amount required for a complete reaction [96].

When the ER is 0, there is no oxidant present in the system, while an ER equal to 1 indicates stoichiometric combustion. An ER greater than 1 signifies fuel-lean combustion, whereas an ER lower than 1 indicates fuel-rich combustion. Gasification, in some sense, can be viewed as fuel-rich combustion, where optimum ER values for the best gasification performance generally range from 0.2 to 0.4 [2].

The ER has a profound influence on the gasification process, as it determines the system's temperature, O_2 availability, syngas yield, and consequently the gas

composition, heating value, and tar content. Identifying the optimal ER for a specific gasification system is crucial, as it directly impacts the conversion of C into gas. Lower ER values result in incomplete conversion of char into volatiles, leading to higher tar production. This is one of the reasons why updraft gasifiers, which typically operate with ER values below 0.25, produce high tar content [85].

The universally accepted definition of the ER is as follows [2]:

$$\text{gasification}\frac{\text{air}}{\text{fuel}} = \text{ER} \times \text{combustion}\frac{\text{air}}{\text{fuel}} \ . \tag{3.27}$$

The gasification air-fuel ratio is the actual amount of air, which is made up of approximately 79% N_2 and 21% O_2 by number of moles (76.6% N_2 and 23.3% O_2 by mass) used in the system divided by the biomass feeding rate or consumption rate. The combustion air-fuel ratio is a constant for a specific biomass feedstock and can be calculated from the ultimate analysis of the biomass - see section 3.1.1. This discussion proceeds from [2], in which they argued that in a combustor, the amount of air supplied is determined by the stoichiometric (or theoretical amount) amount, whereas in a gasifier, the air supply is only a fraction of the stoichiometric amount.

Depending on the units of the gasification and combustion air-fuel ratios, the ER can be determined either on a molar or mass basis. The derivation of the ER equation [87,97] comes from both the global reaction for gasification and combustion of biomass in O_2. According to the global gasification reaction for a particular feedstock [98]:

$$\begin{aligned} \mathrm{CH_\alpha O_\beta N_\lambda S_\delta} + w\mathrm{H_2O} + m_{gas}(\mathrm{O_2} + 3.76\mathrm{N_2}) \rightarrow x_1\mathrm{H_2} + x_2\mathrm{CO} + x_3\mathrm{CO_2} \\ + x_4\mathrm{H_2O} + x_5\mathrm{CH_4} + x_6\mathrm{N_2} + x_7\mathrm{H_2S} \ , \end{aligned} \tag{R17}$$

where m_{gas} is the number of moles of gasifier input air per one mole of biomass, corresponding to the gasification air-fuel ratio in Eq. 3.27, x_1 to x_7 represent the stoichiometric coefficients of the various gaseous species, $\mathrm{CH_\alpha O_\beta N_\lambda S_\delta}$ represents the biomass feedstock with α, β, λ, and δ comprising the number of atoms of H_2, O_2, and N_2, and S per number of atoms of C; where w is the number of moles of H_2O

per one mole of biomass and is calculated from the biomass MC on a wet basis. These quantities can be obtained from the ultimate analysis - see subsection 3.1.1 - of the feedstock.

Conversely, the global combustion reaction for a particular feedstock is:

$$\mathrm{C\,H_\alpha O_\beta N_\lambda S_\delta} + m_{comb}\mathrm{O_2} \rightarrow z_1\mathrm{CO_2} + z_2\mathrm{H_2O} + z_3\mathrm{SO_2} + z_4\mathrm{NO}\ , \tag{R18}$$

where $z_1 - z_4$ are the stoichiometric coefficients of the respective gas species in the combustion reaction, solved using elemental molar balances, m_{comb} is the amount of air needed for the combustion of one mole of biomass, corresponding to the combustion air-fuel ratio in Eq. 3.27. The stoichiometric balance of which consists of elemental molar balances for each of the following species C, H, O, N, S is given:

$$\mathrm{C} : z_1 = 1\ , \tag{3.28}$$

$$\mathrm{H} : z_2 = \frac{\alpha}{2}\ , \tag{3.29}$$

$$\mathrm{O} : 2z_1 + z_2 + 2z_3 + z_4 = \beta + 2m_{comb}\ , \tag{3.30}$$

$$\mathrm{N} : z_4 = \lambda\ , \tag{3.31}$$

$$\mathrm{S} : z_3 = \delta\ . \tag{3.32}$$

By substituting Eqs. (3.28), (3.29), (3.31), and (3.32) into Eq. (3.30), the following expression for m_{comb} is obtained:

$$m_{comb} = \left(1 + \frac{\alpha}{4} - \frac{\beta}{2} + \frac{\lambda}{2} + \delta\right)\ . \tag{3.33}$$

Next, using the definition of the ER in Eq. 3.27:

$$\mathrm{ER} = \frac{m_{gas}}{m_{comb}} = \frac{m_{gas}}{\left(1 + \frac{\alpha}{4} - \frac{\beta}{2} + \frac{\lambda}{2} + \delta\right)}\ , \tag{3.34}$$

Eq. 3.34 can be written as:

$$m_{gas} = \left(1 + \frac{\alpha}{4} - \frac{\beta}{2} + \frac{\lambda}{2} + \delta\right) \times \mathrm{ER}\ . \tag{3.35}$$

Thus the combustion reaction simplifies as follows:

$$\mathrm{C\,H_\alpha O_\beta N_\lambda S_\delta} + \left(1 + \frac{\alpha}{4} - \frac{\beta}{2} + \frac{\lambda}{2} + \delta\right) \mathrm{O_2} \rightarrow \mathrm{CO_2} + \frac{\alpha}{2}\mathrm{H_2O} + \delta\mathrm{SO_2} + \lambda\mathrm{NO}\ . \tag{R19}$$

Therefore, m_{gas} is calculated from ER as per Eq. 3.35.

The gasification air-fuel ratio on a mass basis is calculated by dividing the mass flowrate of the consumed O_2 in the equivalent air (kg/s) by the biomass consumption rate (kg/s) as such:

$$\text{gasification}\frac{\text{air}}{\text{fuel}} = \frac{\dot{m}_{air,eq}}{\dot{m}_{bm}}\ , \tag{3.36}$$

where $\dot{m}_{air,eq}$ is the consumed air mass flowrate (kg/s) in the equivalent air and $\dot{m}_{bm}$ is the biomass consumption rate (kg/s). The combustion mass air-fuel ratio can be expressed as follows:

$$\text{combustion}\frac{\text{air}}{\text{fuel}} = \left(1 + \frac{\alpha}{4} - \frac{\beta}{2} + \frac{\lambda}{2} + \delta\right) \times \left(\frac{M_{O_2} + 3.76 M_{N_2}}{M_{bm}}\right)\ (\mathrm{kg_{air}/kg_{bm}})\ . \tag{3.37}$$

3.3.4.3 Temperature

The temperature of the system plays a crucial role in determining the distribution of gaseous and solid species during pyrolysis, thereby affecting the equilibrium reactions involved in the gasification process. Several authors, such as Mansaray et al. [99] and Narvaez et al. [100], have reported that increasing temperatures lead to higher syngas production and a reduction in tar content.

It is important to note that temperature is primarily considered an operating parameter at the laboratory scale. In actual gasification systems, temperature cannot be directly controlled as it becomes a function of various factors, including the ER, gas and solid flow rates, and thermal dispersions [85]. As a result, achieving precise control over the temperature becomes more challenging in real-world applications. Nonetheless, understanding the influence of temperature on the gasification process remains crucial for optimising gasifier performance and achieving desired syngas composition and tar content.

3.3.4.4 Moisture content

The MC of biomass has a significant impact on its conversion into energy. When biomass has a high MC level (which can be as much as 70% in its natural state), it becomes challenging to maintain self-sustained combustion. Additionally, high MC levels lead to a decrease in the heating value of the syngas, resulting in a reduced overall energetic efficiency of the gasification process. Moreover, higher MC levels also lower the oxidation temperature, leading to incomplete cracking of hydrocarbons formed during pyrolysis.

Among fixed-bed gasifiers, downdraft ones are more sensitive to MC compared to updraft ones. The tolerable limits for MC in downdraft gasifiers typically range between 15% and 55% [85]. It is essential to carefully manage and control the MC of biomass feedstocks to achieve optimal gasification performance and ensure efficient energy conversion.

3.3.4.5 Superficial velocity

The superficial velocity (SV) is defined as the ratio of the syngas production rate at normal conditions to the narrowest cross-sectional area of the gasifier. SV directly influences the energy content of the syngas, the fuel consumption rate, and the rates of char and tar production. When SV is low, slow pyrolysis occurs, leading to higher char and tar contents in the syngas. This is unwanted as the main objective is to reduce tar in the producer gas as much as possible and achieve a high C conversion. On the other hand, high SV values result in fast pyrolysis, leading to lower amounts of char and tar in the producer gas.

However, it is important to note that a high SV also reduces the syngas residence time in the gasifier. This can have a negative impact on the efficiency of the tar cracking process, which is essential for achieving a cleaner syngas. Thus, finding an optimal SV value is crucial to balance the trade-off between minimising tar and char content while ensuring sufficient residence time for efficient tar cracking [101].

3.3.4.6 Particle size

The size of biomass particles is a critical factor in ensuring a specific consumption rate and maintaining an appropriate pressure drop inside the reactor without the formation of preferential channels. Therefore, the particle size must be carefully chosen to ensure optimal gasification performance. The sphericity of the particles also affects the heat transfer between the solid and gaseous phases. Smaller particles have a quicker heating rate and react more rapidly compared to larger particles.

However, it is important to note that the particle size does not directly influence the syngas composition. The composition of the syngas is primarily influenced by the biomass's chemical composition rather than its size [53]. Therefore, while particle size has an impact on the gasification process, its effect on the resulting syngas composition is indirect.

3.3.5 Tar formation and reduction

Tar is a thick, black, and highly viscous liquid that forms in the low-temperature zones of the gasifier and can cause blockages in gas pathways, leading to fouling and disruptions in the gasification system. Various definitions of tar have been proposed in previous publications, with Neeft et al. [102] defining it as "all organic contaminants with a molecular weight larger than benzene." Due to its complex composition, tar is often assumed to possess the same thermodynamic properties as benzene in modelling procedures, simplifying the mathematical model.

As an inevitable by-product of biomass gasification, efforts are focused on limiting its formation rather than completely eliminating it. Tar is predominantly formed in the pyrolysis zone of the gasifier, where the decomposition of biomass occurs at temperatures ranging from 200-500°C. This breakdown of biomass components, such as cellulose, hemicellulose, and lignin, leads to the formation of primary tar (also known as wood oil or wood syrup). At temperatures above 500 °C, primary tars undergo further reactions, transforming into smaller, lighter non-condensable gases, as well as a series of heavier molecules known as secondary tars. At even higher temperatures, primary tar products can be further degraded to produce tertiary

tars [2].

Although tar formation is inherent in biomass gasification, it is essential to understand its behaviour and minimise its impact on the gasification process. The amounts of tar generated in different types of gasifiers are provided in Table 3.5. For the downdraft configuration, the average levels of tar was collected based on a range of feedstocks and operating designs, except for the gasification agent which was only tested for air gasification. Concerning the bubbling and circulating bed gasifiers, the average tar levels were collected based on a plant power of 90 kW for the bubbling-bed and 16,000 kW for the circulating-bed. The feedstock analysed is wood in both configurations and the fuel MC is 14% and 15% respectively. The gasification agent in both configurations was air, which was varied in order to study its effect on the tar content. Finally, for the entrained flow gasifier (EFG), the average tar level collected under air-blown gasification conditions using solid-phase adsorption at an electrically heated EFG with temperatures ranging between 900-1300 °C and varying ER values and feedstock types including raw biomass and lignite.

Table 3.5: Amount of tar produced in each type of gasifier [103].

Gasifier types	**Average tar levels (g/Nm^3)**	**Reference**
Updraft	10-150	[104]
Downdraft	0.01-6	[105]
Circulating fluidised bed	1-30	[106]
Bubbling fluidised bed	1-23	[106]
Entrained flow	0.02	[107]

Several techniques are present for tar removal in experimental investigations of biomass gasifiers, classified as: (a) primary and (b) secondary treatment [2]. Primary treatment examples include modifications such as the injection of secondary gasification agents into the gasifier and passing the pyrolytic products through the char which increases the temperature significantly and thus reduces the tar content. Secondary treatments involve the implementation of a second reactor to degrade and regenerate the tar content in the producer gas to an acceptable level [103].

3.3.6 Gasification performance

Measuring gasification performance involves assessing various parameters and factors to evaluate the efficiency and effectiveness of the gasification process. Gasification performance is measured in terms of both the quality and the quantity of the gas produced [2]. The key procedures and measurements taken to evaluate the performance of a gasifier are summarised below:

1. Syngas composition analysis: One of the primary measurements of a gasifier is the composition of the producer gas. This includes concentrations of H_2, CO, CH_4, and CO_2, including traces of other gases. The syngas composition will dictate the potential applications of the syngas, such as power generation and biofuels production [39].

2. Gasification efficiency: The efficiency of a biomass gasifier is expressed either as cold-gas efficiency (CGE) or hot-gas efficiency (HGE). The CGE is the energy input over the potential energy output. In other words, it is the ratio between energy of generated syngas to the energy of the biomass fed to the gasification system [2, 108].

$$\text{CGE} = \frac{\text{LHV}_{gas}}{\text{LHV}_{bm}} \times N_{gas} \times 100\% \ . \tag{3.38}$$

   where N_{gas} is the number of moles of the dry producer gas at standard temperature. On the other hand, the HGE is the ratio between total chemical energy and sensible heat of produced syngas to the chemical energy and sensible heat of biomass fed to the gasification system and can be calculated as:

$$\text{HGE} = \frac{\text{LHV}_{gas} + C_p(T_f - T_0)}{\text{LHV}_{bm}} \times 100\% \ , \tag{3.39}$$

   where T_f and T_0 are the gas temperature at the gasifier exit and the fuel (i.e. biomass) temperature entering the gasifier, respectively.

3. Gas yield: This performance indicator refers to the amount of syngas produced per unit of feedstock, often expressed in terms of gas volume or energy content.

High gas yields indicate efficient gasification.

4. C conversion efficiency: This factor measures the percentage of C in the feedstock that is converted into CO and H_2 in the syngas. Higher C conversion efficiency indicates better utilisation of the C content and a high syngas production.

5. Tar content: As mentioned previously, due to its complex structure of polyaromatic and condensable hydrocarbons, tar is a problematic by-product of gasification which can give an indication of the gasification process performance. The presence of tars and other impurities causes slagging, blockages and corrosion problems by which the overall gasification process performance is diminished. It also degrades the quality of the produced syngas, therefore lower tar content is desirable to maintain a higher gasification performance [2, 108]

Other factors and measurements can also indicate a gasifier's overall performance and efficiency, such as economic viability, by which the gasification performance includes an economic assessment, considering factors like capital and operating costs, feedstock availability and flexibility and the value of the syngas products.

3.4 Modelling of Biomass Gasification

Conducting experimental investigations to find the correct range of operating conditions needed for a given feedstock, gasification agent, reactor design parameters and thermal efficiency that greatly influence the performance of a gasifier, not to mention the feedstock's variety in terms of its composition and thermochemical properties, is both a time consuming and expensive endeavour. Under these circumstances, developing mathematical models to analyse these parameters against a set of working conditions becomes convenient. Although experimental investigations will result in arguably a more accurate representation, mathematical models are an important, good, and necessary performance tool to study a gasifier's behaviour to optimise its design and operation without resorting to physical experimentation.

Care needs to be taken while developing mathematical models in order not to

overly simplify the process by making simplifying assumptions that fall beyond the reality of the actual process system. As such, different kinds of models exist depending on the inclusion of all or some of the property specifications and the provision of model assumptions. The more the model realistically represents the gasification process, the better the results will compare to experimental data, providing a low enough margin of error and increasing the model's predictive reliability.

Nevertheless, mathematical models have been found to be effective in providing qualitative guidance on the influence of working and design parameters on the gasification process. Modelling approaches can be classified into the following categories:

- thermodynamic equilibrium models,
- kinetic models,
- computational fluid dynamics models, and
- artificial neural network models.

The following sections reviews the theory, possible assumptions and execution methodologies of each of the four approaches.

3.4.1 Thermodynamic equilibrium models

These serve as a tool to predict the concentrations of species in the producer gas, relying on the assumption that the reactants undergo complete mixing and react for an infinite period of time, providing a simplistic approach to their implementation. It is essential to note that in practical applications, the available time for the reactants to interact in the gasifier is finite, which may lead to variations in the gasification process and the resulting gas composition. [2]. Such models are independent of gasifier design and although thermodynamic equilibrium cannot be reached within a gasifier, they offer a reasonable prediction of the maximum achievable yield for a desired product, which is one of their major strengths. However, they are restricted in not being able to analyse the influence of the associated fluid dynamics or design parameters on the gasification process.

Two thermodynamic equilibrium approaches can be adopted: stoichiometric, where chemical equilibrium is determined from the equilibrium constant and non-stoichiometric, where the chemical equilibrium is determined through the minimisation of the Gibbs free energy [98]. Both approaches are reviewed, with a detailed focus on the stoichiometric one.

3.4.1.1 Stoichiometric approach

Thermodynamic equilibrium models incorporating the stoichiometric approach involve chemical reactions and the chemical equilibrium of gaseous species. In more detail, the gasification process of a mole of biomass in m_{gas} moles of air can be represented by the global gasification reaction R17.

It is possible, as is the case in Chapter 4, to portray R17 in terms of additional species including tars and minor gasification products thereby increasing the reliability of the mathematical model. Subsequently, atomic balances are performed on each chemical species along with the definitions of the chemical equilibrium constants of the chosen chemical reactions involved in the process. Calculations of equilibrium constants must be performed for independent chemical reactions, as selecting non-independent reactions results in the model computing repeated information; a more simplistic explanation being that when a reactions group is written as a combination of at least two of the others.

The most important gasification reactions to determine independent combinations are (R3), (R4), (R5), (R11) and (R13). Ten possible combinations stem from these reactions; eight independent and two dependent, specifically the combinations (R3), (R4) and (R11) and (R4), (R5) and (R13). Two independent equilibrium reactions are sufficient to model the gasification process with the species introduced in (R17). As will be seen later, it is possible to include more than two chemical reactions, depending on the additional species being modelled using (R17). The two sets of equations (mass balance and equilibrium constants) can be solved simultaneously to obtain the composition of the produced gas at steady state. Finally, an energy balance is solved to predict the gasification temperature, considering the process is adiabatic. Stoichiometric equilibrium modelling of biomass gasifiers are generally

solved using the iterative Newton-Raphson method, although other possibilities are available [98].

3.4.1.2 Non-stoichiometric approach

This approach involves the minimisation of the Gibbs free energy (GFE) of the system, through the utilisation of only the elemental composition of the feedstock obtained from the ultimate analysis and was not a direct focus of the research undertaken. The GFE is a thermodynamic quantity that indicates the available energy of a substance that can be used in a chemical reaction. It is related to the enthalpy of a system or process minus the product of the systems entropy and absolute temperature. As such, this approach neglects any specific chemical reactions, making it suitable for cases in which all the possible chemical reactions that can occur in the system are not fully known as in the case of gasification. As these methods are based on an atom balance of reactants, specific cases involving biomass, with unknown molecular formula can also be handled. The Gibbs free energy, g_i^*, of the gasification product involving N species (i = 1, ..., N) is given by:

$$g_i^* = \sum_{i=1}^{\mathrm{N}} \mathrm{n}_i \Delta g_{f,i}^\circ + \sum_{i=1}^{\mathrm{N}} \mathrm{n}_i RTln\left(\frac{\mathrm{n}_i}{\sum_{i=1}^{\mathrm{N}} \mathrm{n}_i}\right) \ , \tag{3.40}$$

where $g_{f,i}^\circ$ is the standard Gibbs free energy of formation of species i, at normal pressure, R is the universal gas constant equal to 8.314 J/mol K and T is the temperature in K . The equation must be solved for n_i unknown values to minimise g_i^*, which is subject to the overall mass balance of the individual elements. For each number j:

$$\sum_{i=1}^{\mathrm{N}} = \mathrm{a}_{i,j}\mathrm{n}_i = \mathrm{A}_j \ , \ j = 1, 2, 3, ..., k \ . \tag{3.41}$$

A_j is defined as the total number of atoms of the j^{th} element reaction mixture and $\mathrm{a}_{i,j}$ is the number of atoms of the j^{th} element in a mole of the i^{th} species.

Several possibilities exist to minimise the GFE, with Lagrange multipliers yielding satisfactory results. The Lagrange function (L), is formed through Lagrange

multipliers $\gamma_j = \gamma_1, ..., \gamma_k$ and defined as:

$$L = g_i^* - \sum_{j=1}^{\mathrm{K}} \gamma_i \left(\sum_{i=1}^{\mathrm{N}} \mathrm{a}_{ij} \mathrm{n}_i - \mathrm{A}_i \right) \ . \tag{3.42}$$

Dividing the above equation by RT and setting the partial derivatives equal to zero, the extreme point is found:

$$\left(\frac{\partial L}{\partial \mathrm{n}_i} \right) = 0 \ . \tag{3.43}$$

Replacing the value of g_i^* from Eq. (3.40) in Eq. (3.42) and taking its partial derivatives the Gibbs free energy can be expressed as follows:

$$\left(\frac{\partial L}{\partial \mathrm{n}_i} \right) = \frac{\Delta g_{f,i}^{\circ}}{RT} + \sum_{i=1}^{\mathrm{N}} ln \left(\frac{\mathrm{n}_i}{\sum_{i=1}^{\mathrm{N}} \mathrm{n}_i} \right) + \frac{1}{RT} \sum_{j=1}^{\mathrm{K}} \gamma_i (\sum_{i=1}^{\mathrm{N}} \mathrm{a}_{ij} \mathrm{n}_i) = 0 \ . \tag{3.44}$$

The above equation can be formed in terms of a matrix with i rows and can be solved simultaneously by some iteration technique. As in the stoichiometric approach, several modifications exist within the non-stoichiometric approach, but will not be discussed in detail as they are beyond the research scope of this thesis.

3.4.2 Kinetic models

The limitations of the thermodynamic equilibrium model in correlating reactor design parameters with the final product gas composition have led to the development of kinetic models for evaluating and predicting gasification performances. Kinetic models consider both the kinetics of gasification reactions and the hydrodynamics of the gasifier reactor, incorporating parameters such as reaction rate, residence time, superficial velocity, diffusion rate, and reactor length [3, 109]. This modelling approach enables the prediction of gas composition and operating temperatures profiles for specific operating conditions and reaction kinetic parameters. Kinetic models are particularly suitable and accurate at relatively low temperatures where reaction rates are significantly lower, leading to longer residence times, in contrast to equilibrium models that are more suitable at higher temperatures. Kinetic models play a crucial role in bridging the gap between thermodynamic equilibrium models

and CFD models in the context of biomass gasification. They achieve this in the following way:

1. Inclusion of reaction kinetics; while thermodynamic equilibrium models assume instantaneous reactions and complete mixing, kinetic models consider the kinetics of gasification reactions. They incorporate detailed reaction mechanisms, including the rates at which various chemical species react and the time required for these reactions to occur. This allows kinetic models to capture the time-dependent behaviour of gasification processes and provide more realistic predictions of species concentrations and gasification rates.

2. Incorporation of reactor hydrodynamics; through accounting for reaction rates but also considering the hydrodynamics of the gasifier reactor. This includes parameters such as residence time, SV, diffusion rate, and the flow pattern within the gasifier. By incorporating reactor hydrodynamics, kinetic models provide insights into the spatial distribution of species and temperature profiles within the gasifier, which thermodynamic equilibrium models do not capture.

3. Prediction of species concentrations; by considering both reaction kinetics and reactor hydrodynamics, kinetic models can predict the concentrations of different species in the producer gas as they evolve over time. This capability allows kinetic models to simulate the gasification process more realistically than thermodynamic equilibrium models, which provide only the final product gas composition at equilibrium.

4. Advancement towards CFD models; through the inclusion of time-dependent behaviour, heat transfer, and chemical reactions in the gasifier, kinetic models are a stepping stone towards more complex and detailed CFD models, which are more computationally intensive and require detailed information about flow behaviour, heat and mass transfer and chemical reactions within the gasifier.

Kinetic models can be validated and calibrated using experimental data from practical gasification systems, aiding in ensuring they better represent the actual gasification behaviour as clearly as possible, and can be trusted as reliable tools for

predicting gasifier performance. Once validated, they can be used to develop more advanced CFD models, capable of capturing even finer details of the gasification process.

Kinetic models provide a more detailed and dynamic representation of gasification processes compared to thermodynamic equilibrium models, making them an important link between simple equilibrium models and complex CFD models in understanding and optimising biomass gasification.

Rate laws and kinetic parameters are the important components in an effective biomass gasification kinetic model, where the Arrhenius equations plays a fundamental role in demonstrating the temperature dependence of the reaction rates. As such, the rate laws of the chemical reactions are expressed through the following expression:

$$\Omega_r = k_i \mathrm{C}_A^n \mathrm{C}_B^m - k_{i,2} \mathrm{C}_P^q \ , \tag{3.45}$$

where Ω is the rate of reaction, C_i is the concentration of the component i, subscripts A and B represent the reactants and P the product, superscripts n, m, and q are the orders of the reaction with respect to the component concentration, and k is the Arrhenius constant of the reaction, calculated from the following:

$$k = A \times exp\left(-\frac{Ea}{RT}\right) \ . \tag{3.46}$$

In the above equation A is the pre-exponential factor and Ea is the activation energy. A variety of software applicable platforms for modelling works exist such as spreadsheets for quick and easy arithmetic calculations and numerical modelling solvers such as Mathematica and the ordinary differential equation (ODE) toolbox in MATLAB to solve mass and energy balances [6].

3.4.3 CFD models

Computational fluid dynamics (CFD) models maintain an essential role in the modelling of a biomass gasification system, as they are sophisticated numerical simulation tools to scientifically estimate fluid flow, heat and mass transfer, chemical reaction and other related phenomena by solving a numerical set of governing math-

ematical equations based on the conservation equations of mass, heat, momentum, and species over a defined domain or region within biomass gasification systems. CFD models associated with downdraft gasification systems aim to provide insights into the gasifier's performance, optimise its design, and evaluate its efficiency and emissions. The key aspects and components of CFD models for downdraft biomass gasifiers can be summarised as follows [42, 110]:

1. Geometry and mesh generation; beginning with the creation of a multidimensional digital representation of the gasifier's geometry, including the reactor chamber, gasification agent and biomass inlets and gas outlets. This is subsequently followed by mesh generation which involves dividing the geometry into discrete elements or computational cells to facilitate numerical calculations, forming the computational grid.

2. Multiphase modelling; including solid biomass particles, air and gas products. It is essential to use multiphase modelling approaches to simulate the movement and complex physical and chemical interactions between these phases. Examples of multiphase modelling approaches are the Discrete Phase Model (DPM), which involves tracking the trajectories of biomass particles and the porous media assumption, which treats the solid phase matrix as a porous region with specific properties rather than explicitly simulating the movement and behaviour of individual biomass particles [111].

3. Flow regime; classified as either laminar or turbulent based on the gasifiers operating conditions, primarily the Reynolds number (Re), geometry, and flow characteristics. In small-scale gasifiers with low gas velocities, the flow is often modelled as laminar. In larger gasifiers or regions with high velocity and strong mixing, the flow is modelled as turbulent and a turbulence model is integrated into the CFD model. Various turbulence models, such as the Reynolds-Averaged Navier-Stokes (RANS) or Large Eddy Simulation (LES) approaches can be employed to capture turbulence effects on mixing and heat transfer [109].

4. Chemical reaction modelling; which is typically the most essential component

within CFD modelling of biomass gasification as it involves the conversion of the solid biomass into gaseous products and other by-products. The more sophisticated the chemical reaction mechanism, describing the various stages of biomass gasification, the better the predictions.

5. Heat transfer modelling; including radiation and convective heat transfer models. They play a crucial role in biomass gasification as they account for heat transfer between solid biomass, gaseous components and the surrounding walls.

6. Boundary and initial conditions; which specify the flowrates, temperatures and various compositions at the gasifier's inlets and outlets. Inlet conditions typically involve the flow of air and biomass feedstock, while outlet conditions involve the exit syngas production and gasification by-products.

7. Solver selection and numerical methods; which is a crucial component of CFD modelling of biomass gasification, as it involves choosing an appropriate solver that possesses the required capabilities to address the governing and transport equation inherent to the specific gasification process. This selection process also includes the seamless integration of any supplementary components that might be necessary when incorporating sub-models into the simulation. Additionally, numerical methods, such as the finite volume or finite element methods, are used to discretise and solve these equations.

8. Post-processing and analysis; executed after simulation and involves analysing the results to obtain information on gasification efficiency, temperature profiles, syngas composition, and other predictions associated with the model. Furthermore, visualisation tools are used to present the simulation results in a comprehensive manner.

9. Validation and calibration; involving the comparison of model predictions with experimental data and fine tuning parameters to ensure the model accuracy is close to reality as possible.

The proposed CFD model will be solved in OpenFOAM, which is an open-source CFD software package, widely used for the simulation and the solving of

complex fluid flow and heat transfer problems. As such, regarding the discretisation method employed within the software, OpenFOAM primarily uses the finite volume method (FVM) for solving the governing equations. In brief, the FVM discretise the computational domain into finite volumes (or cells) and calculates the average values of variables (e.g. velocity, pressure, and temperature) within these cells. It is the most routinely used discretisation approach in CFD applications due to its conservation properties and ability to handle complex geometries [6].

The FVM first divides the computational domain into a grid of finite volumes, typically polyhedral or hexahedral encompassing a portion of the domain. Next, it applies the conservation principles of mass, momentum and energy, which come in the form of partial differential equations (PDE) for each finite volume. For each control volume, the governing equations are integrated over the volume to obtain discrete forms of the equations. After integration, the governing equations describing the process model are discretised into algebraic equations for each control volume which relate the average values of flow properties within the volume to the fluxes, representing the flow of conserved quantities, at the faces of each finite volume. The resulting algebraic equations form a system of linear or non-linear equations which are solved numerically using iterative or direct solution methods. The solution provides average values of flow properties at each control volume, representing the state of fluid flow or heat transfer within the domain [110]. The transport equations for modelling a downdraft biomass gasifier by utilising the porous media assumption, as is the case for the proposed CFD model, are a set of PDE's that describe the conservation of mass, momentum, energy, and species transport within the gasifier. The general overview of these equations are given below:

- Mass conservation (continuity):

$$\frac{\partial \rho}{\partial t} + \nabla(\rho \vec{u}) = S_m \ , \tag{3.47}$$

  where $\vec{u}$ is the velocity vector and S_m represents any mass source terms or sinks (e.g. due to chemical reactions). This equation accounts for the mass inflow, outflow, and accumulation within the porous media [112].

- Momentum conservation (Darcy's Law):

$$\frac{\partial}{\partial t}(\rho\vec{u}) + \nabla\cdot(\rho\vec{u}\,\vec{u}) = -\nabla p + \nabla\cdot(\mu_{eff}\nabla\vec{u}) + F\ , \tag{3.48}$$

  where p is the pressure, μ_{eff} is the effective dynamic viscosity of the gas phase in the porous media and F represents the momentum source term induced by the porous media. This general equation describes the flow of gas phase within the porous media [112]. Eq 3.48 also relates the fluid velocity to the pressure gradient within the porous media through Darcy's Law, a fundamental equation in porous media modelling [113]:

$$u = \frac{K}{\mu}\nabla p \tag{3.49}$$

  where K is the permeability of the porous media.

- Energy conservation:

$$\rho C_p\frac{\partial(T)}{\partial t} = \nabla(k_{eff}\nabla T) + H_r + Q\ , \tag{3.50}$$

  where H_r represents the heat generation or absorption due to chemical reactions and Q represents external heat sources. This equation accounts for the temperature distribution within the porous media due to heat transfer and chemical reactions. [112].

- Species transport:

$$\frac{\partial(\rho Y_i)}{\partial t} + \nabla(\rho\vec{u}Y_i) = \nabla(D_i\nabla(\rho Y_i)) + R_i\ . \tag{3.51}$$

where Y_i is the mass fraction of species i, D_i is the species diffusivity, and R_i represents the rate of production/consumption of species i due to chemical reactions. This equation describes the general transport of chemical species within the gasifier [112]. Typically, Eq. (3.51) is formulated in the context of mass transport of a particular species within the porous media.

Eqs. (3.47), (3.48), (3.50), and (3.51) represent the fundamental conservation

principles within the porous bed of the downdraft biomass gasifier. As will be seen later, they are tailored to the specific application of the established **porousGasificationFoam** solver by including additional terms and modifying coefficients to account for complex factors like chemical reactions, heat transfer and resistance factors.

3.5 Summary

In this chapter, the fundamentals and properties of biomass and gasification were thoroughly discussed, laying the necessary groundwork for subsequent modelling approaches in the thesis. Initially, biomass was clearly defined alongside its physical and thermodynamic characteristics. Following that, a comprehensive overview of the gasification process was provided, encompassing its various stages, types of gasifiers, typical chemical reactions, and the diverse operating conditions involved. Numerous methodologies for studying and analysing gasifier performance were explored. Subsequently, the formulations of different modelling approaches were outlined, including the essential mass and energy balances, as well as the mathematical equations associated with each approach. This chapter will serve as a strong foundation to the following chapters, which will detail two distinct mathematical models, developed using different modelling approaches.

CHAPTER 4

An Advanced, Comprehensive Thermochemical Equilibrium Model of a Downdraft Biomass Gasifier

This chapter presents a thermodynamic equilibrium model that eliminates the need for correction factors and accurately predicts CH_4 concentration in producer gas, a challenge for previous models. Char yield is calculated via the boudouard reaction (R3), showing good agreement with experimental data. Tar yield is estimated using a new empirical correlation fitted to experimental data from downdraft gasifiers, as no equilibrium reaction exists for tar formation. Gasification temperature is determined through an energy balance using a coupled equation system, enhancing model robustness and convergence. The model also includes H_2S production and NH_3 formation via the NH_3 synthesis reaction.

The effects of MC and ER on syngas composition, tar and char yields, gasification temperature, LHV, and CGE are thoroughly analysed and compared with literature data. Consistent definitions ensure reproducibility. Feedstock properties, determined through ultimate and proximate analyses, are summarised in Table 3.1, with HHV calculated using Eq. 3.17 - see section 3.1.3.3 of Chapter 3. These properties form the basis for the gasification study.

4.1 Problem formulation and method of solution

The assumptions underpinning the model are that:

1. The gasifier operates under steady state conditions;
2. the residence time is infinite;
3. N_2 is considered inert;
4. the process is adiabatic;
5. the contribution of char and ash to the energy balance equation is negligible;
6. the total pressure is assumed constant (i.e. $P_0 = 101{,}325$ Pa), however the partial pressure of the syngas components is not and is determined via their chemical equilibrium;
7. reactants are at standard temperature (i.e. $T_0 = 298.15$ K), while products are at the unknown gasification temperature, T.
8. tar, at standard conditions, is a mixture of liquid and gas, with its thermodynamic properties taken to be those of benzene;
9. char is assumed to have the same thermodynamic properties as graphite.

The following global gasification reaction is an extension of (R17) of section 3.3.4.2 in Chapter 3, with some additional gaseous components taken into consideration, and forms the basis for determining the various product species:

$$\begin{aligned} &\mathrm{CH_\alpha O_\beta N_\lambda S_\delta} + w\mathrm{H_2O} + m_{gas}(\mathrm{O_2} + 3.76\mathrm{N_2}) \rightarrow x_1\mathrm{H_2} + x_2\mathrm{CO} \\ &+ x_3\mathrm{CO_2} + x_4\mathrm{CH_4} + x_5\mathrm{N_2} + x_6\mathrm{NH_3} + x_7\mathrm{H_2S} + x_8\mathrm{H_2O} + x_9\mathrm{C_6H_{6.2}O_{0.2}} + x_{10}\mathrm{C}\ , \end{aligned} \tag{R20}$$

where w is calculated as follows:

$$w = \frac{M_{bm} \times \mathrm{MC}}{(2M_H + M_O) \times (1 - \mathrm{MC})}\ . \tag{4.1}$$

In the above, the terms x_i, for $i = 1-10$, indicate the number of moles of the various chemical species produced. Among these, $i = 1 - 7$ represent components of dry producer gas. The number of moles of N_2 in the reactants is calculated based on the relative amount of N_2 to O_2 in the air. The chemical formula used to represent tar and char are $C_6H_{6.2}O_{0.2}$ [114] and C, respectively.

The atom balance equations of C, H, O, N and S derived from the global gasification reaction, are:

$$\text{C}: \; x_2 + x_3 + x_4 + 6x_9 + x_{10} = 1 \; , \tag{4.2}$$

$$\text{H}: \; 2x_1 + 4x_4 + 3x_6 + 2x_7 + 2x_8 + 6.2x_9 = \alpha + 2w \; , \tag{4.3}$$

$$\text{O}: \; x_2 + 2x_3 + x_8 + 0.2x_9 = \beta + w + 2m_{gas} \; , \tag{4.4}$$

$$\text{N}: \; 2x_5 + x_6 = \lambda + 7.52m_{gas} \; , \tag{4.5}$$

$$\text{S}: \; x_7 = \delta \; , \tag{4.6}$$

respectively. The specific molar heat capacity for a chemical component is deter-

Table 4.1: Constants for the molar heat capacity of chemical species and their corresponding enthalpy of formation, and GFE of formation [115].

Chemical Species	A	$10^3B, K^{-1}$	$10^6C, K^{-2}$	$10^{-5}D, K^2$	T_{max}	$h_f^\circ, J/mol$	$g_f^\circ, J/mol$
H_2	3.25	0.422	-	0.083	3000	-	-
CO	3.38	0.557	-	-0.031	2500	-110,525	137,169
CO_2	5.46	1.047	-	-1.157	2000	-393,509	-394,359
CH_4	1.7	9.081	-2.164	-	1500	-74,520	-50,460
N_2	3.28	0.593	-	0.04	2000	-	-
NH_3	3.58	3.02	-	-0.186	1800	-46,110	-16,450
H_2S	3.93	1.49	-	-0.232	2300	-20,630	-33,560
$H_2O_{(g)}$	3.47	1.45	-	0.121	2000	-241,818	-228,572
Tar	-2.06	39.064	-13.3	-	1500	82,930	129,665
Char	1.77	0.771	-	-0.867	2000	-	-
NO	3.39	0.629	-	0.014	2000	90,250	86,550
SO_2	5.7	0.801	-	-1.015	2000	-296,830	-300,194
$H_2O_{(l)}$	8.71	1.25	-0.18	-	373.2	-285,830	-237,129

mined from the following [115] empirical relationship:

$$C_{p,i}(T) = R(A_i + B_i T + C_i T^2 + D_i T^{-2}) \ , \tag{4.7}$$

where subscript i denotes a particular chemical component, and A_i, B_i, C_i and D_i represent the dimensionless thermodynamic empirical constants of each; their values are provided in Table 4.1.(4.7) is often used by researchers due to its ability to predict the heat capacity of a given substance over a wide range of temperatures. This makes it appropriate for modelling specific heats for gasification products typical in gasification reactions where temperatures can range from 300 to 1500 °C. The enthalpy for a specific chemical component [86], while ignoring the effect of pressure for an incompressible material (i.e. solid char), is obtained from:

$$h_i(T) = h^{\circ}_{f,i} + \int_{T_0}^{T} C_{p,i} dT = J_i + R\left(A_i T + \frac{B_i}{2}T^2 + \frac{C_i}{3}T^3 - \frac{D_i}{T}\right) \ , \tag{4.8}$$

where J_i is a constant resulting from integrating the right hand side of Eq.(4.8) and incorporating $h^{\circ}_{f,i}$, namely:

$$J_i = h^{\circ}_{f,i} - R\left(A_i T_0 + \frac{B_i T_0^2}{2} + \frac{C_i T_0^3}{3} - \frac{D_i}{T_0}\right) \ , \tag{4.9}$$

where $h^{\circ}_{f,i}$ is the enthalpy of formation at standard conditions for reactants and products - see Table 4.1. (R22) is at a constant total pressure p_0, therefore its enthalpy balance is equal to zero, namely:

$$\Delta H(T) = \sum_i \upsilon_i h_i(T) = 0 \ , \tag{4.10}$$

where υ_i is the stoichiometric number which is positive for products, $\upsilon_i = x_i$ for $i = 1 - 10$, and negative for reactants, $\upsilon_i = (-1, -w, -m_{gas}, -3.76 m_{gas})$ and the summation $\sum_i$ is repeated over all gaseous and solid components. However, note also the enthalpy of moisture is taken in liquid state while the enthalpy of char and ash is ignored. The energy balance, (4.10), is used to predict a uniform T for the entire system in an adiabatic process.

In a thermodynamic equilibrium model, equilibrium constants are used to model chemical reactions - see section 3.4.1.1 in Chapter 3. The equilibrium constant are related to the GFE via Eq. (4.22). To define the equilibrium constants, there is a need to solve the GFE function of each equilibrium reaction involved in the system. This necessitates the introduction of entropy as it is related to GFE via (4.15). At thermodynamic equilibrium, the GFE of the system is minimised, meaning that the changes in enthalpy and entropy balance each other out, resulting in no further occurrence of chemical reactions, thus stabilising the system. The entropy of a chemical component at temperature T can be written [86]:

- for an incompressible material (i.e. solid char) as:

$$ds_i^* = \frac{C_{p,i}}{T}dT = \frac{dh_i}{T} \ , \tag{4.11}$$

$$s_i^*(T) = s_{f,i}^\circ + \int_{T_0}^{T} \frac{C_{p,i}}{T}dT = s_{f,i}^\circ + \int_{T_0}^{T} \frac{dh_i}{T} \ ; \tag{4.12}$$

where $s_{f,i}^\circ$ is the entropy of formation at standard conditions and

- for an ideal gas as:

$$ds_i = ds_i^* - \frac{R}{p_i}dp_i \ , \tag{4.13}$$

$$s_i(T, p_i) = s_i^*(T) - R\log\left(\frac{p_i}{p_0}\right) \ ; \tag{4.14}$$

where p_i is the partial pressure of a gaseous component. The GFE of a chemical component is calculated [86]:

- for an incompressible material (i.e. solid char) as:

$$d\left(\frac{g_i^*}{T}\right) = d\left(\frac{h_i}{T}\right) - ds_i^* = d\left(\frac{h_i}{T}\right) - \frac{dh_i}{T} = -\frac{h_i}{T^2}dT \ , \tag{4.15}$$

$$g_i^*(T) = g_{f,i}^\circ - T\int_{T_0}^{T} \frac{h_i(T)}{T^2}dT = J_i - RT\left(A_i\log(T) + \frac{B_iT}{2} + \frac{C_iT^2}{6} + \frac{D_i}{2T^2} + I_i\right) \ , \tag{4.16}$$

where $g_{f,i}^\circ$ is the GFE of formation at standard conditions given in Table 4.1 and I_i is another integration constant determined from Eq. (4.17) at standard

conditions, namely:

$$I_i = \frac{J_i - g^{\circ}_{f,i}}{RT_0} - \left(A_i \log(T_0) + \frac{B_i T_0}{2} + \frac{C_i T_0^2}{6} + \frac{D_i}{2T_0^2} \right) \; ; \tag{4.17}$$

- for an ideal gas as:

$$d\left(\frac{g_i}{T}\right) = d\left(\frac{g_i^*}{T}\right) + \frac{R}{p_i} dp_i \; , \tag{4.18}$$

$$g_i(T, p_i) = g_i^*(T) + RT \log\left(\frac{p_i}{p_0}\right) \; . \tag{4.19}$$

If a reversible chemical reaction is at chemical equilibrium, then its GFE balance equals zero, and as such:

$$\Delta G(T,p) = \sum_i \upsilon_i g_i(T, p_i) = \sum_i \upsilon_i g_i^*(T) + RT \log \prod_i \left(\frac{p_i}{p_0}\right)^{\upsilon_i} = \Delta G^*(T) + RT \log k(T) = 0 \; . \tag{4.20}$$

Accordingly, the thermodynamic equilibrium constant, $k(T)$, of the reaction is determined from Dalton's law as follows:

$$\log k(T) = \log \prod_i \left(\frac{p_i}{p_0}\right)^{\upsilon_i} = \log \prod_i \left(\frac{x_i}{N_{tot}}\right)^{\upsilon_i} \; , \tag{4.21}$$

where the multiplication $\prod_i$ is repeated over the reactions gaseous components only. $N_{tot} = \sum_{i=1}^{9} x_i$ is the number of moles of the raw producer gas at temperature T and the equilibrium constant is calculated via the standard gibbs free energy, $\Delta G^*(T)$, of a reaction:

$$\log k(T) = -\frac{\Delta G^*}{RT} = -\frac{1}{RT} \sum_i \upsilon_i g_i^*(T) \; , \tag{4.22}$$

where the summation $\sum_i$ is repeated over all the reactions gaseous and solid components.

Four independent equilibrium reactions are implemented to model the gasification process: (R3),(R5), (R11), and the NH_3 synthesis reaction (R21):

$$\mathrm{N_2} + 3\,\mathrm{H_2} \leftrightarrow 2\mathrm{NH_3} \quad -92{,}000 \text{ J/mol} \; , \tag{R21}$$

respectively. Thus, the model considered NH_3 production by determining the equilibrium constant of the NH_3 synthesis reaction. Given the high temperatures in the equilibrium model, the operating conditions strongly support NH_3 production and decomposition. NH_3, though unlikely to occur to a significant extent in reality due to the prevailing high temperatures in biomass gasification which favours its decomposition and not its formation, it is possible for it to be produced in small amounts at low ER values and lower temperatures. Also, the availability of the reactants (N_2 from the biomass source and H_2 from syngas) in the gasifier environment ensures the production of NH_3 though at lower amounts for higher T. As will be seen later on, NH_3 is generated at lower ER, when the T is low, whereas when ER increases and the T in the system is enhanced, NH_3 decomposition starts to occur.(R5) progresses rapidly with H_2 being reduced to form CH_4 in the presence of C; (R11) increases the H_2 concentration at the expense of CO and describes the equilibrium between the two in the presence of H_2O. In the absence of steam and in the presence of air as a gasifying medium, (R3) is dominant; therefore, it is implemented in order to describe the conversion of C to CO in the presence of CO_2. As reported in Gambarotta et al [79], NH_3 is the most abundant nitrogen-based syngas contaminant and its production is accounted for via (R21) [2]. Accordingly, the equilibrium constants, k_{R3}, k_{R11}, k_{R5} and k_{R19} for the above chemical reactions are obtained from Eq.(4.21) as follows:

$$k_{R3}(T) = \frac{x_4 \times N_{tot}}{x_1^2} \ , \ k_{R5}(T) = \frac{(x_2)^2}{x_3 \times N_{tot}} \ , \ k_{R11}(T) = \frac{x_1 \times x_3}{x_2 \times x_8} \ , \ k_{R19} = \frac{x_6^2 \times N_{tot}^2}{x_5 \times x_1^3} \ , \tag{4.23}$$

and at T are calculated from Eq.(4.22).

Tar is modelled by taking its thermodynamic properties to be those of benzene. To account for tar production, a unique empirical correlation is generated in the form of an exponential best fit curve using appropriate tar data, gathered from experiments performed on DBGs [53, 54, 57, 70, 71] using gas chromatography and separation techniques. While corresponding data is available for other than DBGs, it is either not provided in the preferred mass tar yield format or can be converted into the same. Mass tar yield (% d.b.) offers a coherent dimensionless form that

removes any dependence on the dimensional properties of biomass and gasifier length scales. Accordingly, the above tar data (denoted in units of g/Nm^3) was converted to mass tar yield (wt.%) as follows:

$$\text{tar content} = \frac{\text{tar yield}}{\text{syngas yield} \times 100\%}\,, \quad \text{where} \quad \text{syngas yield} = \frac{N_{gas} \times V_m}{M_{bm}}\,; \tag{4.24}$$

where $N_{gas} = \sum_{i=1}^{7} x_i$ and $V_m = 22.4$ L is the volume for an ideal gas at standard temperature and pressure. This was done for all the associated ER values, obtaining the amount of tar per unit mass of biomass, thus achieving consistency in the determination of the mass tar yield between the respective experimental studies.

The resulting data points are plotted in Fig.4.1. The tar yield is primarily dependent on the ER because it is the key factor influencing biomass gasification. ER significantly impacts both the composition of the producer gas and T within the gasifier. As T is an output parameter, its influence is not directly accounted for in the resulting tar yield relationship. On the other hand, the MC of the biomass, another operating condition, has a much lesser impact. This is because ER directly controls the level of combustion within the gasifier, whereas MC primarily affects gasification efficiency, overall process performance, and residence time. While MC can indirectly influence tar content, its effect is generally considered secondary compared to ER [2, 116]. The correlation is generated using the experimental data of [53, 54, 70, 71] and Matlab's Curve Fitting Toolbox app. The tar data from Lv. et al [57] was excluded from the correlation as it exhibits differing tar yields for identical ER values due to variations in other gasification conditions. While the tar data presented in the literature varies widely, it is evident that there is a consistent decline in tar yield with an increase in the ER of the system. This observation is supported by an analysis of experimental tar data from existing literature on DBGs. The variability in reported tar yields can be attributed to differences in operating conditions, including feedstock composition, gasification temperature, residence time, and reactor design. Furthermore, differences in measurement techniques, sampling methods, and analytical procedures among researchers and experimentalists contribute to the observed variability in the collected tar data. The resulting empirical relationship

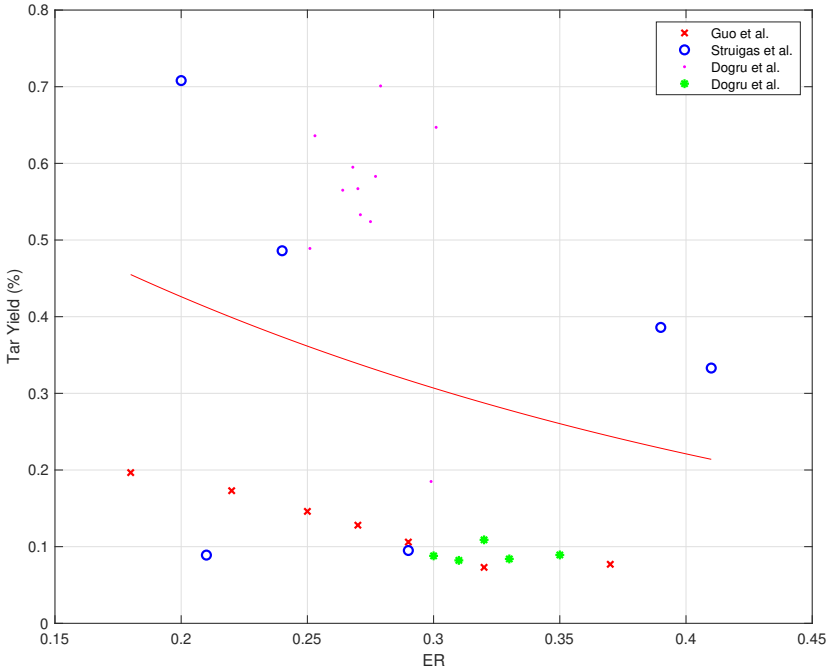

Figure 4.1: Downdraft gasifier tar yield as a function of ER: showing corresponding experimental data and best-fit relationship, Eq. (4.25), based on the datasets [53, 54, 70, 71].

in equation form is given by:

$$\text{tar yield} = 0.8212\exp(-3.281\text{ER}) \times 100\% \,, \tag{4.25}$$

with the molar tar yield, as used in the model formulation, given by:

$$x_9 = 0.8212\exp(-3.281\text{ER}) \times \frac{M_{bm}}{M_{tar}} \quad \text{for} \;\; 0.155 \leq \text{ER} \leq 0.415 \,, \tag{4.26}$$

where $M_{tar} = 6M_C + 6.2M_H + 0.2M_O$ is the molar mass of tar.

The empirical correlation, (4.25), encapsulates the thermochemical processes governing biomass gasification. This relationship is dictated by the interplay between pyrolysis, oxidation, and reforming reactions, which collectively determine tar formation and decomposition. As per the definition of ER - see (3.34), section 3.3.4.2, Chapter 3 - pyrolysis predominates for ER values lower than 0.2, while combustion dominates beyond 0.4. Pyrolysis-driven conditions results in higher tar

yields, whereas excessive combustion compromises syngas efficiency. With increasing ER, the availability of O_2 enhances partial oxidation and secondary tar-cracking reactions, leading to a progressive decline in tar yield. The observed empirical trend aligns with these thermochemical principles, demonstrating higher tar yields at lower ER, a steady reduction as ER increases to an optimal level, and a subsequent plateau at higher ER due to combustion dominance and diminished syngas quality. The goodness of the fit is also assessed using the toolbox app, where R^2, a statistical measure of how well the regression line approximates the actual data, is found to be 0.06282, which is a low value, suggesting that the curve does not explain much of the variability in the dependent variable. In other words, the independent variable (i.e. ER) does not strongly predict the outcomes of the dependent variable (i.e. tar yield). Fig. 4.1 shows that there is correlation between tar yield and ER as when the ER increases, the tar yield decreases, plateauing at higher ER values, as to be expected. However, this indicates that there might be other factors influencing the tar yield, such as type of biomass feedstock, gasification agent, ash content, residence time, particle size, and pressure of the reactor. Table 4.2 summarises the gasifier operating conditions employed in the experimental investigations used to develop the empirical correlation for tar yield. The variation in operating parameters across these experiments is evident, which significantly influences tar production and accounts for the observed variability in the resulting data.

Table 4.2: Gasifier conditions of the experiments used in the generation of the tar empirical model.

Experiment	**Gasifier conditions**				
	Biomass	**Feeding rate (kg/hr)**	**Particle size (cm)**	**MC (%)**	**Ash (%)**
[71]	Corn stalk	7.5	4-5	12.5	5.8
[70]	wood chips & pellets	28-63	0.8-5	4-14.9	0.4-21
[53]	hazelnutt shell	1.73 - 5.40	1.79	12.45	0.77
[54]	sewage sludge	2.86-3.81	3.5	11.75	23.51

All experimental investigations of biomass gasifiers inherently contain a level of uncertainty and standard deviation. Errors and uncertainties in experimental studies can arise from instrument selection, conditions, calibration, observations and reading, and test planning. It is also important to note that experimental

investigations inherently contain uncertainties and are prone to a degree of standard deviation, reflecting the natural variability and possible inconsistencies within the measurements.

The system of Eqs. (4.2) to (4.6) as well as Eqs. (4.10), (4.23) and (4.26) consist of 11 equations for the 11 unknowns x_1, x_2, x_3, x_4, x_5, x_6, x_7, x_8, x_9, x_{10} and T, and are solved numerically using Matlab's built-in function "fsolve" - details of its implementation are provided in [117]. The solver "fsolve" is a Matlab function used to solve systems of nonlinear equations and is part of Matlab's optimisation toolbox, designed to find the roots of a set of nonlinear equations where the number of equations matches the number of variables. The solver's main objective is to minimise the sum of squares of the components to satisfy $f(x) = 0$, where x is a vector of variables and f is a vector of functions. The solution x is found iteratively starting from an initial guess.

The Trust-Region-Dogleg algorithm is implemented as it is the only algorithm that is designed to solve non-linear equations, while the others attempt to minimise the sum of squares of the function. It is efficient because it requires only one linear solve per iteration. This algorithm approximates the function f with some simpler function m_k (called the model function) in a neighbourhood x_k. Over the entire domain, m_k will unlikely be a good approximation for f, and so the domain is restricted to a region of radius r_k, centred at the point x_k, inside of which m_k is reasonably close to f. m_k is then minimised over this region, and set x_{k+1} equal to the minimiser:

$$x_{k+1} = \min_{x \in B(x_k, r_k)} m_k(x) \ . \tag{4.27}$$

The region $B(x_k, r_k)$ is called the trust region as m_k is trusted to give a reasonably accurate approximation of f in this region. m_k is commonly taken to be a quadratic approximation of f based on its Taylor Series expansion as such:

$$m_k(\mathrm{p}) = f(x_k) + \mathrm{p}^T \nabla f(x_k) + \frac{1}{2} \mathrm{p}^T H_k \mathrm{p} \ , \tag{4.28}$$

where H_k is the Hessian matrix of f at x_k and p is the step. The Trust-Region-Dogleg algorithm combines this with the Dogleg method when selecting an appropriate

minimiser of m_k. This method works by minimising m_k along the Dogleg path, which is a particular path extending from the origin out to the boundary of the trust region. The Dogleg path consists of two steps: the steepest descent step and the Gauss-Newton step. Computing both these steps allows for the construction of the Dogleg path, after which the solution converges when the step size is sufficiently small or an improvement in f is below a predefined threshold.

In this model, a set of solver options is specified to ensure an effective solution process. First, the solver is configured to display iteration-level output, allowing MATLAB to print information at each step, including residuals and updates. Second, tolerance values are defined for both the function value and the solution, ensuring that the solver stops when successive values fall below 10^{-24}, indicating sufficient convergence. Lastly, the maximum number of iterations is set to 10^7, allowing the solver to continue searching for a solution until convergence is achieved.

It is also important to select reasonable initial guesses for the species involved to avoid divergence, improve numerical stability, and ensure meaningful predictions. The 11 unknowns were assigned the following initial guesses (x_i, i = 1 - 10, T) = (0.3, 0.25, 0.15, 0.05, 0.35, 0.02, 0.01, 0.05, 0.01, 0.05, 1000). The initial guesses are based on known experimental gasification data.

For all the results generated and discussed subsequently, the 11 unknowns were assigned the same starting values. One of the advantages of the current approach is determination of the gasification temperature, T, via a more robust fully coupled solver offering better convergence properties.

The molar LHV of the dry producer gas at standard temperature (MJ/mol) is given by:

$$\mathrm{LHV}_{gas} = \frac{1}{N_{gas}} \sum_{i=1}^{7} x_i \mathrm{LHV}_i \ , \tag{4.29}$$

where LHV_i is the molar LHV of component i at standard temperature calculated from their complete combustion reactions as follows:

$$\mathrm{LHV}_1 = h^\circ_{f,1} - h^\circ_{f,8} \ , \ \mathrm{LHV}_2 = h^\circ_{f,2} - h^\circ_{f,3} \ , \ \mathrm{LHV}_3 = 0 \ , \ \mathrm{LHV}_4 = h^\circ_{f,4} - h^\circ_{f,3} - h^\circ_{f,8} \ ,$$
$$\mathrm{LHV}_5 = 0 \ , \ \mathrm{LHV}_6 = h^\circ_{f,6} - h^\circ_{f,5} - h^\circ_{f,8} \ , \ \mathrm{LHV}_7 = h^\circ_{f,7} - h^\circ_{f,8} - h^\circ_{f,SO_2} \ . \tag{4.30}$$

The volumetric LHV of producer gas at standard temperature (MJ/mol) is given by the following:

$$\mathrm{LHV}_{gasvol} = \frac{\mathrm{LHV}_{gas}}{V_m} \ . \tag{4.31}$$

The CGE [118], which is the ratio of the LHV of the syngas and the LHV of the biomass feedstock, is calculated based on Eq. (3.38) in section 3.3.6 of Chapter 3.

Detailed evidence of the conservation of the system is provided via atom and energy balances for the case of rubberwood at an ER = 0.2 and MC = 40%. In rubberwood, there is no sulphur contained in the feedstock, therefore H_2S is not produced. According to (3.35), the value for m_{gas} is calculated to be 0.2152. An atom balance is performed, ensuring the mass conservation of the system:

$$\begin{aligned}\mathrm{CH_{1.5415}O_{0.6225}N_{0.0034}} + 0.8722\mathrm{H_2O} + 0.2152(\mathrm{O_2} + 3.76\mathrm{N_2}) \rightarrow 0.6119\mathrm{H_2} + 0.1209\mathrm{CO} \\ + 0.5725\mathrm{CO_2} + 0.1838\mathrm{CH_4} + 0.8105\mathrm{N_2} + 0.0004\mathrm{NH_3} + 0.6589\mathrm{H_2O} \\ + 0.0012\mathrm{C_6H_{6.2}O_{0.2}} + 0.1156\mathrm{C} \ , \end{aligned} \tag{R22}$$

Similarly, an energy balance is performed to ensure the energy is conserved in the system:

$$h^{\circ}_{f,bm} + 0.8722 \times h^{\circ}_{f,H_2O(l)} = x_{1-9}h^{\circ}_{f,1-9} + x_{1-9}C_{p,1-9}(T - T_0) = -359172.67 \text{ J/mol} \tag{4.32}$$

4.2 Results and Discussion

4.2.1 Model validation

The producer gas composition is initially compared with a set of experimental data and corresponding model predictions, highlighting the satisfactory prediction of the CH_4 concentration, with the species concentration of component i at standard temperature is given by:

$$\text{concentration} = \frac{x_i}{N_{gas}} \times 100\% \ . \tag{4.33}$$

Next, the predicted T is compared with experimental data, showing its influence when the operating conditions are manipulated. Finally, the char yield is estimated as a percentage of biomass on a dry basis ($\%d.b.$) as follows:

$$\text{char yield} = \frac{x_{10} \times M_C}{M_{bm}} \times 100\% \,, \tag{4.34}$$

and compared with existing experimental data, evidently demonstrating the reliability of implementing the boudouard reaction.

4.2.1.1 Producer gas composition

The results of this section compare predicted and experimentally observed producer gas compositions for different feedstock as a function of MC and ER. The comparison is based on the main output gases forming the producer gas of a typical DBG (i.e. H_2, CO, CO_2, CH_4 and N_2).

The predictions presented in Figures 4.2(a) and 4.2(b) show reasonably good agreement with the experimental data from Jayah et al. [55] and Barrio et al. [51]. Any disparities observed can be attributed to the model's incorporation of tar, char, and minor gasification products, which enhances its reliability. Comparisons are also shown for the corresponding solutions obtained by Gagliano et al. [22] for the same feedstocks. Both sets of predictions overestimate the H_2 and underestimate the CH_4 concentrations, which is typical behaviour for equilibrium models. This phenomenon has been justified by others [120, 121] on the basis that CH_4 produced in the low-temperature zone can bypass the reaction zone and avoid reduction, as explained in Aydin et al. [26]. Specifically, the current model achieves a better prediction of CH_4 concentration for rubberwood and wood pellets (1.03% and 0.78%, respectively) when compared to the experimental data. It also demonstrates a more sophisticated syngas composition. The main objective of developing biomass gasifiers is to increase the amount of H_2 and CO while keeping CO_2 and tars at relatively low levels. Regarding the results obtained by [22], their model was calibrated to achieve a more favourable outcome by introducing correction factors for reaction (R5), thereby shifting the reaction equilibrium towards more CH_4 and less H_2 production, and for

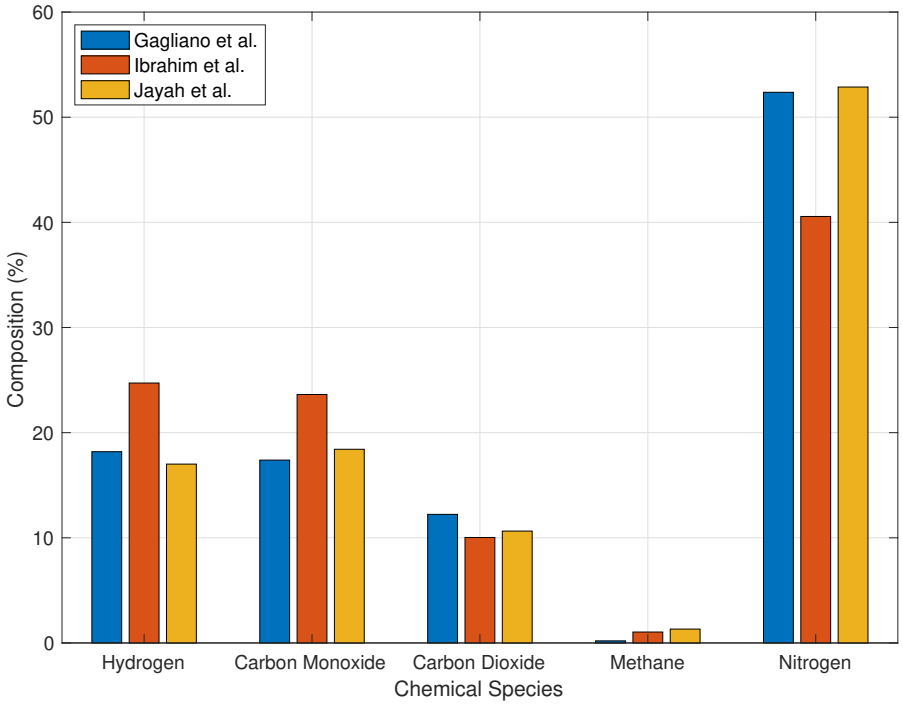

(a)

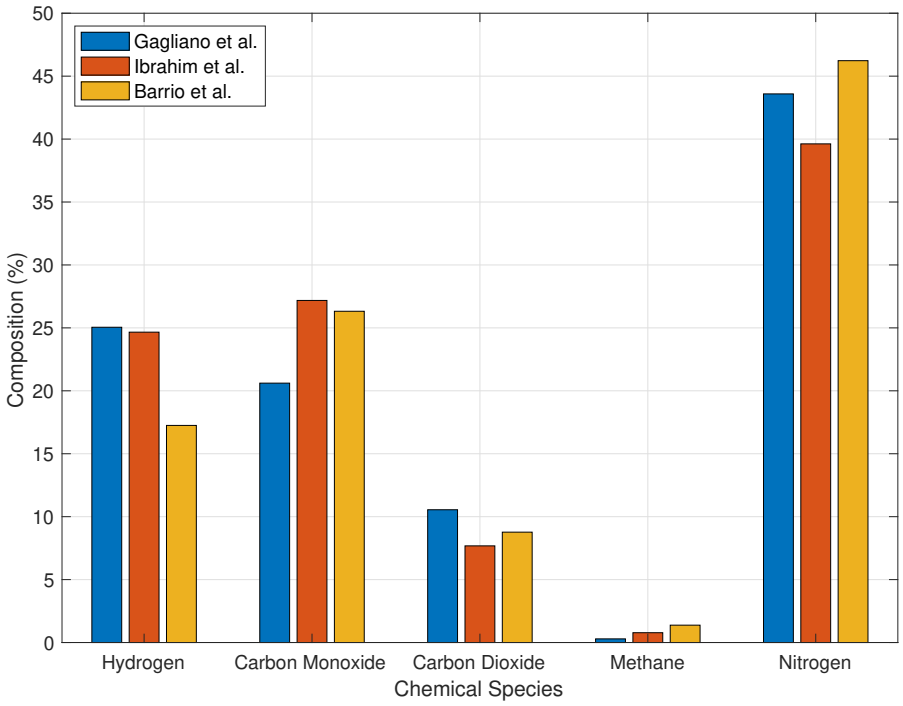

(b)

Figure 4.2: Comparison between predicted (Gagliano et al. [22] and Ibrahim et al. [119]) and experimentally obtained, [51, 55], producer gas composition for (a) rubberwood (MC=16%, ER=0.314) and (b) wood pellets (MC=8% and ER=0.266).

reaction (R11), to promote more CO and less H_2 production. However, it is evident that the current model outperforms the equilibrium model of Gagliano et al. [22] in predicting the concentration of CH_4, and in some cases, the syngas composition as well. This comparison is also preferable for the current model when considering the experimental data of Barrio et al. [51], as shown in Fig. 4.2(b).

Fig. 4.3 provides a comparison of the producer gas composition obtained using the current model with experimental data from [64, 68]. Specifically, Fig. 4.3(a) pertains to the gasification of Rice Husk at an ER of 0.45 on a moisture-free basis. The predictions show excellent agreement with the data of Yoon et al. [64], particularly for the N_2 concentration. The model slightly overestimates the CO concentration but still exhibits good alignment with the experimental study. Moving to Fig. 4.3(b), it relates to the gasification of Bamboo at an ER of 0.3 and a MC of 10%. Here, the model demonstrates overall good agreement with the data of Dutta et al. [68]. Lastly, Fig. 4.3(c) represents the gasification of Neem at an ER of 0.3 and an MC of 20%. The predictions again show good agreement with the experimental data from [68]. In all three cases, the current model's producer gas composition predictions align well with the corresponding experimental results, highlighting its capability to effectively simulate gasification processes for different feedstocks under varying operating conditions.

A comprehensive comparison between the estimated syngas composition and the measurements conducted by [55] is presented in Table 4.3, from which it is evident that as the MC decreases and the ER increases, the concentrations of H_2 and CO_2 decrease.. This is expected since higher ER values indicate an increased amount of air in the system, leading to a rise in N_2 levels. Under the same operating conditions, the model's predicted syngas composition aligns well with the corresponding measured values. However, the model overestimates the production levels of H_2 and CO. The experiment carried out by [55] presents a formal calibration of their measured values with a gasification model. It was noted that the gas compositions predicted by their gasification model are within 5.8% of the measured values. This underlies a certain level of standard deviation inherent in experimental investigations. Furthermore, it is important to highlight that almost all thermodynamic equilibrium

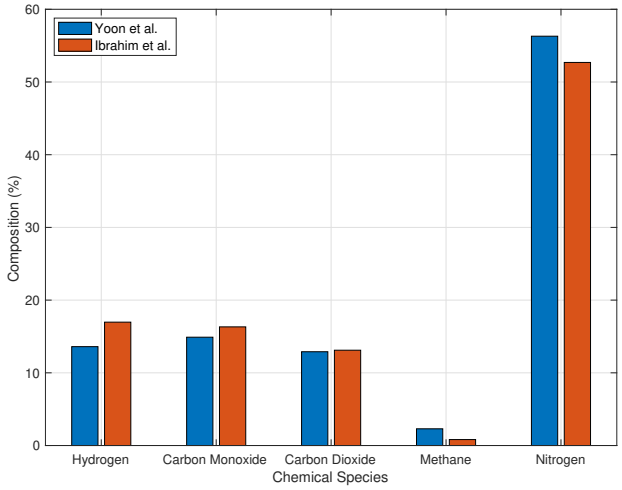

(a)

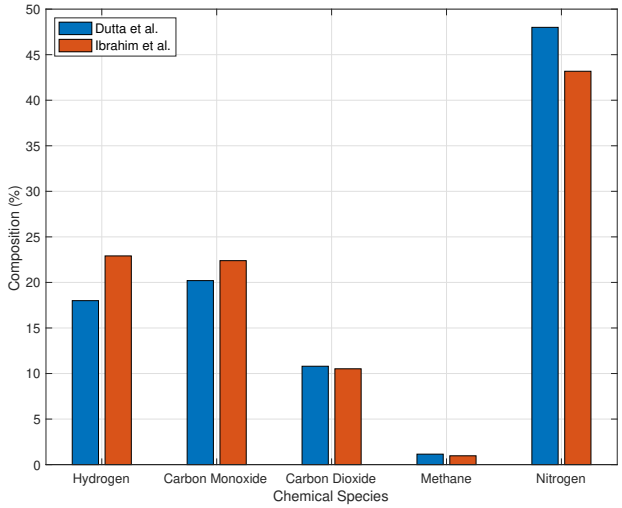

(b)

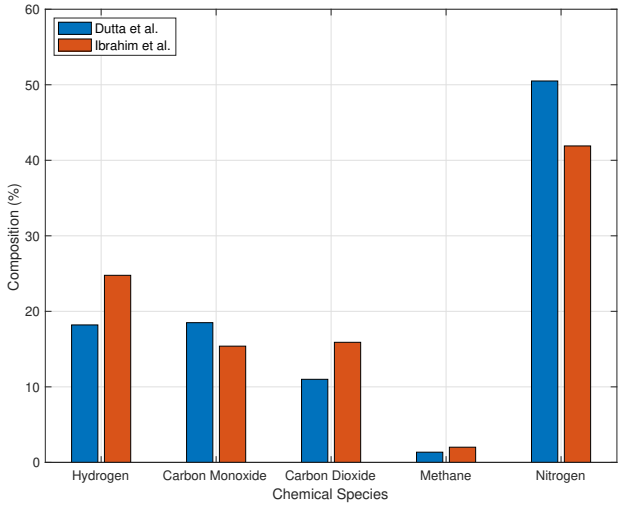

(c)

Figure 4.3: Comparison of the producer gas composition obtained experimentally, [64,68] and predicted by Ibrahim et al. [119] for (a): rice husk (MC=0%, ER=0.45), (b): bamboo (MC=10%, ER=0.3) and (c): neem (MC=20%, ER=0.3).

models in the literature including [22,26] have reported high error difference between equilibrium models and experimental measurements with errors reaching up to 40% in some cases.

Table 4.3: Syngas composition (%) and absolute error (%), for different operating conditions, predicted by the model and obtained experimentally [55].

	MC	**ER**	**H_2**	**CO**	**CO_2**	**CH_4**	**N_2**
Jayah et al. [55]	18.5	0.33	17.2	19.6	9.9	1.4	51.9
	16	0.35	18.3	20.2	9.7	1.1	50.7
	14.7	0.38	17.2	19.4	9.7	1.1	52.6
Prediction	18.5	0.33	24.5	22.93	10.53	1.08	40.92
	16	0.35	23.83	23.59	10.01	0.96	41.57
	14.7	0.38	22.21	26.33	7.96	0.67	42.8
Error (%)	18.5	0.33	42.44	16.99	6.36	22.86	21.16
	16	0.35	30.22	16.78	3.20	12.73	18.01
	14.7	0.38	29.13	35.72	17.94	39.09	18.63

Lastly, the model's predicted syngas composition is compared to a broader range of experimental datasets obtained from state-of-the-art small-scale DBGs currently in operation, as depicted in Fig. 4.4 [75]. This comparison is performed for different feedstocks, evaluating the producer gas composition at specific ER and MC relevant to each technology. The predicted results show reasonably good agreement with the experimental studies. Any differences observed can be attributed to other significant operating conditions affecting gas composition in operational downdraft gasifiers, such as thermal and electrical efficiencies, as well as gasifier design. In equilibrium models, the ER holds the most significant influence on producer gas composition, particularly the proportional relationship between ER and N_2 content. Notably, the predicted CH_4 aligns well with the corresponding experimental values, particularly for feedstocks in Figs. 4.4(a) and 4.4(c), showcasing the uniqueness of the current model. This achievement has not been previously accomplished by equilibrium models without the introduction of empirical correction factors. Regarding H_2 prediction, there are instances where it is slightly overestimated, but this can be reasonably explained by the aforementioned reasons. [75] performed a quantita-

tive analysis on the overall gasifier efficiency and performance and found that the maximum percentage error for the mass balance closure was associated with pellets feedstock at 5.37%. With respect to the gasifier thermal losses, they vary from 2.5% to 26.5% for the 4 different gasifiers, while biomass conversion ranges between 66.2% to 91.3% for the 4 gasifiers. Overall, the model's predicted syngas composition demonstrates promising agreement with experimental data, underscoring its utility and potential in understanding gasification processes for various feedstocks.

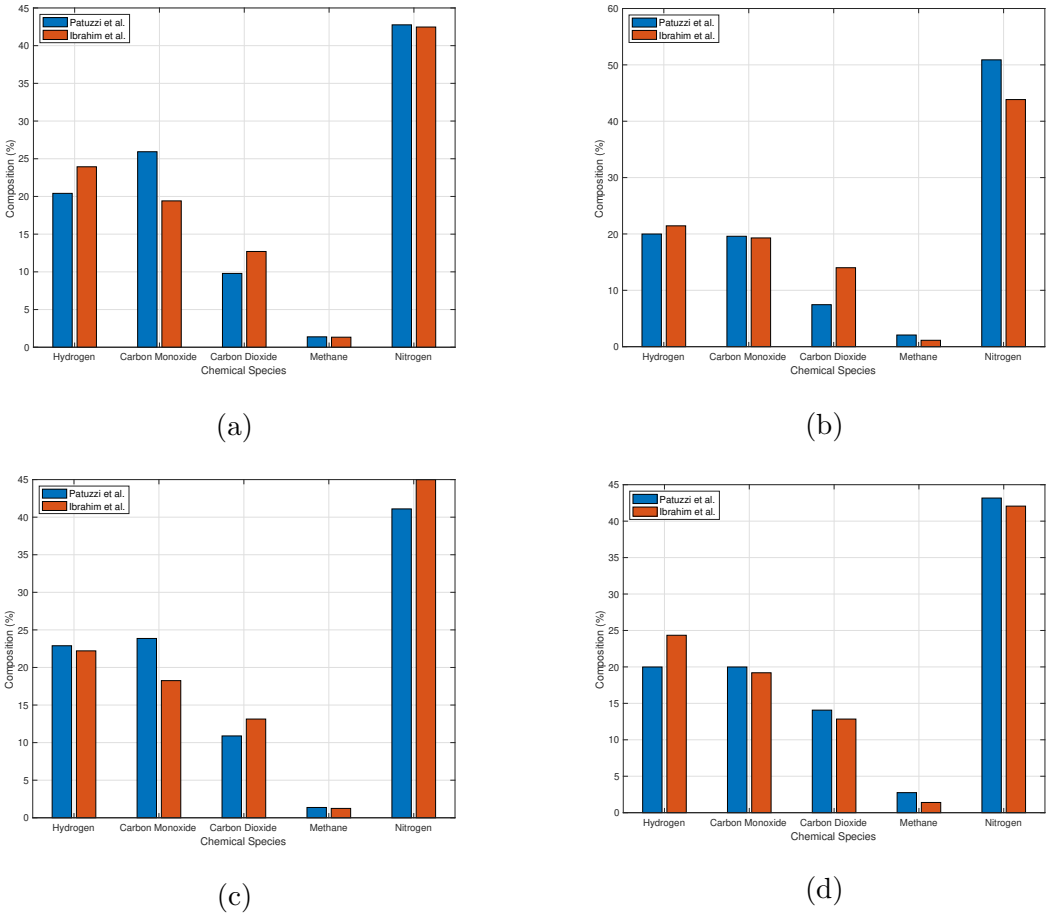

Figure 4.4: Comparison between predicted [119] and experimentally obtained [75] producer gas composition for (a): pellets (MC=6.32%, ER=0.26), (b): wood chips 1 (MC=3.39%, ER=0.25), (c): wood chips 2 (MC=10.30%, ER=0.29) and (d): wood chips 3 (MC=7.65%, ER=0.26).

4.2.1.2 Gasification temperature

Fig.4.5(a) presents a comparison between the predicted T and the experimental data from Upadhyay et al [74]. Both profiles exhibit a similar trend, with T increasing

as ER rises. This outcome is expected since a higher ER indicates more air in the system, leading to increased combustion reactions, and consequently, a higher amount of heat released, thus promoting higher T. The feedstock used is a mixture of lignite and sawdust briquettes (70:30 wt%), and minor discrepancies between the model and experimental results can be attributed to the various gasifier conditions present in experimental studies. In contrast, equilibrium models primarily consider the influence of ER and MC on T. Clearly, Fig.4.5(a) demonstrates a favourable comparison between the model's predicted T and the experimental data obtained by [74].

Fig.4.5(b) illustrates the impact of MC on the predicted T in comparison to the experimental results of [73] at an ER of 0.25. Both the model and the experiment demonstrate a decrease in T as MC increases, which is attributable to the fact that higher MC in the feedstock promotes endothermic behaviour, leading to a decrease in the reaction temperature, consequently lowering the T [122]. Notably, The highest difference in T between the predicted value and the experimental result is at an MC of approximately 21%, where the difference between the values is 9%. [73] also performed a regression analysis to present syngas calorific value, gasifier capacity, and CGE and HGE as a function of gasifier operating setup. In this model, they calculated the mean absolute error for the gasifier thermal capacity and found it to be around 8.78%. As such, within the range of MC, there is reasonable agreement between the model and the experimental investigation regarding T. It is important to acknowledge that additional operating parameters influence the T in experimental investigations, as demonstrated by [73].These factors include primary and secondary air flow, fuel supply rate, and the thermal capacity of the gasifier. All of these parameters have an effect on the resulting T during the gasification process. Furthermore, it is noteworthy to reiterate that equilibrium models typically estimates the average gasification temperature based on a global reaction, whereas in experiments, the temperature is predicted from different reacting zones of the gasifier. According to the Stefan-Boltzmann law, radiative losses scale with the fourth power of the absolute temperature, meaning even small increases in temperature can result in disproportionately large heat losses. By assuming an adiabatic process, the

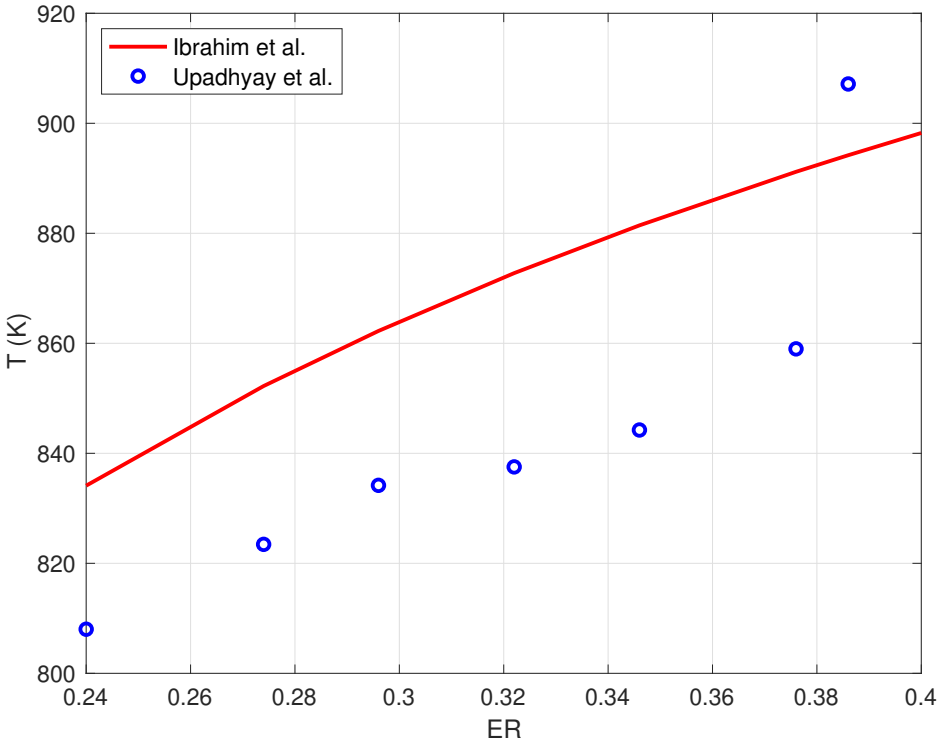

(a)

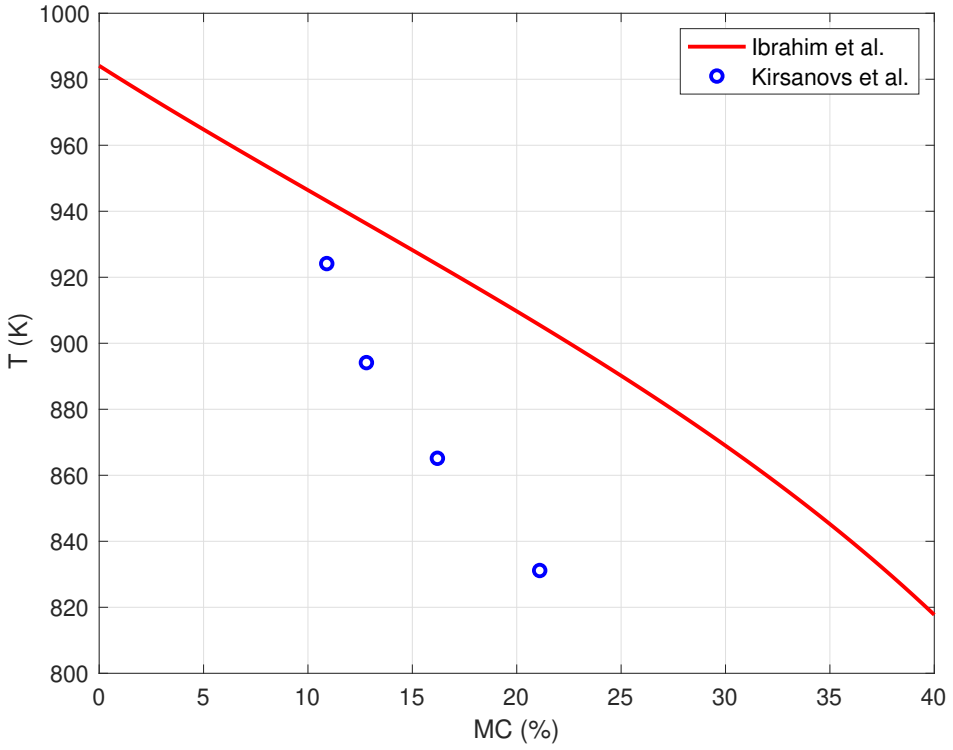

(b)

Figure 4.5: Variation of T with ER for (a) lignite (MC=12%) and with MC for (b) wood chips 5 (ER=0.25).

model retains more thermal energy internally than would occur in a real system, leading to overpredicted equilibrium temperatures and possibly an overestimation of reaction extent for endothermic reactions such as R3.

4.2.1.3 Char yield

(R3) is utilised to factor in the C yield prediction, as it is the dominant reaction when using air as the gasifying medium [2], rather than employing an empirical correlation to describe the C fraction, a correlation representing the amount of C involved in equilibrium reactions, as previously done in thermodynamic equilibrium models - see for example [19, 25, 26, 123]. To validate the feasibility and reliability of implementing (R3), the predicted char yield is compared with results obtained from experimental investigations of a DBG conducted by [70] in Fig. 4.6 for a variety of biomass feedstock and different operating conditions. Overall, the two sets of data show reasonably good agreement. In thermodynamic equilibrium models, the ER significantly influences main and by-product yields. Normally, the char yield decreases with an increase in ER because higher ER promotes elevated bed temperature, leading to enhanced char reactions through (R3) and (R11) and, consequently, a higher amount of gas formation. This explains the substantial variation in the char yield comparison for softwood pellets, as the experiments were conducted at an ER of 0.2. For both the model and the experiment, the lowest char yield is observed for the gasification of mixed wood chips. In experiments, the variation of char yield depends on many factors, including the amount of ash in the raw material, ER and T. For instance, the mixed wood chips contain only 0.8% of ash, which is 24 times less than the amount of ash found in softwood pellets. A high ash content results in a lower temperature distribution in the gasifier, potentially increasing char yield.

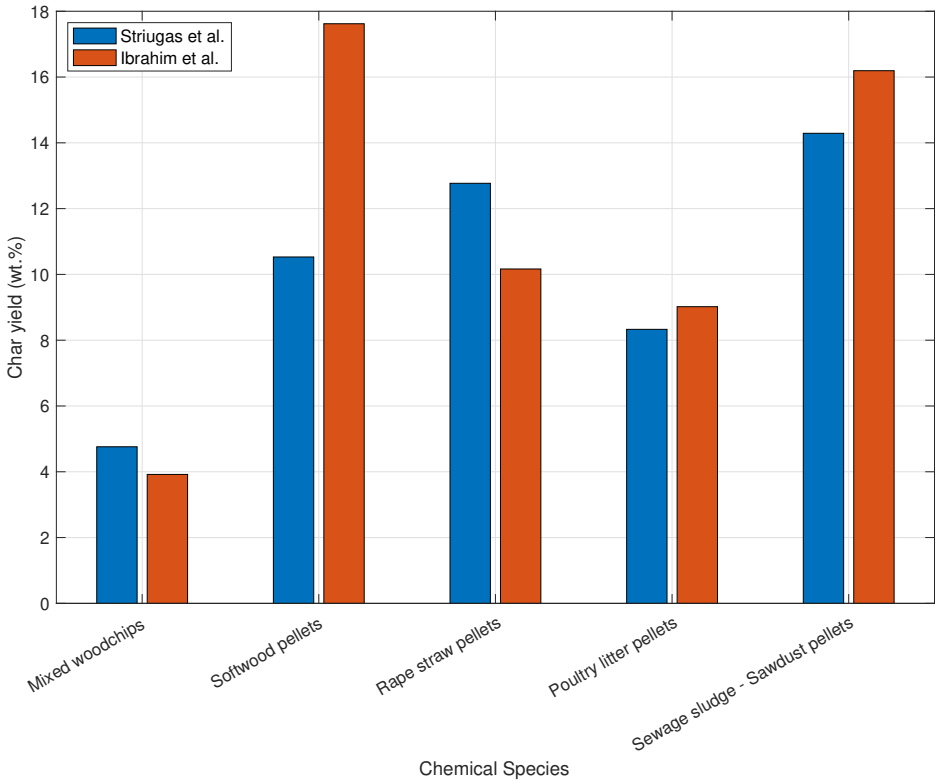

Figure 4.6: Comparison of predicted char yield with that obtained experimentally by [70] for mixed wood chips (ER=0.21), softwood pellets (ER=0.20), rape straw pellets (ER=0.29), poultry litter pellets (ER=0.41) and sewage sludge - sawdust pellets (ER=0.39).

Now, the focus shifts to utilising the model to investigate how operational factors, such as MC and ER, influence the gasification process for both rubberwood and wood pellets. Subsequently, we will examine the impact of NH_3 and H_2S concentrations as constituents of the producer gas composition.

4.2.2 Effect of moisture content

MC is an essential property of biomass and an important operating parameter when developing a gasifier since it can strongly influence the conversion of biomass into energy. Increasing levels of moisture affects the self-sustainability of the combustion process, ultimately decreasing the heating value of the syngas and reducing the efficiency of the process. Furthermore, high levels of moisture reduce the oxidation

temperature leading to an incomplete cracking of the hydrocarbons produced during pyrolysis. Tolerable biomass moisture level limits range from 15% to roughly 55% [85].

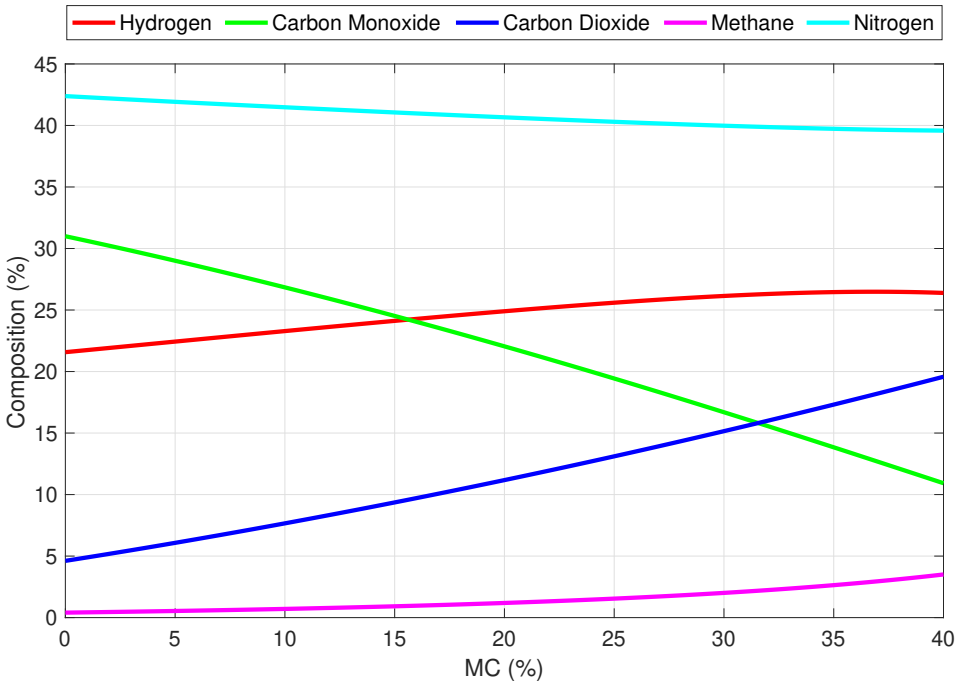

Figure 4.7: Predicted variation of syngas composition with MC for rubberwood (ER=0.326).

In Fig. 4.7, the effect of MC in rubberwood on the composition of the resulting producer gas is revealed. As MC increases from 0% to 40%, the percentage CO decreases from approximately 31% to 11%. The N_2 concentration remains almost constant with increasing MC, as expected due to it being an inert species, while the CH_4 produced varies marginally from 0.5% to around 3.5%, indicating the improved prediction of CH_4 by the current equilibrium model relative to experimental studies of DBGs. As MC increases, (R11) is enhanced due to the increased levels of H_2O. This prompts the rise in concentrations of H_2 and CO_2 from approximately 22% to around 26% and from about 5% to 20%, respectively, alongside the corresponding decline in CO levels due to increased consumption with H_2O. These observations align with the conclusions drawn by [8, 124], who noted similar alterations in syngas composition with rising MC. In their studies, the biomass MC emerged as a significant operational parameter influencing the efficiency of biomass gasification,

prompting detailed analyses of its impact on gasifier performance.

Figs.4.8(a) and 4.8(b) consider the LHV and the CGE, for both rubberwood and wood pellets, respectively, as a function of the MC and a fixed ER of 0.326. Both decrease with increasing MC, which is expected as a higher MC reduces the efficiency of the gasifier. A higher MC indicates that more energy is required to vaporise the water, reducing the amount of available energy for actual gasification reactions. This means that as the MC increases, the heat available for gasification is partially used to evaporate the water, leading to less C being converted to gas, reducing the LHV and the CGE. In the case of the CGE, increasing MC decreases the efficiency of the gasifier as T decreases with MC resulting in a weaker production of syngas.

The corresponding variation of tar content with MC is shown in Fig. 4.9, that for rubberwood being slightly greater than that of wood pellets for the same operating conditions. The decrease in tar content with MC is in line with the results of [125] who studied the influence of MC on the tar characteristics of wood pellet feedstock in a DBG using gas chromatography, mass spectrometry and gravimetric analysis to identify and analyse the tar samples. In their study, they varied the MC of wood pellets from 2% to 6% and found after performing mass spectrometry and gravimetric analysis that the results showed a decrease in total tar formation with an increase in MC. Although light tars decreased in their experiment, heavy tars increased and caused major clogging. In the model, this influence might seem counter-intuitive at first since normally when increasing the MC in the feedstock, this will lead to more energy being consumed for water evaporation, which lowers the temperature in the system and increases tar formation. However, there are a number of reasons why the opposite trend is being observed in the model. The model is mainly influenced by R11 and an increase in MC shifts the equilibrium to produce H_2 and CO_2, increasing the driving force for tar cracking in an overall equilibrium system. Furthermore, the tar yield in the model is mainly influenced by the ER of the system and not by the MC and as such there is not real representation of direct MC influence on tar yield. This is a demonstration of the various limitations of equilibrium models to reflect the real influence of MC on tar yield.

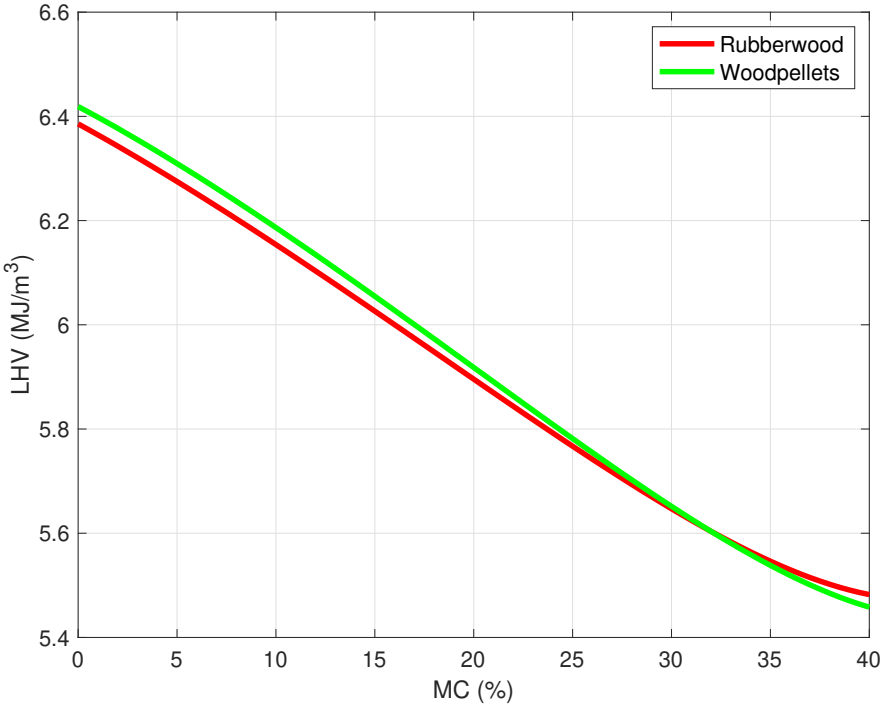

(a)

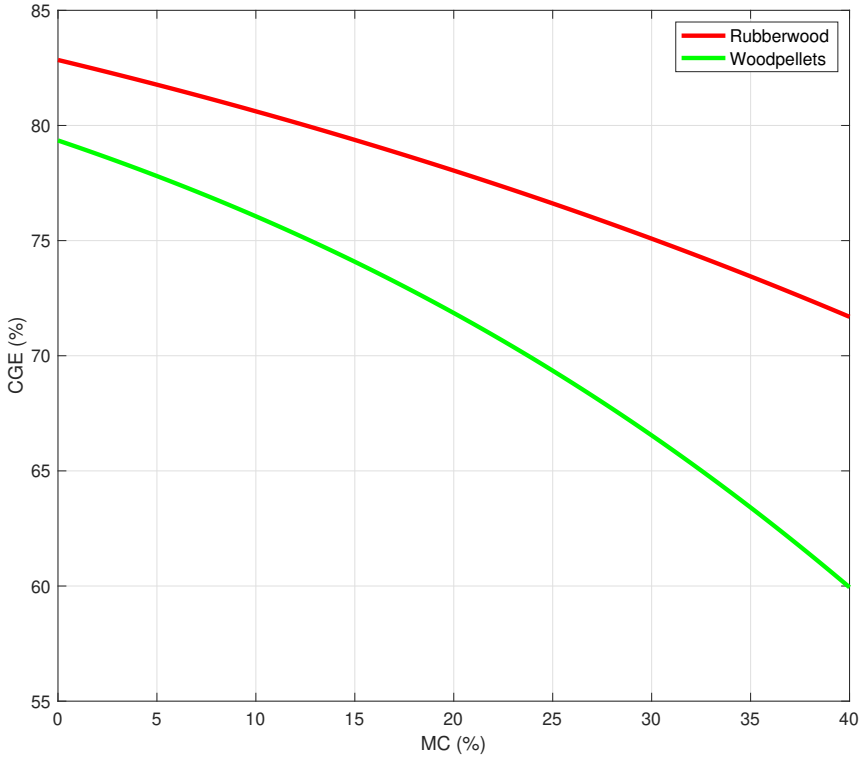

(b)

Figure 4.8: Predicted variation with increasing MC for (a) LHV_{gas} and (b) CGE for two different biomass feedstocks (ER=0.326).

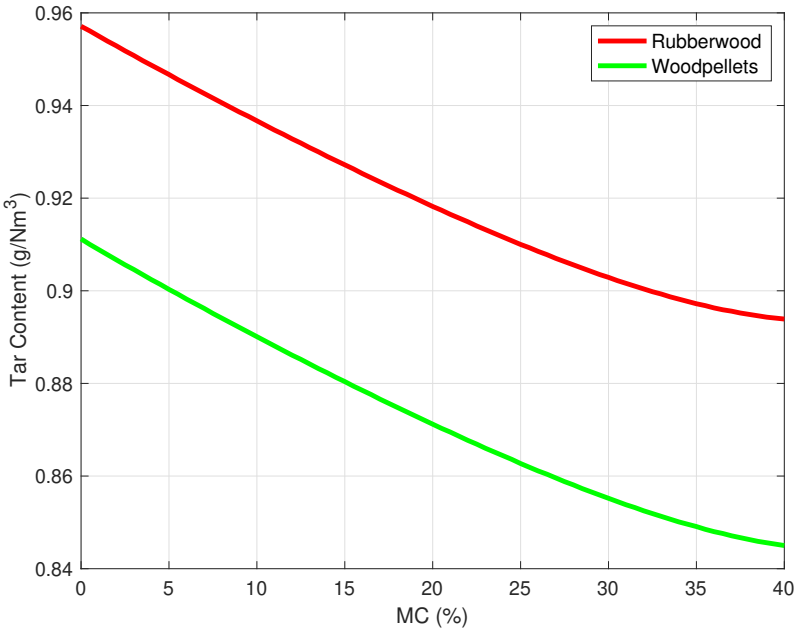

Figure 4.9: Predicted variation of tar with MC for the same biomass feedstocks (ER=0.326).

4.2.3 Effect of equivalence ratio

ER is the main operating parameter influencing biomass gasification, which is considered as a fuel rich combustion when the ER is less than 1. Typical values usually range from 0.2 to 0.4, and strongly affect the gasification process as explained in section 3.3.4.2 of Chapter 3.

The influence of the ER on the syngas composition at 18.5% MC for rubberwood is shown in Fig. 4.10. The decrease in H_2 suggests that the system is becoming more oxidising with the introduction of more oxygen into the system and is in agreement with the results of [74, 126, 127]. Upadhyay et al. [74] studied the effects of ER on the performance of a downdraft biomass gasifier both experimentally and theoretically. According to Le Chatelier's principle [128], the increase of ER will lead to an increase in T, shifting the equilibrium of exothermic reaction (R11) to produce CO and consume CO_2 and H_2. With increasing T, the rate of (R11) increases, but H_2 production becomes less favourable thermodynamically. A higher CO concentration with increasing ER also means that (R3) becomes active, producing more CO as more O_2 becomes available. This in turn will decrease the amount of CO_2

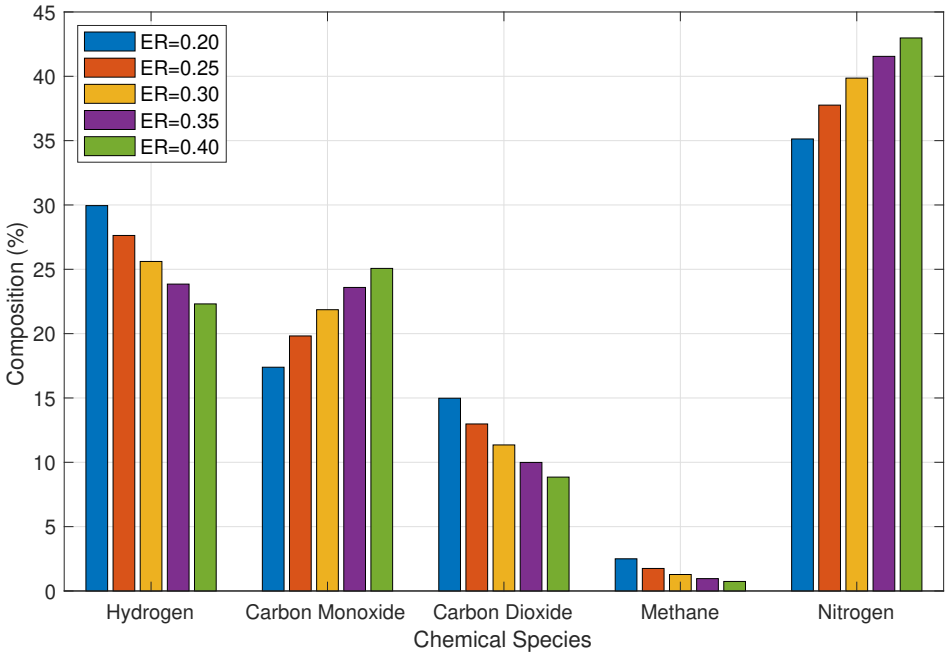

Figure 4.10: Predicted variation of producer gas composition with ER for rubberwood (MC=18.5%).

in the producer gas which explains the decline of CO_2 as ER increases. The CH_4 concentration is found to decrease fractionally from around 2.5% to 0.75%; this is due to the fact that the higher T facilitates the rate of (R3) but decreases the rate of (R5). Finally, the N_2 concentration in the producer gas increases because the N_2 is mainly in air and at a higher ER, more air is present in the system.

The predicted variation of tar content with increasing ER for both rubberwood and wood pellets is considered in Fig.4.11. As mentioned earlier, increasing ER enhances T as a result of a higher input air within the gasifier. Consequently, a higher quality syngas is produced resulting in a reduction of the tar content. The increased T also facilitates tar cracking and thus the tar may decompose into lighter gases which may assist in increasing the combustible products in the syngas, ultimately decreasing the tar content [74, 129].

Fig. 4.12(a) explores the variation of the LHV for rubberwood with MC for different ER values. It is shown that the reduction of high heating value gases such as H_2 and CH_4 and heavier hydrocarbons, in addition to the dilution effects of N_2, decreases the LHV of the producer gas with increasing ER. The same outcome was

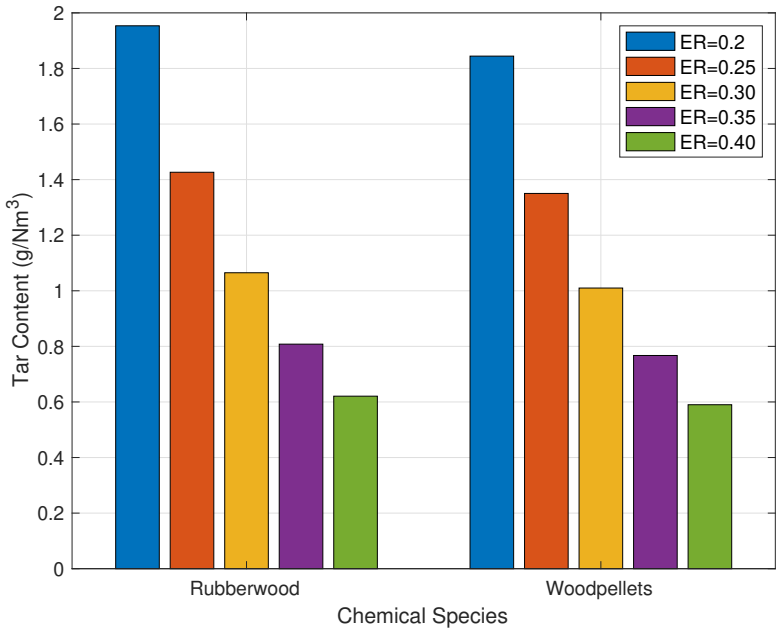

Figure 4.11: Predicted variation of tar production for different values of ER for both rubberwood and wood pellet feedstocks (MC=18.5%).

obtained by Cho et al [130], who reported that increasing ER from 0.21 to 0.41 led to a reduction of LHV from 13.42 to 7.05 MJ/Nm^3. A similar result was reported by [131] with the heating value decreasing from 11.3 to 5.17 MJ/Nm^3 for an increase of ER from 0.2 to 0.45. At a low ER (≤ 0.25), the low quality syngas results in an increase followed by a sudden decrease of H_2 values, in line with the results of [8,12] and with the reasoning of (R11). As this happens, and since the syngas LHV is partly influenced by H_2 production, the syngas LHV demonstrates this trend. The variation of CGE with MC for increasing values of ER in Fig. 4.12(b) shows a general improvement of CGE with increasing ER. For dry feedstock, the CGE of the gasifier increases from approximately 71% to around 83% between ER of 0.2 and 0.35. However, as ER increases further to 0.4, the gasifier becomes oxygen-rich and complete combustion starts taking place, resulting in a lower CGE.

4.2.4 Minor gasification products

This section focuses on the minor gasification products encapsulated within the model, H_2S and NH_3. H_2S is modelled using atom balances as S is only found in the

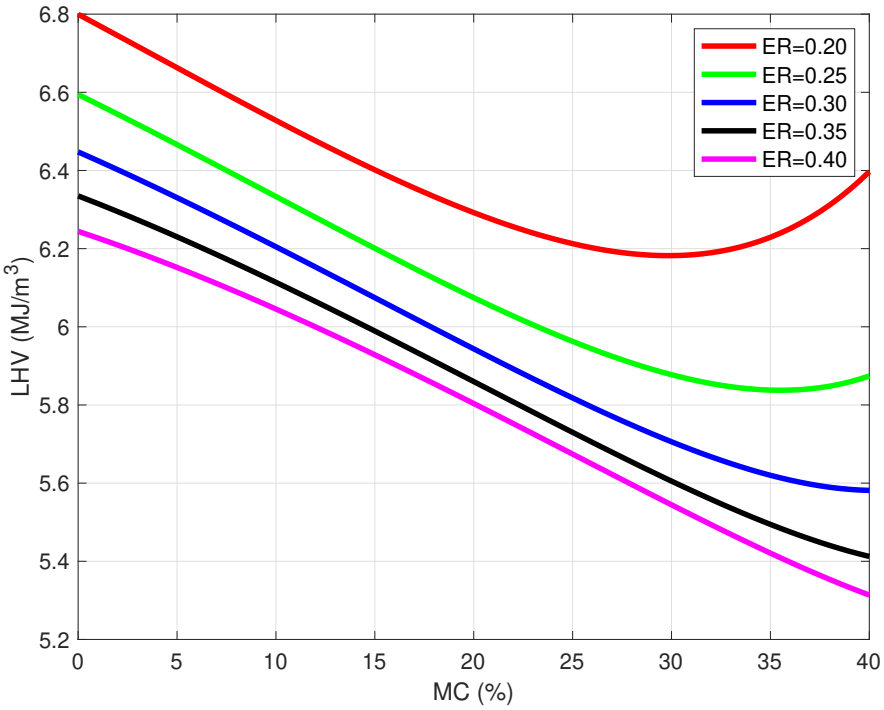

(a)

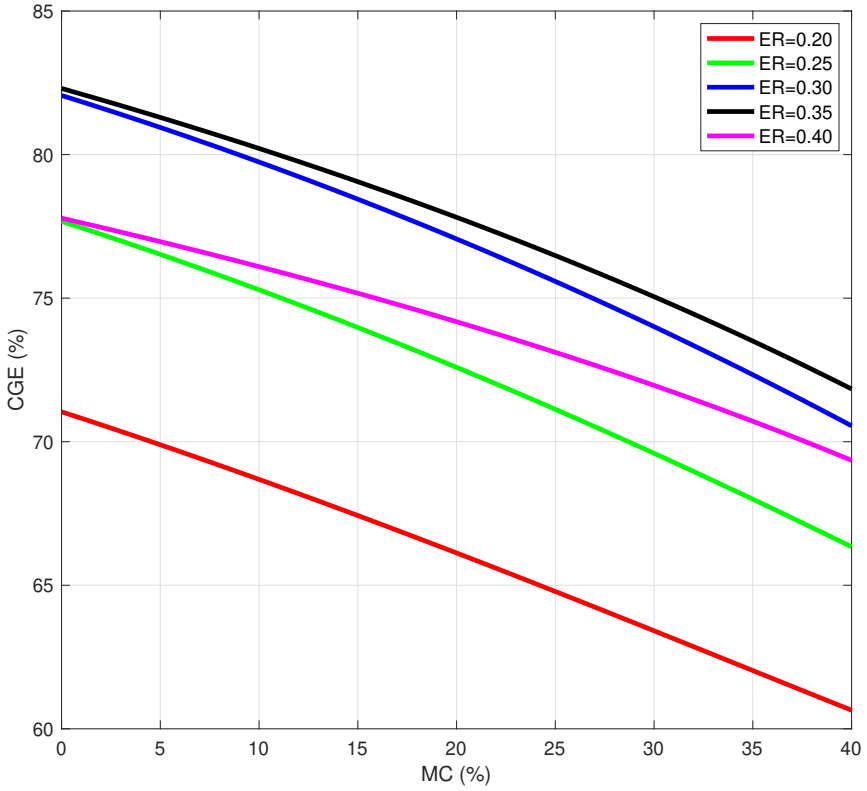

(b)

Figure 4.12: Predicted variation for different ER values for (a) LHV_{gas} and (b) CGE, for rubberwood.

biomass feedstock and not involved in chemical reactions in the model. Since the sulphur in the biomass feedstock converts predominantly to H_2S under gasification conditions, the amount of H_2S can be estimated directly from the sulphur content in the biomass. The purpose of including them is to estimate the concentrations of the primary sulphur-based and primary nitrogen-based contaminants within biomass gasification. Although some previous authors have considered the production of H_2S [13], the production of NH_3 is novel in stoichiometric equilibrium modelling.

Fig 4.13 illustrates the changes in NH_3 and H_2S concentrations for forest waste residue under different ER values and increasing MC, respectively. Forest waste residue contains 0.07% S in the feedstock according to Table 3.1. In Fig. 4.13(a), a comparison is made with the modelling results of Gambarotta et al. [79]. At an MC of 40%, the model's predicted NH_3 and H_2S concentrations show good agreement with those estimated by Gambarotta et al. [79]. For instance, at an ER of 0.1275, the NH_3 concentration is approximately 0.0122% in the model, and around 0.015% in [79], both displaying a sharp decrease as the ER increases towards 0.255. It is also shown that the influence of ER on the minor gasification species results in agreed behaviour as both NH_3 and H_2S decrease with increasing ER, highlighting the effectiveness of the parametric study of the model. This behaviour can be attributed to a number of factors; including the enhancement of T at increasing ER values which leads to a greater transformation of biomass into syngas, consequently reducing the production of volatiles, tar, char, and contaminating gases like NH_3 and H_2S. Higher ER values often results in more complete combustion, promoting the conversion of sulphur and nitrogen-containing compounds into less harmful compounds. Additionally, it is worth noting that the output of the gasifier contains only trace amounts of H_2S since S is generally absent or present in very small quantities in the feedstock. As a result, authors often neglect H_2S as an output since its presence does not significantly contribute to the main products of the gasifier.

In Fig. 4.13(b), the variation of NH_3 and H_2S concentrations with increasing MC is shown. It is evident that the NH_3 concentration increases with higher MC, while the concentration of H_2S remains almost constant. This behaviour is expected as there is a higher likelihood of the formation of NH_3 and H_2S as the increased MC

can promote the breakdown of organic matter in the biomass, leading to increased availability of sulphur and N_2 compounds, which can then react to form NH_3 and H_2S. Also, with increased MC, the overall temperature distribution in the gasifier will diminish due to the enhanced evaporation energy required to absorb the moisture, potentially affecting the efficiency of certain reactions and favouring the formation of NH_3 and H_2S.

Table 4.4: Error analysis between the model prediction and the experimental data from [79].

	Error (%)	
ER	**NH_3**	**H_2S**
0.1275	18.27	1.87
0.255	23.85	20
0.3401	16	23.08
0.3826	16.13	25
0.4251	12.20	18.18

While there is a agreement between the experimental data and the model predictions of the contaminating species in gasification, especially with analysing their influence against operating parameters, the error analysis presented in Table 4.4 is evidence that there remains an uncertainty when comparing experimental results with predictions from equilibrium models. This further highlights the limitations of equilibrium models, and ascertains the need for more sophisticated modelling approaches to have a better understanding the behaviour of contaminating by-products in biomass gasification.

4.3 Summary

A thermodynamic equilibrium model is established to analyse biomass gasification processes across various operating parameters. This model incorporates a newly devised empirical correlation to estimate tar yield within the system, enhances prediction of gasification temperature by integrating a coupled system of equations, thereby improving overall robustness and convergence properties. Furthermore, the

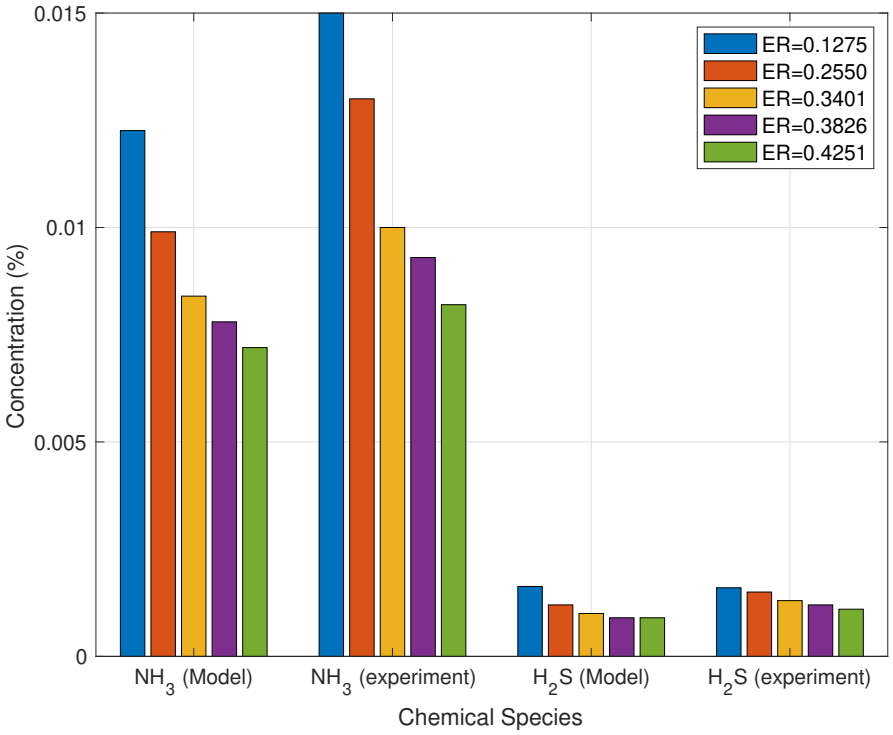

(a)

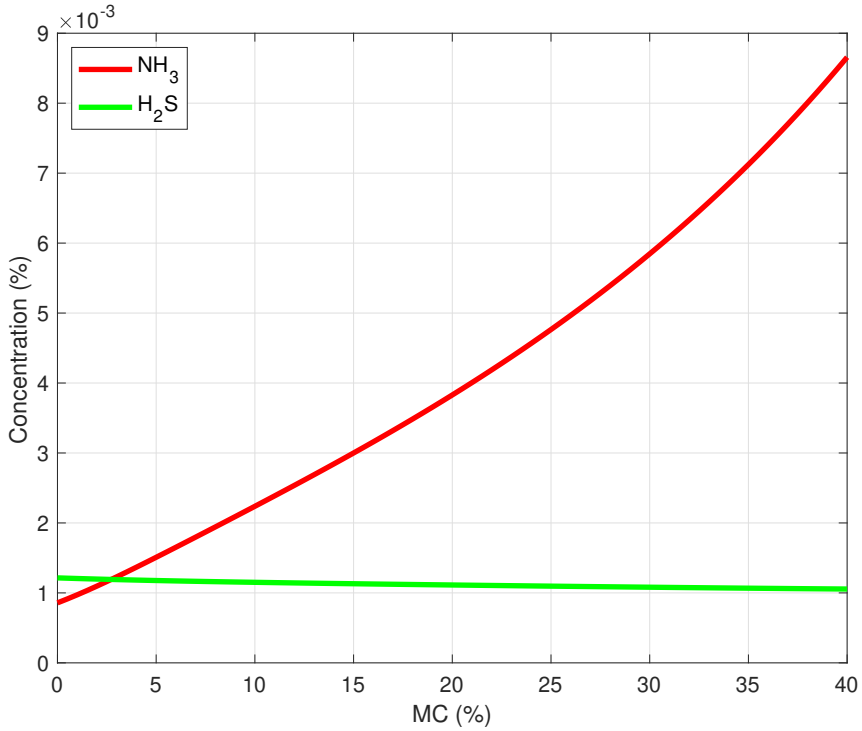

(b)

Figure 4.13: Predicted variation in NH_3 and H_2S concentration for forest waste residue for (a) different ER values compared with the model results of [79] (MC=40%) and (b) increasing MC (ER=0.326).

model comprehensively considers the formation of minor contaminating species and examines their impact under different operating conditions. The study systematically analyses the effects of MC and ER on the gasification process, providing valuable insights into process optimisation and performance enhancement. The restrictions of the equilibrium model, which can solely provide insight into the overall gasification process yield without offering an intricate portrayal of the flow dynamics within the gasifier, including the multi-phase characteristics inherent in biomass gasification, create an opportunity for the formulation of a CFD model tailored to biomass gasifiers. This CFD model can effectively address significant aspects associated with the gasification process.

CHAPTER 5

A Thermochemical CFD (Thermo-CFD) Model of a Downdraft Biomass Gasifier with Moving Porous Fuel Bed.

A 2D DBG model has been developed using a CFD approach, with a specific focus on the porous media assumption - see section 3.4.3 of Chapter 3. The model is built using the **porousGasificationFoam** solver which, while previously applied to pyrolysis and combustion, is now used for gasification for the first time.

The model includes two air inlets to accommodate the gasification agent's flow. The process begins with moist feedstock entering the system, transitioning to dry feedstock in the pyrolysis and oxidation stages. The char bed ignition initiates chemical reactions, consuming the porous feedstock and generating reaction products. A key feature is its ability to differentiate between endothermic and exothermic reactions while incorporating biomass replenishment via a moving porous bed.

The porous media assumption offers several advantages:

1. Improved computational efficiency; instead of resolving individual biomass particles, the porous media approach models the packed bed as a one whole medium, reducing computational costs.

2. Capturing flow distributions, particularly for gas and solid phase interactions.

This is crucial for understanding the mixing and transport of reactants, species, and heat transfer during the gasification process.

3. Allowing for the simultaneous occurrence of chemical reactions which sets the model apart from the continuous flow assumption, where a direct output-input relationship is assumed between reacting zones. This feature enables a more representative portrayal of the processes taking place inside an actual biomass gasifier.

The solver is capable of handling skew geometrical regions, allowing the construction of a throated oxidation zone for the gasifier. Lastly, A pyrolysis model presenting an effective approach to calculate distributed coefficients among pyrolytic products is provided alongside the Thermo-CFD model.

5.1 Model description and methodology

5.1.1 Governing equations and assumptions

As with any multiphase process application investigated using a time-dependent CFD mathematical model, conservation laws are applied for each phase involved. Typically in a biomass gasification system, the two phases are gas and solid with the conservation of mass, species, momentum, and energy applied to both phases, stemming from the general transport equations highlighted in section 3.4.3, Chapter 3. As the porous media assumption is invoked in this model, computational domain regions filled only with gas and regions filled with porous media are established, where each control volume V considered in the computational domain is characterised by ϵ as in Eqs.(3.13) and (3.14) in Chapter 3.

A spatial averaging procedure is applied to obtain space averaged conservation equations to be solved over the computational domain. The space averaged gas phase conservation equations are as follows in order of species mass conservation, continuity, momentum, and energy conservation, with the source terms written on

the right hand side of the equations [112]:

$$\frac{\partial}{\partial t}\epsilon\rho^f\langle Y_i\rangle^f + \nabla\left(\rho^f\langle Y_i\rangle^f\langle\vec{u}\rangle^f\right) - \nabla\cdot\left(\epsilon\rho^f D_{eff}\nabla\langle Y_i\rangle^f\right) = \epsilon\langle\dot{\omega}_i\rangle^f + (1-\epsilon)\langle \mathrm{R}_i\rangle^s \ , \quad (5.1)$$

$$\frac{\partial}{\partial t}\epsilon\rho^f + \nabla\cdot(\rho^f\langle\vec{u}\rangle) = (1-\epsilon)\sum_i\langle \mathrm{R}_i\rangle^s \ , \quad (5.2)$$

$$\frac{\partial}{\partial t}\rho^f\vec{u} + \nabla\cdot\left(\rho^f\langle\vec{u}\rangle\langle\vec{u}\rangle\right) + \epsilon\nabla\langle p\rangle^f - \nabla\cdot(\mu\nabla\langle\vec{u}\rangle) - \rho^f\langle\vec{g}\rangle = -\mu\mathrm{D}\cdot\langle\vec{u}\rangle - \mathrm{F}\cdot\langle\vec{u}\rangle \ , \quad (5.3)$$

$$\begin{aligned}\frac{\partial}{\partial t}\epsilon\rho^f C_p^f\langle T\rangle^f + \nabla\cdot\left(\rho^f C_p^f\langle T\rangle^f\langle\vec{u}\rangle\right) - \nabla\cdot\nabla\left(\epsilon k_{eff}^f\langle T\rangle^f\right) = -\epsilon\sum_i h_{f,i}^\circ\langle\dot{\omega}_i\rangle^f \\ - C_{conv}\mathrm{SA}\left(\langle T\rangle^f - \langle T\rangle^s\right) + (1-\epsilon)\langle T\rangle^f\sum_i C_{p,i}\langle \mathrm{R}_i\rangle^s + \langle S^{f,radiation}\rangle \ . \quad (5.4)\end{aligned}$$

In the above, superscript f denotes gas phase (fluid), $\vec{u}$ is the velocity vector of the fluid, Y_i^f is the mass fraction of the individual gas species, D_{eff} is the fluid diffusion coefficient, μ is the dynamic fluid viscosity, $\vec{g}$ is the acceleration due to gravity, and SA is the surface area-to-volume ratio of the porous media. The symbol $\langle\cdot\rangle$ stands for the local phase average (integrated over the whole control volume), while $\langle Y_i\rangle^f$ and $\langle Y_i\rangle^s$ are the local phase intrinsic averages for gas phase (integrated over the fraction of control volume occupied by the fluid) and solid phase (integrated over the solid occupied fraction of control volume), respectively [112, 132]. $S^{f,radiation}$ is the source term for radiation in the gas phase.

The subscript eff includes the participation of the correlations generated by the local averaging procedure [112]. The term $\langle\dot{\omega}_i\rangle$ describes the volumetric mass change rate for gas species i resulting from homogeneous reactions, in which $\sum_i\dot{\omega}_i = 0$ within the gas phase as homogeneous reactions conserve mass. Homogeneous reactions introduce the source term $\sum_i h_{f,i}^\circ\langle\dot{\omega}_i\rangle^f$ in the sensible enthalpy equation, calculated from the mass source terms and the enthalpies of formation of each gaseous component $h_{f,i}^\circ$. D refers to Darcy's resistance to the flow through the porous media completely analogous with the porous media assumption mentioned in section 3.4.3, Chapter 3. It is linear with the fluid velocity and proportional to a tensor representative of the structure of the porous media, where in the limiting anisotropic case,

$\mathrm{D} = D_c I$. The Forchheimer term is modelled as:

$$\mathrm{F} = F_c \rho^f |\langle \vec{u} \rangle| \frac{\sqrt{3}}{|\mathrm{D}|} \mathrm{D} \ , \tag{5.5}$$

where F_c is Forchheimer's coefficient and $|\cdot|$ is the Euclidean norm. The Forchheimer term is modelled so that it has the same spatial direction as the Darcy term. It is a modification or extension of Darcy's law, accounting for the nonlinear effects that arise at higher flow rates and describes fluid flow through porous media under conditions where Darcy's law alone may not be sufficient. Its omission is justified based on the predominated viscous flow regime in which Darcy's law applies. In the Thermo-CFD model, Forchheimer's model is not implemented and as such $\mathrm{F} = 0$.

The corresponding solid-phase conservation equations are:

$$\frac{\partial}{\partial t}(1-\epsilon)\rho^s \langle Y_k^s \rangle = (1-\epsilon)\langle \mathrm{R}_k^s \rangle \ , \tag{5.6}$$

$$\frac{\partial}{\partial t}(1-\epsilon)\rho^s = (1-\epsilon)\sum_k \langle \mathrm{R}_k \rangle^s \ , \tag{5.7}$$

$$\begin{aligned} \frac{\partial}{\partial t}(1-\epsilon)\rho^s C_p^s \langle T \rangle^s - \nabla \cdot \left((1-\epsilon)\mathrm{K} k_{eff}^s \cdot \nabla \langle T \rangle^s \right) = -(1-\epsilon)\sum_k h_{f,k}^{\circ} \langle \mathrm{R}_k \rangle^s \\ - (1-\epsilon)\sum_i C_{p,i} \langle T \rangle^f \langle \mathrm{R}_i \rangle^s + C_{conv} \mathrm{SA} \left(\langle T \rangle^f - \langle T \rangle^s \right) + \langle S^{s,radiation} \rangle \ , \end{aligned} \tag{5.8}$$

where superscript s denotes solid phase, Y_k^s is the mass fraction of the solid species k, ρ^s is the density of the solid matrix, and K is the anisotropy tensor of the solid matrix. $S^{s,radiation}$ is the source term for radiation in the solid phase.

The assumptions underpinning the model are that:

1. N_2 is considered an inert gas;
2. the contribution of ash is neglected;
3. reactants are at standard temperature T_0;
4. tar is a gaseous component and its thermodynamic properties taken to be those of benzene;

5. char possesses the same thermodynamic properties as graphite;

6. the flow is in the laminar regime;

7. the bed is randomly close packed with spheres (initial $\epsilon = 0.4$);

8. the Darcean resistance is low (i.e. $D_c = 10^9$ m^{-2}), introducing only a small pressure change upstream.

5.1.2 Thermochemical reaction submodel

Biomass conversion includes comprehensive chemical and physical processes, one of which is the reaction kinetics model involving homogeneous and heterogeneous chemical reactions and can be formulated in the form of Arrhenius equations - see Eq. (3.46) in section 3.4.2 of Chapter 3, where k is the rate coefficient for each reaction, defined per 1 kg of solid reactant. From k, the reaction rate Ω_r is calculated as:

$$\Omega_r = \begin{cases} \rho^s \prod_i (Y_i^f)^{n_{r,i}^f} \prod_k (Y_k^s)^{n_{r,k}^s} k, & T > T_c \\ 0, & T \leq T_c \ , \end{cases}$$

where $n_{r,i}^f$ is the reaction order for gas specie reactant i, $n_{r,k}^s$ is the reaction order for the solid specie reactant k, and T_c is the cutoff temperature which can be defined for each separate reaction. The reaction rates are multiplied by the stoichiometric coefficients $\nu_{r,i}^f$ and $\nu_{r,k}^s$ to calculate the source terms $\mathrm{R}_{r,i}^f$ and $\mathrm{R}_{r,k}^s$ according to the conservation equations.

Due to the potential participation of every substrate in more than one chemical reaction, the net rate of species production and consumption is summed up over the reactions r giving:

$$\mathrm{R}_i = \sum_r \nu_{r,i}^f \Omega_r \ , \tag{5.9}$$

for the source terms in Eq. (5.1) and Eq. (5.2) and

$$\mathrm{R}_k = \sum_r \nu_{r,k}^s \Omega_r \ , \tag{5.10}$$

for the source terms in Eq.(5.6) and Eq.(5.7). The summation of gas and solid mass source terms in every control volume is equal to 0 to satisfy mass conservation. The solid phase chemical reactions proceed at a gas-solid interface, limiting their rate by the diffusive transport of gaseous reactants to the surface [133]. This is directly linked to the dimensionless Damkohler number, Da_i, for the specie i given by:

$$Da_i = \frac{\tau_{diff,i}}{\tau_{chem,i}} \ , \tag{5.11}$$

where $\tau_{diff,i}$ is the characteristic diffusion time and $\tau_{chem,i}$ the characteristic surface reaction time. Two limits of the solid phase reactions are modelled; first when the reaction is much slower than diffusion, $Da_i \rightarrow 0$ and when the reaction rate is faster than diffusion, $Da_i \rightarrow \infty$. As such Ω_r should reflect the Da_i number, therefore the solid volume-average Ω_r based on the species diffusion is modelled as:

$$\langle \Omega_r \rangle^s{}_{diff} = C_{mass} \mathrm{SA} \rho^f \left(\langle Y_i \rangle^f - \langle Y_i \rangle^{surface} \right) \ , \tag{5.12}$$

where C_{mass} represents the mass transfer coefficient. In the Thermo-CFD model, an initial ϵ of 0.4 and diameter of the pore is equal to 6.4 mm, which gives an SA equal to 468 m^{-1} [7]. Finally, Ω_r is evaluated over the entire range as:

$$\langle \Omega_r \rangle^s = \frac{1}{\frac{1}{\langle \Omega_r \rangle^s{}_{diff}} + \frac{1}{\langle \Omega_r \rangle^s{}_{kin}}} \ , \tag{5.13}$$

whereby, adding a subscript kin, the solid volume-average of kinetics reaction rate (Eq.(5.1.2)) is emphasised.

Another important property of the thermochemical reaction sub-model is determination of the source terms for the enthalpy in the solid phase according to the heterogeneous reactions. The solver gives a choice of either calculating them based on the enthalpies of formation of each specie involved as follows:

$$S_{heter} = (1 - \epsilon) \sum_k h^\circ_{f,k} \mathrm{R}_k \ , \tag{5.14}$$

or based on the enthalpy of reaction ΔH_r, provided by the user as:

$$S_{heter} = (1-\epsilon)\sum_r \Delta H_r \Omega_r \ . \tag{5.15}$$

The absence of thermal equilibrium in porous media, introduces an alternative method of energy transfer between solid and gas phases resulting from heterogeneous reactions. The reactions occur at the surface of the solid phase temperature, $\langle T\rangle^s$, yet the released gases abruptly equilibrate their temperature with the gas phase, $\langle T\rangle^f$. Consequently, the enthalpy:

$$S_{heating} = (1-\epsilon)\left(\langle T\rangle^f - \langle T\rangle^s\right)\sum_i C^f_{p,i}\mathrm{R}_i \ , \tag{5.16}$$

is transferred between the solid and gas phases.

5.1.3 Heat transfer

In section 3.4.3 of Chapter 3, different heat transfer submodels were discussed thoroughly. In the current CFD model, two separate convective and radiative heat transfer models, between the gas and solid phases, are introduced. According to the spatial averaging procedure of the energy equation, the convective heat transfer between the gas and solid matrix is evaluated as:

$$\langle q_{conv}\rangle = C_{conv}\mathrm{SA}\left(\langle T\rangle^f - \langle T\rangle^s\right) \ , \tag{5.17}$$

where C_{conv} represents the convective heat transfer coefficient. The value for C_{conv} is taken to be a constant equal to 8 [134]. In addition to heat transfer by convection, heat is also exchanged through radiation. The primary radiation model is a participating media approach based on the radiative transfer equation (RTE) [113] in the form of the incident radiation, G. The RTE governs radiation propagation in participating media, accounting for the overall balance of radiative energy transport by considering the effects of absorption, scattering, and emission processes that cause attenuation and augmentation of the radiative energy in the medium [135]. In porous materials, the RTE involves two components: the gas phase, represented

as "gray gas," and the solid phase, represented as "gray body." This setup enables a mutual interaction between the energy conservation equations for both phases and the RTE. The solver provides an option to incorporate a radiation model based on the RTE, simplified using the P-1 approximation. This method is the the first order spherical harmonics approximation of the RTE and it eliminates the wavelength dependency, resulting in a diffusion conservation equation of G, expressed as follows:

$$\nabla \cdot (\Gamma \nabla G) + 4\pi \left(a \frac{\sigma T_{gas}^4}{\pi} + a_s \frac{\sigma T_s^4}{\pi} \right) - (a + a_s) G = 0 \, , \tag{5.18}$$

where a is the gas mixture absorption coefficient, a_s is the equivalent absorption coefficient in the solid, and Γ is the radiation flux. $\sigma = 5.67 \times 10^{-8}$ W/m^{2}K^4, is the Stefan-Boltzmann coefficient, taking into account the source of radiative energy due to the gas and solid phases emitting radiation according to the Stefan-Boltzmann law. In Eq. (5.18), the first term represents the spatial diffusion of radiative energy in the medium, where radiation flows from high to low intensity regions. The second term represents how much radiation is being generated locally by hot gas and solids. The last term is a sink term and describes how much of the incident radiation is absorbed by the medium. Eq. (5.18) is simplified by using the P-1 approximation. The following relation is obtained for Γ:

$$\Gamma = \frac{1}{(3(a + a_s + \sigma_{scatter}) + C\sigma_{scatter})} \, , \tag{5.19}$$

where $\sigma_{scatter}$ is the scattering coefficient and C is the coefficient associated with forward/backward scattering. Γ is calculated locally in each control volume. This approach is simple since it is only necessary to find a solution for G rather than determine the direction dependent intensity. As such, the simplified equation describes how the incident radiation diffuses through the medium, with source terms representing thermal emission from gas and solid phases. As a result, the source term $S^{f,radiation}$ for the gas phase energy equation is:

$$S^{f,radiation} = -4\pi \left(a \frac{\sigma T_{gas}^4}{\pi} \right) + aG \, , \tag{5.20}$$

and the source term $S^{s,radiation}$ for the solid phase is:

$$S^{s,radiation} = -4\pi \left(a_s \frac{\sigma T_s^4}{\pi} \right) + a_s G \, . \tag{5.21}$$

Table 5.1 presents a list of values which are taken to solve the radiation model in the Thermo-CFD model.

Table 5.1: Values used in the Thermo-CFD model needed to solve the radiation model.

a (m^{-1})	0.5 [7]
a_s (m^{-1})	10 [7]
G (W. m^{-2})	18 [7]
$\sigma_{scatter}$	1 [7]
C	1 [7]

5.1.4 Flow regime

The flow regime, characterised as either laminar, transitional, or turbulent, is a fundamental aspect of fluid mechanics, particularly in thermochemical processes like biomass gasification. In biomass gasifiers, the flow regime depends on several factors, including the gasifier's design, operating conditions, and the physical properties of the gases involved.

The flow regime in porous media modelling has been sporadically addressed in the literature, with limited information available on the wide range of applications. The understanding of flow regime within porous media is still in its early stages. A key challenge lies in characterising the flow in macroscopic porous media, which is the focus of the proposed CFD model. This issue has been raised and discussed by several authors [136–140].

In order to determine the flow regime in the Thermo-CFD model and before running the simulations, theoretical calculations of the Re are estimated at different characteristic length scales across the geometry: at the inlet pipe, the gasifier throat,

and the pore. The Re is given by:

$$Re = \frac{\rho u d}{\mu} \, , \tag{5.22}$$

where d is the characteristic length scale (m), typically represented by the diameter of the length scale in question. The Re is calculated at the maximum examined velocity for the case of the inlet pipe diameter and the maximum average fluid velocity for the remaining characteristic length scales. For example, if the calculation proceeds at the pore characteristic length scale, then the parameters used to calculate the Re are taken at that specific region. To calculate the theoretical values of the velocities used at the gasifier throat and the pore, u^f, the following mass balance is used:

$$u_{air} \times \rho_{air} \times d_{in} = u^f \times \rho^f \times d_{eff} \, , \tag{5.23}$$

where d_{in} is the inlet pipe diameter and d_{eff} is the effective flow diameter at the examined region. For the gasifier throat region, d_{eff} is taken as the average length between the oxidation zone throat and the gasifier outlet, d_{avg}, equal to 0.143 m. For the pore length scale, d_{eff} is calculated using the following:

$$d_{eff} = d_{avg} \times \sqrt{\epsilon} \, . \tag{5.24}$$

By assuming the dry producer gas consists of 40% N_2, 20% H_2 and CO each, 15% CO2, and 5% CH4, ρ^f is calculated using the ideal gas law, following the same ratio of producer gas:

$$\rho^f = \frac{P \times M}{R \times T} \, . \tag{5.25}$$

Finally, the average μ is taken to be equal to 2.55 $\times$ 10^{-5} kg/m.s by assuming the same producer gas ratio.

Several factors influence the Re in a biomass gasifier, including air inlet velocity, gasifier dimensions, temperature distribution, and the porous properties of biomass. The characteristic velocity is determined by the air supply rate at the inlet—higher

inlet velocities lead to an increase in Re, making turbulence more likely. The gasifier dimensions directly impact the characteristic length scale of each region. For example, when analysing the flow regime at the air inlet, the characteristic length is defined as the inlet nozzle diameter. In contrast, for the throat and outlet regions, it is typically taken as the average of the throat diameter and the gasifier outlet diameter. Additionally, temperature distribution across the gasifier affects gas properties. According to the ideal gas law, gas density decreases with increasing temperature, while Sutherland's law dictates that dynamic viscosity increases. Both effects contribute to a reduction in Re at higher temperatures. Lastly, ϵ and pore size distribution significantly impact flow characteristics in the porous media region. Here, the characteristic length is represented by the effective flow diameter, which depends on ϵ. As ϵ decreases, the effective velocity within the pores increases, leading to a higher Re, and vice versa.

Table 5.2: Calculated Re at the highest examined velocity in the Thermo-CFD model and the critical Re for each region.

Region	u (m/s)	ρ (kg/m^3)	d (m)	μ (kg/m.s)	Re	Re_{crit}
Inlet pipe	1	0.599	0.016	3.017×10^{-5}	317.67	2000 [141]
Gasifier throat	0.1343	0.499	0.143	2.55×10^{-5}	376.05	2000 [141]
Porous media	0.2649	0.499	0.0064	2.55×10^{-5}	33.19	375 [142]

In Table 5.2, Re_{max} represents the Reynolds number based on the maximum fluid velocity used in the Thermo-CFD model, while Re_{crit} is the critical Reynolds number marking the onset of laminar flow transition. Calculations confirm that, at the various velocities examined in the Thermo-CFD model in different characteristic length regions, the flow is strictly laminar. According to [142], the transitional regime of the flow in porous media occurs for $375 < Re < 750$, with Re numbers greater than 750 indicating turbulent flow.

5.1.5 Materials properties

The conservation equations for the gas and solid phases Eq.(5.1) - Eq.(5.8) are accompanied by the appropriate definition of the material properties of the gas and

solid. First, ϵ of the biomass is defined. Together with ϵ, the distribution of the viscous resistance tensor D_c is required, which can be used to introduce anisotropy to the material. An additional required parameter is the density, ρ_k^s, and mass, m_k^s, of the solid matrix, which is the material that constitutes the space unoccupied with gas inside the porous media. It is calculated as the weighted average of the densities of the solid components:

$$\rho_k^s = \frac{\mathrm{m}_k^s}{V_k^s} = \left(\sum_k \frac{\langle Y_k \rangle^s}{\rho_k^s} \right)^{-1} . \tag{5.26}$$

5.1.6 Porosity

The increase in ϵ from its initial value demonstrates the conversion of one species to another or the release of matter into the gas phase. This is a result of unequal solid species densities and as the matter is transferred to the gas phase. This change is modelled via the volume conservation equation:

$$\frac{d}{dt}\epsilon = -(1-\epsilon) \sum_{k=1}^{N} \frac{1}{\rho_k^s} \mathrm{R}_k \ , \tag{5.27}$$

which states that the volume occupied by the gas phase changes with the mass change of solid species k divided by its density ρ_k^s [7].

5.1.7 Pyrolysis submodel

The most efficient method of establishing the coefficients of the char, tar and volatiles in the pyrolysis stage of the gasification process is to carry out experimental investigations on a range of biomass feedstock, since different feedstocks will yield a different decomposition. This is both a time consuming and expensive endeavour. As such, a pyrolysis model is encapsulated within the current CFD model in order to appropriately predict the coefficient distribution between the pyrolysis components. The model is based on Sharma's approach in predicting the product composition in the slow pyrolysis of wood [143]. In this approach, the thermal decomposition of biomass is described on the basis of decomposition of its three main constituents,

viz., cellulose, hemicellulose and lignin.

A complete elemental balance coupled with empirical correlations established from data in the literature on the relationship between CO/CO_2, H_2O/ CO_2, and CH_4/CO_2 ratios is implemented for the determination of the product composition as a function of pyrolysis temperature, T_{pyro}. Following from the assumption that char is pure C, the process of pyrolytic decomposition can be represented as:

$$CH_\alpha O_\beta \rightarrow n_1 C + n_2 CO + n_3 CO_2 + n_4 H_2 + n_5 H_2O + n_6 CH_4 + n_7 \text{tar} \ . \quad \text{(R23)}$$

In the above, $CH_\alpha O_\beta$ is the chemical formula of the dry and ash-free biomass and n represents the number of moles of a given species involved in the process. The chemical formula of any biomass species can be obtained from its ultimate analysis. The justification behind the chemical composition of the biomass feedstock in (R23), including the omission of the N_2 species in the pyrolysis model proposed by [143] is due to the fact that it is assumed N_2 is found in negligible amounts in the feedstock and does not contribute significantly to the feedstock's thermal decomposition.

Zaror and Pyle [144] reported that the char yield, n_1, from biomass pyrolysis is relatively insensitive to heating rate and temperature, therefore, the char residue from biomass decomposition, namely the char mass fraction in the biomass, Y_{char}, can be obtained from the mass fractions of cellulose, Y_{cl}, hemicellulose, Y_{hc}, and lignin, Y_{lg}, of the feedstock as follows:

$$Y_{char} = Y_{cl} f_{char,cl} + Y_{hc} f_{char,hc} + Y_{lg} f_{char,lg} \ , \quad (5.28)$$

where $f_{char,cl}$, $f_{char,hc}$, and $f_{char,lg}$ are the fractions of char found in cellulose, hemicellulose, and lignin, respectively. The values for these are $f_{char,cl} = 0.05$, $f_{char,hc} = 0.10$, and $f_{char,lg} = 0.55$ according to Tillman et al. [145]. Y_{char} is therefore the equivalent of n_1, but in mass basis. As rubberwood is a type of hardwood, and as such, the values of hardwood are considered. This enables the fraction of the remaining volatiles from dry and ash-free biomass, Y_{vol}, to be found from:

$$Y_{vol} = 1 - Y_{char} \ . \quad (5.29)$$

The proportion of cellulose, hemicellulose and lignin for a range of biomass types are provided in Table 5.3.

Table 5.3: Proportion of cellulose, hemicellulose, and lignin in different types of wood (dry basis) [146].

Type of Wood	Y_{cl}	Y_{hc}	Y_{lg}	**Ash + Extractives**
hardwood	0.452	0.313	0.217	0.027
softwood	0.458	0.244	0.28	0.017
woodbark	0.248	0.298	0.438	0.016
rice husk	0.313	0.243	0.143	0.319

As n_1 is computed from the constituent proportions of the biomass by solving (5.28) , the remaining 6 components, n_2 to n_7 require 6 equations. Performing an elemental balance on (R23) yields the following:

$$\mathrm{C}: \; n_1 + n_2 + n_3 + n_6 + 6n_7 = 1 \; , \tag{5.30}$$

$$\mathrm{H}: \; 2n_4 + 2n_5 + 4n_6 + 6.2n_7 = \alpha \; , \tag{5.31}$$

$$\mathrm{O}: \; n_2 + 2n_3 + n_5 + 0.2n_7 = \beta \; , \tag{5.32}$$

whereby an additional 3 equations are required to close the system. As such, the mass ratios in the biomass feedstock $\frac{Y_{\mathrm{CO}}}{Y_{\mathrm{CO_2}}}$, $\frac{Y_{\mathrm{H_2O}}}{Y_{\mathrm{CO_2}}}$, and $\frac{Y_{\mathrm{CH_4}}}{Y_{\mathrm{CO_2}}}$ were taken as a function of T_{pyro} as in Sharma [143], and the remaining 3 equations are:

$$\frac{Y_{\mathrm{CO}}}{Y_{\mathrm{CO_2}}} = exp\left(-1.845 + \frac{7730.3}{T_{pyro}} - \frac{5019898}{T_{pyro}^2}\right) \; , \tag{5.33}$$

$$\frac{Y_{\mathrm{H_2O}}}{Y_{\mathrm{CO_2}}} = 1 \; , \tag{5.34}$$

$$\frac{Y_{\mathrm{CH_4}}}{Y_{\mathrm{CO_2}}} = 5 \times 10^{-16} T_{pyro}^{5.06} \; . \tag{5.35}$$

T_{pyro} is chosen to be 873 K in the Thermo-CFD model based on the value of Salem and Paul [34]. The above 6 equations (3 elemental balances and 3 empirical correlations) were solved numerically using Matlab's "fsolve" function following the same numerical procedure described in Chapter 4. This method represents a rigorous approach in the determination of the distributed coefficients of the pyrolytic

products, including tar and char as it offers a method for selecting a wide range of biomass feedstock, each of which will demonstrate a different decomposition distribution. As such, it is possible to characterise a pyrolysis process for a range of feedstocks without resorting to experimental investigations. This demonstrates the models capability to analyse different feedstock. The pyrolytic product coefficients, with the exception of char, are initially determined in moles. Subsequently, they are transformed into mass fractions using the molar masses of the substances to align with the functionality of the solver. While rubberwood serves as the primary feedstock in this model, alternative feedstocks can be incorporated by adjusting the thermophysical properties of the solid matrix. By employing the thermochemical pyrolysis sub-model, one can establish the pyrolytic product distribution specific to the examined species for a given feedstock, enabling the flexibility to explore different materials in the simulation. Rubberwood's stoichiometric devolatilisation is expressed as:

$$\mathrm{CH_{1.5417}O_{0.6225}} \rightarrow 0.0144\mathrm{C} + 0.1731\mathrm{CO} + 0.1781\mathrm{CO_2} + 0.3336\mathrm{H_2} + 0.0729\mathrm{H_2O} + 0.0247\mathrm{CH_4} + 0.1016\mathrm{tar}\ . \quad \text{(R24)}$$

5.1.8 Chemical reaction scheme

The comprehensive heterogeneous chemical reaction scheme includes a drying reaction, a pyrolysis reaction whereby the feedstock is decomposed into char, tar and volatiles through a comprehensive pyrolysis model that determines the distributed coefficients of the pyrolytic products, the boudouard reaction (R3), the water-gas reaction (R4), the hydrogasification reaction (R5), and the char oxidation reactions (R6) and (R7) - see section 3.3.3 of Chapter 3. Table 5.4 lists the kinetic parameters used for the calculation of the reaction rates in the model.

The heat of reaction of the drying reaction was obtained from [148]. As the **porousGasificationFoam** solver characterises the heat of reaction in J/kg of substrates, the heats of reactions for the remainder have to be converted from J/mol to

Table 5.4: Heterogeneous chemical reaction scheme used in the CFD model.

Heterogeneous Reactions	**Pre-exponential Factor (1/s)**	**Activation Temperature (K)**	**Cut-off Temperature (K)**	**Reaction Enthalpy (J/kg)**
(R1) [147]	5.13×10^6	1.06×10^4	300	2.26×10^6
(R24) [60]	1.38×10^{10}	1.90×10^4	300	3.85×10^5
(R6) [112]	5.61×10^9	1.96×10^4	300	-3.95×10^6
(R7) [112]	5.61×10^9	1.96×10^4	300	-8.94×10^6
(R5) [114]	4.19	2.31×10^3	300	-4.66×10^6
(R3) [114]	3.62×10^4	9.31×10^3	300	3.07×10^6
(R4) [114]	1.52×10^7	1.46×10^4	300	4.38×10^6

J/kg. An example calculation is followed for (R3), which can be written as:

1 mol (12g) C + 1 mol (44g) CO_2 = 2 mol (28g) CO which is equivalent to

12 C + 44 CO_2 = 56 CO which is equivalent to

C + 3.66 CO_2 = 4.66 CO

Normally the heat of the reaction is calculated on a mole basis, however in the **porousGasificationFoam** solver, the heats of reactions are provided on the basis of mass. As such, the value for the heat of reaction in J/mol must be divided by the molar mass of the substrates (kg/mol) in order to determine the heat of reaction in J/kg. In the above, the calculation of the heat of reaction, ΔH_r proceeds from the enthalpies of formation as:

$$\Delta H_r = [2(-110525)] - [(-393509) + (0)] = 172459 \text{ J/mol} ,$$
$$\Delta H_r = \frac{172459 \text{ J/mol}}{0.056 \text{ kg/mol}} = 3.07 \times 10^6 \text{ J/kg} .$$

This calculation is repeated for all the remaining heterogeneous reactions in order to determine the heat of the reaction in J/kg. The homogeneous chemical reaction scheme is comprehensive, including reactions (R8), (R9), (R10), (R11), (R15), (R16)

- see section 3.3.3 of Chapter 3, and an additional tar cracking reaction (R25):

$$\text{tar} + 3O_2 \rightarrow 6CO + 3H_2 \ , \tag{R25}$$

as indicated in Table 5.5. For the gas phase reactions, only the pre-exponential factor A and the activation temperature T_a are required. The oxidation reactions (R8), (R9) and (R10) occur in the oxidation zone of the gasifier, while the shift reaction (R11) is the most important chemical reaction involved in gasification occurring in the reduction zone. The steam reforming reactions (R15) and (R16) are crucial reactions in the production of H_2, and finally a tar cracking reaction (R25) is implemented in order to reduce the amount of tar produced from the pyrolysis stage.

Table 5.5: Homogeneous chemical reaction scheme used in the CFD model.

Homogeneous Reactions	**Pre-exponential Factor (1/s)**	**Activation Temperature (K)**
(R8) [149]	$1.00\times\ 10^{10}$	15155.16
(R9) [149]	$4.40\times\ 10^{11}$	15155.16
(R10) [149]	$2.20\times\ 10^{9}$	13110.42
(R11) [150]	$2.778\times\ 10^{2}$	1510.705
(R15) [150]	$4.99\times\ 10^{13}$	24368.53
(R16) [149]	$3.00\times\ 10^{8}$	15034.88
(R25) [150]	$1.58\times\ 10^{15}$	24368.53

The above gas and solid phase chemical reaction scheme was constructed based on the complex, but essential processes occurring in a realistic gasifier. The proposed chemical reaction scheme enables the prediction of the producer gas composition for the respective gaseous species and solid species crucial in the gasification process.

5.1.9 Model geometry and mesh

The geometry of the CFD model is based on the shape and dimensions of that used by Kumar and Paul [41] in their investigations as shown schematically in Fig. 5.1

As can be seen, the gasifier converges in the oxidation zone and diverges in the reduction zone in order to enhance the gasification process and control the reactions taking place in the gasifier. This configuration is chosen in order to achieve efficient conversion of biomass into syngas with minimal tar and char content. The constriction in the oxidation zone promotes heat generation and helps ensure thorough mixing and efficient combustion, necessary for the breaking down of complex biomass compounds in a high temperature environment.

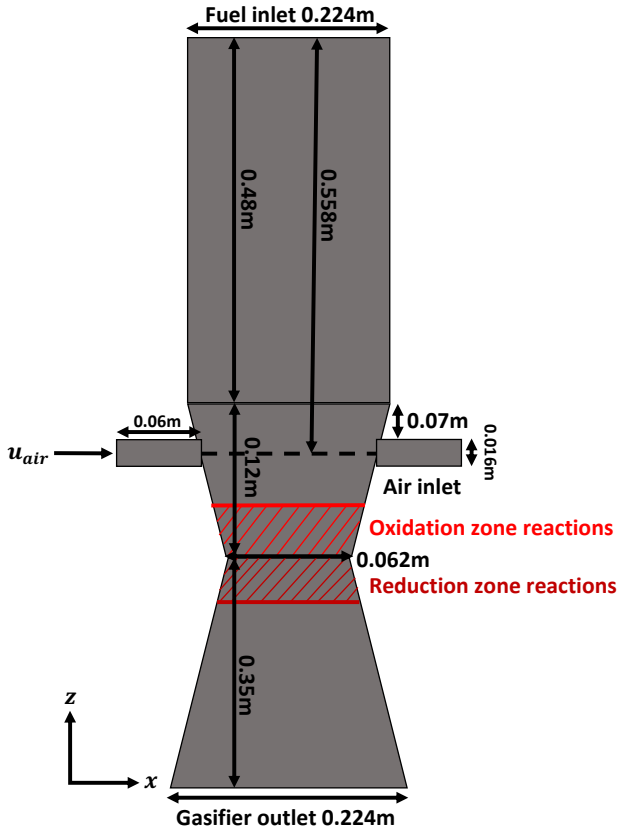

Figure 5.1: Schematic of the 2D downdraft biomass gasifier.

In the reduction zone, the primary objective is to minimise oxygen and create conditions conducive to producing syngas rather than continuing combustion. Therefore, expanding the flow of hot gases from the descending biomass aids in preventing excess oxygen exposure, which could lead to more complete combustion and the generation of unwanted by-products like CO_2. Other than that, the expansion of the configuration aids in minimising the tar content, allowing high temperature gases to break down tars into simpler gases. This occurs because the expansion results in a lower flow velocity, giving the hot gases more time to stay in contact

with hot char and undergo cracking and reforming.

The gasification agent is injected through the air nozzles from the side and the porous media assumption allows for the entirety of the gasifier to be filled with biomass feedstock except for gaseous regions, namely, the air nozzles and the reduction zone.

As for the computational meshing of the unit, this is shown in Fig. 5.2 as being fine and equally distributed in both coordinated directions. A key feature of the solver is its adaptability for use with skew-like geometries as present in the oxidation zone, where it is firstly reduced at the throat, before expanding again synonymous with throated DBGs. The purpose of this is to allow the oxidation zone to be at the narrowest part of the throat to force all the pyrolytic gases to pass through this narrow pathway [2].

As the model forms a 2D symmetrical geometry, splitting the model down the axis line and applying the symmetry plane boundary condition saves computational resource enabling very fine mesh results to be generated that would be a significant challenge for the full problem and the same fine mesh. The flow domain and typical mesh used in the current model is show in Fig. 5.2.

Experimental configurations of DBGs differ in dimensions, shapes and sizes. Some configurations are throatless (stratified) whereas others are throated (Imbert), reduced at the throat and then expanded to promote the conversion of biomass into gases. With commercial DBGs, there are small-scale, medium-scale and large-scale configurations depending on the design and intended use of the unit. Most commercial applications using DBGs are either small or medium scale. Table 5.6 offers the general dimensions of some of the experimental gasifiers investigated. The data in Table 5.6 reveals a consistent pattern among medium-scale DBGs in commercial designs, where the height and throat diameter exhibit close similarities.

5.1.10 Motion of the bed

Fig. 5.3 illustrates the essential aspects of the porous media motion model. At the outset of the simulation, the porous media is initially delineated across the

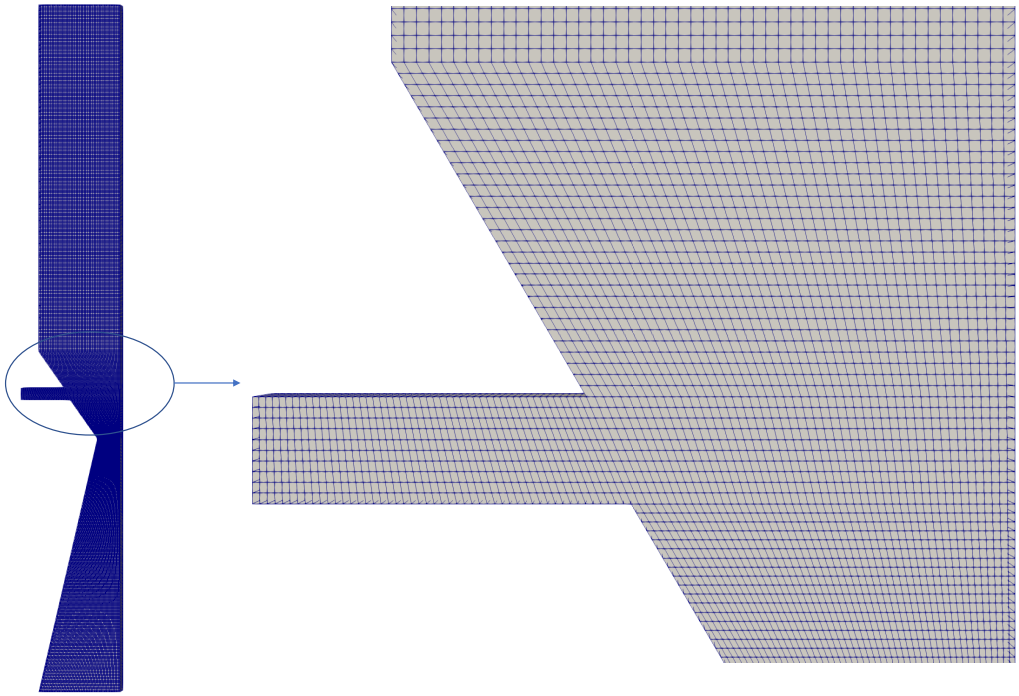

Figure 5.2: Computational mesh spanning the entire gasifier (left), together with a magnified section highlighting the oxidation zone. Note that only half of the full solution domain shown in Fig. 5.1 is shown since the flow can be considered symmetric about the vertical centre line.

Table 5.6: Downdraft gasifier configuration dimensions for a range of experimental investigations.

Experimental gasifier	**Height of gasifier (m)**	**Throat diameter (m)**
Jayah et al. [55] (Imbert)	1.15	0.1
Babu and Sheth [59] (Imbert)	1.1	0.15
Guo et al. [71] (Imbert)	1.05	-
Gai and Dong [67] (stratified)	0.85	0.3
Striugas et al. [70] (Imbert)	1.03	0.13
Dogru et al. [53] (imbert)	0.81	0.135
Galindo et al. [72] (stratified)	1.06	0.3
Ma et al. [151] (stratified)	1.8	0.35

geometric unit within user-defined regions, depicted in black in Fig. 5.3. As the simulation progresses and chemical reactions commence with air inflow through the unit, ongoing depletion of material occurs, indicated by gray shading. Consequently,

ϵ increases as material is consumed. Upon reaching a specified ϵ threshold (i.e., ϵ = 0.99), denoting the conversion of biomass to gas, activation of the porous media motion model is triggered, as shown in red. Execution of the porous media motion model (depicted on the right side of the figure) enables the removal of depleted material, displacing it, and replenishing it with fresh biomass at the gasifier's top. This process is automatically executed as biomass undergoes consumption. Fig.**??** illustrates a flowchart explaining the porous media motion algorithm from the starting position to the replenishment position in a cyclic process [114].

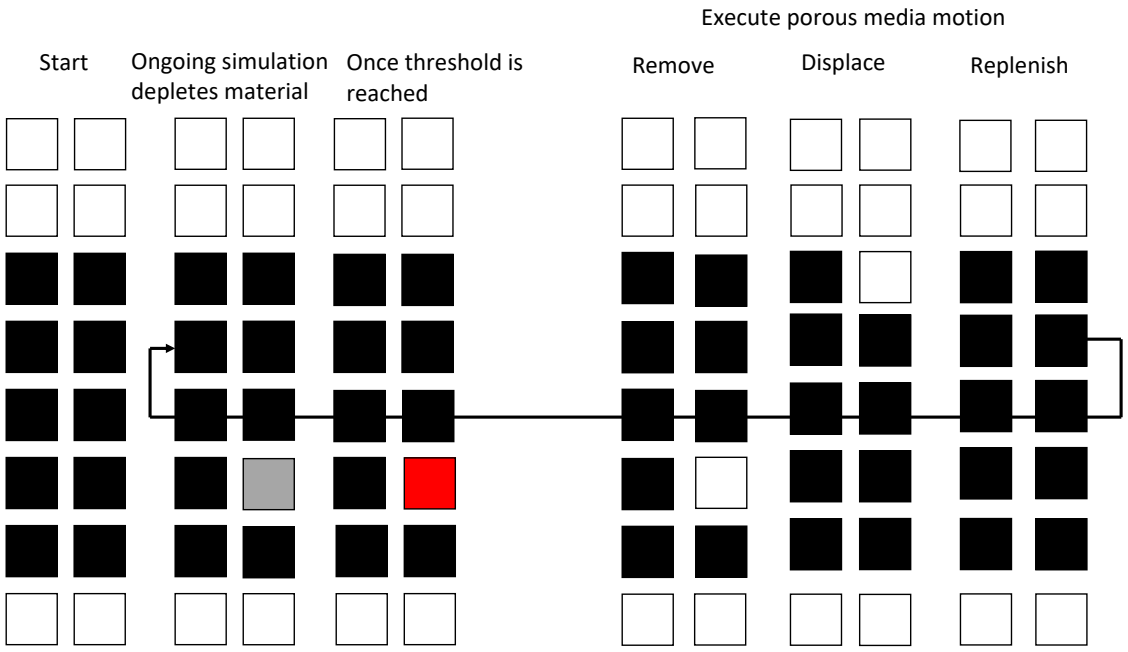

Figure 5.3: Visualisation of the porous media motion model, showing initial and progressive simulation stages. White computational cells represent the gas phase, while black cells represent the porous medium. The three sets of cells on the left illustrate the starting and intermediate positions during the simulation, while those on the right depict the execution phase of the porous media motion model.

5.1.11 Initial and boundary conditions

The initial and boundary conditions employed in generating results using the Thermo-CFD model are listed below:

- Feedstock: Rubberwood is selected as the initial biomass feedstock. The initial MC of rubberwood is taken to be 18.5% as in Jayah et al. [55] and Kumar and Paul [41]. The remaining dry rubberwood, possessing an MC of 5%, is

loaded across the pyrolysis and oxidation zones. This is shown explicitly in both Figs. 5.4 and 5.5.

- Pressure: The gasifier outlet enforces a pressure outlet boundary condition, maintaining atmospheric pressure at the outlet of the gasifier, while the walls apply a zero gradient boundary condition for the pressure field.

- Air velocity (u_{air}): The u_{air} entering through the side inlets is adjusted to regulate the ER. The values of u_{air} explored using the Thermo-CFD model include 0.2 m/s, 0.3 m/s, 0.4 m/s, 0.5 m/s, 0.6 m/s, 0.8 m/s, and 1 m/s. u_{air} is interconnected, but not entirely dependant on the biomass consumption rate. At the walls, the velocity adheres to the no-slip boundary condition, while the outlet satisfies a zero-gradient boundary condition.

- Gas phase temperature: The initial temperature of air injected through the nozzles is 600 K. However, it is established that an air temperature of 600 K proves insufficient for achieving an optimal conversion of biomass into syn-gas. Consequently, the air temperature is raised to 1000 K to enhance the conversion efficiency.

- Solid phase temperature: The temperature of the biomass feedstock is given a value of 400 K throughout the gasifier, increasing to around 600 K at the oxidation zone and 1200 K at the char bed to facilitate chemical reactions in the form of an ignition strip (0.04 m in height). The initial distribution of the solid phase temperature is shown in Fig. 5.6

- Thermophysical properties: The thermophysical properties of the solid species including rubberwood and char were taken from Park et al. [60]. This includes $C_{p,bm}$ = 2000 J/kg K, $k_{eff,bm}$ = 0.23 W/mK, $h^{\circ}_{f,bm}$ = -109870 J/mol, and ρ_{bm} = 1050 kg/m^3.

- ϵ: The initial ϵ of the rubberwood feedstock was assumed to be equivalent to that of biomass char (i.e. $\epsilon = 0.4$) [2], but subject to change depending on the amount of moisture in the biomass, explaining the different ϵ values in

Fig. 5.7. A sample calculation of how these values are obtained is given in Appendix C.

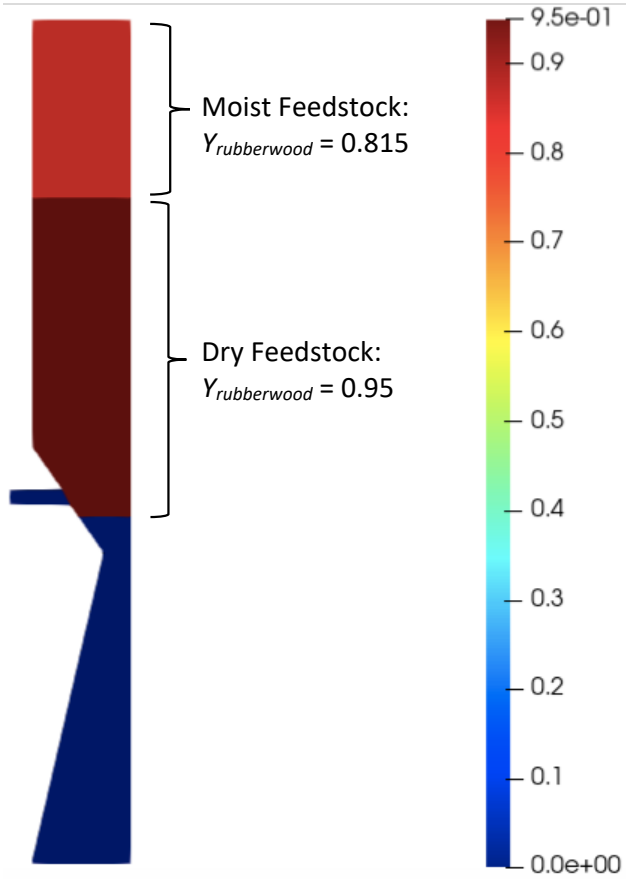

Figure 5.4: Initial rubberwood mass fraction spanning the computational domain.

The initial ϵ field throughout the gasifier is shown in Fig. 5.7. Notably, the reduction zone of the gasifier intentionally lacks any biomass to prevent machine clogging and to enhance the conversion of biomass into gases, a practice commonly employed to enhance gasification efficiency. In practice, biomass is exclusively present in the drying, pyrolysis, and oxidation zones. The two air inlets are also devoid of biomass, whereby $\epsilon = 1$ indicating gas phase only. The char produced from the pyrolysis zone creates a char bed in the reduction zone to be further reacted as part of char gasification reactions. This explains the presence of only char below the oxidation zone whereby $\epsilon = 0.88$. This value can be obtained from the distribution of rubberwood into char from reaction (R24).

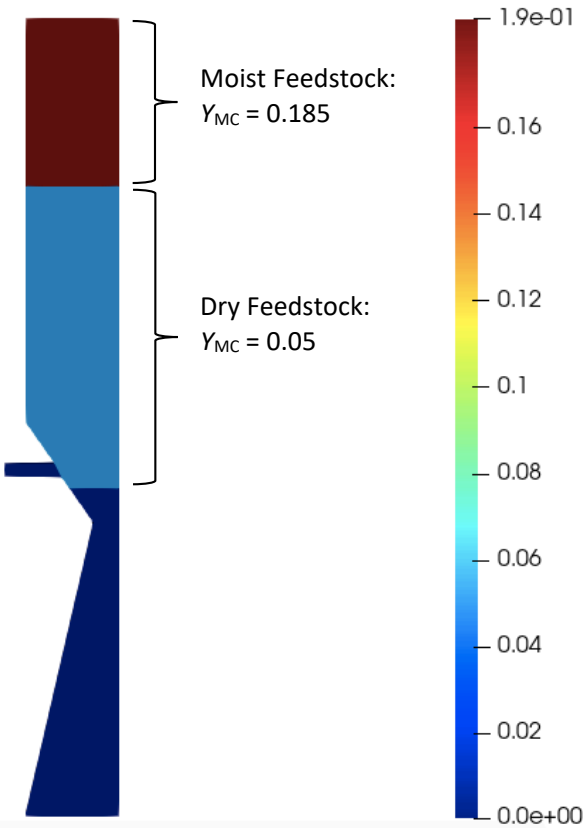

Figure 5.5: Initial humidity mass fraction spanning the computational domain.

The distribution of rubberwood and MC across the gasifier as indicated in Figs. 5.4 and 5.5 is used to scrutinise the impact of MC on the gasification process using these two distinct values. As the bed undergoes ignition and chemical reactions unfold, the dry feedstock is initially consumed, eventually reaching a juncture in which either all of it or most of it is exhausted, contingent upon the efficacy of the chemical reactions under specific operating conditions, such as u_{air} as will be seen in section 5.2.5. Subsequently, the replenishment feature of the model comes into play, introducing fresh feedstock and culminating in the consumption of wet feedstock.

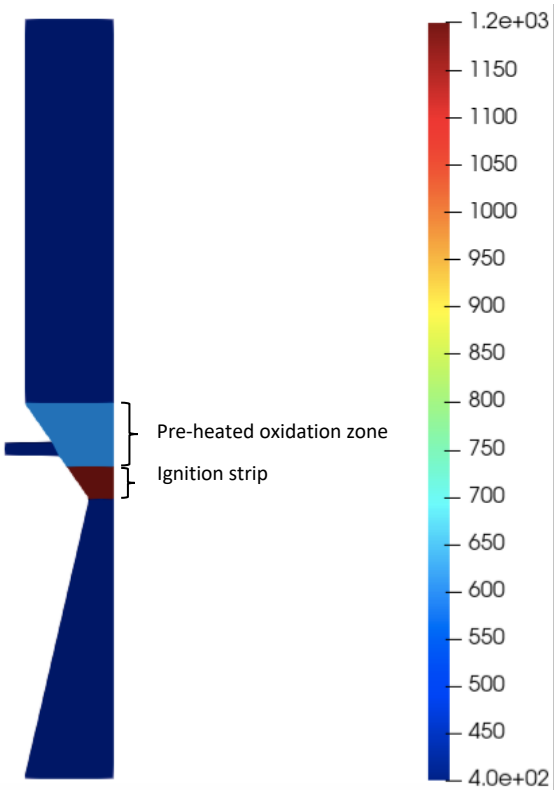

Figure 5.6: Initial solid phase temperature distribution spanning the computational domain.

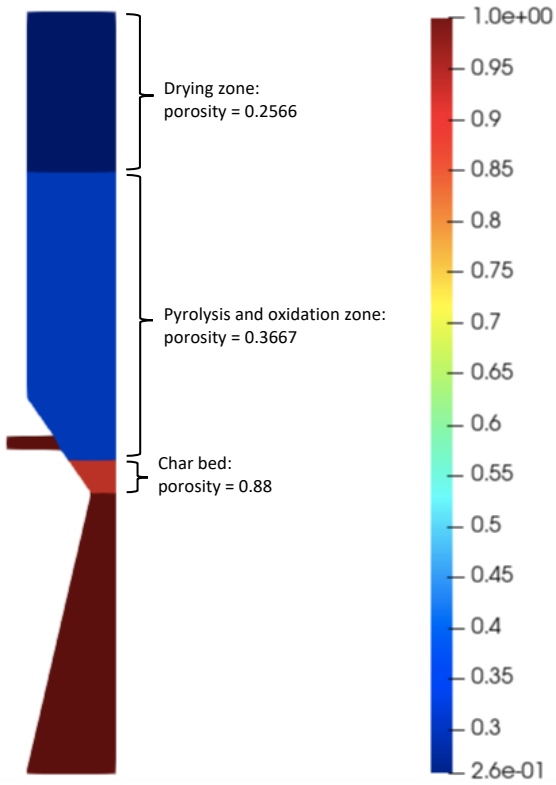

Figure 5.7: Initial ϵ field distribution spanning the computational domain.

The ultimate and proximate analysis of the feedstock was obtained from Table 3.1.

5.1.12 Running a typical simulation

The simulations conducted to generate the results are performed on "Hamilton", a centrally managed supercomputer recognised as an HPC service (High Performance Computing), accessible for researchers at Durham University. The initial time-step used is typically small enough (around $1e^{-7}$ seconds) due to the complexity of the chemical reaction scheme. This means that some of the chemical reactions involved are fast and others are slow. Large enough time steps can skip over fast reactions, leading to divergence and numerical inaccuracies. Furthermore, at the start of the simulation, the system experiences rapid changes in temperature, pressure, and species concentration as the system adjusts to the initial conditions. A small enough time step ensures numerical stability by preventing excessive fluctuations that could cause divergence. The choice was made to adopt an adjustable time step control instead of fixed one, but limiting the adjustability to a maximum allowed time step beyond which the simulation does not exceed 0.0005 seconds. The rationale behind incorporating this approach is to accelerate simulations in areas where the solution exhibits smooth and gradual changes, while simultaneously imposing constraints to preserve numerical stability.

Within the solver, two additional switches, stemming from the resolution of chemical reactions, can be specified in the *chemistryProperties* dictionary. These switches facilitate the reduction of the time step through mass balance equation solvers, catering to both homogeneous and heterogeneous chemical reactions. The computational time for a simulation to reach steady state from an initial condition close to steady state of the chosen mesh size is approximately 72 hours, but can vary depending on the operating conditions specified.

Numerical stability is physically justified based on the Courant-Friedrichs-Lewy (CFL) condition, in which the dimensionless Courant number is calculated from the chosen time step, characteristic velocity, and the spatial grid size, and is given by:

$$\text{CFL} = \frac{u\Delta t}{\Delta x} \,, \tag{5.36}$$

where Δt is the representative time step and Δx is the characteristic size of the mesh cell. The CFL condition for stability in explicit schemes typically requires that the maximum Courant number for transient multiphase simulations be less than or equal to 1. The calculated Courant number for the maximum air velocity used in the Thermo-CFD model (i.e. $u_{air} = 1\text{m/s}$), taking into account the chosen time step is 0.2632, given a grid size equal to 0.0019 m. This was obtained for a time step of 0.0005 seconds. As the CFL is less than 1, the simulations is resolved stably within each time step.

It is also required to justify the chosen time step based on the rate of the fastest chemical reaction. Based on this, the rate constant of the fastest chemical reaction is 1.73×10^1 s^{-1} and its characteristic time scale is 0.0578 seconds. In order to ensure chemical stability, the time step should be several orders of magnitude smaller than the characteristic time scale. As such, 0.0005 seconds is justifiably taken as a maximum allowable time step, ensuring a stable process.

5.1.13 Grid independency test

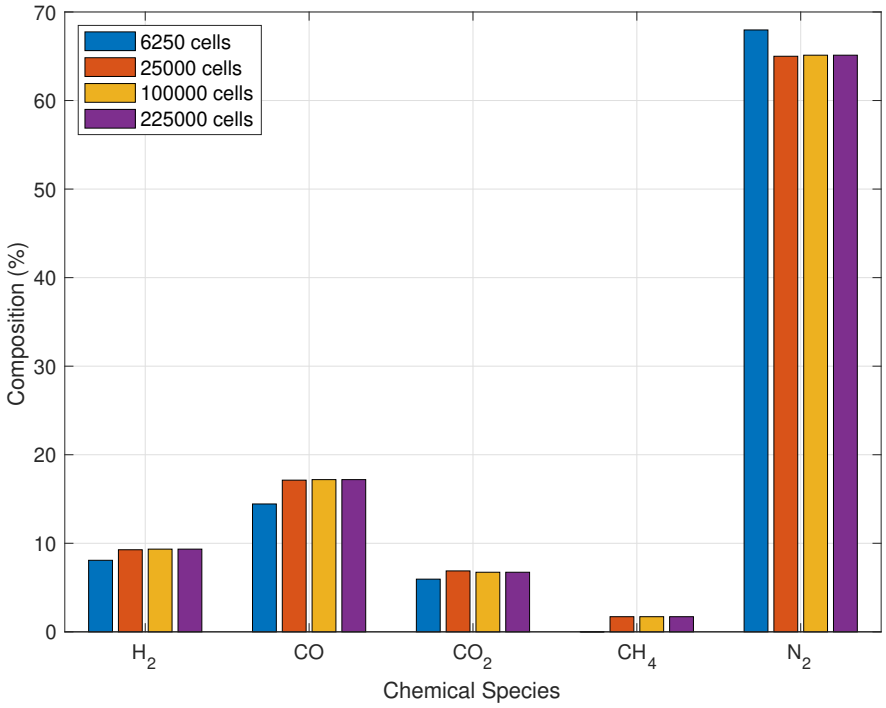

Figure 5.8: Producer gas composition at the gasifier outlet predicted using different mesh cell densities from 6250 to 225,000, for rubberwood.

A grid dependency test was carried out using four different computational grid cells count, 6250, 25,000, 100,000, and 225,000 for the rubberwood feedstock, the results of which are shown in Fig. 5.8. Initially, simulated results were analysed using 6,250 computational cells, followed by a refinements of the mesh to 25,000, 100,000, and finally 225,000 cells respectively. Regarding the outcomes observed at the gasifier's exit, minimal disparities are evident when using the 100,000 or 225,000 cells. As such, the grid containing 100,000 cells was chosen for all the simulated cases presented subsequently.

5.2 Results and Discussion

This section presents findings from the Thermo-CFD model simulations. Initially, a grid independence assessment was conducted to justify the chosen mesh configu-

ration used to generate the results presented in subsequent sections. Final model Predictions are confirmed through comparisons with experimental data and prior modelling outcomes. Lastly, a parametric investigation is performed to scrutinise how various operational factors impact the model's predictions. The mass fractions of the gaseous species are calculated from Eq. 5.1 and converted to molar fraction through the following:

$$X_i^f = \frac{\frac{Y_i^f}{M_i}}{\sum \frac{Y_i^f}{M_i}} \ , \tag{5.37}$$

where X_i^f is the mole fraction of species i and the summation is over all the main gaseous species forming the producer gas (i.e. N_2, CO, CO_2, H_2, and CH_4). In order to time-average the molar fraction, the following calculation is performed [152]:

$$\bar{X}_i^f = \frac{1}{\mathrm{N}} \sum_{t=1}^{\mathrm{N}} X_{t,i}^f \ , \tag{5.38}$$

where $\bar{X}_i^f$ is the time-averaged molar fraction of species i, N is the total number of time steps, and $X_{t,i}^f$ is the molar fraction of species i at time step t. $\bar{X}_i^f$ is further patch integrated over the gasifier outlet surface area in order to establish a consistent representation of the molar composition of the producer gas:

$$X_{i,P} = \frac{1}{A_s} \int_{patch} \bar{X}_i^f dA_s \ , \tag{5.39}$$

where $X_{i,P}$ is the integrated molar fraction over the patch and A_s is the cross-sectional area of the patch. After this is achieved, the molar composition is calculated using:

$$\text{composition}(\%) = \frac{X_{i,P}}{\sum_i X_{i,P}} \times 100\% \ . \tag{5.40}$$

5.2.1 Spacial variation of composition

To assess the model's stability and justify the achievement of a stationary state, the standard deviation of the gaseous species across the outlet is depicted in Fig 5.9 for a $u_{air} = 0.2$m/s. The standard deviation, σ_i, of species i is obtained from the

following [153]:

$$\sigma_i\ (\%) = \sqrt{\frac{(\sum_i^{ts} X_i^f - \bar{X}_i^f)^2}{ts}} \times 100\% \ , \tag{5.41}$$

where ts is the number of time steps. Due to the gasifier design, the producer gas generated at the outlet of the gasifier is non-uniform along the exit of the unit, having a maximum and a minimum value. Additionally, the model's automatic replenishment feature, which introduces fresh feedstock as biomass is consumed, coupled with the movement of the porous media bed and the skewness of the geometrical unit, causes variations in the bed dynamics which is the reason for this phenomenon.

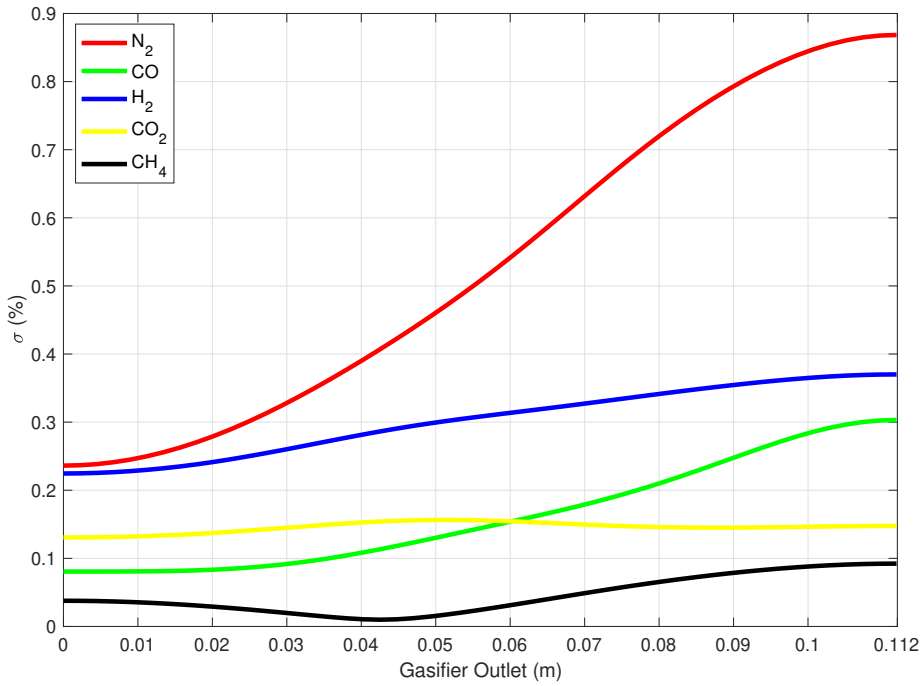

Figure 5.9: Standard deviation of gaseous components along the gasifier exit, with 0 denoting the outer edge of the outlet and 0.112 the gasifier's vertical centre line, for rubberwood.

These variations are influenced by u_{air} introduced through the air inlets. The higher u_{air}, the higher the frequency of variations, and the greater the movement of the porous media front. For a lower u_{air}, less movement is observed in the porous bed, indicating less conversion of biomass. As u_{air} increases, and with the continuous arrival of fresh feedstock to the reacting zone, the biomass feedstock is continuously being consumed and replenished, causing the bed to behave in an oscillatory manner

due to its movement feature. It is apparent that Fig.5.9 is reflective of the results obtained from Fig. 5.10, which demonstrates how the producer gas composition varies with time at the gasifier outlet.

It can be deduced that the major component variation is associated with N_2 whereby it deviates by a maximum of around 0.89%, mirroring the CO composition variance. The remaining components remain relatively constant throughout the observed time period. The transient simulations exhibit a tendency to undergo regular variations, which is again attributed to the movement feature of the porous bed. These variations are described as having a cyclic behaviour, causing the feedstock to continually be consumed and generated.

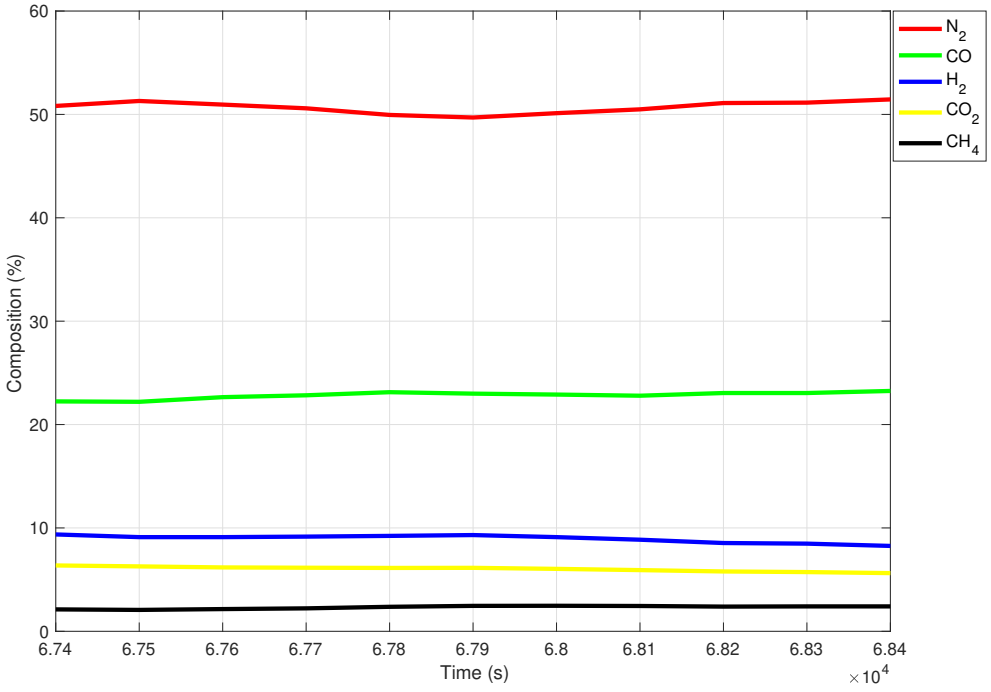

Figure 5.10: Variation of the producer gas composition at the outlet with time, for rubberwood

5.2.2 Model comparison

Initially, the producer gas composition generated from the model is compared with a set of experimental [55] and corresponding model predictions ([41] and [34]) under identical operating conditions of the biomass gasifier. It is important to

distinguish the differences in the fundamentals of the Thermo-CFD model and the model developed by [41]. The Thermo-CFD model accounts for a packed bed reactor filled with porous biomass feedstock, whereas [41] implement the continuous flow assumption in their problem. As such, the predictions obtained from [41] were not used to validate the Thermo-CFD model, but rather as a means of comparison of the end result.

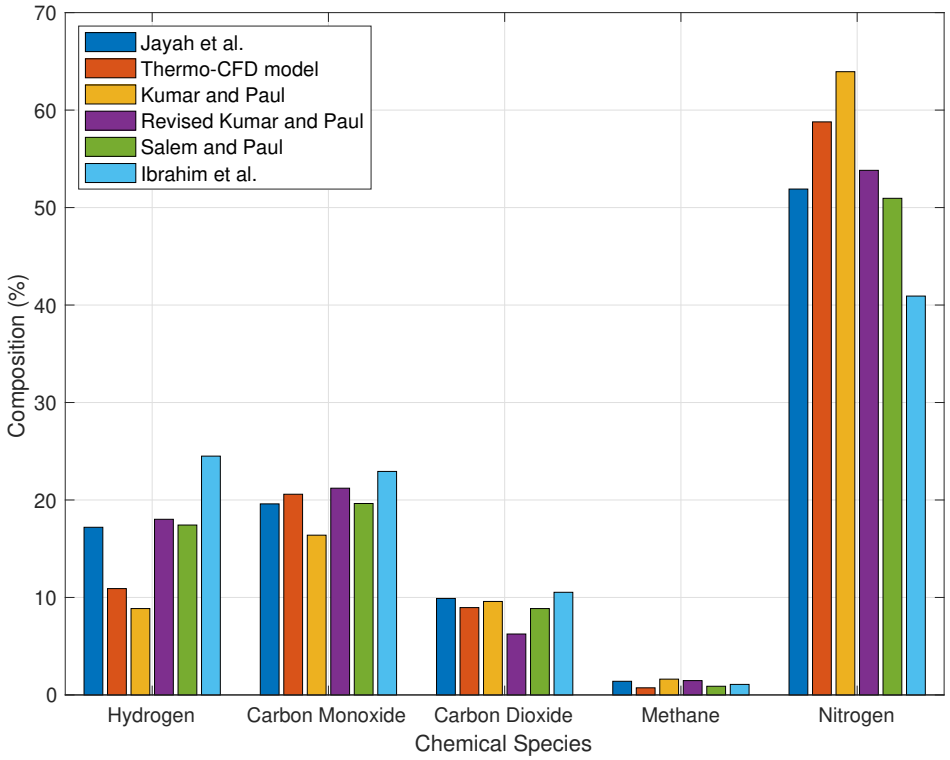

Figure 5.11: Comparison between predicted (Thermo-CFD model, Kumar and Paul [41], Salem and Paul [34], and Ibrahim et al. [119]) and experimentally obtained [55] producer gas composition for rubberwood feedstock.

As per Fig. 5.11, the overall predicted producer gas composition compares relatively well with experimental data and modelling results. It can be observed that the H_2 concentration deviates from the experimental result of [55], demonstrating a lower yield than the comparisons. The remaining components compare well with the predicted concentrations in the producer gas. The variations observed can be attributed to the adoption of different modelling approaches. The Thermo-CFD model utilises the porous media assumption to solve transport equations, while the

model by [41] incorporates the discrete phase model (DPM) using a Lagrangian approach. Both models feature distinct formulations and divergent methods for simulating process dynamics.

A detailed examination of the syngas composition reveals lower production of H_2 from the Thermo-CFD model compared to the kinetic model of Salem and Paul [34] and the equilibrium model of Ibrahim et al. [119]. Differences arises because these models assume an equilibrium approach, whereas the Thermo-CFD model relaxes this assumption. Equilibrium and kinetic models are not limited by transport phenomena such as diffusion and mixing, whereas CFD models simulate detailed fluid flow, heat and mass transfer, and reaction kinetics within the gasification unit. Incomplete mixing, local temperature variations, and reaction zone spatial variation leads to lower H_2 concentrations.

5.2.3 Flow distribution

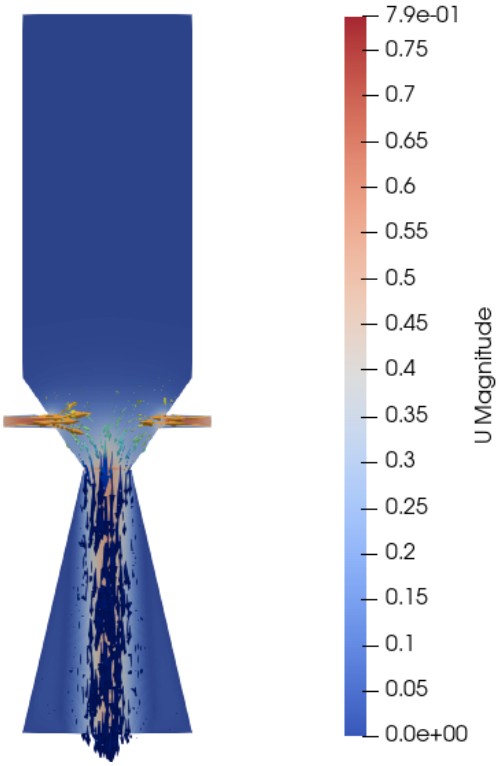

Figure 5.12: Flow distribution inside the biomass gasifier for rubberwood and u_{air} = 0.5 m/s.

Fig. 5.12 shows the velocity distribution within the gasifier. As expected, the velocity is the highest at the air inlet which is the point of injection. As the air moves from the inlet towards the centre of the gasifier, its velocity decreases due to biomass mixing coupled with the resistance imposed by the fuel bed. The velocity drops in the oxidation zone due to the restricted flow through the dense char bed and the presence of hot gases. The subsequent cooling of the air as it passes through the oxidation zone and into the reduction zone results in the velocity increasing as the air is being moved down, but also much lower than the velocity at the air inlets.

5.2.4 ER vs air velocity

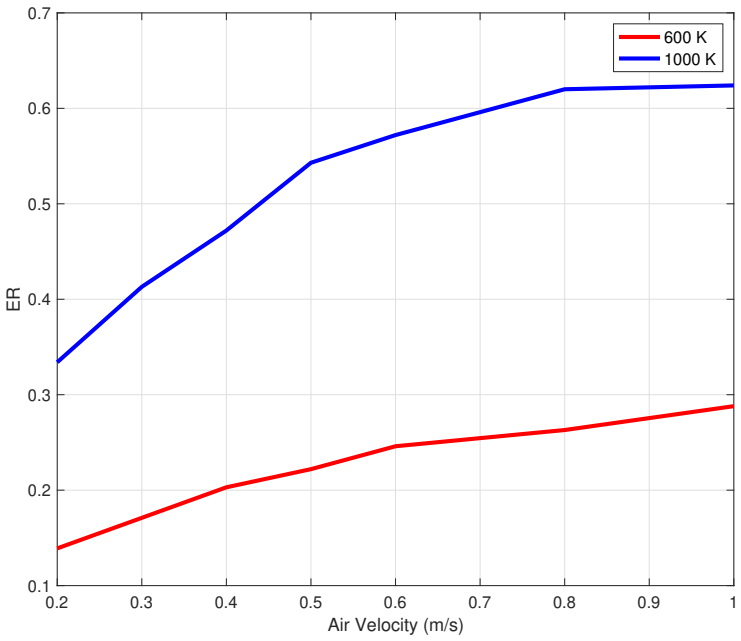

Figure 5.13: The influence of air velocity on the ER of the system, for rubberwood.

The utilisation of the porous media assumption makes it difficult to properly identify the ER in the system. However, from the mass balance of solid species, it can be deduced that the biomass feed rate is proportionate to the rate of biomass consumption (kg/s). Moreover, the O_2 mass flowrate in the system can be obtained from the following:

$$\dot{m}_{O_2} = m_{O_2} \times \rho_{apparent} \times u_{air} \times A_s \ , \tag{5.42}$$

where $\dot{m}_{O_2}$ is the mass flowrate of the O_2 in kg/s and m_{O_2} is the mass fraction of O_2. After determining $\dot{m}_{O_2}$ at the inlet and outlet, the O_2 consumption is determined via:

$$O_2 \text{ consumption} = \text{inlet } \dot{m}_{O_2} - \text{outlet } \dot{m}_{O_2} \ . \tag{5.43}$$

The O_2 consumption when divided by the O_2 mass fraction in air (i.e. 23.3%) gives the amount of equivalent air in the system. This value when further divided by the rate of biomass consumption (kg/s) leads to the gasification air-fuel ratio and subsequently via the combustion air-fuel ratio as per Eq. (3.27) of Chapter 3, enables the prediction of the ER for a variety of u_{air} values.

Fig. 5.13 illustrates the impact of u_{air} on the ER at both 600 K and 1000 K. It is evident that the relationship between ER and u_{air} is directly proportional, as anticipated. This is due to the fact that an increase in u_{air} results in greater oxygen availability within the system, thereby leading to an increase in ER. According to the model, a u_{air} lower than 0.2 m/s would result in the system extinguishing, as the amount of air provided would be insufficient to sustain the necessary chemical reactions and facilitate the advancement of the porous media's reacting front. Conversely, a u_{air} exceeding 1 m/s would compromise the quality of the producer gas, as an excessive amount of air is introduced into the system. This would result in an abundance of N_2 at the gasifier outlet, occupying available space as an inert gas.

It is evident that the process yields a low quality syngas with an operating temperature of 600 K, resulting in a large portion of the O_2 being left unreacted. This is addressed by elevating the air inlet temperature, as detailed in section 5.2.8. Consequently, the increased temperature promotes endothermic reactions of the system, prompting the initiation of additional chemical reactions that were inactive at 600 K to be active at an air inlet temperature of 1000 K.

5.2.5 Effect of air velocity

The air velocity, u_{air}, plays a significant role in influencing the performance of the gasifier and ultimately the end product. u_{air} directly influences the value of the ER, which is one of the main parameters affecting biomass gasification as mentioned in

Chapters 3 and 4. In the Thermo-CFD model it influences producer gas composition, the temperature of the system in both the gas and solid phases, and the tar and char contents.

Fig. 5.14 shows the temperature profiles along the gasifier height halfway across the configuration, for increasing u_{air} values. The influence of u_{air} on the temperature in the system is justifiable considering that in experimental DBGs, the temperature in the system starts at around 400 K and reaches a peak at the oxidation zone. After which, the temperature starts descending to reach a constant value at the reduction zone. The temperature profiles show similar trends with that predicted by [41] and that generated experimentally [71]. In commercial DBGs, the temperature is relatively low in the drying zone, rising in the pyrolysis zone as the biomass undergoes severe devolatilisation. In the oxidation zone, the temperature continues increasing until it reaches a peak due to the triggering of char combustion and volatile combustion reactions which are all exothermic. The temperature starts to descend in the reduction zone as the O_2 starts diminishing and endothermic reactions are triggered. The predicted temperature distribution along the gasifier is very different to that predicted by the thermodynamic equilibrium model in Chapter 4. In the Thermo-CFD model, the temperature is predicted via solid and gas phase energy transport equations and includes a radiation model to account for radiative heat transfer. In the equilibrium model, the temperature is predicted uniformly via an energy balance in an adiabatic system given a chemical composition of the feedstock and a set of operating parameters and assumes no heat losses. This characterisation of the temperature distribution along the gasifier height supports the reliability of the model in predicting the temperature of the system with increasing u_{air}.

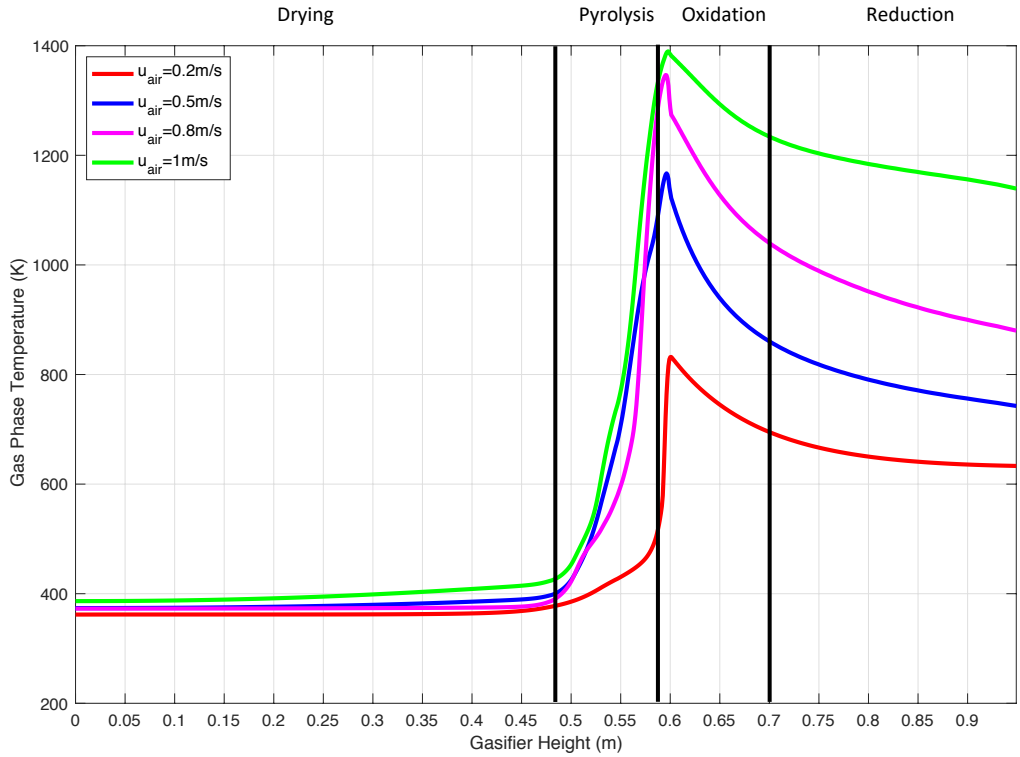

Figure 5.14: Gas phase temperature as a function of gasifier height for different u_{air} values for rubberwood, with 0 representing the top of the gasifier, and 0.95 the bottom of the gasifier (gasifier outlet) - see Fig. 5.1.

Fig. 5.15 displays the average ϵ distribution for different u_{air}. Beginning with Fig. 5.15(a), $u_{air} = 0.2$ m/s, it's apparent that this low value, some unreacted biomass remains at the centre of the unit. Additionally, the low u_{air} leads to the formation of a thin char bed at the end of the oxidation zone.

For $u_{air} = 0.5$ m/s, see Fig. 5.15(b), a gradual increase in char is observed and the unreacted dry biomass is now entirely consumed by the reactions, leaving only the replenished wet feedstock participating in chemical reactions.

Moving to $u_{air} = 0.8$ m/s, shown in Fig. 5.15(c), the char bed continues to expand, and the average ϵ distribution illustrates how increased u_{air} promotes chemical reactions, particularly with regard to (R24).

Finally, in Fig. 5.15(d), the average ϵ distribution for $u_{air} = 1$ m/s demonstrates the char bed expansion. This highlights the cyclic replenishment feature of the model, where the char bed continuously collapses and regenerates, effectively generating specific compositions of chemical species.

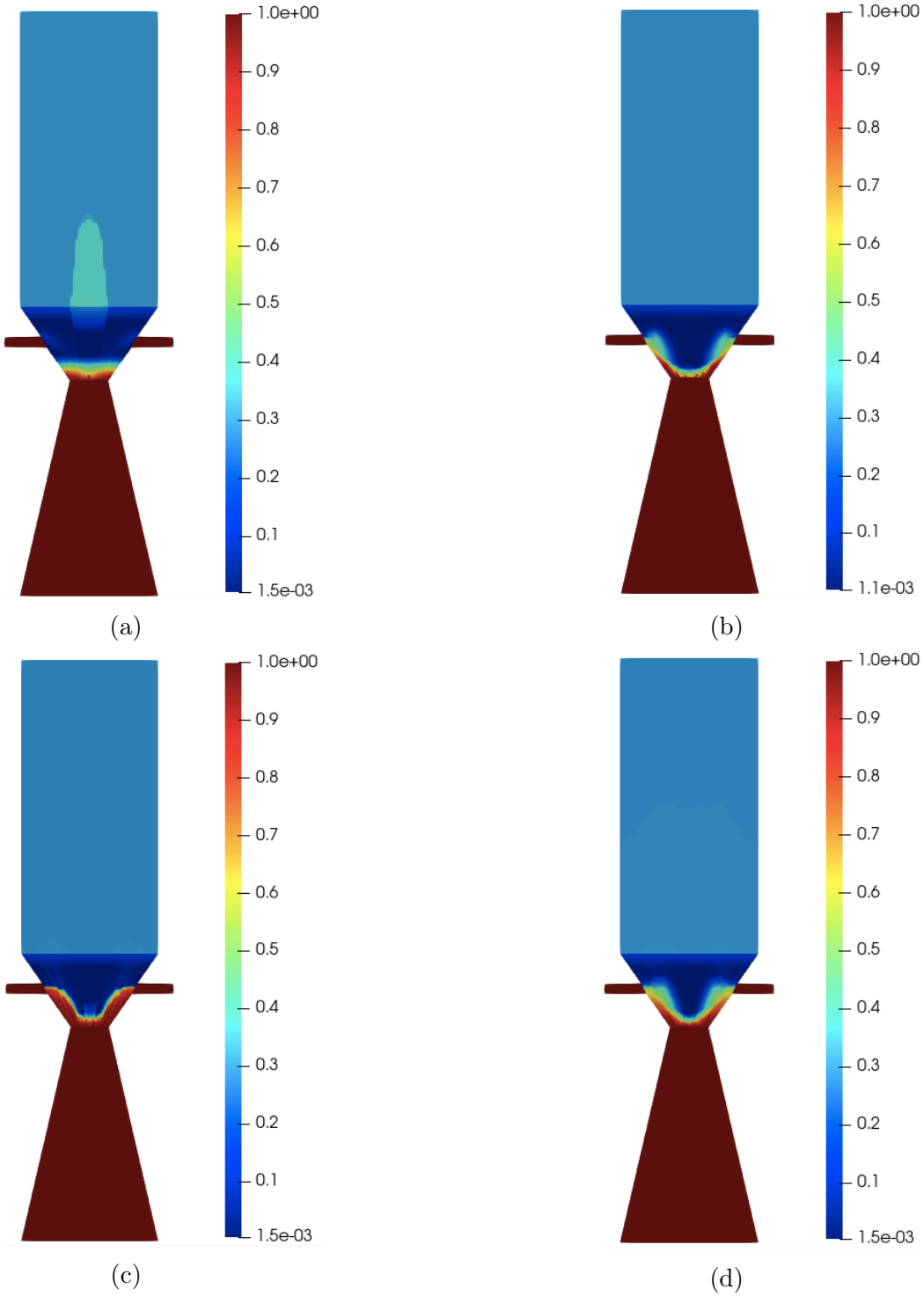

Figure 5.15: Thermo-CFD predicted ϵ distribution contours for (a) u_{air}=0.2m/s, (b) u_{air}=0.5m/s, (c)u_{air}=0.8m/s, and (d) u_{air}=1m/s, for rubberwood.

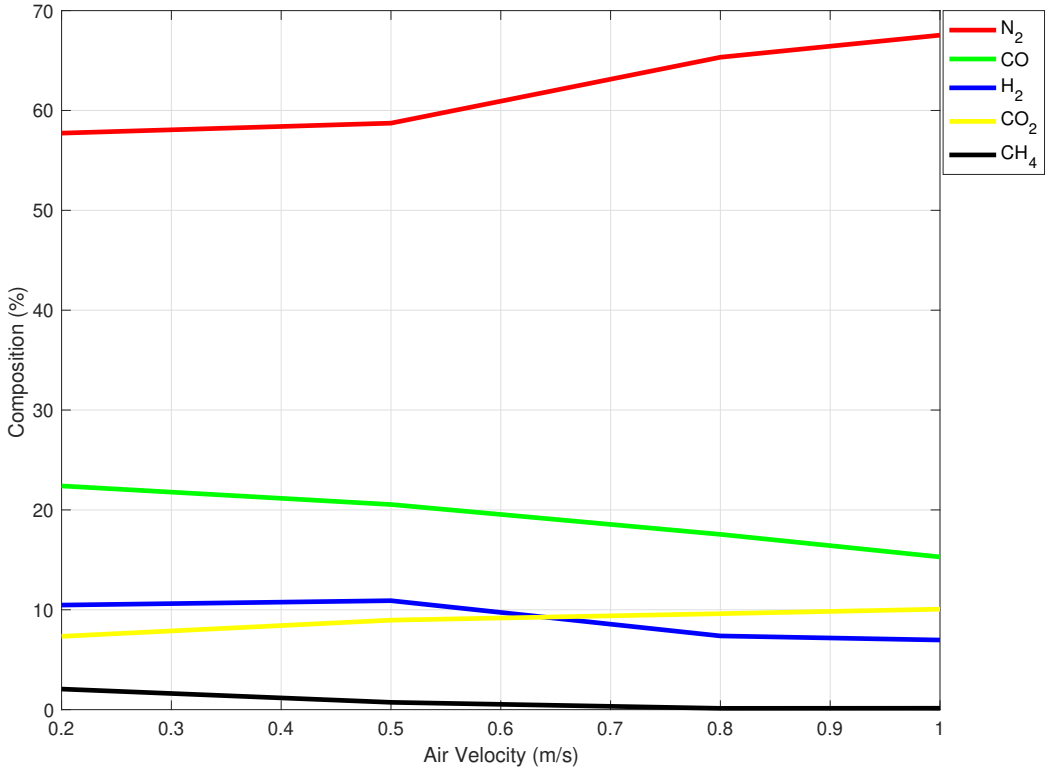

Figure 5.16: Producer gas composition at the gasifier exit for increasing u_{air}, for rubberwood.

Fig 5.16 depicts reasonably well the effects of increasing the u_{air} on the composition of the primary components constituting the producer gas. As in the case of the thermochemical equilibrium model developed in Chapter 4, an increase in u_{air} leads to the proportional increase in N_2 concentration as more air is introduced into the gasifier. CH_4 is typically produced in the lower temperature zones of the gasifier, where partial combustion occurs. Higher u_{air} can lead to higher temperatures and more complete combustion, reducing the CH_4 concentration in the producer gas. H_2 concentration is favoured at moderate temperatures and with sufficient residence time. Increased u_{air} can raise the temperature, leading to more complete combustion of H_2 and a reduction in its concentration. CO concentration decreases as expected since it is mainly produced via partial oxidation of C. Increasing u_{air} will enhance the availability of O_2 in the gasifier, promoting more complete combustion of C into CO_2 rather than CO, thereby reducing the CO and increasing the CO_2 concentrations.

5.2.6 Gas species distribution

Fig. 5.17 depicts the distribution of gas species representing the key components of the producer gas for $u_{air} = 0.5$ m/s. The contour plots showing the concentrations of the producer gas, reveal important insights into the thermochemical processes taking place inside the gasifier. Figs. 5.17(a) and 5.17(b) reveal that the generation of syngas predominantly occurs within the reduction zone. This zone is where endothermic gasification reactions, specifically (R11) and (R3), take place. Furthermore, H_2 is formed from the decomposition of biomass during pyrolysis and CO is also produced in the oxidation zone, where the partial combustion of C takes place (R6). These findings confirm the model's predictive ability in representing the typical behaviour of the syngas generated in a DBG.

Fig. 5.17(c) represents the distribution of N_2 within the gasifier. It shows that N_2 is mainly found in the oxidation zone, where the air inlet are situated. Being an inert gas, N_2 does not directly participate in the chemical reaction scheme, and only fills up the spaces not occupied by other reactive gases. A higher u_{air} could potentially increase the amount of N_2 present in the unit.

Fig. 5.17(d) shows the distribution of CH_4, which occurs during the later stages of gasification, particularly in the tar cracking and reforming zones. CH_4 is not typically a major component of the gas produced in a DBG, as conditions are generally unfavourable for its production. It can be seen that CH_4 is mainly found in the pyrolysis zone, during the pyrolysis of the biomass feedstock and can also be formed in the reduction zone via the methanation reactions (R12) - (R14).

Lastly, Fig. 5.17(e) depicts the distribution of CO_2 within the unit. CO_2 is mainly produced at the exit of the gasifier, during the reduction of the biomass, but is also found in the pyrolysis zone. Efficient gasification processes aim to manage and reduce the amount of CO_2 produced throughout the gasifier, while promoting complete combustion and controlling gasification conditions to favour the production of H_2 and CO.

As it will become apparent in section 5.2.8, the gas species distributions demonstrated in Fig. 5.17 represent an inefficient gasification process. From the distribu-

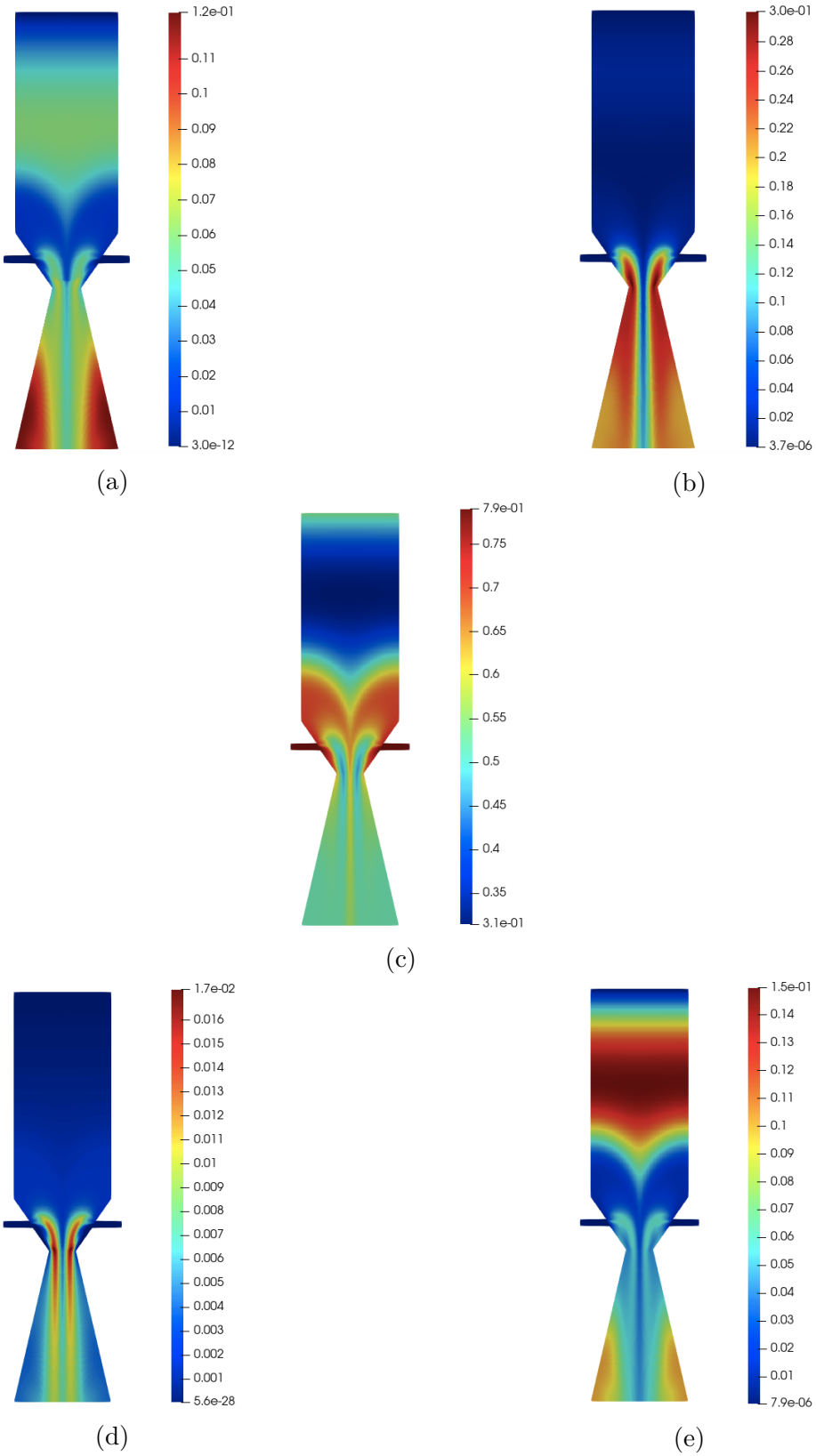

Figure 5.17: Thermo-CFD model predicted producer gas composition distribution for (a) H_2, (b) CO, (c) N_2, (d) CH4, and (e) CO_2, for rubberwood; $u_{air} = 0.5$ m/s

tion of gas species, it is evident that some O_2 escapes the porous media, avoiding chemical reactions necessary for increasing the quality of the syngas.

5.2.7 Effect of moisture content

Table 5.7: Comparison of producer gas composition predicted by the Thermo-CFD model for different feedstock MC.

MC	**5%**	**18.5%**
H_2	6.53	10.91
CO	21.04	20.59
CO_2	7.31	8.96
CH_4	1.16	0.73
N_2	61.96	58.79

Table. 5.7 illustrates how MC impacts the composition of producer gas. This comparison is consistent with that exhibited by the thermodynamic equilibrium model - see Fig. 4.7 in section 4.2.2 of Chapter 4. The major influencing chemical reaction when analysing different MC values inherent in biomass feedstock is the water-gas shift reactions, (R11). Biomass with a higher MC contains more inherent water, highlighting the importance of (R11). As the MC increases, the H_2 concentration increases at the expense of CO. On the other hand, (R16) ensures that CH_4 decreases with increasing MC. However, this might not always be the case if incomplete gasification dominates due to lower temperatures.

5.2.8 Effect of inlet air temperature

Jayah et al. [55] state that in general, ambient air at 300 K is used for gasification. However, Chen [154] concludes that a higher inlet air temperature (T_{air}) improves the conversion efficiency. The conversion efficiency of the process increases as T_{air} increases due to hot air being introduced, providing additional enthalpy necessary for chemical reactions to take place. This is especially true in the case of the Thermo-CFD model, whereby increasing the temperature of the injected air will enhance the ability of the system to convert biomass into useful gases, enhancing the gasification

process. Using the Thermo-CFD model, it is evident that T_{air} of 600 K results in O_2 by-passing the porous media reaction front, consequently prohibiting some chemical reactions from occurring due to the presence of cold regions in the gasifier. This causes some O_2 to be present at the outlet of the gasifier. To increase the conversion efficiency and enhance the gasification process, T_{air} is increased from 600 K to 1000 K.

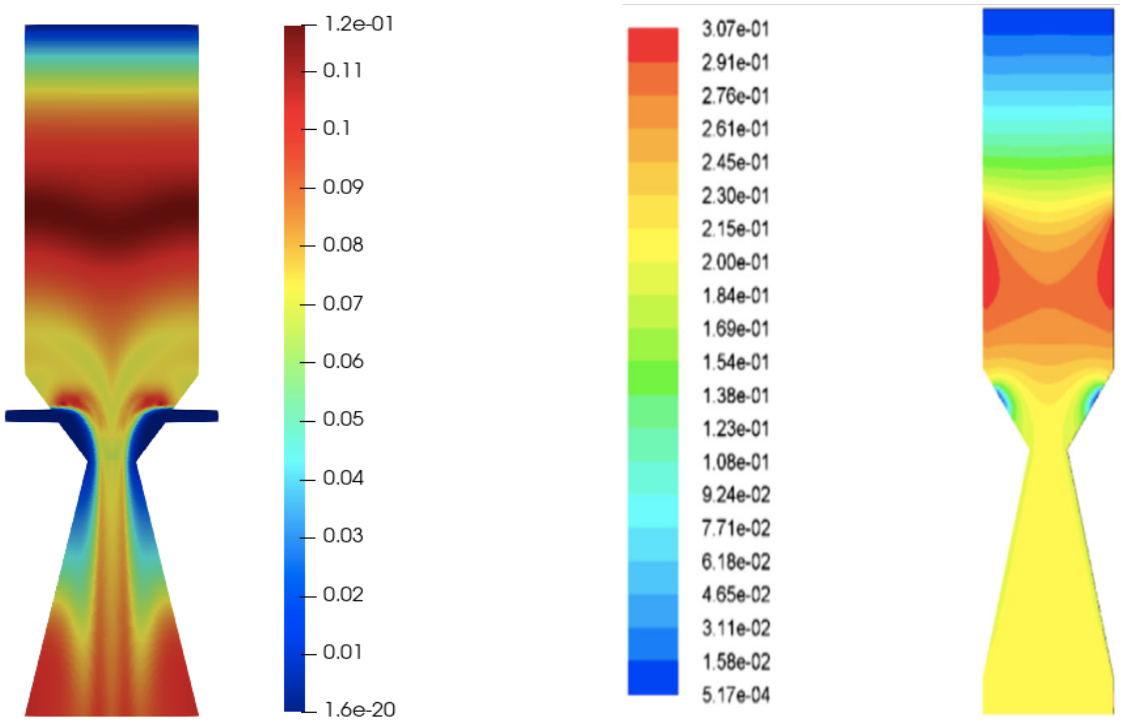

Figure 5.18: Predicted H_2 composition distribution for rubberwood for Thermo-CFD model at T_{air}=1000 K and u_{air}=0.2 m/s (left), and the prediction of Kumar and Paul (right) [41].

Fig. 5.18 illustrates the distribution of H_2 composition throughout the entire gasifier using the Thermo-CFD model for T_{air} = 1000 K in comparison to the same predicted by Kumar and Paul [41]. In contrast to the prediction at 600 K, the H_2 composition for the Thermo-CFD model, generated with T_{air} = 1000 K, exhibits a more consistent distribution along the gasifier. The elevation in T_{air} leads to a more frequent production of H_2 in the pyrolysis zone and a higher concentration of H_2 at the gasifier exit, achieving better agreement with the prediction obtained by [41]. This is especially true because a higher T_{air} leads to accelerated pyrolysis and decomposition of biomass and promotes (R11) and (R16).

A noteworthy observation is the similarity in the distribution patterns between the two models, characterised by significant H_2 production in the pyrolysis zone and moderate production at the gasifier exit. Both the drying zone and air inlets remain devoid of H_2 in both model predictions, as expected.

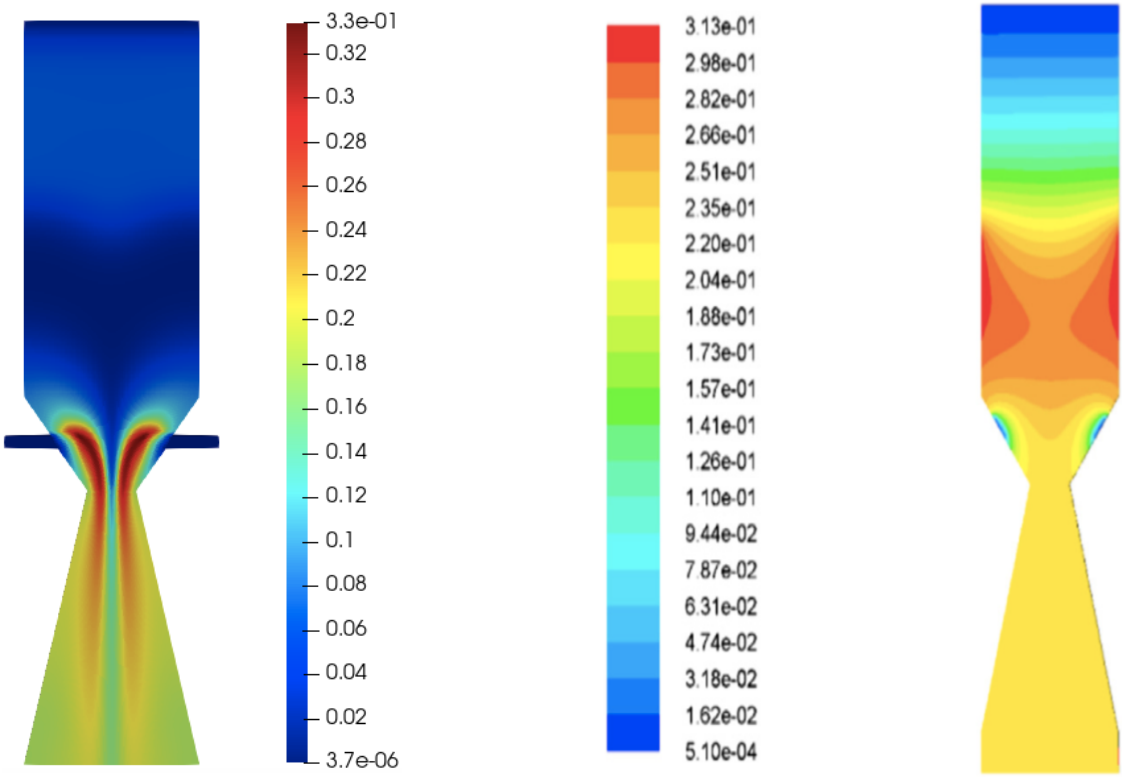

Figure 5.19: Predicted CO composition distribution for rubberwood for Thermo-CFD model at T_{air}=1000 K and u_{air}=0.2 m/s (left), and the prediction of Kumar and Paul (right) [41].

Fig. 5.19 displays the distribution of CO in the Thermo-CFD model at T_{air} = 1000 K and that predicted by Kumar and Paul [41]. Clear disparities emerge in the pyrolysis zone of the gasifier, where the prediction by [41] shows a substantial presence of CO, while that obtained from the Thermo-CFD model at 1000 K indicates minimal CO production in the same zone, but better when compared with the prediction obtained at 600 K. This improvement underscores the credibility of the Thermo-CFD model in depicting a promising syngas composition when compared with previous model predictions upon increasing the T_{air}. Increasing the T_{air} promotes (R3) as it is highly endothermic and becomes favourable at higher temperatures. As temperature increases, the equilibrium of (R3) shifts towards the

production of CO, increasing CO concentration.

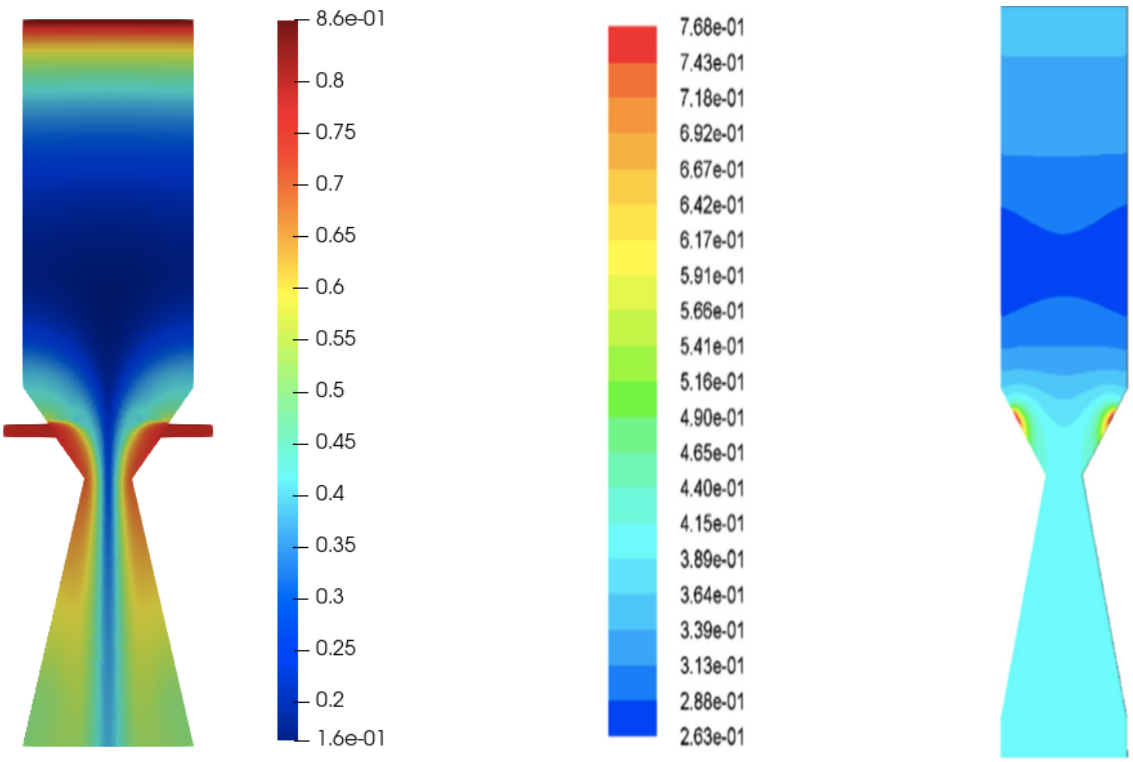

Figure 5.20: Predicted N_2 composition distribution for rubberwood for Thermo-CFD model at T_{air}=1000 K, u_{air}=0.2 m/s (left), and the prediction of Kumar and Paul (right) [41].

Regarding the N_2 concentration distribution illustrated in Fig. 5.20, it is anticipated that a significant quantity of N_2 will accumulate near the air inlet, as evident by the two predictions. However, it is important to notice the differences between the prediction of the Thermo-CFD model at 600 K and 1000 K. at 600 K, the N_2 was by-passing the reaction front and accumulating at the pyrolysis, oxidation, and gasifier outlet. Upon increasing the temperature to 1000 K, N_2 is no longer found in abundance at the gasifier outlet.

Moving forward, Fig. 5.21 shows the CH_4 distribution predicted by the Thermo-CFD model at T_{air} = 1000 K and that of Kumar and Paul [41]. Notably, CH_4 is prominently generated in the pyrolysis zone, right above the air inlet. However, in the case of the Thermo-CFD model at T_{air} = 1000 K, CH_4 is absent at the gasifier outlet. Instead, it is concentrated in the pyrolysis zone, forming a distinct strip along the symmetry plane. This is in contrast to the prediction at 600 K, where

the CH_4 was concentrated at the edge of the unit just below the air inlet and found moderately at the gasifier exit. CH_4 requires elevated temperatures to break down and the increased T_{air} leads to enhanced steam methane reforming, producing H_2 and CO. The prediction obtained by [41] shows a heavy CH_4 concentration in the pyrolysis zone.

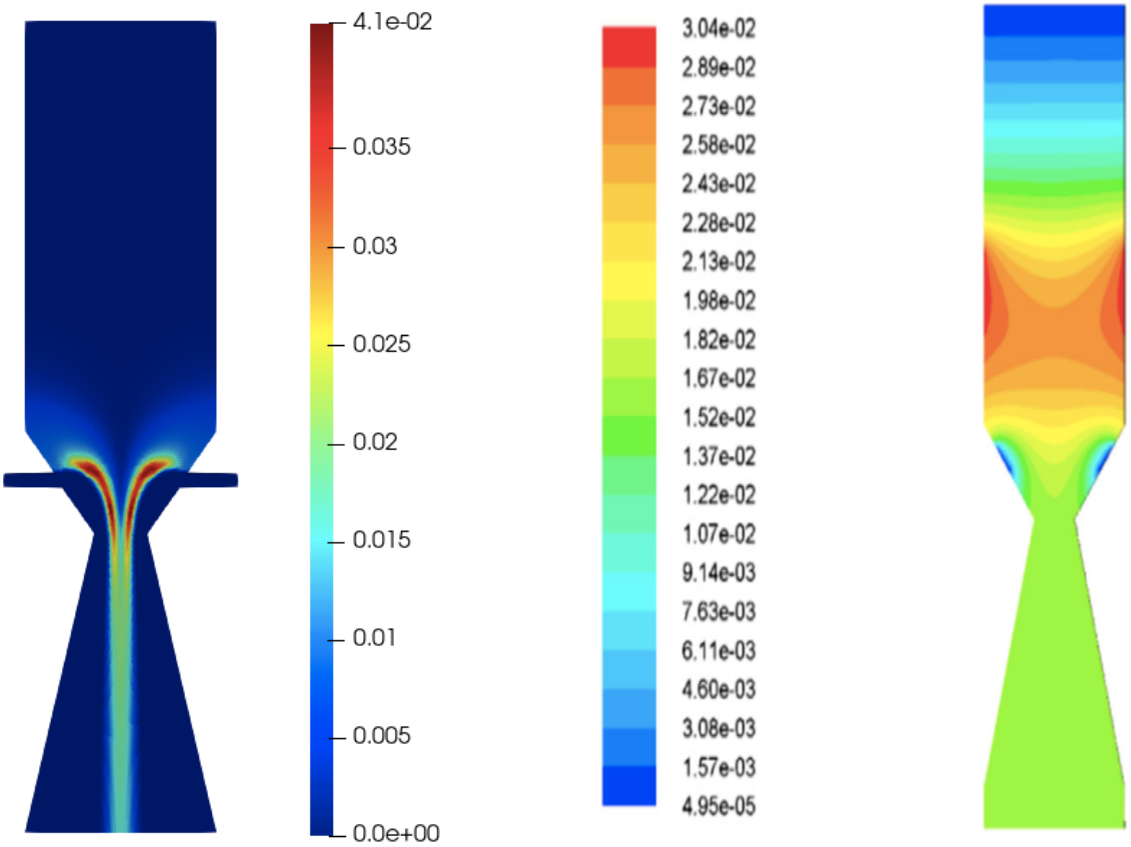

Figure 5.21: Predicted CH_4 composition distribution for rubberwood for Thermo-CFD model at T_{air}=1000 K and u_{air}=0.2 m/s (left), and the prediction of Kumar and Paul (right) [41].

Finally, Fig. 5.22 shows the distribution of CO_2 predicted at 1000 K. The one estimated by Kumar and Paul [41] demonstrates an absence of CO_2 in the drying and pyrolysis zones, with a moderate production in the oxidation and reduction zones. Likewise, the CO_2 distribution predicted by the Thermo-CFD model at T_{air} = 1000 K resembles a similar distribution. Heavy production is observed in the oxidation and reduction zones, with a minimal production in the pyrolysis zone. Increased air temperature may result in more intense and complete combustion reactions, promoting (R7). This results in more CO_2 being produced at the gasifier exit.

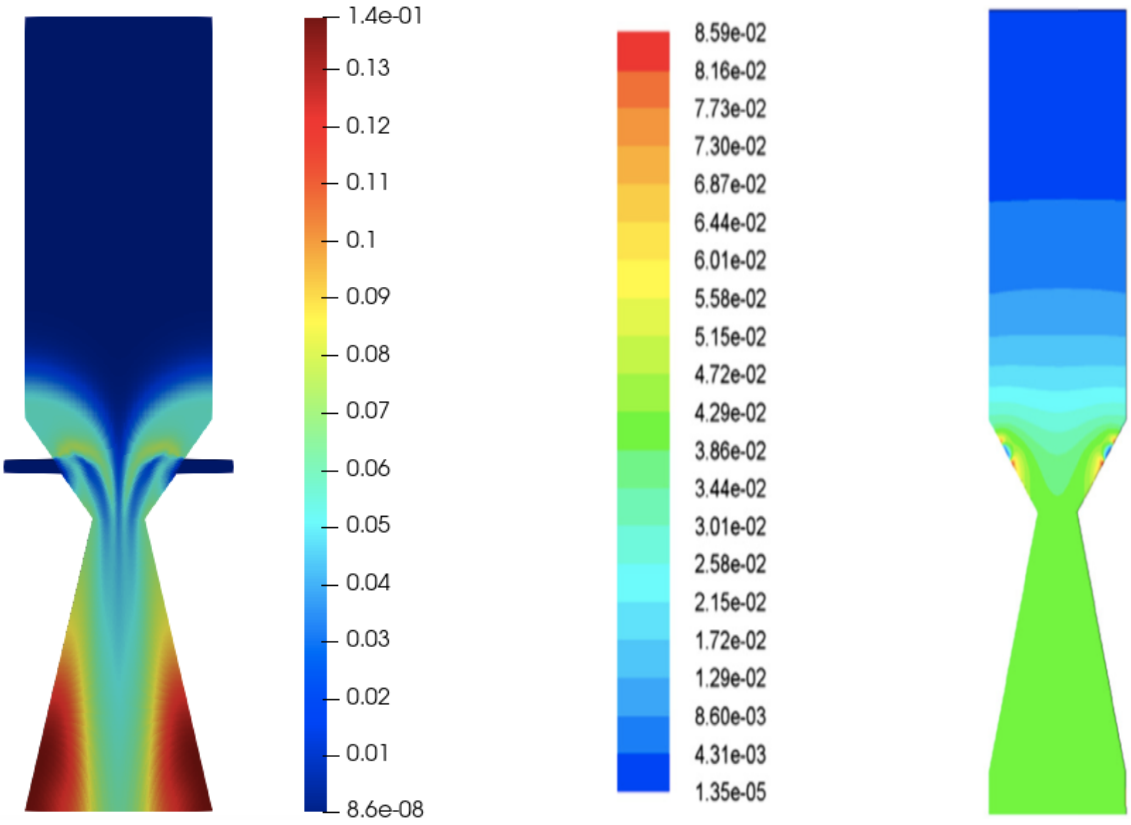

Figure 5.22: Predicted CO_2 composition distribution for rubberwood for Thermo-CFD at T_{air}=1000 K and u_{air}=0.2 m/s (left), and the prediction of Kumar and Paul (right) [41].

Fig. 5.23 shows how the syngas composition compares with the same predictions as in Fig. 5.11, but including those estimated by the Thermo-CFD model at T_{air} = 1000 K. A higher syngas composition is maintained at this temperature, with a lower CH_4 and N_2 concentrations. This proves that the Thermo-CFD model produces a higher conversion efficiency when T_{air} is increased.

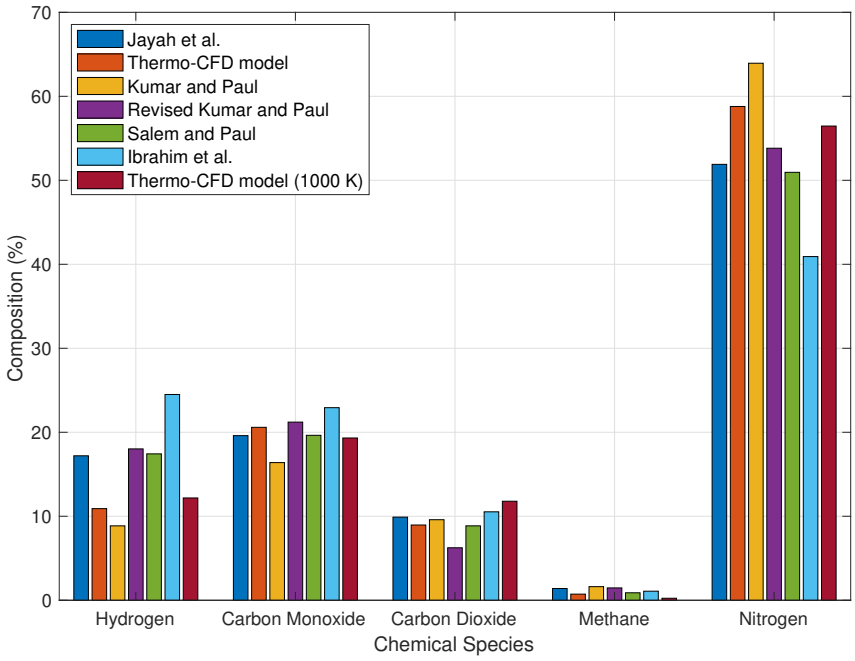

Figure 5.23: Comparison between predicted (Thermo-CFD model, Kumar and Paul [41], Salem and Paul [34], Ibrahim et al. [119], and Thermo-CFD model ($T_{air} = 1000$ K and $u_{air} = 0.2$ m/s)) and experimentally obtained [55] producer gas composition for rubberwood.

5.2.9 Effect of radiation

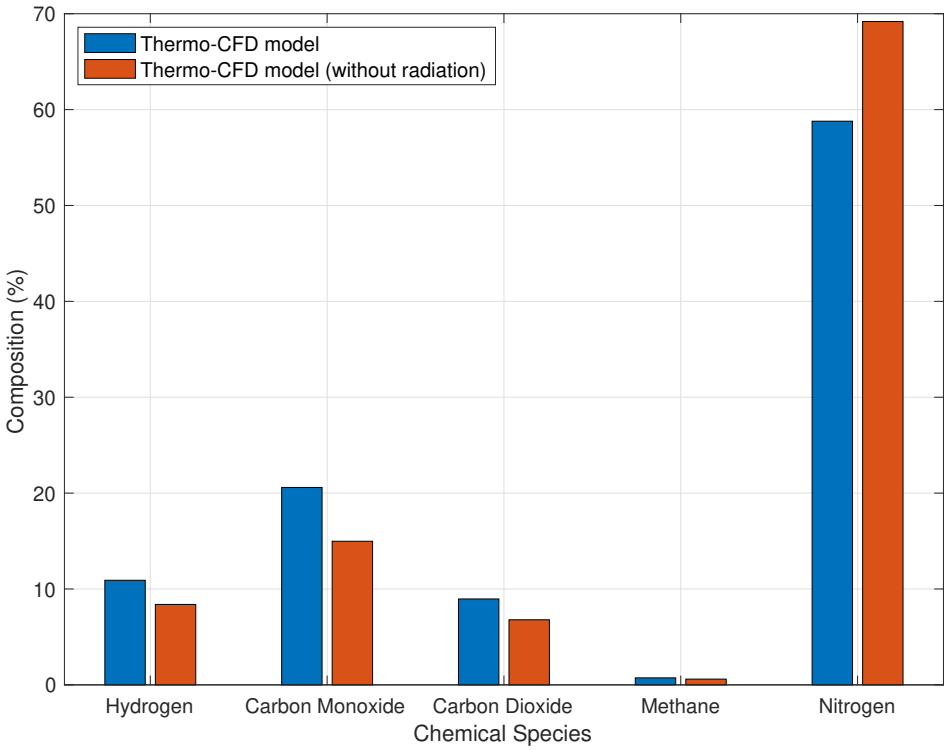

Figure 5.24: Comparison of producer gas composition between predicted Thermo-CFD model (T_{air} = 600 K and u_{air} = 0.5m/s) with and without radiative heat transfer for rubberwood.

Fig. 5.24 demonstrates the predicted producer gas composition comparison between the Thermo-CFD model including and excluding radiative heat transfer model. In the gasification system, heat is primarily transferred through convection and radiation. Radiation improves the heat distribution, leading to more uniform temperature profiles within the gasifier. This has a strong influence on thermal cracking of tars, reducing their concentration in the producer gas and increasing the yield of lighter gases like H_2 and CO.

The pyrolysis, oxidation, and reduction gasification reactions are highly temperature-dependent. With the inclusion of radiation, higher temperatures in critical zones can accelerate endothermic reactions, such as (R3), (R4), and (R16), shifting the equilibrium of reactions towards the production of CO and H_2, improving the overall

syngas quality.

5.2.10 Tar content

As mentioned in section 3.3.5, Chapter 3, the management of tar is crucial in DBGs as it can lead to issues such as equipment fouling, reduced efficiency, and a degradation in syngas quality. In the Thermo-CFD model, tar is assumed to be in the gaseous state and possess identical thermophysical properties to benzene, as in the thermodynamic equilibrium model of Chapter 4. In DBGs, tar primarily participates in the pyrolysis zone and the reduction zone of the unit.

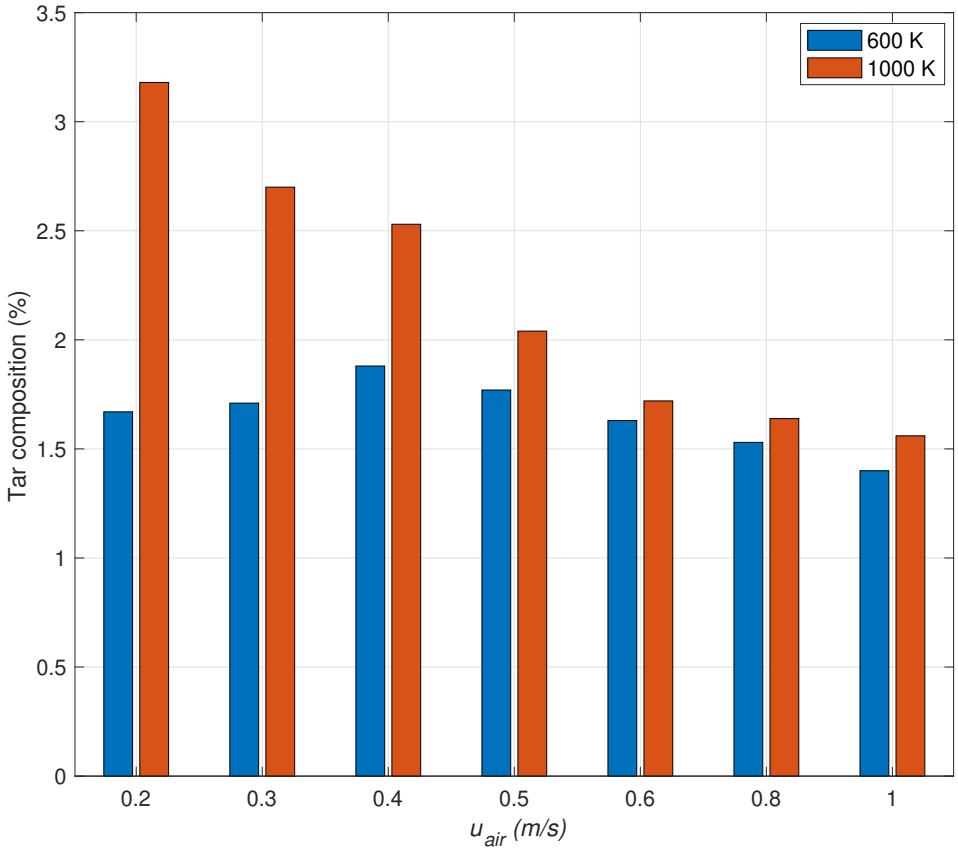

Figure 5.25: Tar molar composition generated with increasing u_{air} values at T_{air} of 600 K and 1000 K, using the Thermo-CFD model, for rubberwood

Fig. 5.25 shows the tar concentration in vol% which is found in the producer gas for increasing values of u_{air} and at air inlet temperatures of 600 K and 1000 K. Higher u_{air} means more O_2 is introduced into the oxidation zone of the gasifier,

which enhances the rate of combustion and tar cracking reactions (R24), leading to higher temperatures. The increased temperatures favour the breakdown of complex hydrocarbons such as tars into smaller molecules. As such, elevated temperatures reduce overall tar yield by breaking down larger tar compounds, which is advantageous for cleaner producer gas. Furthermore, higher u_{air} can promote better mixing and can extend the time biomass particles and intermediate products remain at high temperatures. The prolonged exposure to high temperatures allows more time for thermal cracking and reforming reactions, resulting in more complete breaking down of tar components. The figure also shows the tar composition at $T_{air} = 1000$ K where the tar composition is significantly reduced at the examined u_{air}, proving the benefit of elevated temperatures and its effect on reducing tar composition. The effect of the tar cracking reaction is observed at $T_{air} = 1000$ K as the difference between the tar composition at both temperatures is bigger for low u_{air}. This shows that at $T_{air} = 1000$ K, (R25) is more likely to occur, as the increased temperature accelerates the reaction rate and makes it easier for tar molecules to break apart. It is important to highlight that the tar composition behaviour as u_{air} increases directly mirrors the that estimated in the equilibrium model - see Fig. 4.1 in section 4.1, Chapter 4. The increase in u_{air} promotes tar cracking reactions leading to a heavy decline at the beginning, but starts to plateau at higher u_{air} due to combustion dominance and diminished syngas quality. This justifies the tar empirical correlation generated in the equilibrium model [155].

5.3 Summary

A 2D CFD model of a DBG with a specific focus on the porous media assumption is developed. The model was developed using a newly established solver capable of thermal and chemical conversion in porous media, integrated with pyrolysis and heat transfer sub-models.

The Thermo-CFD model incorporates a moving porous media bed, where the biomass feedstock is replenished from the top as it is consumed due to a comprehensive chemical reaction scheme. It highlights the simultaneous occurrence of chemical

reactions rather than a sequential output-input relationship between reacting zones. The model estimates the producer gas composition and its distribution along the geometry, temperature profiles in the solid and gas phases, and the effects of the moving porous bed.

It is important to highlight that parameters such as T_{air} and u_{air} heavily influence the composition of the producer gas. Furthermore, radiative heat transfer affects temperature distribution, which has an influence on syngas composition and conversion efficiency.

CHAPTER 6

Conclusions and Future Work

The main focus of this body of work is to provide comprehensive and reliable mathematical models aimed at better understanding the performance and predictive nature of DBGs. Initially, a methodical examination was conducted on the fundamentals of biomass and the underlying principles governing the gasification procedure, encompassing the diverse physical and thermochemical properties linked with biomass, alongside the inherent physical and chemical occurrences and interactions within a gasifier. Subsequently, a comprehensive examination of existing literature was undertaken to grasp the characteristics, including the constraints and scope of each modelling approach. The literature review also encompasses a detailed appraisal of past modelling and experimental work performed in the field of biomass gasification.

The above gave rise to two distinct and comprehensive mathematical models capable of predicting the behaviour of downdraft biomass gasification systems. The first model takes into account a thermochemical equilibrium approach, incorporating a global gasification reaction that encompasses all gaseous species, as well as the tar and char yields. The char yield is determined through the application of reaction (R3). Furthermore, the gasification temperature is computed by solving a fully

coupled set of equations, and in improved convergence of the solver. To consider tar production within the framework, a new exponential best-fit curve is created, derived from previous experimental data concerning tar formation in downdraft gasifiers. The resulting correlation is then employed to account for the molar tar yield.

The predicted syngas composition, gasification temperature, as well as the projected tar and char yields, along with the concentrations of contamination gases, exhibit a strong concurrence with values obtained through experimental means and analysis of recent analogous gasification models.

From the results obtained from the proposed equilibrium model, the following conclusions are drawn:

1. The concentrations of H_2 and CO_2 increase with MC, while the CO concentration decreases. The N_2 concentration remains constant while the CH_4 concentration gradually increases with increasing MC of Chapter 4.

2. T increases with ER and decreases with MC for gasification reasons mentioned in section 4.2.1.2.

3. The tar yield decreases with increasing ER and MC due to a better quality syngas.

4. Reaction R3 is a reliable approach for predicting char yield.

5. The LHV and CGE decrease with an increase in ER and T.

6. The concentration of NH_3 decreases with increasing ER values and increases with increasing MV, while the concentration of H_2S remains almost constant, decreasing slightly with increasing ER and MC.

7. It is shown that equilibrium model are able to provide reliable predictions of syngas composition.

The second model incorporates a comprehensive CFD framework through the utilisation of a solver capable of thermal and chemical conversion in porous media, but has never before been tested on biomass gasifiers. A 2D model of a DBG

is developed, which is integrated with a comprehensive pyrolysis sub-model. An exhaustive chemical reaction scheme is incorporated, taking into consideration drying, pyrolysis, oxidation, and reduction reactions. The code incorporates a moving porous bed, characterised by a replenishment feature that refills the gasifier with fresh feedstock as it is being consumed. The chemical reactions occurring are not restricted to specific zones of the gasifier and they occur simultaneously rather than obeying an input-output relationship, resulting in a robust method of accounting for both the gas and solid phase chemical reactions.

The resulting Thermo-CFD model has the capability to forecast the composition of producer gas, tar and char yields, as well as distributions in both the gas and solid phases and porosity. Additionally, it can predict the distributions of feedstock and humidity while identifying regions where endothermic and exothermic chemical reactions occur. When the output is compared to experimental and previous modelling results, it demonstrates favourable agreement with them.

From the results obtained using the Thermo-CFD model, the following conclusions are drawn:

1. The producer gas composition reaches a maximum ratio at an optimum u_{air} and ER.

2. $u_{air} < 0.2$ results in the chemical reactions dying out, while $u_{air} > 1$ results in excessive products of complete combustion being formed such as CO_2 and H_2O at the expense of CO and H_2, aligning with the conclusions of previous studies.

3. The gas phase temperature follows a consistent pattern characteristic of downdraft gasification systems, beginning with a low temperature in the drying zone and gradually rising to reach a peak in the oxidation zone, followed by a plateau in the reduction zone. It is clear that the gas phase temperature exhibits an upward trend as u_{air} increases.

4. u_{air} is directly proportional with ER, exhibiting an increasing trend of ER as u_{air} increases.

5. T_{air} = 600 K results in O_2 by-passing the reaction front, avoiding its participation in chemical reactions. This leads to a reduction in the quality of the syngas. To tackle this issue, T_{air} is raised to 1000 K to improve the conversion efficiency of the gasification process and enhance the quality of the resulting syngas.

6. The movement of the porous media front exhibits distinct behaviour with varying u_{air}. A low u_{air} leads to minimal displacement of the porous media front, while a high u_{air} is associated with more pronounced movement.

7. The behaviour of the producer gas composition with respect to MC aligns with that of the equilibrium model developed in Chapter 4.

8. Tar cracking reactions involve elevated temperatures in order to occur.

9. It is concluded that the Thermo-CFD model is capable of demonstrating good comparison of the producer gas composition with those of pertinent experimental investigation and previous modelling predictions.

From the conclusions drawn, it is evident that both the equilibrium and CFD models reported in this work are capable of delivering predictions that align with each other, indicating their reliability in facilitating engineering simulations of gasification systems. Additionally, they underscore the models capacities in relation to undertaking process design, evaluation, and optimisation of gasification technology.

6.1 Future work

Both models are ripe for further development. Concerning the equilibrium model derived in Chapter 4, it is important to consider the following recommendations:

1. Utilising different gasification agents, such as a combination of air and steam, adjusting their proportions, and assessing their impact on the producer gas composition.

2. Implementing additional species/chemical reactions to further improve the reliability of the model.

3. As highlighted in section 2.1 of Chapter 2, an intriguing approach involves integrating the equilibrium model with a kinetic model. This should enhance comprehension of the gasification process by incorporating reaction rates and the kinetics of chemical reactions.

4. Explore avenues for tar cracking and cleaning to decrease the tar content.

5. Assess the economic feasibility of the biomass gasification process by considering factors such as capital and operating costs, energy efficiency, and the potential for by-product utilisation.

Regarding the Thermo-CFD model developed in Chapter 5, it is crucial to take into account the subsequent recommendations and areas for future investigation:

1. Explore the development of a mesh strategy to proficiently handle the variations outlined in section 5.2 of Chapter 5, arising from the dynamic nature of the moving porous bed. This would aim to attain a state in which there is no variations in gas composition over time.

2. Explore the implementation of different biomass feedstocks through the use of the pyrolysis sub-model detailed in section 5.1.7 of Chapter 5. This will increase the reliability of the Thermo-CFD model by assessing a wide range of feedstock and assessing their impact on the gasification process.

3. Instead of assuming an initial pyrolysis temperature of 873 K, the temperature-dependent pyrolysis sub-model proposed by Sharma [143] could be incorporated into the **porousGasificationFoam** solver. The aim would be to encompass a broad spectrum of pyrolytic product coefficients across different pyrolytic temperatures.

4. Optimise the gasification process by pre-heating the solid walls of the configuration, leading to increased conversion efficiency and a higher tar cracking ability and syngas ratio.

Bibliography

[1] Naeem Abas, A Kalair, and Nasrullah Khan. Review of fossil fuels and future energy technologies. *Futures*, 69:31–49, 2015. 1.1

[2] Prabir Basu. *Biomass gasification and pyrolysis: practical design and theory*. Academic press, 2010. (document), 1.1, 1.1, 1.2, 3.1, 3.1.1, 3.1.2, 3.1.2, 3.1.3.1, 3.1.3.1, 3.1.3.1, 3.1.3.2, 3.1.3.3, 3.2, 1, 3.3.2, 3.4, 3.5, 3.3.2.1, 3.6, 3.7, 3.8, 3.9, 3.3.3, 3.3.4.2, 3.3.4.2, 3.3.5, 3.3.5, 3.3.6, 2, 5, 3.4.1, 4.1, 4.1, 4.2.1.3, 5.1.9, 5.1.11

[3] Dipal Baruah and DC Baruah. Modeling of biomass gasification: A review. *Renewable and Sustainable Energy Reviews*, 39:806–815, 2014. 1.1, 3.4.2

[4] Somya Mishra and Rajesh Kumar Upadhyay. Review on biomass gasification: Gasifiers, gasifying mediums, and operational parameters. *Materials Science for Energy Technologies*, 4:329–340, 2021. 1.1

[5] Erik Dahlquist. *Technologies for converting biomass to useful energy: combustion, gasification, pyrolysis, torrefaction and fermentation*. CRC Press, 2013. 1.1

[6] Tigabwa Y Ahmed, Murni M Ahmad, Suzana Yusup, Abrar Inayat, and Zakir Khan. Mathematical and computational approaches for design of biomass gasification for hydrogen production: A review. *Renewable and Sustainable Energy Reviews*, 16(4):2304–2315, 2012. 1.2, 3.4.2, 3.4.3

[7] Paweł Jan Żuk, Bartosz Tużnik, Tadeusz Rymarz, Kamil Kwiatkowski, Marek Dudyński, Flavio CC Galeazzo, and Guenther C Krieger Filho. Openfoam solver for thermal and chemical conversion in porous media. *Computer Physics Communications*, 278:108407, 2022. (document), 1.2, 1.3, 5.1.2, 5.1, 5.1.6, A.1.1, A.1.1, A.2, A.1.2, A.3, B.2

[8] ZA Zainal, R Ali, CH Lean, and KN Seetharamu. Prediction of performance of a downdraft gasifier using equilibrium modeling for different biomass materials. *Energy conversion and management*, 42(12):1499–1515, 2001. 2.1.1, 4.2.2, 4.2.3

[9] A Mountouris, E Voutsas, and D Tassios. Solid waste plasma gasification: equilibrium model development and exergy analysis. *Energy Conversion and Management*, 47(13-14):1723–1737, 2006. 2.1.1

[10] Andrés Melgar, Juan F Pérez, Hannes Laget, and Alfonso Horillo. Thermochemical equilibrium modelling of a gasifying process. *Energy conversion and management*, 48(1):59–67, 2007. 2.1.1

[11] Sompop Jarungthammachote and Animesh Dutta. Thermodynamic equilibrium model and second law analysis of a downdraft waste gasifier. *Energy*, 32(9):1660–1669, 2007. 2.1.1

[12] Avdhesh Kr Sharma. Equilibrium modeling of global reduction reactions for a downdraft (biomass) gasifier. *Energy Conversion and Management*, 49(4):832–842, 2008. 2.1.1, 4.2.3

[13] Hua-Jiang Huang and Shri Ramaswamy. Modeling biomass gasification using thermodynamic equilibrium approach. *Applied biochemistry and biotechnology*, 154(1-3):14–25, 2009. 2.1.1, 4.2.4

[14] Rade Karamarkovic and Vladan Karamarkovic. Energy and exergy analysis of biomass gasification at different temperatures. *Energy*, 35(2):537–549, 2010. 2.1.1

[15] A Abuadala, I Dincer, and GF Naterer. Exergy analysis of hydrogen production from biomass gasification. *International Journal of Hydrogen Energy*, 35(10):4981–4990, 2010. 2.1.1

[16] J Corella, J Herguido, and J Gonzalez-Saiz. Steam gasification of biomass in fluidized bed-effect of the type of feedstock. In *Pyrolysis and gasification*, pages 618–623. Elsevier Applied Science London, 1989. 2.1.1

[17] Mahdi Vaezi, Mohammad Passandideh-Fard, Mohammad Moghiman, and Majid Charmchi. Gasification of heavy fuel oils: A thermochemical equilibrium approach. *Fuel*, 90(2):878–885, 2011. 2.1.1

[18] H Roesch, J Dascomb, B Greska, and A Krothapalli. Prediction of producer gas composition for small scale commercial downdraft gasifiers. In *Proceedings of 19th European biomass conference and exhibition, Berlin, Germany*, pages 1594–1601, 2011. 2.1.1

[19] Emanuele Azzone, Mirko Morini, and Michele Pinelli. Development of an equilibrium model for the simulation of thermochemical gasification and application to agricultural residues. *Renewable energy*, 46:248–254, 2012. 2.1.1, 4.2.1.3

[20] Niladri Sekhar Barman, Sudip Ghosh, and Sudipta De. Gasification of biomass in a fixed bed downdraft gasifier–a realistic model including tar. *Bioresource technology*, 107:505–511, 2012. 2.1.1

[21] Andres Z Mendiburu, Joao A Carvalho Jr, and Christian JR Coronado. Thermochemical equilibrium modeling of biomass downdraft gasifier: Stoichiometric models. *Energy*, 66:189–201, 2014. 2.1.1

[22] Antonio Gagliano, Francesco Nocera, Francesco Patania, Maria Bruno, and Davide Giovanni Castaldo. A robust numerical model for characterizing the syngas composition in a downdraft gasification process. *Comptes Rendus Chimie*, 19(4):441–449, 2016. (document), 2.1.1, 4.2.1.1, 4.2, 4.2.1.1

[23] Takashi Yamazaki, Hirokazu Kozu, Sadamu Yamagata, Naoto Murao, Sachio Ohta, Satoru Shiya, and Tatsuo Ohba. Effect of superficial velocity on tar from downdraft gasification of biomass. *Energy & Fuels*, 19(3):1186–1191, 2005. 2.1.1

[24] Anthony V Bridgwater. Review of fast pyrolysis of biomass and product upgrading. *Biomass and bioenergy*, 38:68–94, 2012. 2.1.1

[25] S Rupesh, C Muraleedharan, and P Arun. A comparative study on gaseous fuel generation capability of biomass materials by thermo-chemical gasification using stoichiometric quasi-steady-state model. *International Journal of Energy and Environmental Engineering*, 6(4):375–384, 2015. 2.1.1, 4.2.1.3

[26] Ebubekir Siddik Aydin, Ozgun Yucel, and Hasan Sadikoglu. Development of a semi-empirical equilibrium model for downdraft gasification systems. *Energy*, 130:86–98, 2017. 2.1.1, 4.2.1.1, 4.2.1.1, 4.2.1.3

[27] Y Wang and CM Kinoshita. Kinetic model of biomass gasification. *Solar energy*, 51(1):19–25, 1993. 2.2.1

[28] DL Giltrap, R McKibbin, and GRG Barnes. A steady state model of gas-char reactions in a downdraft biomass gasifier. *Solar Energy*, 74(1):85–91, 2003. 2.2.1

[29] Colomba Di Blasi. Dynamic behaviour of stratified downdraft gasifiers. *Chemical engineering science*, 55(15):2931–2944, 2000. 2.2.1

[30] ED Gordillo and Abdelhamid Belghit. A downdraft high temperature steam-only solar gasifier of biomass char: a modelling study. *Biomass and bioenergy*, 35(5):2034–2043, 2011. 2.2.1

[31] Abrar Inayat, Murni M Ahmad, MI Abdul Mutalib, and Suzana Yusup. Process modeling for parametric study on oil palm empty fruit bunch steam gasification for hydrogen production. *Fuel Processing Technology*, 93(1):26–34, 2012. 2.2.1

[32] BV Babu and Pratik N Sheth. Modeling and simulation of reduction zone of downdraft biomass gasifier: effect of char reactivity factor. *Energy conversion and management*, 47(15-16):2602–2611, 2006. 2.2.1

[33] Benny Gøbel, Ulrik Henriksen, Torben Kvist Jensen, Bjørn Qvale, and Niels Houbak. The development of a computer model for a fixed bed gasifier and its use for optimization and control. *Bioresource Technology*, 98(10):2043–2052, 2007. 2.2.1

[34] Ahmed M Salem and Manosh C Paul. An integrated kinetic model for downdraft gasifier based on a novel approach that optimises the reduction zone of gasifier. *Biomass and bioenergy*, 109:172–181, 2018. (document), 2.2.1, 5.1.7, 5.2.2, 5.11, 5.2.2, 5.23

[35] A Rogel and J Aguillon. The 2d eulerian approach of entrained flow and temperature in a biomass stratified downdraft gasifier. *American Journal of Applied Sciences*, 3(10):2068–2075, 2006. 2.3.1

[36] Yueshi Wu, Qinglin Zhang, Weihong Yang, and Wlodzimierz Blasiak. Two-dimensional computational fluid dynamics simulation of biomass gasification in a downdraft fixed-bed gasifier with highly preheated air and steam. *Energy & Fuels*, 27(6):3274–3282, 2013. 2.3.1

[37] I Janajreh and M Al Shrah. Numerical and experimental investigation of downdraft gasification of wood chips. *Energy Conversion and Management*, 65:783–792, 2013. 2.3.1

[38] David Ting. *Basics of engineering turbulence*. Academic Press, 2016. 2.3.1

[39] Augustina Ephraim, Victor Pozzobon, Olivier Louisnard, Doan Pham Minh, Ange Nzihou, and Patrick Sharrock. Simulation of biomass char gasification in a downdraft reactor for syngas production. *AIChE Journal*, 62(4):1079–1091, 2016. 2.3.1, 1

[40] PC Murugan and S Joseph Sekhar. Species–transport cfd model for the gasification of rice husk (oryza sativa) using downdraft gasifier. *Computers and electronics in agriculture*, 139:33–40, 2017. 2.3.1

[41] Umesh Kumar and Manosh C Paul. Cfd modelling of biomass gasification with a volatile break-up approach. *Chemical Engineering Science*, 195:413–422, 2019. (document), 2.3.1, 5.1.9, 5.1.11, 5.2.2, 5.11, 5.2.2, 5.2.5, 5.18, 5.2.8, 5.19, 5.2.8, 5.20, 5.2.8, 5.21, 5.2.8, 5.22, 5.23

[42] Jiri Blazek. *Computational fluid dynamics: principles and applications*. Butterworth-Heinemann, 2015. 2.3.1, 3.4.3

[43] Nathada Ngamsidhiphongsa, Pimporn Ponpesh, Artiwan Shotipruk, and Amornchai Arpornwichanop. Analysis of the imbert downdraft gasifier using a species-transport cfd model including tar-cracking reactions. *Energy Conversion and Management*, 213:112808, 2020. 2.3.1

[44] Bhoopendra Pandey, Yogesh K Prajapati, and Pratik N Sheth. Cfd analysis of biomass gasification using downdraft gasifier. *Materials Today: Proceedings*, 44:4107–4111, 2021. 2.3.1

[45] Ahmed M Salem and Manosh C Paul. Cfd modelling of spatiotemporal evolution of detailed tar species in a downdraft gasifier. *Biomass and Bioenergy*, 168:106656, 2023. 2.3.1

[46] Wei-Cheng Yan, Ye Shen, Siming You, Soong Huat Sim, Zheng-Hong Luo, Yen Wah Tong, and Chi-Hwa Wang. Model-based downdraft biomass gasifier operation and design for synthetic gas production. *Journal of Cleaner Production*, 178:476–493, 2018. 2.3.1

[47] Maria Puig-Arnavat, J Alfredo Hernández, Joan Carles Bruno, and Alberto Coronas. Artificial neural network models for biomass gasification in fluidized bed gasifiers. *biomass and bioenergy*, 49:279–289, 2013. 2.4.1

[48] CC Sreejith, C Muraleedharan, and P Arun. Performance prediction of fluidised bed gasification of biomass using experimental data-based simulation models. *Biomass Conversion and Biorefinery*, 3(4):283–304, 2013. 2.4.1

[49] Dipal Baruah, DC Baruah, and MK Hazarika. Artificial neural network based modeling of biomass gasification in fixed bed downdraft gasifiers. *Biomass and Bioenergy*, 98:264–271, 2017. 2.4.1

[50] Simon Ascher, William Sloan, Ian Watson, and Siming You. A comprehensive artificial neural network model for gasification process prediction. *Applied Energy*, 320:119289, 2022. 2.4.1

[51] M Barrio, JE Hustad, and M Fossum. A small-scale stratified downdraft gasifier coupled to a gas engine for combined heat and power production. *Progress in thermochemical biomass conversion*, pages 426–440, 2001. (document), 2.5.1, 3.1, 4.2.1.1, 4.2

[52] ZA Zainal, Ali Rifau, GA Quadir, and KN Seetharamu. Experimental investigation of a downdraft biomass gasifier. *Biomass and bioenergy*, 23(4):283–289, 2002. 2.5.1

[53] M Dogru, CR Howarth, G Akay, B Keskinler, and AA Malik. Gasification of hazelnut shells in a downdraft gasifier. *Energy*, 27(5):415–427, 2002. (document), 2.5.1, 3.3.4.6, 4.1, 4.1, 4.1, 4.2, 5.6

[54] Murat Dogru, Adnan Midilli, and Colin R Howarth. Gasification of sewage sludge using a throated downdraft gasifier and uncertainty analysis. *Fuel Processing Technology*, 75(1):55–82, 2002. (document), 2.5.1, 4.1, 4.1, 4.1, 4.2

[55] TH Jayah, Lu Aye, Robert J Fuller, and DF Stewart. Computer simulation of a downdraft wood gasifier for tea drying. *Biomass and bioenergy*, 25(4):459–469, 2003. (document), 2.5.1, 3.1, 4.2.1.1, 4.2, 4.2.1.1, 4.3, 5.6, 5.1.11, 5.2.2, 5.11, 5.2.2, 5.2.8, 5.23

[56] Tuan Haris Jayah. Evaluation of a downdraft wood gasifier for tea manufacturing in sri lanka. *Melbourne University*, 2002. 2.5.1

[57] Pengmei Lv, Zhenhong Yuan, Longlong Ma, Chuangzhi Wu, Yong Chen, and Jingxu Zhu. Hydrogen-rich gas production from biomass air and oxygen/steam gasification in a downdraft gasifier. *Renewable energy*, 32(13):2173–2185, 2007. 2.5.1, 4.1, 4.1

[58] Avdhesh Kr Sharma. Experimental study on 75 kwth downdraft (biomass) gasifier system. *Renewable Energy*, 34(7):1726–1733, 2009. 2.5.1

[59] Pratik N Sheth and BV Babu. Production of hydrogen energy through biomass (waste wood) gasification. *International journal of hydrogen energy*, 35(19):10803–10810, 2010. 2.5.1, 5.6

[60] Won Chan Park, Arvind Atreya, and Howard R Baum. Experimental and theoretical investigation of heat and mass transfer processes during wood pyrolysis. *Combustion and flame*, 157(3):481–494, 2010. 2.5.1, 5.4, 5.1.11

[61] Juan Daniel Martínez, Electo Eduardo Silva Lora, Rubenildo Viera Andrade, and René Lesme Jaén. Experimental study on biomass gasification in a double air stage downdraft reactor. *Biomass and Bioenergy*, 35(8):3465–3480, 2011. 2.5.1

[62] Catharina Erlich and Torsten H Fransson. Downdraft gasification of pellets made of wood, palm-oil residues respective bagasse: experimental study. *Applied energy*, 88(3):899–908, 2011. 2.5.1

[63] Yasuaki Ueki, Takashi Torigoe, Hirofumi Ono, Ryo Yoshiie, Joseph H Kihedu, and Ichiro Naruse. Gasification characteristics of woody biomass in the packed bed reactor. *Proceedings of the Combustion Institute*, 33(2):1795–1800, 2011. 2.5.1

[64] Sang Jun Yoon, Yung-Il Son, Yong-Ku Kim, and Jae-Goo Lee. Gasification and power generation characteristics of rice husk and rice husk pellet using a downdraft fixed-bed gasifier. *Renewable Energy*, 42:163–167, 2012. (document), 2.5.1, 3.1, 4.2.1.1, 4.3

[65] Fiseha M Guangul, Shaharin A Sulaiman, and Anita Ramli. Gasifier selection, design and gasification of oil palm fronds with preheated and unheated gasifying air. *Bioresource technology*, 126:224–232, 2012. 2.5.1

[66] Fiseha M Guangul, Shaharin A Sulaiman, and Anita Ramli. Study of the effects of operating factors on the resulting producer gas of oil palm fronds gasification with a single throat downdraft gasifier. *Renewable energy*, 72:271–283, 2014. 2.5.1

[67] Chao Gai and Yuping Dong. Experimental study on non-woody biomass gasification in a downdraft gasifier. *International Journal of hydrogen energy*, 37(6):4935–4944, 2012. 2.5.1, 5.6

[68] PP Dutta, V Pandey, AR Das, S Sen, and DC Baruah. Down draft gasification modelling and experimentation of some indigenous biomass for thermal applications. *Energy Procedia*, 54(0):21–34, 2014. (document), 2.5.1, 3.1, 4.2.1.1, 4.3

[69] Subarna Maiti, Pratap Bapat, Prasanta Das, and Pushpito K Ghosh. Feasibility study of jatropha shell gasification for captive power generation in biodiesel production process from whole dry fruits. *Fuel*, 121:126–132, 2014. 2.5.1

[70] Nerijus Striūgas, Kestutis Zakarauskas, Algis Dziugys, Robertas Navakas, and Rolandas Paulauskas. An evaluation of performance of automatically operated multi-fuel downdraft gasifier for energy production. *Applied thermal engineering*, 73(1):1151–1159, 2014. (document), 2.5.1, 3.1, 4.1, 4.1, 4.1, 4.2, 4.2.1.3, 4.6, 5.6

[71] Feiqiang Guo, Yuping Dong, Lei Dong, and Chenlong Guo. Effect of design and operating parameters on the gasification process of biomass in a downdraft fixed bed: An experimental study. *International journal of hydrogen energy*, 39(11):5625–5633, 2014. (document), 2.5.1, 4.1, 4.1, 4.1, 4.2, 5.6, 5.2.5

[72] Ana Lisbeth Galindo, Electo Silva Lora, Rubenildo Viera Andrade, Sandra Yamile Giraldo, Rene Lesme Jaén, and Vladimir Melian Cobas. Biomass gasification in a downdraft gasifier with a two-stage air supply: Effect of operating conditions on gas quality. *biomass and bioenergy*, 61:236–244, 2014. 2.5.1, 5.6

[73] Vladimirs Kirsanovs, Dagnija Blumberga, Ivars Veidenbergs, Claudio Rochas, Edgars Vigants, and Girts Vigants. Experimental investigation of downdraft gasifier at various conditions. *Energy Procedia*, 128:332–338, 2017. 2.5.1, 3.1, 4.2.1.2

[74] Darshit S Upadhyay, Anil Kumar Sakhiya, Krunal Panchal, Amar H Patel, and Rajesh N Patel. Effect of equivalence ratio on the performance of the downdraft gasifier–an experimental and modelling approach. *Energy*, 168:833–846, 2019. 2.5.1, 3.1, 4.2.1.2, 4.2.3, 4.2.3

[75] Francesco Patuzzi, Daniele Basso, Stergios Vakalis, Daniele Antolini, Stefano Piazzi, Vittoria Benedetti, Eleonora Cordioli, and Marco Baratieri. State-of-the-art of small-scale biomass gasification systems: An extensive and unique monitoring review. *Energy*, 223:120039, 2021. (document), 2.5.1, 3.1, 4.2.1.1, 4.4

[76] Muhammad Awais, Wei Li, Anjum Munir, Muhammad Mubashar Omar, and Muhammad Ajmal. Experimental investigation of downdraft biomass gasifier fed by sugarcane bagasse and coconut shells. *Biomass Conversion and Biorefinery*, 11:429–444, 2021. 2.5.1

[77] Anne Loppinet-Serani, Cyril Aymonier, and François Cansell. Current and foreseeable applications of supercritical water for energy and the environment.

ChemSusChem: Chemistry & Sustainability Energy & Materials, 1(6):486–503, 2008. 3.1

[78] Alen Horvat. *A study of the uncertainty associated with tar measurement and an investigation of tar evolution and composition during the air-blown fluidised bed gasification of torrefied and non-torrefied grassy biomass*. PhD thesis, University of Limerick, 2016. (document), 3.1

[79] Agostino Gambarotta, Mirko Morini, and Andrea Zubani. A non-stoichiometric equilibrium model for the simulation of the biomass gasification process. *Applied Energy*, 227:119–127, 2018. (document), 3.1, 4.1, 4.2.4, 4.4, 4.13

[80] Anna Strandberg, Per Holmgren, David R Wagner, Roger Molinder, Henrik Wiinikka, Kentaro Umeki, and Markus Broström. Effects of pyrolysis conditions and ash formation on gasification rates of biomass char. *Energy & Fuels*, 31(6):6507–6514, 2017. 3.1.2

[81] Qianqian Guo, Beibei Yan, Yanjun Hu, Xiang Guo, Wenzhu Wu, Zhanjun Cheng, Guanyi Chen, et al. A novel reutilization of ash from biomass gasification process: Feasibility and products improvement analysis. *Fuel*, 339:127386, 2023. 3.1.2

[82] Harold Ernest Desch, John M Dinwoodie, et al. *Timber: its structure, properties and utilisation.* Number Ed. 6 in 1. MacMillan Press Ltd., 1981. 3.1.3.1

[83] Cement Science. What is density? how to distinguish different density definitions? https://www.cementscience.com/2013/03/what-is-density-how-to-distinguish-different-density-definitions.html, March 2013. (document), 3.2

[84] James E Funk and Dennis R Dinger. *Predictive process control of crowded particulate suspensions: applied to ceramic manufacturing*. Springer Science & Business Media, 2013. (document), 3.3

[85] M La Villetta, M Costa, and N Massarotti. Modelling approaches to biomass gasification: A review with emphasis on the stoichiometric method. *Renewable and Sustainable Energy Reviews*, 74:71–88, 2017. 3.1.3.2, 3.1.3.3, 3.3.2.1, 3.3.2.2, 3.3.2.3, 3.3.4.1, 3.3.4.2, 3.3.4.3, 3.3.4.4, 4.2.2

[86] Robert T Balmer. *Modern engineering thermodynamics-textbook with tables booklet*. Academic Press, 2011. 3.1.3.2, 3.1.3.3, 4.1, 4.1, 4.1

[87] Marcio L de Souza-Santos. *Solid fuels combustion and gasification: modeling, simulation*. CRC Press, 2010. 3.1.3.2, 3.1.3.3, 3.3.4.2

[88] SA Channiwala and PP Parikh. A unified correlation for estimating hhv of solid, liquid and gaseous fuels. *Fuel*, 81(8):1051–1063, 2002. 3.1.3.2

[89] Osamu Kitani, Carl W Hall, and Klaus Wagener. *Biomass handbook*. Gordon and Breach Science Publishers, 1989. 3.1.3.3

[90] Henrik Thunman, Fredrik Niklasson, Filip Johnsson, and Bo Leckner. Composition of volatile gases and thermochemical properties of wood for modeling of fixed or fluidized beds. *Energy & Fuels*, 15(6):1488–1497, 2001. 3.1.3.3, 3.1.3.3, 3.2

[91] BM Jenkins. Physical properties of biomass. *Biomass handbook*, pages 860–891, 1989. 3.1.3.3, 3.1.3.3, 3.2

[92] Anton TenWolde, J Dobbin McNatt, and Lorraine Krahn. Thermal properties of wood and wood panel products for use in buildings. Technical report, Forest Service, Madison, WI (USA). Forest Products Lab., 1988. 3.1.3.3, 3.1.3.3, 3.2

[93] AAP Susastriawan, Harwin Saptoadi, et al. Small-scale downdraft gasifiers for biomass gasification: A review. *Renewable and Sustainable Energy Reviews*, 76:989–1003, 2017. 1, 3

[94] FN Sidek, NAF Abdul Samad, and S Saleh. Review on effects of gasifying agents, temperature and equivalence ratio in biomass gasification process. In *IOP Conference Series: Materials Science and Engineering*, volume 863, page 012028. IOP Publishing, 2020. (document), 3.4

[95] L Douglas Smoot and Philip J Smith. *Coal combustion and gasification*. Springer Science & Business Media, 2013. 3.3.3

[96] Javier Gil, María P Aznar, Miguel A Caballero, Eva Francés, and José Corella. Biomass gasification in fluidized bed at pilot scale with steam- oxygen mixtures. product distribution for very different operating conditions. *Energy & Fuels*, 11(6):1109–1118, 1997. 3.3.4.2

[97] Jorge Ancheyta. *Modeling of processes and reactors for upgrading of heavy petroleum*. CRC Press, 2013. 3.3.4.2

[98] Sérgio Ferreira, Eliseu Monteiro, Paulo Brito, and Cândida Vilarinho. A holistic review on biomass gasification modified equilibrium models. *Energies*, 12(1):160, 2019. 3.3.4.2, 3.4.1, 3.4.1.1

[99] KG Mansaray, AE Ghaly, AM Al-Taweel, F Hamdullahpur, and VI Ugursal. Air gasification of rice husk in a dual distributor type fluidized bed gasifier. *Biomass and bioenergy*, 17(4):315–332, 1999. 3.3.4.3

[100] Ian Narvaez, Alberto Orio, Maria P Aznar, and Jose Corella. Biomass gasification with air in an atmospheric bubbling fluidized bed. effect of six operational variables on the quality of the produced raw gas. *Industrial & Engineering Chemistry Research*, 35(7):2110–2120, 1996. 3.3.4.3

[101] TB Reed, R Walt, S Ellis, A Das, and S Deutch. Superficial velocity–the key to downdraft gasification. *Overend, R., and Chornet, E., Biomass–a Growth Opportunity in Green Energy, Pergamon*, 1999. 3.3.4.5

[102] JPA Neeft, HAM Knoef, Uwe Zielke, K Sjöström, Philipp Hasler, PA Simell, MA Dorrington, L Thomas, N Abatzoglou, S Deutch, et al. Guideline for sampling and analysis of tar and particles in biomass producer gases. *Energy project ERK6-Ct199-2002 www. tarweb. net*, 1999. 3.3.5

[103] A Kushwah, TR Reina, and M Short. Modelling approaches for biomass gasifiers: A comprehensive overview. *Science of the Total Environment*, page 155243, 2022. (document), 3.5, 3.3.5

[104] PH Hasler and Th Nussbaumer. Gas cleaning for ic engine applications from fixed bed biomass gasification. *Biomass and bioenergy*, 16(6):385–395, 1999. 3.5

[105] Thomas A Milne, Robert J Evans, and N Abatzaglou. Biomass gasifier"tars": their nature, formation, and conversion. Technical report, National Renewable Energy Laboratory, Golden, CO (US), 1998. 3.5

[106] Jun Han and Heejoon Kim. The reduction and control technology of tar during biomass gasification/pyrolysis: an overview. *Renewable and sustainable energy reviews*, 12(2):397–416, 2008. 3.5

[107] Ludwig Briesemeister, Michael Kremling, Sebastian Fendt, and Hartmut Spliethoff. Air-blown entrained-flow gasification of biomass: influence of operating conditions on tar generation. *Energy & fuels*, 31(10):10924–10932, 2017. 3.5

[108] Abdelmalik M Shakorfow. Operating and performance gasification process parameters. *Int. J. Sci. Res*, 5(6):1768–1775, 2016. 2, 5

[109] Tapas Kumar Patra and Pratik N Sheth. Biomass gasification models for downdraft gasifier: A state-of-the-art review. *Renewable and Sustainable Energy Reviews*, 2015. 3.4.2, 3

[110] Marwan Darwish and Fadl Moukalled. *The finite volume method in computational fluid dynamics: an advanced introduction with OpenFOAM® and Matlab®*. Springer, 2016. 3.4.3, 3.4.3

[111] Clayton T Crowe, John D Schwarzkopf, Martin Sommerfeld, and Yutaka Tsuji. *Multiphase flows with droplets and particles*. CRC press, 2011. 2

[112] Maasoud Kaviany. *Principles of heat transfer in porous media*. Springer Science & Business Media, 2012. 3.4.3, 3.4.3, 3.4.3, 3.4.3, 5.1.1, 5.1.1, 5.4

[113] Yiqun Wang and Lifeng Yan. Cfd studies on biomass thermochemical conversion. *International journal of molecular sciences*, 9(6):1108–1130, 2008. 3.4.3, 5.1.3

[114] Avdhesh Kr Sharma. Modeling and simulation of a downdraft biomass gasifier 1. model development and validation. *Energy conversion and management*, 52(2):1386–1396, 2011. 4.1, 5.4, 5.1.10

[115] H Perry Robert, W Green Don, and O Maloney James. Perry's chemical engineers' handbook. *Nova Iorque*, 1984. (document), 4.1

[116] Rufei Wei, Haiming Li, Yulong Chen, Yulin Hu, Hongming Long, Jiaxin Li, and Chunbao Charles Xu. Environmental issues related to bioenergy. *Comprehensive Renewable Energy*, 2020. 4.1

[117] A Ibrahim, S Veremieiev, and P.H. Gaskell. Equilibrium model solver (ems), May 2022. Mendeley Data, Version 1, DOI: 10.17632/jtwtrbhfcb.1. 4.1

[118] Victoria Maxim, Calin-Cristian Cormos, Ana-Maria Cormos, and Serban Agachi. Mathematical modeling and simulation of gasification processes with carbon capture and storage (ccs) for energy vectors poly-generation. In *Computer Aided Chemical Engineering*, volume 28, pages 697–702. Elsevier, 2010. 4.1

[119] A Ibrahim, S Veremieiev, and PH Gaskell. An advanced, comprehensive thermochemical equilibrium model of a downdraft biomass gasifier. *Renewable Energy*, 194:912–925, 2022. (document), 4.2, 4.3, 4.4, 5.11, 5.2.2, 5.23

[120] XT Li, JR Grace, CJ Lim, AP Watkinson, HP Chen, and JR Kim. Biomass gasification in a circulating fluidized bed. *Biomass and bioenergy*, 26(2):171–193, 2004. 4.2.1.1

[121] Lorenzo Damiani and Angela Trucco. Biomass gasification modelling: an equilibrium model, modified to reproduce the operation of actual reactors. In *ASME Turbo Expo 2009: Power for Land, Sea, and Air*, pages 493–502. American Society of Mechanical Engineers Digital Collection, 2009. 4.2.1.1

[122] Manish Kumar, Bireswar Paul, and Dhananjay Singh Yadav. Effect of moisture content and equivalence ratio on the gasification process for different biomass fuel. *International Journal of Mechanical Engineering and Technology*, 7(6), 2016. 4.2.1.2

[123] Young-il Lim and Uen-Do Lee. Quasi-equilibrium thermodynamic model with empirical equations for air–steam biomass gasification in fluidized-beds. *Fuel processing technology*, 128:199–210, 2014. 4.2.1.3

[124] Vladimirs Kirsanovs, A Zandeckis, Dagnija Blumberga, and Ivars Veidenbergs. The influence of process temperature, equivalence ratio and fuel moisture content on gasification process: A review. In *Proceedings of the 27th International Conference on Efficiency, Cost, Optimization, Simulation and Environmental Impact of Energy Systems—ECOS, Turku, Finland*, 2014. 4.2.2

[125] Rizqi Fitri Naryanto, Hiroshi Enomoto, Anh Vo Cong, Kazuki Fukadu, Zheng Zong, Mera Kartika Delimayanti, Chuntima Chunti, and Reiji Noda. The effect of moisture content on the tar characteristic of wood pellet feedstock in a downdraft gasifier. *Applied Sciences*, 10(8):2760, 2020. 4.2.2

[126] E Shayan, V Zare, and IJEC Mirzaee. Hydrogen production from biomass gasification; a theoretical comparison of using different gasification agents. *Energy Conversion and management*, 159:30–41, 2018. 4.2.3

[127] Zhiyi Yao, Siming You, Tianshu Ge, and Chi-Hwa Wang. Biomass gasification for syngas and biochar co-production: Energy application and economic evaluation. *Applied Energy*, 209:43–55, 2018. 4.2.3

[128] Zi-Kui Liu, John Ågren, and Mats Hillert. Application of the le chatelier principle on gas reactions. *Fluid phase equilibria*, 121(1-2):167–177, 1996. 4.2.3

[129] SA Salaudeen, P Arku, and Animesh Dutta. Gasification of plastic solid waste and competitive technologies. In *Plastics to Energy*, pages 269–293. Elsevier, 2019. 4.2.3

[130] Min-Hwan Cho, Tae-Young Mun, and Joo-Sik Kim. Air gasification of mixed plastic wastes using calcined dolomite and activated carbon in a two-stage gasifier to reduce tar. *Energy*, 53:299–305, 2013. 4.2.3

[131] Rui Xiao, Baosheng Jin, Hongcang Zhou, Zhaoping Zhong, and Mingyao Zhang. Air gasification of polypropylene plastic waste in fluidized bed gasifier. *Energy Conversion and Management*, 48(3):778–786, 2007. 4.2.3

[132] Stephen Whitaker. Simultaneous heat, mass, and momentum transfer in porous media: a theory of drying. In *Advances in heat transfer*, volume 13, pages 119–203. Elsevier, 1977. 5.1.1

[133] Kenneth K Kuo. Principles of combustion. *Principles of Combustion*, 1986. 5.1.2

[134] Noriaki Wakao and Seiichirō Kagei. *Heat and mass transfer in packed beds*, volume 1. Taylor & Francis, 1982. 5.1.3

[135] JM Zhao and LH Liu. Radiative transfer equation and solutions. *Handbook of Thermal Science and Engineering; Springer International Publishing: Cham, Switzerland*, pages 933–978, 2018. 5.1.3

[136] BV Antohe and JL Lage. A general two-equation macroscopic turbulence model for incompressible flow in porous media. *International Journal of Heat and Mass Transfer*, 40(13):3013–3024, 1997. 5.1.4

[137] Yan Jin, M-F Uth, Andrey V Kuznetsov, and Heinz Herwig. Numerical investigation of the possibility of macroscopic turbulence in porous media: a direct numerical simulation study. *Journal of Fluid Mechanics*, 766:76–103, 2015. 5.1.4

[138] Yan Jin and Andrey V Kuznetsov. Turbulence modeling for flows in wall bounded porous media: an analysis based on direct numerical simulations. *Physics of Fluids*, 29(4), 2017. 5.1.4

[139] Lee Kum-Bae and John R Howell. Theoretical and experimental heat and mass transfer in highly porous media. *International journal of heat and mass transfer*, 34(8):2123–2132, 1991. 5.1.4

[140] DA Nield. The limitations of the brinkman-forchheimer equation in modeling flow in a saturated porous medium and at an interface. *International Journal of Heat and Fluid Flow*, 12(3):269–272, 1991. 5.1.4

[141] E Shashi Menon. *Transmission pipeline calculations and simulations manual*. Gulf Professional Publishing, 2014. 5.2

[142] Brian D Wood, Xiaoliang He, and Sourabh V Apte. Modeling turbulent flows in porous media. *Annual Review of Fluid Mechanics*, 52:171–203, 2020. 5.2, 5.1.4

[143] Avdhesh K Sharma, MR Ravi, and S Kohli. Modelling product composition in slow pyrolysis of wood. *SESI J*, 16(1):1–11, 2006. 5.1.7, 5.1.7, 5.1.7, 3

[144] CA Zaror and DL Pyle. The pyrolysis of biomass: A general review. *Proceedings of the Indian Academy of Sciences Section C: Engineering Sciences*, 5:269–285, 1982. 5.1.7

[145] David A Tillman. *Wood Combustion: Principle, processes, and economics*. Elsevier, 2012. 5.1.7

[146] Rolando Zanzi. *Pyrolysis of biomass. Rapid pyrolysis at high temperature. Slow pyrolysis for active carbon preparation.* PhD thesis, Kemiteknik, 2001. (document), 5.3

[147] C Dejtrakulwong and S Patumsawad. Four zones modeling of the downdraft biomass gasification process: effects of moisture content and air to fuel ratio. *Energy Procedia*, 52:142–149, 2014. 5.4

[148] Gary L Borman and Kenneth W Ragland. Combustion engineering, 1998. 5.1.8

[149] Alberto Gómez-Barea and Babu Leckner. Modeling of biomass gasification in fluidized bed. *Progress in Energy and Combustion Science*, 36(4):444–509, 2010. 5.5

[150] I Petersen and J Werther. Experimental investigation and modeling of gasification of sewage sludge in the circulating fluidized bed. *Chemical Engineering and Processing: Process Intensification*, 44(7):717–736, 2005. 5.5

[151] Zhongqing Ma, Jiewang Ye, Chao Zhao, and Qisheng Zhang. Gasification of rice husk in a downdraft gasifier: the effect of equivalence ratio on the gasification performance, properties, and utilization analysis of byproducts of char and tar. *BioResources*, 10(2):2888–2902, 2015. 5.6

[152] R Byron Bird. Transport phenomena. *Appl. Mech. Rev.*, 55(1):R1–R4, 2002. 5.2

[153] Jay L Devore. Probability and statistics for engineering and the sciences. -, 2008. 5.2.1

[154] Jin-Shi Chen and Wesley W Gunkel. Modeling and simulation of co-current moving bed gasification reactors—part ii. a detailed gasifier model. *Biomass*, 14(2):75–98, 1987. 5.2.8

[155] Maryem Dhrioua, Kaouther Ghachem, Walid Hassen, Ahmed Ghazy, Lioua Kolsi, and Mohamed Naceur Borjini. Simulation of biomass air gasification in a bubbling fluidized bed using aspen plus: A comprehensive model including tar production. *ACS omega*, 7(37):33518–33529, 2022. 5.2.10

[156] Bahram Haddadi Sisakht, Christian Jordan, and Michael Harasek. Openfoam® basic training, 2019. A

[157] MP Escudier, PJ Oliveira, and RJ Poole. Turbulent flow through a plane sudden expansion of modest aspect ratio. *Physics of Fluids*, 14(10):3641–3654, 2002. B.1, B.1, B.1

[158] SRN De Zilwa, L Khezzar, and JH Whitelaw. Flows through plane sudden-expansions. *International Journal for Numerical Methods in Fluids*, 32(3):313–329, 2000. B.1

APPENDIX A

Overview of OpenFOAM

OpenFOAM is an open-source Computational Fluid Dynamics (CFD) software known as "Open source Field Operation and Manipulation." This powerful tool is built in C++ and serves as a toolbox for crafting customized numerical solvers. It comes equipped with pre- and post-processing utilities to tackle a wide array of continuum mechanics problems, with a significant emphasis on CFD applications. OpenFOAM finds widespread use in research organizations, academic institutions, and industries.

However, in the realm of biomass gasification, it hasn't been as frequently employed. One key factor is that many users tend to gravitate toward the commercial software package Ansys Fluent. This preference arises due to Fluent's perceived simplicity in handling fixed bed gasification problems.

Within OpenFOAM's extensive library, you can discover numerous numerical solvers designed to address specific problem scenarios. Nevertheless, users with a solid foundation in the underlying methods, physics, and programming techniques can craft their custom solvers and utilities by building upon existing ones. The choice of which solver to use hinges on how closely the problem being modeled aligns with the available solver options.

In the upcoming section, we will delve into the functionalities offered by Open-

FOAM and provide guidance on pre-processing, running simulations, and post-processing results for a standard test case problem. Typically, the steps involved in a CFD procedure revolve around numerical algorithms capable of addressing fluid flow challenges and encompass three main components [156]:

1. Pre-processing; whereby the definition of the geometry of the region of interest is structured which is referred to as the computational domain. It includes also grid generation, which is the sub-division of the flow region into a number of smaller, non-overlapping sub-domains called a mesh (a grid of cells or control volumes). This is extremely important since the solution of a flow problem is defined at nodes or cell centres inside each cell, resulting in the accuracy of a CFD solution depending heavily on the number of cells in the grid. Typically, the larger the number of cells, the better the solution accuracy. Meshes with optimal results are often non-uniform, with a finer mesh in areas where large variations occur and coarser in regions with relatively minimal change, and will be explained in heavier detail henceforth. Furthermore, pre-processing allows for the definition of fluid properties and the specification of the appropriate chemical and physical boundary conditions at cells which coincide with or touch the domain boundary.

2. Solver; whereby the finite volume method will be implemented as it is central to the most well-established CFD solvers a procedural outline will follow in a sequence of steps mentioned previously.

3. Post-processing; whereby an analysis and visualisation are carried out on the results obtained from the model. Typical elements of post-processing are: definition of suitable cutting planes for visualisation, contour plots of properties/flow variables, vector plots, streamlines, line plots and balances. Several post-processing tools exist including the commercial fluent built-in processing tool, ensight and TecPlot, whereas open source tools include Paraview and SALOME and OpenFOAM's GNUPLOT option.

The basic directory structure for an OpenFOAM case, containing the minimum set of files required to run an application is as such:

- A **constant** directory; containing a full description of the case mesh and files specifying physical properties for the intended application.

- A **system** directory; for setting parameters associated with the solution procedure. It contains a file responsible for setting run control parameters including start/end time, time step and parameters for data output. fvSolution and fvSchemes are also files in this directory, responsible for setting equation solvers, tolerances and other algorithm controls and selecting discretisation schemes used in the solution at run-time.

- The **'time'** directories; containing individual files of data for particular fields. The data can either be initial values and boundary conditions that the user must specify to define the problem, or results written to file by OpenFOAM. The OpenFOAM fields must always be initialised, even when the solution does not require it, as in steady state problems. Since simulations are normally started from time $t = 0$, the initial conditions are usually stored in a directory named '0'.

Meshes are an integral part of the numerical solution in OpenFOAM and must assure certain criteria to ensure a valid and accurate solution. Meshes can be created in OpenFOAM using a range of generating utilities including blockMesh; a utility for generating simple meshes of blocks of hexahedral cells and snappyHexMesh; a utility for generating complex meshes of hexahedral and split-hexahedral cells automatically from triangulated surface geometries. Furthermore, there are options available for conversion of a mesh, generated by third-party products into a format in which OpenFOAM can read. In this thesis and for the models developed hereafter, the blockMesh utility is used. blockMesh creates parametric meshes with grading and curved edges. The mesh is generated from a dictionary file named *blockMeshDict* located in the **constant** directory of the case. blockMesh reads this dictionary, generates the mesh and writes out the mesh data to *points*, *faces*, *cells* and *boundary* files in the same directory. The purpose of this utility is to decompose the domain geometry into a set of 1 or more three-dimensional, hexahedral blocks, where edges of the blocks can be either straight lines, arcs or splines. Each block of the geometry

is defined by 8 vertices, one at each corner of a hexahedron.

A.1 porousGasificationFOAM

A.1.1 Solver - porousGasificationFoam

porousGasificationFoam is an OpenFOAM solver, capable of comprehensive simulation of thermochemical conversion processes in porous media. It is an extension of the built-in solver **reactingFoam** and integrates gas flow through a porous media with models of homogeneous and heterogeneous chemical reactions. As previously detailed, the collection of solvers and libraries embedded in the standard OpenFOAM distributions are capable of modelling pyrolysis using the **fireFoam** solver and chemical reactions using the **reactingFoam** solver and even gasification in fluidised bed using the **coalChemistryFoam** solver, but none of them are appropriate and usable in case of fixed-bed applications with heterogeneous reactions.

As such, **porousGasificationFoam**, along with its supported library *porousGasificationMedia* are developed to simulate an extensive range of processes and applications related to heterogeneous reactions. Transient flow through and around porous media, heat and mass transfer between gas and solid phases, modifiable thermochemical properties in porous media and homogeneous and heterogeneous reactions with enthalpies of reactions either defined directly or derived from the enthalpies of formation were implemented and integrated into the solver. The **porousGasificationFoam** solver solves coupled gas and solid phase conservation equations - see section 5.1 in Chapter 5 through the utilisation of the porous media assumption. The porous media is defined by two fields: scalar porosity field (ϵ, porosityF in the code) and tensor viscous resistance field (D, Df in the code). The solver allows for the complete gasification of the biomass porous media in some volume of the computational domain, effectively changes from occupied by the biomass porous media to occupied by the gas phase only as ϵ reaches 1. The solution algorithm for the gas phase equations is based on the algorithm used in the transient solver **reactingFoam**, which is designed for reacting laminar or turbulent flows. The solid phase equations are incorporated into the code to establish the **porousGasifica-**

tionFoam solver, namely heterogeneous reaction model, porous media model and a radiation model. The solver was developed by Zuk et al. [7] and their contributions towards CFD modelling in this thesis has been extensively recognised.

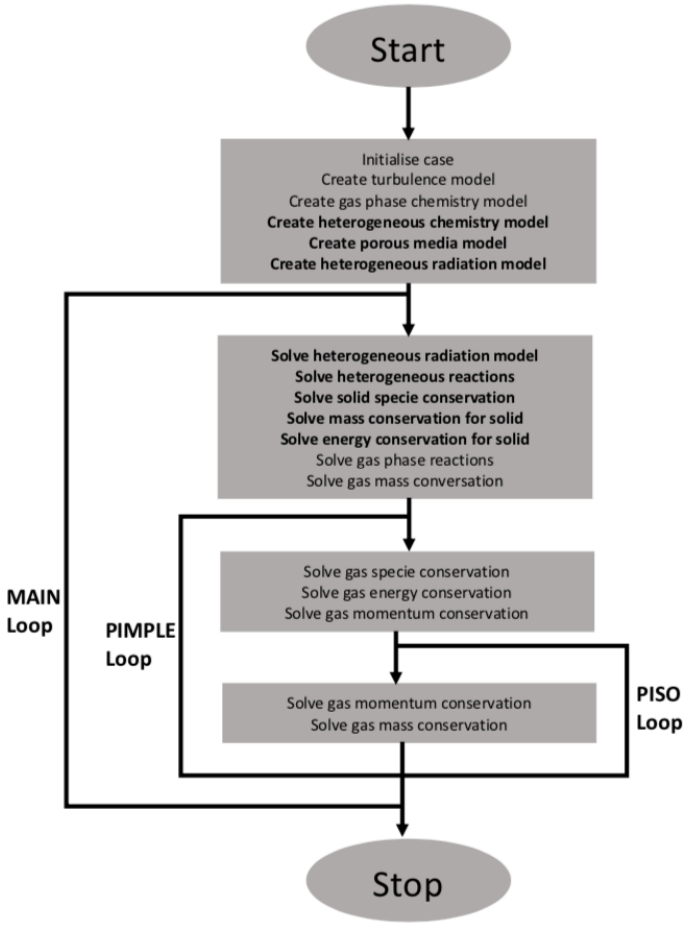

Figure A.1: Schematic showing the main loop of the **porousGasificationFoam** solver featuring the PIMPLE algorithm. New additions in comparison to the **reactingFoam** solver are highlighted with bold font.

Fig. A.1 presents the procedure of iteratively solved equation algorithm in the **porousGasificationFoam** solver. The steps for **reactingFoam** are presented in regular font, while the bold font is used to highlight the elements of the solution algorithm new in the **porousGasificationFoam** solver. The solution starts from the initialisation of fields, physical models and variables, which are turbulence and gas phase chemical reaction model prevalent in **reactingFoam** and heterogeneous reaction model, porous media model, and radiation model that the new solver introduces.

The main computational loop begins with a block of calculations required to evaluate the source terms for computing transport equations. This block involves the calculation of the heat transfer due to radiation, source terms from heterogeneous reactions, conservation of solid species, conservation of solid mass with the evolution of porosity, conservation of solid energy, and the source terms from the gas phase reactions.

Next, the main computational loop enters the PIMPLE (PISO-SIMPLE) loop, used for computing the pressure-velocity coupling. The loop includes gas species conservation equations and gas phase energy conservation equation. The PISO pressure-velocity coupling involves solving the continuity and momentum equations. It is corrected for the presence of the porous medium in accord with OpenFOAM practice for the flow through the porous media (isotropic part of viscous resistance is included implicitly and anisotropic explicitly in the velocity solution matrix). The only difference is that the porous medium is contained inside the computational domain and does not involve a separate domain on its own. Therefore, the additional resistance due to porosity is added only to the computational cells where the porous medium is present. The gas-solid interaction in the solver can be switched on or off in an appropriate control dictionary, in which case when switched off, the **reactingFoam** solver functionality is retrieved [7].

A.1.2 Solver library - porousGasificationMedia

The library *porousGasificationMedia* that underlies the **porousGasificationFoam** solver constitutes three separate parts:

1. *porousReactingMedia*: is the definition of a porous media and its mechanical properties.

2. *thermophysicalModels*: is the definition of thermal, chemical, and radiation properties of the solid phase.

3. *heterogeneousPyrolysisModels*: is assembling the previous two into the porous media model.

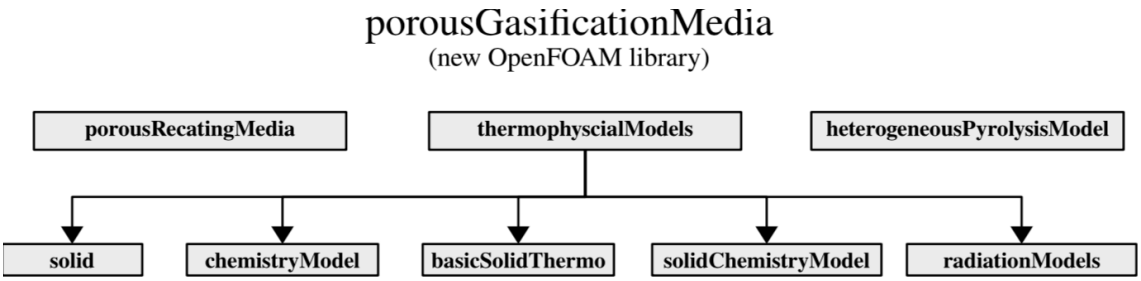

Figure A.2: Structure of the porousGasificationMedia library [7].

The structure is shown schematically in Fig. A.2. The organisation of a case file highlighting with bold borders the elements introduced from the **porousGasificationFoam** solver and those involving new elements in addition to the files present in *reactingFoam* from the main OpenFOAM distribution are presented in Fig. A.3. A thorough analysis and discussion of the different fields containing initial and boundary conditions for the gas and solid phases as well as the thermophysical models can be found in [7].

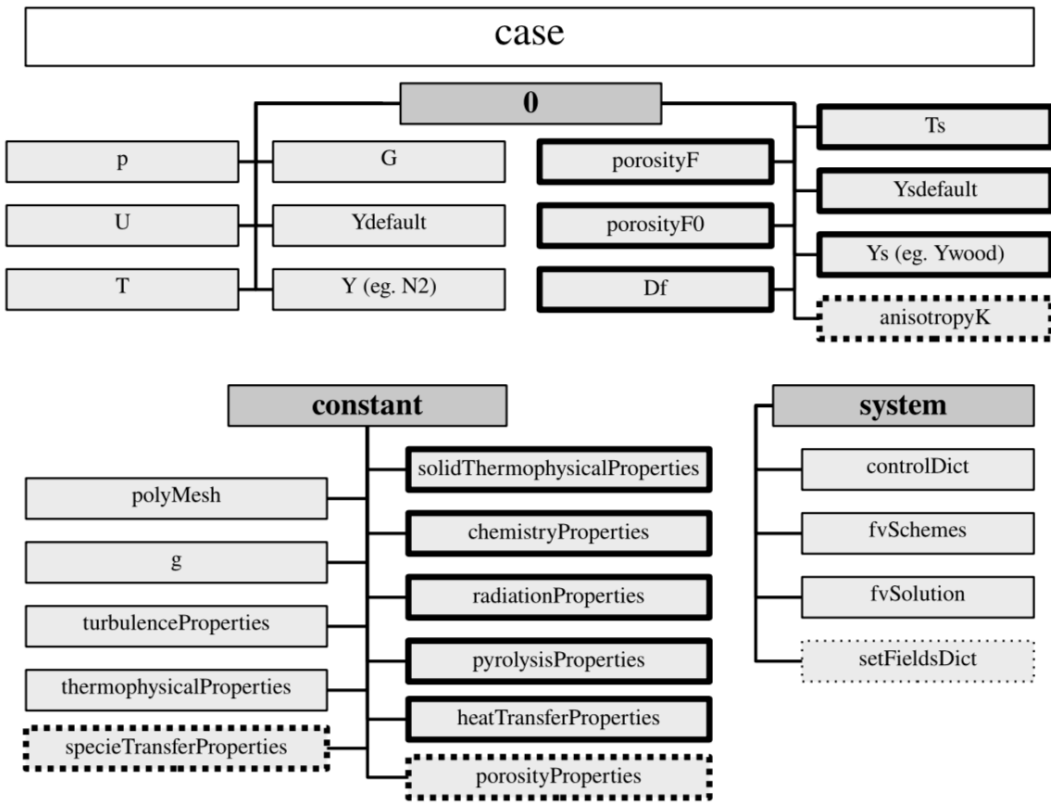

Figure A.3: Structure of the dictionaries and files in the computational case folder. Inside the bold black frames are files modified or introduced (bold borders) with the new solver, while dashing denotes files that are optional to specify [7].

In the *porousGasificationMedia* library, the *porousReactingMedia* directory is responsible for the implementation of the porosity model based on Darcy's law, highlighted and discussed in section 3.4.3. This model is introduced primarily by two volume fields in the computational domain; volScalarField porosityF, which denotes the void fraction ϵ and volTensorField Df, which denotes linear viscous resistance tensor D in Eq (5.3) and can be arbitrarily defined in space. Additionally there is the *thermophysicalModels* directory that contains the various submodels interacting with the porous media such as numerical procedures and interfaces to the OpenFOAM routines necessary for solving Ordinary Differential Equations and radiational models containing procedures to calculate source terms for the radiative heat transfer. Finally, the directory *pyrolysisModels* creates and manages all necessary fields for the modelling of the solid phase and schedules calculations of conservation equations for the solid phase, which will be detailed later on in section 5.1. it computes solid species evolution Eq. (5.6), mass conservation of the solid phase Eq. (5.7), and energy conservation of the solid phase Eq. (5.8).

APPENDIX B

Test case simulations

Following the development of the equilibrium model, test case simulations were conducted using OpenFOAM to become familiar with the software. A sudden expansion test case simulation was created, and its results were compared with experimental data. The primary objectives of this simulation were to gain a deeper understanding of OpenFOAM's functionalities, learn how to set up and run cases, construct geometric meshes, and appropriately refine them. Additionally, the simulation aimed to develop proficiency in post-processing the results for further analysis and interpretation.

B.1 Abrupt sudden expansion

A model for a turbulent flow through a plane sudden expansion of expansion ratio $R = D/d = 4$ and aspect ratio $A = w/h = 5.33$ was developed and its results compared with that of an experimental investigation by Escudier et al. [157]. One of the main objectives of the experimental study was to investigate the assumption that nominally two-dimensional sudden expansions produce two-dimensional flows. The model is capable of implementing different turbulence models such as $k - \epsilon$ and

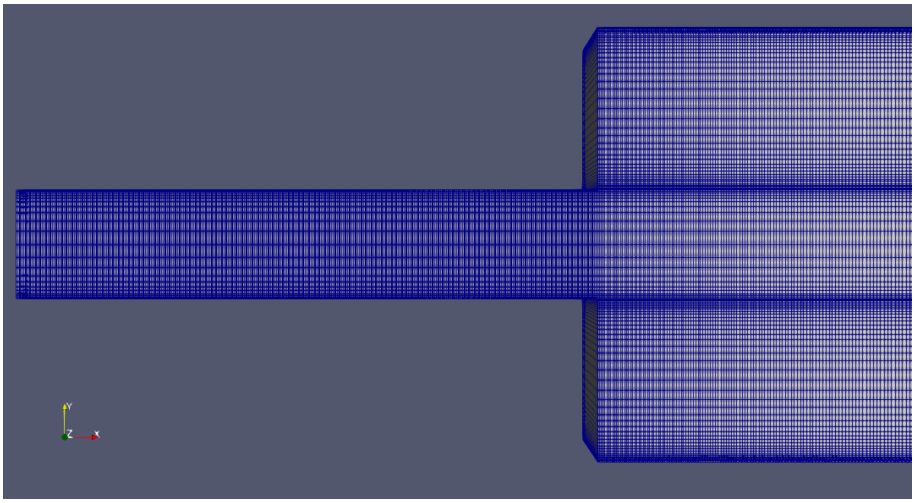

Figure B.1: Mesh of the sudden expansion geometry generated with blockMesh.

$k-\omega$ and will analyse the flows under these varying conditions. Fig. B.1 shows the geometrical mesh of the plane sudden expansion, generated with blockMesh and refined accordingly on the walls of the pipe and at the point of sudden expansion. The dimensions of the geometry, including all operating conditions such as inlet velocity, type of fluid (water) and Reynolds number were all taken from [157] in order to accurately validate their experimental results.

The Reynolds number was calculated to be 55,500 based on a mean bulk velocity $U_B = 5.57m/s$, and a duct height immediately upstream of the expansion, $d = 10mm$. Fig. B.2 shows the axial velocity contour of the simulation, proving the reported discussions of previous experimental studies that the flow downstream of the expansion is found to be asymmetric about the XZ centre plane.

Fig. B.3 shows the velocity vector plots of the simulation, evidently establishing two recirculation zones, one in the upper region and the other in the lower region. This behaviour was also observed by [157], where the maximum axial turbulence intensity occurred in the upper recirculation region with values as high as 26% of the bulk velocity at the inlet, while the lower region exhibited values close to 20%. This is also validated in the model as the upper region is much bigger and more intense than the lower one.

In order to compare the results of the model with the experimental data of [157], profiles of mean axial velocities across the expansion must be generated. As

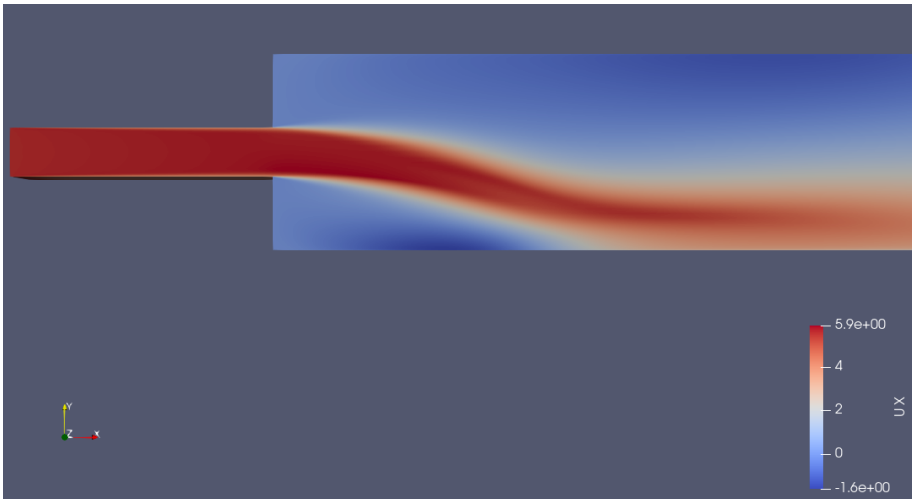

Figure B.2: Axial velocity contour for the plane sudden expansion.

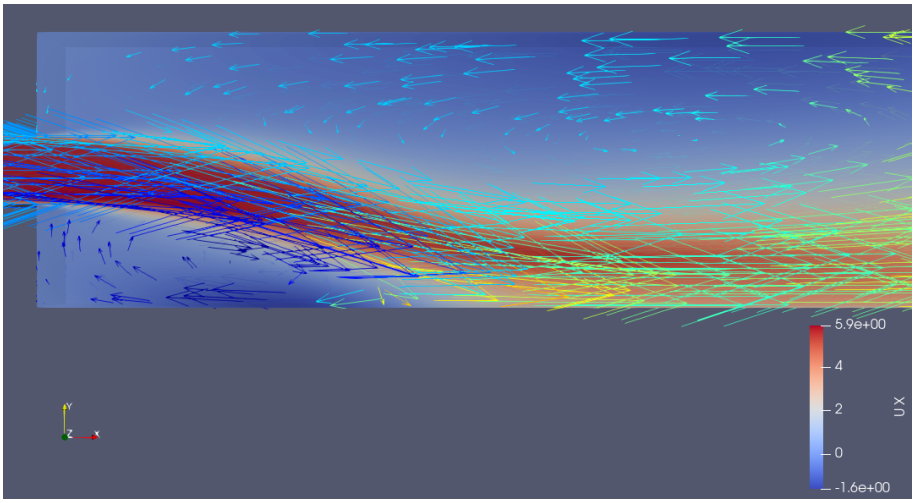

Figure B.3: Velocity vectors of the plane sudden expansion.

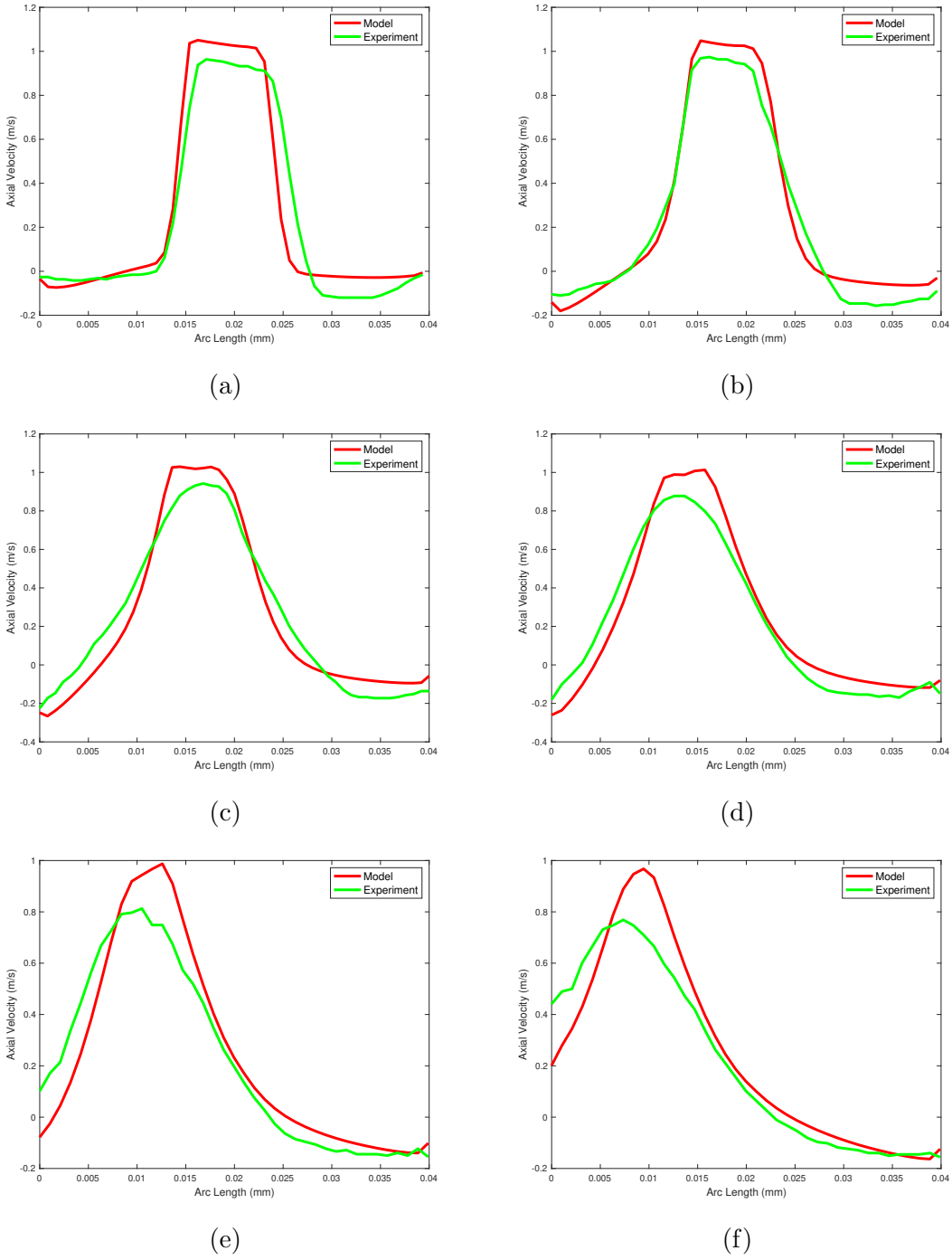

Figure B.4: Mean axial velocity comparison between model predictions and experiment for (a) 10 mm, (b) 20 mm, (c) 30 mm, (d) 40 mm, (e) 50 mm, and (f) 60 mm from the expansion.

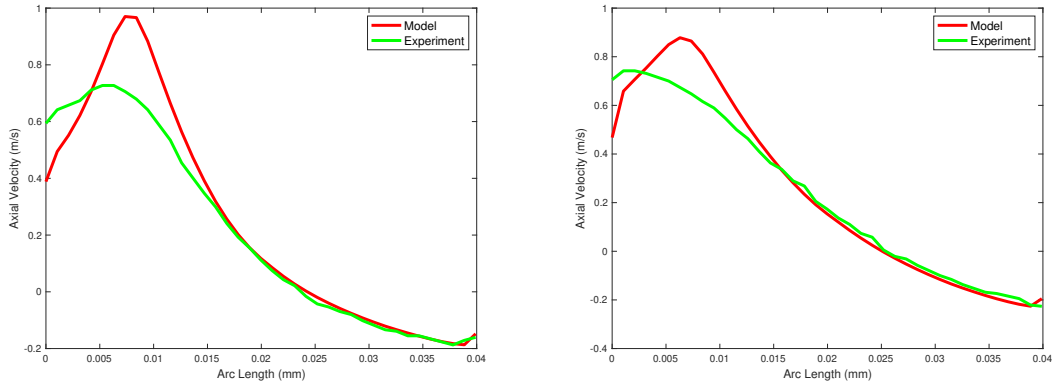

(a)

(b)

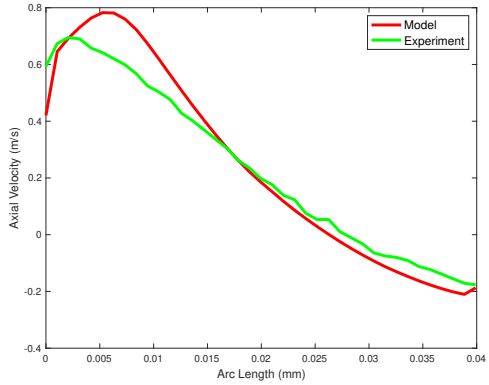

(c)

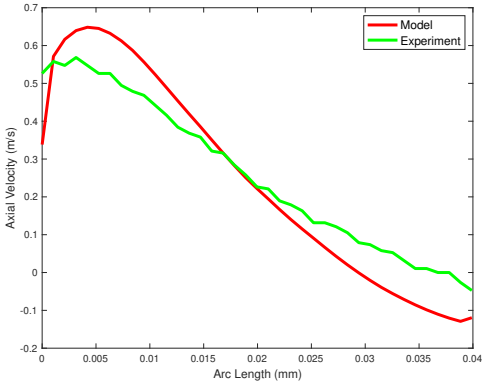

(d)

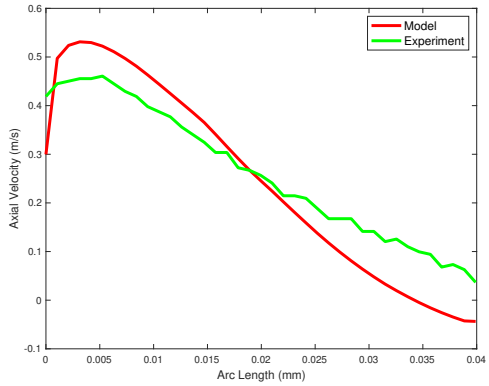

(e)

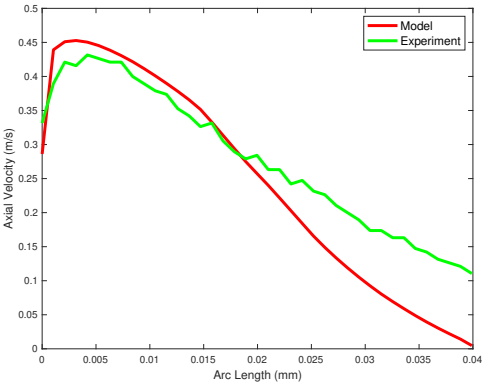

(f)

Figure B.5: Mean axial velocity comparison between model predictions and experiment for (a) 70 mm, (b) 100 mm, (c) 120 mm, (d) 150 mm, (e) 180 mm, and (f) 210 mm from the expansion.

such, distributions of mean axial velocity were obtained at 12 axial locations (10 mm, 20 mm, 30 mm, 40 mm, 50 mm, 60 mm, 70 mm, 100 mm, 120 mm, 150 mm, 180 mm and 210 mm) from the expansion. Figs. B.4 and B.5 show the comparisons, demonstrating the agreement of the model results with experimental data. An agreement can be reached that the flow is symmetrical at and close to the expansion, becoming asymmetrical the more the flow moves away from the expansion with unequal recirculation regions at the top and bottom walls in accordance with previous studies - see [157, 158].

B.2 Porous medium flow in a cylindrical gasifier

After conducting test case simulations to achieve familiarisation with the OpenFOAM software, the intricate chemical reaction scheme of the Thermo-CFD model was constructed, including the solid and gas phase reactions - see section 5.1.8 Chapter 5. It was essential that the chemical reaction scheme be tested in a simplified geometry and mesh to establish a propagating front. This procedure was significant in confirming that the chemical reaction scheme will not extinguish the porous bed.

The geometry and mesh for this study was taken from Zuk et al. [7]. The height of the slice (h_{bottom}, h_{top} = 16 cm). The boundary conditions for the system are taken:

1. Rubberwood is selected as the feedstock for the case

2. The gasifier outlet enforces a pressure outlet boundary condition, maintaining atmospheric pressure at the outlet of the gasifier, while the walls apply a zero gradient boundary condition for the pressure field.

3. The initial ϵ of the wood feedstock was assumed to be equivalent to that of biomass char (i.e. $\epsilon = 0.4$) as in the Thermo-CFD model.

4. Gas and solid phase temperatures: The porous bed is ignited at 1200 K, while the initial temperature of the air is taken at 300 K. The temperature of the occupying gas is kept at 400 K.

5. The thermophysical properties of the wood and char were taken to be the same as the case in the Thermo-CFD model.

6. The u_{air} entering from the bottom of the unit is taken to be 0.2 m/s, which is the minimum u_{air} used in the Thermo-CFD model.

Only the porosity and temperature profiles were studied in this test case simulation.

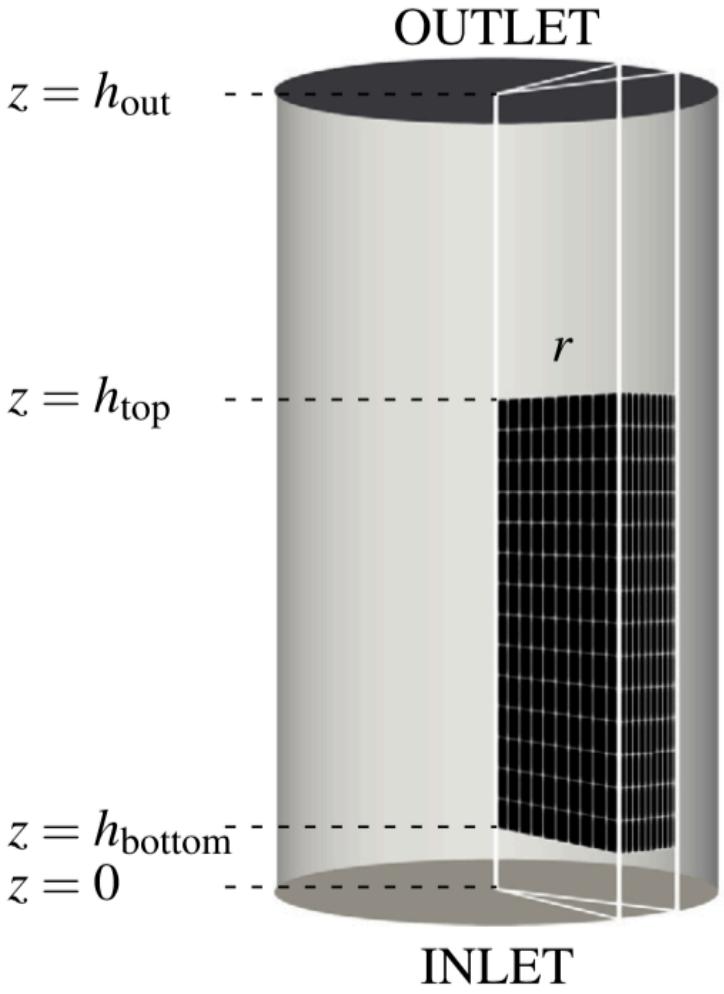

Figure B.6: Schematic of the system.

Fig. B.7 illustrates the distribution of porosity at the initial stage and subsequent stages of propagation. As depicted in Fig. B.7(a), the porosity field constitutes a distinct segment of the cylindrical unit, with an initial value of $\epsilon = 0.33$. Subsequently, as illustrated in Fig. B.7(b), it becomes apparent that over time, ϵ begins to escalate from the ignition point, indicating the progression of the chemical reaction mechanism. The observed rise in ϵ from 0.33 to approximately 0.8 signifies the

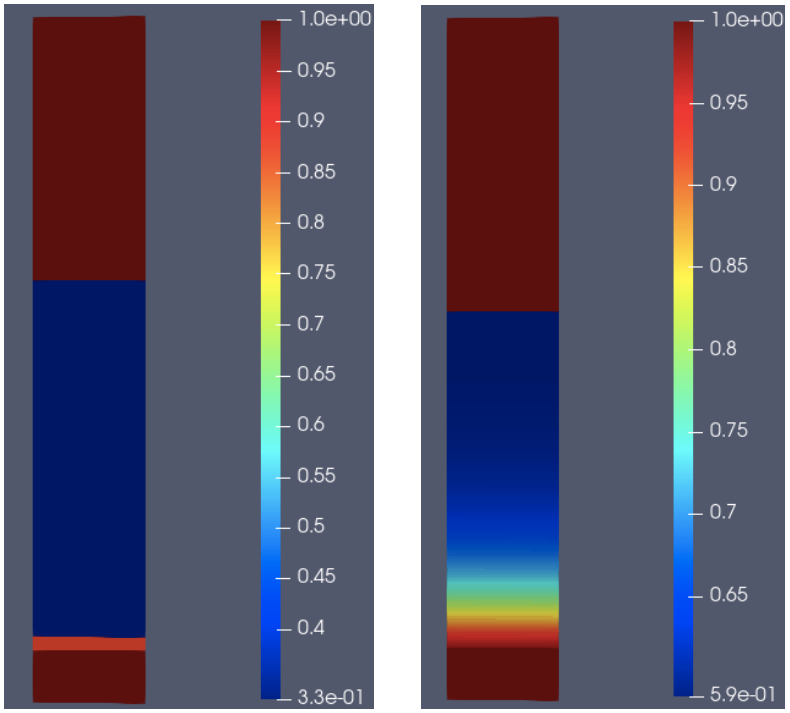

(a) (b)

Figure B.7: The porosity distribution in a cylindrical gasifier for (a) the initial condition and (b) post-propagation.

conversion of solid biomass into gas.

Fig. B.8 portrays the distribution of solid temperature both at the initial stage (Fig. B.8(a)) and subsequent stages after the establishment of the propagating front (Fig. B.8(b)). It is evident that, with the passage of time, a self-sustaining traveling front emerges, as indicated by the escalation in solid temperature from the initial ignition temperature of 1200 K to approximately 2400 K. This rise in temperature signifies the development of a sustained thermal reaction within the system, ultimately contributing to the propagation and progression of the reaction front. The observed increase in temperature highlights the progression of the thermal conversion process within the cylindrical unit, pointing towards the generation of significant heat and energy as a result of the ongoing reaction.

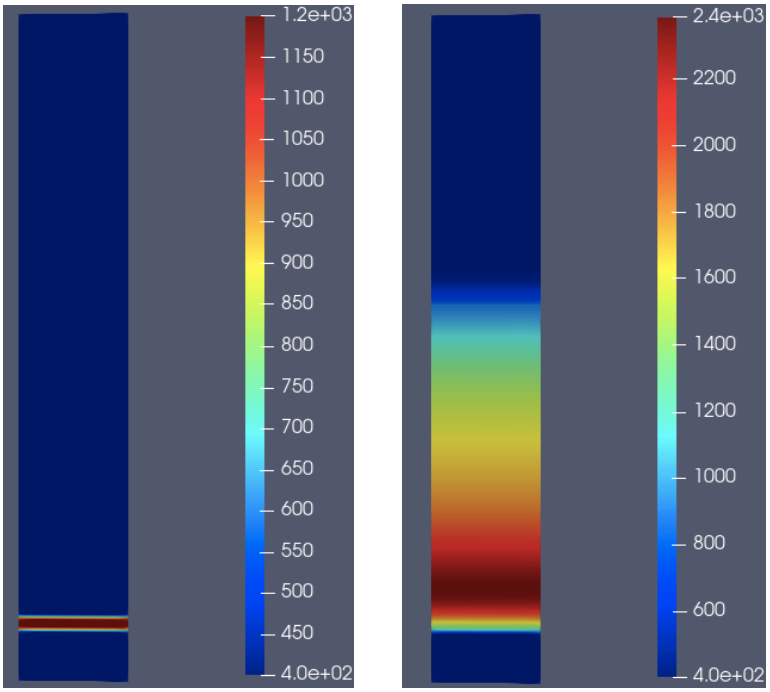

(a) (b)

Figure B.8: The solid temperature distribution in a cylindrical gasifier for (a) the initial condition and (b) post-propagation.

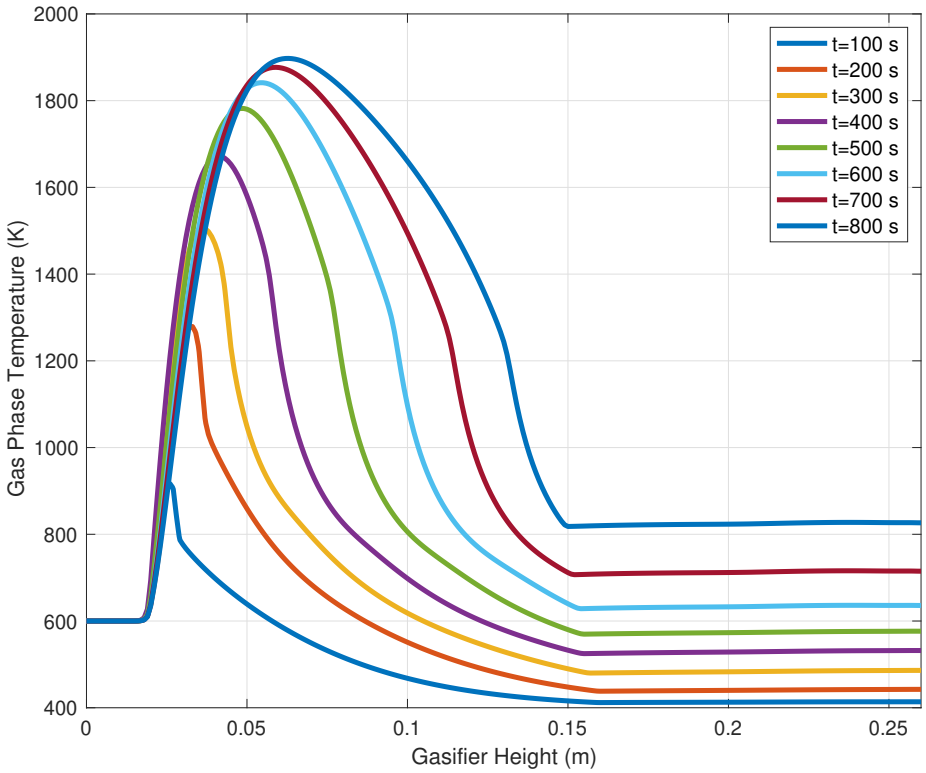

Figure B.9: Gas phase temperature showing a propagating front with increasing time along the height of the unit.

Figure B.9 demonstrates the successful formation of a propagating front using the developed chemical reaction scheme. As time progresses, the gas-phase temperature increases, leading to the propagation of the reaction front. This behaviour aligns with the trends observed in Figure B.8.

APPENDIX C

Porosity values sample calculation

Starting from Eq.(5.26), m_k^s can be expressed using the following:

$$\mathrm{m}_k^s = V_k^s \times \rho_k^s \tag{C.0.1}$$

The calculation of the porosity proceeds as follows:

- Drying zone: 81.5% dry rubberwood and 18.5% MC, therefore;

$$\mathrm{m}_{rubberwood}^s = \frac{81.5}{100}\mathrm{m}_{total} \ , \tag{C.0.2}$$

$$\mathrm{m}_{\mathrm{MC}}^s = \frac{18.5}{100}\mathrm{m}_{total} \ . \tag{C.0.3}$$

  where, $\mathrm{m}_{rubberwood}^s$, $\mathrm{m}_{\mathrm{MC}}^s$, are the masses of rubberwood and MC in the solid matrix respectively, and m_{total} the total mass occupying the solid matrix.

  Starting from an initial porosity $\epsilon = 0.4$, the fraction of the volume occupied by the solid matrix will be $1 - \epsilon$ therefore, the calculation will proceed:

$$\mathrm{m}_{rubberwood}^s = (1 - \epsilon) \times 1050 = 630 \text{ kg} \ . \tag{C.0.4}$$

Substituting the value of $\mathrm{m}^s_{rubberwood}$ into Eq. (C.0.2):

$$630 = \frac{81.5}{100}\mathrm{m}_{total} \ , \tag{C.0.5}$$

$$\mathrm{m}_{total} = 773.0061 \text{ kg} \ . \tag{C.0.6}$$

Substituting the value of m_{total} into Eq.(C.0.3):

$$\mathrm{m}^s_{\mathrm{MC}} = \frac{18.5}{100} \times 773.0061 = 143.0061 \text{ kg} \ . \tag{C.0.7}$$

Therefore, the volume occupied by the solid matrix is:

$$V^s_k = V^s_{rubberwood} + V^s_{\mathrm{MC}} = \frac{630}{1050} + \frac{143.0061}{997} = 0.7434 \ , \tag{C.0.8}$$

and consequently:

$$\epsilon = 1 - 0.7434 = 0.2566 \ . \tag{C.0.9}$$

- Pyrolysis and oxidation zones: follows the same calculation for 95% rubberwood and 5% moisture, and 100% char for the char bed.